Analysis of Current Transport and Recombination Mechanisms in Chalcopyrite-Based Thin-Film Solar Cells with RbF Treatment

vorgelegt von
M.Sc.
Alejandra Villanueva Tovar

an der Fakultät IV - Elektrotechnik und Informatik
der Technischen Universität Berlin
zur Erlangung des akademischen Grades

Doktorin der Ingenieurwissenschaften
- Dr.-Ing. -

genehmigte Dissertation

Promotionsausschuss

Vorsitzender:	Prof. Dr. Bernd Szyszka
Gutachter:	Prof. Dr. Bernd Rech
	Prof. Dr. Rutger Schlatmann
	Prof. Dr. Roland Scheer

Tag der wissenschaftlichen Aussprache: 22. Juni 2021

Berlin 2021

Abstract

In recent years, post deposition treatment (PDT) of the absorber with RbF has led to a significant improvement in the efficiency of $Cu(In,Ga)Se_2$ (CIGSe) thin-film solar cells. In this work, the influence of RbF by PDT on the recombination and current transport mechanisms was studied. Temperature-dependent current-voltage (JVT) measurements were performed with a set of CIGSe samples prepared under various preparation conditions at Helmholtz-Zentrum Berlin (HZB) and in other laboratories. Based on JVT measurements, CIGSe cells with RbF-PDT present non-ideal current-voltage ($J-V$) characteristics especially at low temperatures such as a roll-over of the diode current, a cross-over between the dark and illuminated curves, a saturation of the open-circuit voltage (V_{oc}) and, examined in detail here for the first time, a discrepancy between dark and light $J-V$s. These negative and positive (typically an increased V_{oc}) effects of PDT may derive from different physical mechanisms since these non-idealities are not necessary linked to the high efficiency presented in some measured solar cells. The open-circuit voltage (V_{oc}) can be influenced by the phototransistor effect visible at low or in some cases even at higher temperatures, reducing its value and extrapolating to lower activation energies than expected without any V_{oc} clamping.
Analysis of recombination mechanisms showed that typical CIGSe solar cells without or with RbF-PDT present dominant recombination within the bulk therefore contradicting those studies that assume a transition from interface to recombination in the bulk due to changes especially observed at or near the absorber surface after PTD. The behavior of the deduced diode quality factors as a function of the temperature suggested a recombination in the space charge region with an exponential defect distribution, and a transition towards recombination in the quasi neutral region in samples with RbF-PDT.
The influence of electronic material parameters on the blocking of the forward diode current across the heterojunction and at the back contact of the device was studied by numerical simulations. These models are focused on barriers at the heterointerfaces of the solar cell device in order to consider some of the effects of RbF reported in previous studies such as the alkali diffusion from the absorber into the buffer or window layer and their interfaces. It was found that a low-doped ZnO window layer, the presence of acceptor defects at the buffer/window interface or a high band offset at that interface all lead to a similar diode current limitation as a result of a low carrier concentration in the buffer layer.
The reduction of the Na content especially at the back contact of the absorber with long Rb deposition times revealed in previous studies is consistent with the introduction of a back barrier in numerical simulations, exhibiting the aforementioned non-idealities and describing those cells which present a strong V_{oc} saturation at low temperatures.
This work provides a better understanding of the electronic parameters that may

have an influence on the blocking mechanisms when alkalis are deposited on CIGSe absorbers.

Zusammenfassung

Die Nachbehandlung des Absorbers mit RbF hat in den letzten Jahren zu einer signifikanten Verbesserung der Wirkungsgrade von Cu(In,Ga)Se_2 Dünnschicht-Solarzellen geführt. In dieser Arbeit wird der Einfluss der Nachbehandlung auf die Rekombinations- und Stromtransportmechanismen untersucht. Mit einem Satz von am Helmholtz-Zentrum Berlin und in anderen Laboren mit unterschiedlichen Parametern präparierten Proben wurden Messungen der temperaturabhängigen Strom-Spannungskennlinien durchgeführt. Nachbehandelte Proben zeigen insbesondere bei niedriger Temperatur nicht ideale Kennlinien, d.h. ein Abknicken der Kennlinie, Überschneidung von Dunkel- und Hellkennlinien, eine Sättigung der Leerlaufspannung und die hier zum ersten Mal im Detail untersuchte Diskrepanz zwischen Dunkel- und Hellkennlinien. Diese negativen und die positiven (typisch Erhöhung der Leerlaufspannung) Auswirkungen der Nachbehandlung sind nicht notwendigerweise mit denselben physikalischen Mechanismen verknüpft.

Die Leerlaufspannung kann, insbesondere bei niedrigen Temperaturen, durch einen Phototransistor-Effekt beeinflusst werden, der die Leerlaufspannung reduziert und in ihrer Extrapolation zu kleineren Aktivierungsenergien führt als ohne diese Sättigung zu erwarten wäre.

Die Analyse der Rekombinationsmechanismen zeigt, dass, unabhängig davon, ob eine Nachbehandlung erfolgte, die dominierende Rekombination im Absorber stattfindet. Dies widerlegt andere Untersuchungen, die mit der Nachbehandlung einen Übergang von dominierender Rekombination an der Heterogrenzfläche zur Rekombination im Absorber postulieren. Die als Funktion der Temperatur bestimmten Diodenfaktoren sprechen für eine Rekombination in der Raumladungszone über exponentielle Defektverteilung, die sich in nachbehandelten Proben in das Bahngebiet verschiebt.

Der Einfluss elektronischer Parameter auf das Sperren des Durchlassstromes am Heteroübergang oder am Rückkontakt des Bauelementes wurde mit numerischen Rechnungen bestimmt. Die Modelle berücksichtigen Barrieren an den Grenzflächen, um die in vorherigen Studien festgestellte Diffusion von Alkalimetallen aus dem Absorber in die Puffer- und Fensterschichten und deren Grenzflächen einzubeziehen. Man findet, dass eine geringe Dotierung der ZnO-Fensterschicht, Akzeptor-Defekte an der Grenzfläche zwischen Puffer und Fenster oder eine signifikante Diskontinuität der Leitungsbänder an dieser Grenzfläche in Folge einer geringen Dichte freier Ladungsträger in der Pufferschicht alle zu einer ähnlichen Beschränkung des Durchlassstromes führen können.

Die Verringerung des Natriumgehaltes, vor allem am Rückkontakt, der in vorherigen Studien mit langer Nachbehandlung in Verbindung gebracht wurde, kann in seinen Auswirkungen (nicht ideale Kennlinien, starke Sättigung der Leerlaufspannung bei niedrigen Temperaturen) durch die Einführung einer Barriere am Rückkontakt in den numerischen Modellen beschrieben werden.

Diese Arbeit eröffnet ein besseres Verständnis der durch die Nachbehandlung beeinflussten elektronischen Parameter, die zu einer teilweisen Sperrung des Durchlassstromes führen.

Contents

Symbols and acronyms

A	Diode quality factor
AM	Air mass
ARC	Anti-reflective coating
BSF	Back surface field
C	Capacitance
CBD	Chemical bath deposition
CBM	Conduction band minimum
CGI	Ratio of [Cu]/([Ga]+[In])
CIGSe	$Cu(In,Ga)Se_2$
CIGSSe	$Cu(In,Ga)(S,Se)_2$
d	Layer thickness
E_A	Activation energy of the saturation current density
E_C	Energy level for the conduction band edge
E_def	Energetic position of the defect level
E_F	Fermi level energy
$E_{\mathrm{F},n}$	Quasi-Fermi level for electrons
$E_{\mathrm{F},p}$	Quasi-Fermi level for holes
E_g	Band gap energy
$E_\mathrm{g,IF}$	Band gap energy at the interface
$E_\mathrm{g,min}$	Minimum band gap energy
E_ph	Photon energy
E_V	Energy level for the valence band edge
EQE	External quantum efficiency
EMPA	Swiss Federal Laboratories for Materials Science and Technology
FF	Fill factor
FLP	Fermi level pinning
G_0	Generation rate
GD-OES	Glow discharge optical emission spectrometry
GGI	Ratio of [Ga]/([Ga]+[In])
h	Planck's constant
HZB	Helmholtz-Zentrum Berlin
I	Light intensity
J	Current density
J_0	Saturation current density
J_{00}	Reference current density
J_d	Diode current density
J_L	Light current density
J_mpp	Current density at the maximum power point
J_ph	Photocurrent density

J_{sc}	Short-circuit current density
JVT	Temperature-dependent current-voltage
k	Boltzmann constant (8.62×10^{-5} eV·K^{-1})
L_n	Diffusion length of electrons
n	Electron density
n^*	Auxiliary density for the electron emission from the trap states
N_{A}	Acceptor density
N_{C}	Effective density of states in the conduction band
N_{CV}	Charge carrier concentration determined by $C-V$ measurement
N_{D}	Donor density
N_{def}	Bulk defect density
n_i	Intrinsic carrier concentration
N_{IF}	Density of interface states
N_{V}	Effective density of states in the valence band
ODC	Ordered defect compound
OVC	Ordered vacancy compound
p	Hole density
p^*	Auxiliary density for the hole emission from the trap states
P_{in}	Incident power
P_{mpp}	Maximum power point
PDT	Post deposition treatment
PV	Photovoltaic
PVD	Physical vapor deposition
q	elemental charge
QNR	Quasi neutral region
R	Net recombination rate
R_{s}	Series resistance
R_{sh}	Shunt resistance
RF	Radio frequency
RIS	$RbInSe_2$
RTP	Rapid thermal processing
$S_{n,p}$	Surface or interface recombination velocity of electrons/holes
SCAPS	Solar cell capacitance simulator
SCR	Space charge region
SRH	Shockley-Read-Hall recombination rate
STC	Standard test conditions
STEM-EDX	Energy-dispersive X-ray spectroscopy using a scanning transmission electron microscope
t	Time
T	Temperature
T^*	Characteristic temperature for defect distribution
TCO	Transparent conductive oxide
T_{sub}	Substrate temperature
U	Recombination rate
V	Voltage
$v_{n,p}$	Thermal velocity of electrons/holes
V_{mpp}	Voltage at the maximum power point

V_{oc}	Open-circuit voltage
VBM	Valence band maximum
XPS	X-ray photoelectron spectroscopy
ZSW	Center for Solar Energy and Hydrogen Research Baden-Württemberg

Greek

ΔE_{C}	Conduction band offset
ε	Permittivity
η	Efficiency
Θ_{BC}	Energetic height of a back contact barrier
$\mu_{n,p}$	Mobility of an electron/hole
ν	Frequency of a photon
$\sigma_{n,p}$	Capture cross section for electrons/holes
$\tau_{n,p}$	Carrier lifetime of an electron/hole
ϕ	Electric potential

1. Introduction

The importance of implementing renewable energies has been rising due to the unfavorable environmental changes that the Earth has been undergoing in the last decades. As confirmed by scientists of the National Aeronautics and Space Administration (NASA) and the National Oceanic and Atmospheric Administration (NOAA), August 2020 was about 2.14 °C hotter than the average recorded on Earth since 1880 [1, 2]. The Earth has been gradually heating up since the late 19th century but it has not been since the year 2000 that this trend has been accelerated [3]. Carbon dioxide emissions are the primary driver of global climate change, therefore it is urgently necessary to reduce these emissions [4]. These emissions stem from fossil energy carriers, the use of which must be reduced.

Photovoltaic (PV) devices are important energy supply systems which directly convert sunlight into electrical energy and thus enable reduction of fossil fuels. Today, Si-based solar cells are dominating the world PV market [5], nevertheless thin-film photovoltaic technologies based on polycristallline chalcopyrite absorbers allows a significant reduction of the semiconductor material when compared to crystalline (c-Si), besides exhibiting a shorter energy payback time (less than 12 months for thin-films vs 12-18 months for c-Si) and a lower carbon footprint (12-20 gr CO_2 equivalent/kilowatt hour for thin-films vs 50-60 gr CO_2 equivalent/kilowatt hour of electricity for c-Si) [6]. Thin-film devices can be produced on flexible as well as on conventional rigid substrates with high performance [7, 8].

Thin-film solar cell devices based on the chalcopyrite absorber material Cu(In,Ga)Se_2 (CIGSe) have proven to be one of the most suitable to convert sunlight into electricity with high efficiencies. The basic concept of a CIGSe cell has remained unaltered over the years with a p-absorber/n-buffer/n^+ TCO (transparent conductive oxide) layer configuration [9, 10]. Since the beginning of the 1990s, diffusion of alkaline elements, mainly Na, from soda-lime glass (SLG) through the Mo back contact layer into the CIGSe during the deposition process has been identified to be an effective way to achieve a suitable doping concentration and good performance of the device. During the last years, CIGSe solar cells have been significantly improved where the recent boost in efficiency was triggered by heavy alkali fluoride (KF, RbF, CsF) post deposition treatment (PDT) [7, 11]. One of the main beneficial effects of PDT is the

gain in open-circuit voltage. However, this positive effect is accompanied by non-idealities that mainly affect the behavior of the exponential diode current at forward bias and the photocurrent. In this work, the influence of RbF-PDT on the electrical transport and the dominant recombination path of a large set of CIGSe thin-film solar cell devices, especially in thermally evaporated absorbers, are investigated by electrical characterization techniques such as temperature-dependent current-voltage measurements (JVT). Device simulations are performed to be correlated with the experimental measurements in order to better understand the physical mechanisms that lead to detrimental effects.

This thesis is structured in the following way:

Chapter 2 describes the configuration and the standard layer stack of a typical CIGSe-based solar cell. The main function of each of these layers is briefly described in order to understand the role played by these (semi)conductors in the absorption of photons and the conversion of sunlight into electricity. Definition of the main PV parameters, transport equations as well as the diode parameters which can describe the dominant recombination mechanism in a chalcopyrite solar cell are also given. Finally, the last section of this chapter summarizes the main findings corresponding to the non-electronic/electronic effects reported in literature for alkali fluoride PDT in CIGSe cells especially when it comes to RbF.

Chapter 3 introduces the main electrical characterization methods used in this thesis as well as the description of the method and programs used to fit the experimental current-voltage characteristics measured in dark and under illumination conditions. This chapter also provides the device and material properties set in the reference CIGSe model for device simulations.

Chapter 4 includes an extensive survey of sets of different CIGSe samples without/with RbF-PDT produced at Helmholtz-Zentrum Berlin (HZB) and external laboratories and characterized by temperature-dependent current-voltage measurements, external quantum efficiencies, standard current-voltage measurements and capacitance-voltage measurements. Plots of the diode factors obtained from the fits of the current-voltage curves and plots of the open-circuit voltage with respect to the temperature are included. From these, the different effects of RbF-PDT on CIGSe solar cells are described.

Chapter 5 explores variations of the device and material properties of the numerical reference model presented in Chapter 3. Special attention is focused on the heterojunction interface and back contact barrier models in order to explain the non-ideal effects previously observed in Chapter 4 once the samples are treated with RbF. Variations in the band alignment, doping concentration, interface defects, back barrier height,

temperatures, among others, are performed. At the end of this chapter, a summary of the non-idealities for each model studied is also given.

Chapter 6 connects the proposed models previously obtained from the numerical simulations with the main non-electronic findings reported in literature and fundamental mechanisms given in Chapter 2. Positive and negative consequences of RbF-PDT either due to the electrical transport and/or recombination mechanisms are identified in order to have a more detailed understanding of the mechanisms involved with RbF-PDT.

2. Fundamentals

In this chapter, the electrical transport and the different recombination processes which may dominate the chalcogenide solar cells are discussed. The basics of a CIGSe solar cell are introduced at the beginning of this chapter to give an overview of the structure and operation of type of devices studied in this work including the definition of the main electrical parameters and the characteristics of a typical current-voltage curve that are crucial for the analysis of solar cells. Moreover, a brief but comprehensive review of the main findings of alkali fluoride post deposition treatment reported in literature can be found at the end of this chapter including some of the main results of the PDT cell produced at HZB.

2.1. Basics of a CIGSe solar cell

The configuration of a CIGSe-based solar cell is sketched in Figure 2.1a. Typically, a molybdenum layer is deposited on top of a glass substrate and used as a back contact. A $p-n$ junction is formed by the p-type $Cu(In,Ga)_2$ absorber layer and the n-type material which comprises the buffer layer, typically CdS, and a double window layer formed by an typically undoped ZnO (i-ZnO) and a highly doped ZnO:Al (AZO) used as the front contact of the device. At the top of the front contact a metal contact grid of Ni-Al-Ni is deposited, establishing an ohmic contact for current collection. The CIGSe absorber is a polycrystalline semiconductor well suited for thin-film devices because of its direct band gap and its high absorption coefficient α in the order of 10^5 cm^{-1} to 10^6 cm^{-1} so film thicknesses around 1-3 μm are enough to absorb most of the incident photons with energies above its band gap. A distinctive aspect of the CIGSe material is its variable band gap which can be changed by varying the [Ga]/([Ga]+[In]) ratio (GGI). In $Cu(In_{1-x}Ga_x)Se_2$ alloys, a higher Ga content widens the band gap energy (E_g) from 1.02 for Ga free $CuInSe_2$ to 1.69 eV for $CuGaSe_2$ following the approximate expression $E_g(x) = 1.02 + 0.67x + 0.11x(x-1)$ with x being the respective GGI ratio [12]. From this, the band gap energy not only can be adjusted to the desired level but also the absorber can present different band gaps at different depths in the CIGSe film, so-called band gap grading.

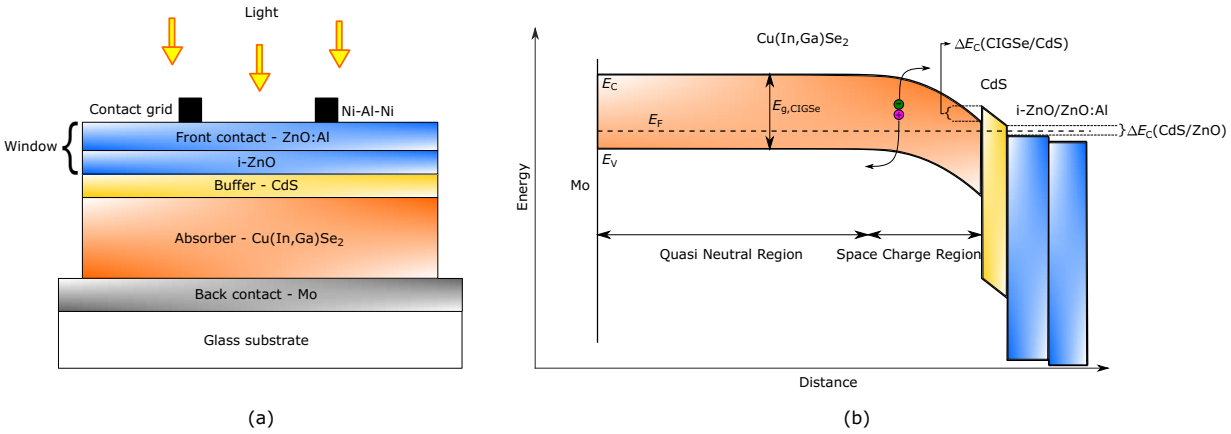

Figure 2.1.: (a) Schematic representation of a CIGSe solar cell , and (b) energy band diagram of a CIGSe solar cell in equilibrium.

CdS polycrystalline films posses a direct band gap energy at around $E_g = 2.4$ eV [13] and the wide band gap of CdS permits the sunlight to enter the absorber material more readily [14]. However, the light absorption in the buffer still reduces the spectral response of the solar cell in the blue region of the solar spectrum. The role of a buffer layer in addition to forming a $p-n$ junction with the p-type CIGSe is to provide a favorable band alignment and charge density [15] at the absorber/window interface. The double ZnO layer acts as a window with high conductivity and with a wider band gap than the CdS at around $E_g = 3.3$ eV [13] in order to allow the incident photons to pass through and to reach the absorber film.

The energy band diagram of a typical CIGSe solar cell without illumination at zero bias voltage is illustrated in Figure 2.1b. When the sunlight hits the front contact of the solar cell, those photons with energies lower than the corresponding band gap energies of the window and buffer layer ($E_{ph} = h\nu < E_{g,ZnO}$ and $E_{g,CdS}$) pass through these layers and are absorbed by the CIGSe layer. During this process, by the absorption of a photon with an energy above or equal to the band gap of the CIGSe ($E_{ph} \geq E_g$), an electron is excited from the valence band into the conduction band creating an electron-hole pair in the absorber. The electrons are excited to a broad range of energy states in the conduction band. When $E_{ph} = E_g$, the excited electrons lie near the conduction band edge or so-called conduction band minimum (CBM), while when $E_{ph} > E_g$, the excited electrons relax from a higher energy level to the conduction band edge before they reach the contacts. The excess of energy ($\Delta E = h\nu - E_g$) is lost and transformed into heat and this process is called thermalization. The excited electrons do not stay at the conduction band edge for a long time, and they either reach the metal contacts or relax back to the valence band to fill the holes again (recombination). Those photon energies lower than the band gap of the absorber ($E_{ph} < E_g$) do not contribute to the photocurrent. The separation of electrons and holes occurs mainly in

the space charge region (SCR) [16]. The SCR is located mainly within the absorber, close to the interface between the p-type CIGSe and the n-type material. When these two materials are brought into contact, the free electrons of the n-type material diffuse to the p-type absorber an recombine with the free holes of the absorber, leaving a negatively charged region in the CIGSe and a positively charged region in the buffer. Due to the charge separation an electrical field is generated which limits the diffusion of free electrons and holes, leading to an equilibrium between the diffusion current (due to the carrier density gradient) and the drift current (due to the difference of electric potentials) and forming the SCR. The width of the SCR is dependent on the charge carrier concentrations of both p-type and n-type materials. Once the equilibrium is reached, the Fermi level (E_{F}) is flat throughout the device. This leads to a bending of the conduction bands as illustrated in Figure 2.1b. Under illumination or when bias is applied (non-equilibrium state), electron-hole pairs are created and the Fermi distribution is different for electrons and holes, so a quasi-Fermi level for electrons ($E_{\mathrm{F},n}$) and a quasi-Fermi level of holes ($E_{\mathrm{F},p}$) are introduced in the energy diagram [17] (not shown here).

A typical current-voltage ($J-V$) characteristic of a CIGSe solar cell under dark and illuminated conditions in linear plot is shown in Figure 2.2. The main photovoltaic parameters to describe the perfomance of a solar cell are the short-circuit current density (J_{sc}), open-circuit voltage (V_{oc}), fill factor (FF) and efficiency (η).

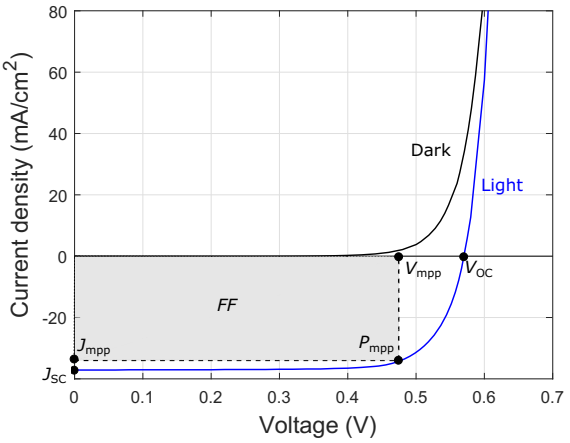

Figure 2.2.: $J-V$ curves under dark and light conditions of a solar cell showing the J_{sc} and V_{oc} points, the maximum power point (J_{mpp}, V_{mpp} and P_{mpp}), as well as the area that defines the FF.

J_{sc} depends directly on the light intensity, so the total current is the result of the generated and collected charge carriers.

The open-circuit voltage is the maximum voltage given by the the solar cell and this occurs when the current is equal to zero ($J=0$). From the one-diode model equation

under illumination (described in Section 2.2) by setting the current density equal to zero, the V_{oc} can be calculated from the resulting equation:

$$V_{oc} = \frac{AkT}{q} \ln\left(\frac{J_{\mathrm{ph}}}{J_0} + 1\right) \tag{2.1}$$

with A as the diode quality factor, k as the Boltzmann constant and q as the elemental charge. The saturation current density (J_0) describes the recombination losses in the solar cell. Therefore, the open-circuit voltage is a measure of the amount of recombination in the device. In relation to the band gap energy, the short-circuit current density decreases with increasing band gap, while the open-circuit voltage increases as the band gap increases.

The fill factor determines the maximum power from a solar cell, in conjunction with V_{oc} and J_{sc}. The FF is defined as the ratio of the maximum power from the solar cell to the product of the V_{oc} and J_{sc} so that

$$FF = \frac{V_{\mathrm{mpp}} J_{\mathrm{mpp}}}{V_{oc} J_{\mathrm{sc}}} = \frac{P_{\mathrm{mpp}}}{V_{oc} J_{\mathrm{sc}}} \tag{2.2}$$

where V_{mpp} and J_{mpp} are the voltage and current density at the maximum power point (P_{mpp}), respectively. In Figure 2.2, the FF can be seen as the area of a rectangle where the V_{mpp} and J_{mpp} intersect.

The efficiency denotes the performance of a solar cell and is defined as the ratio of the maximum generated power from the solar cell to the incident power (P_{in}) from the irradiation source so that

$$\eta = \frac{P_{\mathrm{mpp}}}{P_{\mathrm{in}}} = \frac{V_{oc} J_{\mathrm{sc}} FF}{P_{\mathrm{in}}} \tag{2.3}$$

2.2. Electrical transport in CIGSe solar cells

When a voltage bias is applied to the solar cell in the dark, a pure diode current (bucking current) is flowing. When the light shines on the cell, the $J-V$ curve shifts to the fourth quadrant and the cell generates power. The current under illumination determines the V_{oc} of the device, so experimentally both $J-V$ curves, with and without illumination, are analyzed. The superposition principle states that the total light current ($J_{\mathrm{L}}(\mathrm{V})$) is the sum of the diode current ($J_{\mathrm{d}}(\mathrm{V})$) and photocurrent ($J_{\mathrm{ph}}(\mathrm{V})$) [17]:

$$J_{\mathrm{L}}(V) = J_{\mathrm{d}}(V) + J_{\mathrm{ph}}(V) \tag{2.4}$$

The diode current density is described by the Shockley equation (or ideal diode law):

$$J_{\mathrm{d}} = J_0 \left[\exp\left(\frac{qV}{AkT}\right) - 1\right] \tag{2.5}$$

For CIGSe solar cells, it is generally assumed that [18]

$$J_0 = J_{00} \cdot \exp\left(-\frac{E_{\mathrm{A}}}{AkT}\right) \tag{2.6}$$

in which J_0 is activated by the activation energy (E_{A}) as a result of recombination of charge carriers. The activation energy describes the temperature dependence of the saturation current density. J_{00} may be called reference current density and is only weakly temperature dependent. The diode quality factor moderates the voltage dependence of the current density and together with J_{00} and E_{A}, these are important parameters to describe the recombination mechanisms in the cell, as will be described in Section 2.3.

Introducing Equation 2.6 into 2.5, the general expression for the dark diode current density is [18]:

$$J_{\mathrm{d}} = J_{00} \cdot \exp\left(-\frac{E_{\mathrm{A}}}{AkT}\right)\left[\exp\left(\frac{qV}{AkT}\right) - 1\right] \tag{2.7}$$

Substituting Equation 2.6 for J_0 in Equation 2.1 previously given to calculate the open-circuit voltage, and neglecting the 1 in the argument of the natural logarithm, it leads to the expression:

$$V_{oc} \approx \frac{E_{\mathrm{A}}}{q} - \frac{AkT}{q}\ln\left(\frac{J_{00}}{J_{\mathrm{ph}}}\right) \tag{2.8}$$

From here, the activation energy E_{A} for temperature-independent diode factor A, J_{00} and the photocurrent density J_{ph} can be deduced by plotting the open-circuit voltage against the temperature T from the extrapolation of the V_{oc} to $T = 0$ K. However, there are certain dominant recombination processes where the diode quality factor shows a weak temperature dependence, such as tunneling process (see Section 2.3). The activation energy can be easily extracted from assisted Equation 2.6 [19]:

$$A\ln(J_0) = -\frac{E_\mathrm{A}}{kT} + A\ln(J_{00}) \tag{2.9}$$

By plotting the left part of the equation $A\ln(J_0)$ vs $1/T$, the activation energy can again be determined [20].

An ideal solar cell which obeys the superposition principle is described by an equivalent circuit with only two components: a current source which delivers the photocurrent density and a diode component that represents the dark characteristics of the junction with its corresponding current density. However, a real solar device presents some non-ideal elements, e.g., parasitic resistances which generally reduce the FF: a shunt resistance (R_sh) and a series resistance (R_s). The series resistance comprises ohmic losses in the bulk, TCO and/or at the metal contacts. Another series element can be a back contact diode with opposite polarity [17]. The main impact of a series resistance is to reduce FF, but high values of R_s may also reduce the J_sc, thus low values of the series resistance are needed for a good device performance. In case of an ohmic series resistance, the voltage drop at this element is $V_\mathrm{s} = R_\mathrm{s}J$. The shunt resistance describes parasitic current pathways and is typically due to manufacturing defects. Low shunt resistance causes power losses in the device by generating current pathways for the photocurrent, causing a reduction of the amount of current flowing through the solar cell and a reduction of the voltage, thus high values of the shunt resistance are desirable to reduce the losses. Including these elements to describe the current-voltage dependence of solar devices, the equivalent electric circuit of a heterostructure solar cell is shown in Figure 2.3.

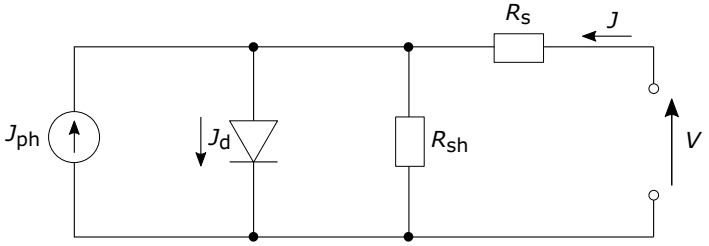

Figure 2.3.: Equivalent electric circuit of the one-diode model of a non-ideal solar cell including the parasitic resistances R_s and R_sh.

Including a series resistance and a shunt resistance to the Shockley equation (Equation 2.5) and under illumination conditions, the one-diode model is described as:

$$J(V) = J_0\left[\exp\left(\frac{q(V - R_\mathrm{s}J)}{AkT}\right) - 1\right] + \frac{V - R_\mathrm{s}J}{R_\mathrm{sh}} - J_\mathrm{ph} \tag{2.10}$$

Here, J_0 describes the recombination mechanism under illumination. In the simplest case, $A = 1$ is referred to recombination outside the space charge region and recombi-

nation at the interface of the absorber (back contact or absorber/buffer interface), and $A = 2$ is denoted for recombination in the SCR.

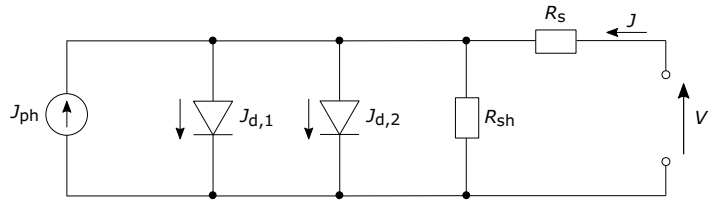

Figure 2.4.: Equivalent electric circuit of the two-diode model of a non-ideal solar cell including a second diode connected in parallel and the parasitic resistances R_{s} and R_{sh}.

As it will been shown in Chapter 3 and 4, the one-diode model is not sufficient to describe the $J-V$ curves of the CIGSe thin-film solar cells characterized in this work, and therefore a two-diode model equation was more suitable to fit the obtained $J-V$ curves and to determine the main parameters to describe the recombination processes. The two-diode model introduces a second diode connected in parallel to the main diode as shown in Figure 2.4 and its corresponding equation is:

$$J(V) = J_{0,1}\left[\exp\left(\frac{q(V-R_{\mathrm{s}}J)}{A_1kT}\right)-1\right]+J_{0,2}\left[\exp\left(\frac{q(V-R_{\mathrm{s}}J)}{A_2kT}\right)-1\right]+\frac{V-R\mathrm{s}J}{R_{\mathrm{sh}}}-J_{\mathrm{ph}} \tag{2.11}$$

With the aim of describing the electrical transport mechanisms that dominates at different voltage ranges of the $J-V$ curve and determining the main parameters of the diode equation, the dark $J-V$ characteristics are shown in semi-logarithmic plot as seen in Figure 2.5. In the same way, all JVT measurements presented in Chapter 4 are plotted in semi-logarithmic scale.

A typical dark $J-V$ characteristic of a reference CIGSe solar cell in Figure 2.5 described by the one-diode model is divided in three main regions [21]: (1) the shunt resistance dominates the current at low negative and positive bias voltages. The current does not flow only over the diode but also over the shunt resistance. (2) As the current and voltage increase, the diode factor can be deduced from the straight line of the semi-logarithmic plot. For a steeper slope, smaller A. (3) The series resistance dominates at higher voltages. Part of the voltage drops over the series resistance when a current flows and the R_{s} can be seen from the bending of the straight line of the diode factor where the stronger the bending, the stronger the series resistance.
In the voltage range of the straight line representative of the diode factor, between 0.5 V to 0.65 V, typically the V_{oc} of a standard CIGSe solar cell can be found, thus the transport mechanism that dominates within this region influences the open-circuit voltage, as well as information about the recombination mechanism can be deduced

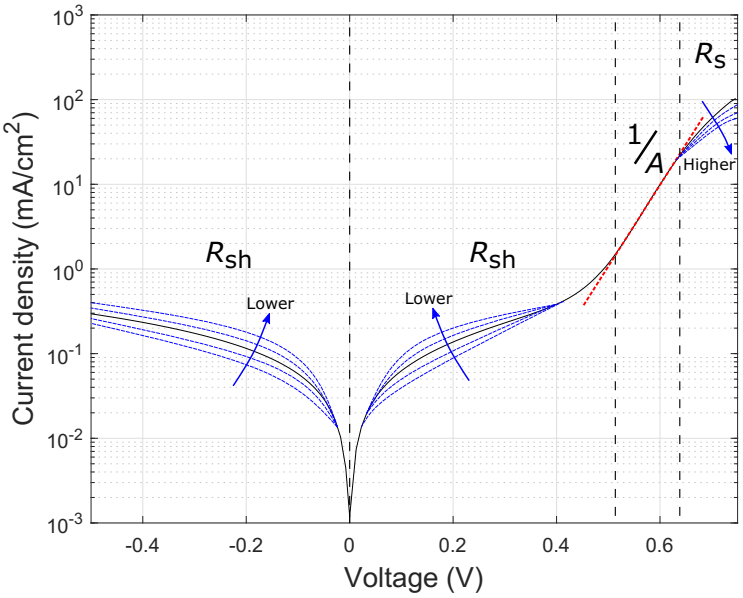

Figure 2.5.: A typical dark $J-V$ curve in semi-logarithmic scale of a CIGSe thin-film solar cell including the voltage ranges where the diode factor, and the series and shunt resistance influence the $J-V$ curve.

from the value of this diode factor. However, as previously mentioned, CIGSe devices measured in this work can be described by the two-diode model where a second diode (a parasitic diode), with very high values of A and dominating at low voltages, is only needed to achieve a good fit of the $J-V$ characteristics (see Chapter 4) within the research area of this thesis.

2.3. Recombination mechanisms in CIGSe solar cells

The $J-V$ curve can be described by the two-diode model (for the case of this work) which includes the exponential function of the current with respect to the voltage and the parasitic resistances, R_s and R_{sh}. Important parameters of the two-diode equation are deduced to describe the different recombination mechanisms present in the solar cell: from the main diode its reference saturation current density, diode quality factor and activation energy of the saturation current density. The diode current can be due to different recombination paths.

Generally, there are three types of recombination [17]: radiative recombination, Auger recombination and defect related recombination. Radiative recombination refers to the inverse process of optical absorption with a direct band to band recombination of

electrons and holes that cannot be avoided. This process is considered in the Shockley-Queisser limit of an ideal $p-n$ junction [22]. Auger recombination is a non-radiative process that cannot be avoided. This type of recombination involves three carriers where a conduction band electron recombines with a valence band hole, but instead of producing a photon or heat, the excess of energy is transferred to another electron raising it higher into the conduction band or to another hole pushing it deeper into the valence band, and then thermalizing it back down to the band edges [23, 24]. Because this process is based on the ability of charge carriers to exchange energy, the Auger recombination rate increases with a higher concentration of charge carriers, especially in Si solar devices [25, 26], and can be reduced if the doping density is kept below a limiting value, becoming critical for doping densities in the range of 10^{18} cm^{-3} which is usually not the case for CIGSe solar devices. Recombination via defect states is a process that can be avoided since, in principle, defects can be removed or decreased from the heterostructure device but even for state-of-the-art chalcogenide thin film absorbers, defect recombination is still the dominant limiting process. Although all these mechanisms happen at the same time, this thesis is focused on describing the different sets of CIGSe solar cells presented in this work from the main recombination mechanism as pointed out in the literature, and therefore the influence of Auger and radiative recombination are neglected in this work.

Figure 2.6 illustrates the main recombination process in a heterostructure solar cell due to defect related recombination. Recombination may take place in four regions of the absorber: in the SCR (path 1) and the area outside the SCR, the so-called Quasi Neutral Region (QNR) (path 2), at the absorber surface (path 3) and the absorber back contact (path 4). At first sight, recombination at the absorber surface of a heterostructure solar cell against a homojunction is complicated by the band misalignment between the layers and/or impurities not only at the absorber surface but also at each interface formation of the device. However, in a homojunction, surface recombination is harder to control than interface recombination, thus a heterojunction is a better structure for a solar device as we can see also in Si cells [27, 28]. Several recombination mechanisms may happen in parallel where each one carries a certain share of the current. Recombination in the buffer and window layer usually is insignificant because of the wide band gap and therefore does not contribute to the diode current. Recombination paths in the SCR (1) and at the absorber surface (3) can be enhanced by tunneling [20, 29].

Defect related recombination via a defect level in the energy band gap of the absorber is referred as the Shockley-Read-Hall (SRH) recombination [30, 31]. The four principal transitions involved in SRH recombination are: the capture of an electron or hole, and the re-emission of an electron or hole.

The general expression for the Shockley-Read-Hall recombination reads as:

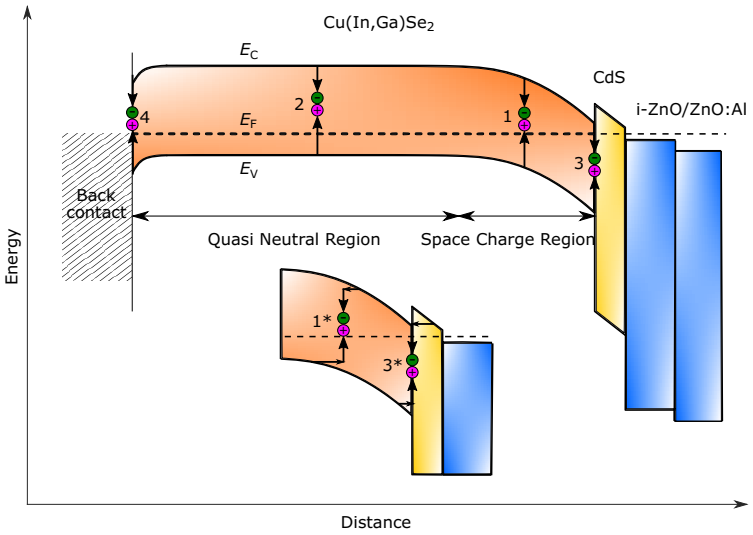

Figure 2.6.: Schematic representation of the main recombination paths in a heterostructure solar cell. Recombination within the absorber: (1) SCR and (2) QNR, recombination (3) at the absorber surface and recombination (4) at the back contact of the absorber. The sketch also includes a tunneling enhanced recombination (1*) in the SCR and (3*) at the absorber surface.

$$R = U - G_0 = \frac{np - n_i^2}{\tau_p(n + n^*) + \tau_n(p + p^*)} \tag{2.12}$$

In this equation, R is the net recombination rate which describes the complete recombination process and equals the difference between recombination rate (U) and generation rate (G_0). τ_p and τ_n denote the minimum lifetimes of holes and electrons, respectively.[1] The quantities n and p are the carrier densities and n^* and p^* expressed as $n^* = N_\mathrm{C} \exp\left[\frac{(E_\mathrm{def} - E_\mathrm{C})}{kT}\right]$ and $p^* = N_\mathrm{V} \exp\left[\frac{(E_\mathrm{V} - E_\mathrm{def})}{kT}\right]$ are the auxiliary density of carriers which indicate the charge carrier concentrations that would originate if the Fermi level is located at the energetic position of the defect level (E_def).

Reorganizing Equation 2.12 by inserting the previous expressions, the SRH equation yields:

$$R = U - G_0 = \frac{np - n_i^2}{\tau_p\left(n + N_\mathrm{C} \exp\left[\frac{(E_\mathrm{def} - E_\mathrm{C})}{kT}\right]\right) + \tau_n\left(p + N_\mathrm{V} \exp\left[\frac{(E_\mathrm{V} - E_\mathrm{def})}{kT}\right]\right)} \tag{2.13}$$

[1] It is assumed a minimum lifetime because all the trap centers (N_def) in the band gap are assumed to be non-occupied by the carriers: $\tau_{n,p} = (\sigma_{n,p} v_{n,p} N_\mathrm{def})^{-1}$ with $\sigma_{n,p}$ as the capture cross section of the defect recombination and $v_{n,p}$ as the thermal velocity of the corresponding charge carriers.

The defect level can be positioned in any region along the band gap energy of the absorber. As it can be deduced from the simplified SRH equation (see Equation 2.12), when n^* and p^* are large, i.e., when the defect level is close to either the conduction band edge (E_C) or valence band edge (E_V), the net recombination rate becomes small. Conversely, if n^* and p^* are small, the net recombination rate becomes large when the defect level is close to the mid-gap energy. The net recombination rate will be the highest when the defect level is positioned at the mid-gap (if capture cross sections are the same for electron and hole). In other words, the probability of an electron to be captured is high when the defect level is close to the conduction band and decreases when the defect level moves closer to the valence band (and vice versa for a hole), therefore the highest recombination occurs when the defect level is positioned in the middle of the band gap where the defect can capture efficiently both, electrons and holes.

Using the relation between n and p under bias voltage, $np = n_i^2 \exp(qV/kT)$ and the relation of the intrinsic carrier concentration, $n_i^2 = N_V N_C \exp(-E_g/kT)$ and introducing them in the equation of the SRH recombination (Equation 2.13), it can be deduced that the smallest band gap within the heterostructure solar cell leads to the highest recombination and contributes to the main part of the diode current, which is typically in the absorber layer, and only a minor part of the diode current results from the recombination in the buffer and window layer. In equilibrium state, $np = n_i^2$, the net recombination rate becomes zero. Analyses have shown that the limiting process in CIGSe-based thin-film solar cells is mainly bulk recombination for a standard absorber thickness [17, 18, 20]. Moreover, the highest recombination in the bulk can take place either in the QNR or SCR. Assuming equal carrier lifetimes in the absorber, $\tau_p \approx \tau_n$, the maximum recombination takes place at the position when $n = p$, and following the condition for the maximum recombination rate, $\tau_n p = \tau_p n$, its position is commonly within the SCR. However, such maximum recombination will depend on the value of the carrier lifetime. SCAPS simulations performed by Scheer et al. [17] showed that for shorter carrier lifetimes, the SCR is the main recombination zone, while for larger lifetimes, the recombination rate becomes approximately constant in the QNR with only a small maximum recombination in the SCR. In this case, both recombinations occur in parallel with a higher recombination rate in the QNR. Thus, the dominance of the SCR recombination or the QNR recombination changes with respect to the carrier lifetime. Also see chapter on numerical calculations, Figure 5.2.

In the following sections, the main recombination paths occurring in a heterostructure solar cell as shown in Figure 2.6 are briefly analyzed separately.

2.3.1. SCR recombination

The SRH formula (Equation 2.12) describes the recombination rate occurring in the SCR of the absorber layer. It is within this region where the relation $\tau_n p = \tau_p n$ takes place for the maximal recombination rate for a single defect, and then V_{oc} is dominated by recombination in the SCR [18]. The recombination rate varies with $\exp\{qV/2kT\}$ and the diode quality factor is deduced from the variation of the current density in a semi-logarithmic plot. The quasi Fermi levels $E_{\mathrm{F},n}$ and $E_{\mathrm{F},p}$ at the position $\tau_n p = \tau_p n$, vary symmetrically with respect to the defect level at mid-gap. When a voltage V is applied, both quasi Fermi levels are modulated and the applied voltage splits between n and p, so each quasi Fermi level varies as $qV/2$ as illustrated in Figure 2.7.

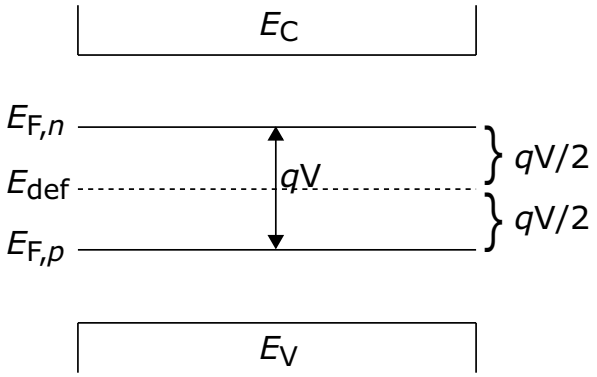

Figure 2.7.: Schematic representation of the defect related recombination in the SCR.

In this case, the number of electrons are increased by a small amount, only by a half of the applied voltage, $n \propto \exp(qV/2kT)$, with a small increase of recombination with respect to the voltage. Therefore, if the recombination is dominant in the SCR, the diode quality factor is $A = 2$ or close to 2 since experimental devices limited by SCR recombination may show a diode factor slightly smaller than 2 due to an additional voltage dependence [17]. The general expression in Equation 2.7 gives an activation energy of the saturation current density equal to the band gap of the absorber, $E_{\mathrm{A}} = E_{\mathrm{g}}$ via a single defect in the SCR, and the open circuit voltage is given by Equation 2.8.

Nevertheless, the value of the diode quality factor will depend on the location of the defect level. If the defect level is close to one of the band edges, the diode quality factor becomes $A = 1$. A diode with a shallow defect ($A = 1$) exhibits a stronger voltage dependence of the diode current in comparison to a diode with a deep defect ($A = 2$). However, if the defect level is located close to a band edge, such defect level is not within the region of the highest recombination, thus the total recombination rate given by a shallow defect is small. In the case of having a combination of a shallow and deep defect level in the absorber, the recombination will be dominated by the deep defect and the diode quality factor will be $A = 2$ (as long as the forward bias is not too large).

If the defect is located at an intermediate level between the mid-gap and one of the band edges, the diode factor changes its slope from 1.1 up to 1.8 with increasing voltage bias [17]. When the voltage bias increases, the region of the efficient recombination widens and at certain bias the defect level is included within this region, thus a change in the slope of the $J-V$ curve may indicate such an intermediate defect level.

Different defect distributions may also be considered for recombination. A constant defect density or a linear defect distribution decreasing from the band edges leads to a voltage dependence of the diode factor. Since the carrier concentrations at the point of a maximum recombination vary exponentially with voltage bias, an exponential defect distribution (with a maximum defect distribution at the band edge and decaying into the band gap) has a stronger impact on the diode quality factor [32]. The current density can also be calculated from Equation 2.7 where J_{00} is slightly temperature-dependent and the temperature dependence of the diode quality factor is given by $1/A = 1/2(1 + (T/T^*)$ with kT^* as the characteristic energy of the distribution. The diode quality factor can vary between 1 and 2 in case of having an exponential defect distribution [33] in the band gap with $E_\mathrm{A} = E_\mathrm{g}$. The open circuit voltage from Equation 2.8 is therefore temperature-dependent.

Recombination in the SCR can also be enhanced by tunneling (see path (1*) of Figure 2.6) for a discrete level or for an exponential defect distribution in the band gap if a strong electric field is present, causing an increase of density of carriers available to contribute to the recombination rate at a certain location within the SCR with diode quality factors larger than 2. Previous studies by Rau et al. [18, 20] have shown that tunneling is typically not significant around room temperature but becomes more important as the temperature decreases.

2.3.2. QNR recombination

As previously mentioned in Section 2.2, recombination in the QNR becomes dominant for long carrier lifetimes and/or narrow SCR since a large number of carriers pass through the SCR without recombining and are injected into the QNR being there the minority carriers. The QNR comprises the area outside the SCR with a gradient of the electric potential of zero and extends up to the back contact. Therefore, the charge carriers generated in the QNR of the absorber will either diffuse to the SCR or recombine. In the same way as the SCR recombination, defect states can be located via shallow and deep defect level as well as an exponential defect distribution. The recombination rate can be calculated following the SRH equation (Equation 2.12) without the generation term:

$$R = U = \frac{np}{\tau_p(n + n^*) + \tau_n(p + p^*)} \tag{2.14}$$

and for a deep defect the recombination rate where holes are majorities, $p >> p^*, n^*, n$, it can be approximated as:

$$R = U = \frac{n}{\tau_n} \tag{2.15}$$

When a bias voltage is applied (see Figure 2.8), the density of electrons is mainly modulated, thus only the Fermi level for electrons $E_{\mathrm{F},n}$ moves with respect to the voltage, leading to a strong increase of the number of electrons, $n \propto \exp(qV/kT)$, and a strong increase of recombination rate. A diode quality of $A = 1$ is obtained for deep and shallow defects as well as for a defect distribution, and only valid if the absorber thickness (d_{abs}) is much larger than the diffusion length of electrons (L_n), $d_{\mathrm{abs}} >> L_n$, i.e., if the majority carriers do not reach the back contact of the absorber (without back contact recombination).

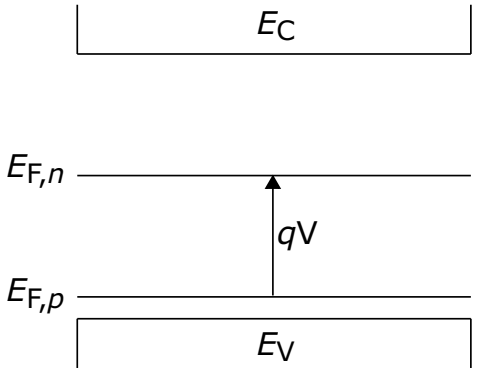

Figure 2.8.: Schematic representation of the defect related recombination in the QNR.

2.3.3. Back contact recombination

Back contact recombination may become the dominant process if the carrier lifetime in the bulk is very large and the interface recombination is very small. The effect relatively becomes larger by reducing the absorber thickness, $d_{\mathrm{abs}} << L_n$, and is enhanced for ultra-thin films [34, 35]. For a smaller distance between the back contact and collection junction [36], the minority carrier electrons (in a p-type material) diffuse to the back contact and recombine with the high amount of holes. The dominance of bulk recombination or back contact recombination will depend mainly on the absorber thickness d_{abs}, and diffusion length of the minority charge carriers L_n.

A normal grading increases the band gap energy towards the back surface or towards the front surface, while a double grading has a minimum band gap at some depth point of the absorber and increases the band gap towards the front and back surface. The effect of a back surface grading in samples with standard absorber thickness is to decrease minority carrier recombination at the back contact [37, 38]. This leads to an increased photocurrent, decreased diode current and even to an increase in the V_{oc} [39, 40].

2.3.4. Interface recombination

A large number of interface states can be present at the absorber/buffer interface which leads to an interface recombination path, especially if the interface band gap ($E_{\mathrm{g,IF}}$) is smaller than the absorber band gap ($E_{\mathrm{g,abs}}$), as seen in Figure 2.9a. If the interface band gap equals the absorber band gap ($E_{\mathrm{g,IF}} = E_{\mathrm{g,abs}}$), the recombination occurs between the electrons from the absorber conduction band and the holes from the absorber valence band. In contrast, if the interface band gap is smaller than the absorber band gap ($E_{\mathrm{g,IF}} < E_{\mathrm{g,abs}}$), then there are two different recombination paths: one directly from the recombination of electrons and holes from the absorber and the other one from the cross-recombination where the electrons from the buffer conduction band recombine with the holes from the absorber valence band. It is assumed to have an inversion layer at the interface, i.e., electrons are the majority charge carriers at the interface instead of holes as the p-type material is usually used as an absorber. When a voltage is applied, the hole quasi Fermi level $E_{\mathrm{F},p}$ is modulated, similar as the QNR recombination, but limited in this case by holes for recombination $p \propto \exp(qV/kT)$ (see Figure 2.9b). There is a strong increase of recombination with respect to the voltage leading to a diode quality factor of $A = 1$.

However, the diode quality factor depends on the interface charge density. If the Fermi energies are not pinned[2], two cases can occur: a nonsymmetric heterojunction and a symmetric heterojunction. Based on this, the diode quality factor for interface recombination via a single defect in the middle of the interface band gap $E_{\mathrm{g,IF}}$ can be determined by $A = 1/(1\text{-}\theta)$, with $\theta = \varepsilon_{\mathrm{abs}} N_{\mathrm{A,abs}} / (\varepsilon_{\mathrm{abs}} N_{\mathrm{A,abs}} + \varepsilon_{\mathrm{buffer}} N_{\mathrm{D,buffer}})$ where ε represents the permittivity, and N_{A} and N_{D} represent the acceptor and donor density, respectively. For a highly nonsymmetric heterojunction, i.e., if $\varepsilon_{\mathrm{buffer}} N_{\mathrm{D,buffer}} >> \varepsilon_{\mathrm{abs}} N_{\mathrm{A,abs}}$ or $\varepsilon_{\mathrm{buffer}} N_{\mathrm{D,buffer}} << \varepsilon_{\mathrm{abs}} N_{\mathrm{A,abs}}$, the diode factor is generally $A = 1$. Considering the case of a symmetrical heterojunction, that is, $\varepsilon_{\mathrm{buffer}} N_{\mathrm{D,buffer}} = \varepsilon_{\mathrm{abs}} N_{\mathrm{A,abs}}$, the diode

[2]The position of the Fermi level at the interface is not only determined by the doping ratio of the absorber and buffer, but can also be determined by interface charge. If the interface charge density either for donors or acceptors is relatively high, then a variation of the absorber acceptor concentration or buffer donor concentration has no influence on the Fermi level position at the interface. This effect is denoted as Fermi level pinning (FLP).

factor is $A = 2$. This can be explained due to the symmetrical variation of both quasi Fermi levels at the interface with respect to the deep interface defect level when a bias voltage is applied, in a similar way as in the SCR recombination illustrated in Figure 2.7.

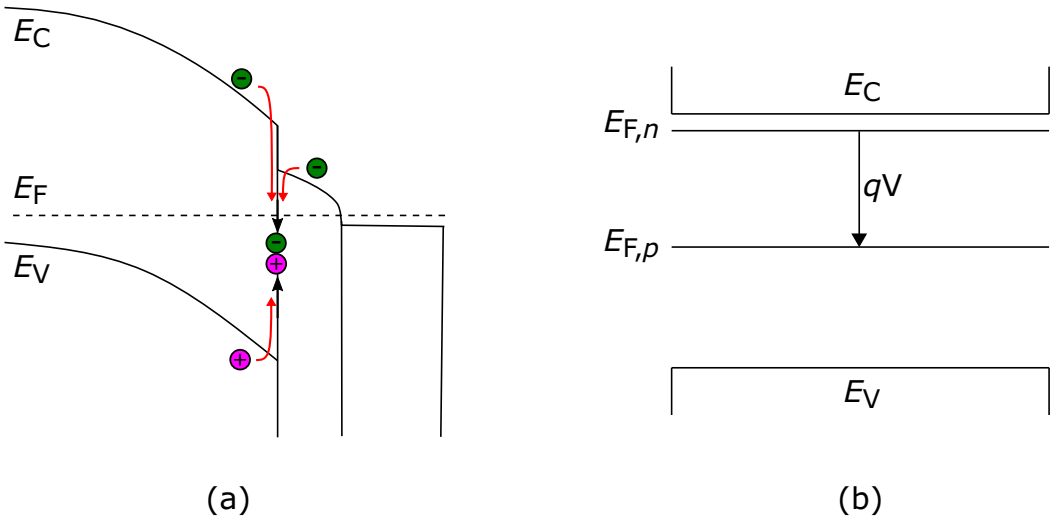

Figure 2.9.: Defect related recombination at the absorber/buffer interface: (a) energy band diagram and (b) schematic representation of the energy levels under applied bias.

Similarly as the SCR recombination, the interface recombination follows the SRH expression given in Equation 2.12, except that the carrier lifetimes are replaced by the interface recombination velocities, S_p^{-1} and S_n^{-1}, respectively. The recombination velocities are defined as $S_{n,p} = N_{\mathrm{IF}}\sigma_{n,p}\upsilon_{n,p}$ for a discrete interface state of density N_{IF}. The interface recombination velocity increases directly with the interface state density with an upper limit defined by the thermal velocity. Similar to the SCR recombination, the interface recombination may be enhanced by tunneling (see path (3*) in Figure 2.6).

For the energy band diagram given in Figure 2.9a, the difference of the conduction bands between the absorber and the buffer, $\Delta E_{\mathrm{C}} = E_{\mathrm{C,abs}} - E_{\mathrm{C,buffer}}$, results $\Delta E_{\mathrm{C}} < 0$. The activation energy of the saturation current density is given by $E_{\mathrm{g,IF}} = E_{\mathrm{g,abs}} + \Delta E_{\mathrm{C}}$ and since $\Delta E_{\mathrm{C}} < 0$, the activation energy is smaller than the absorber band gap, $E_{\mathrm{A}} < E_{\mathrm{g,abs}}$ [41].
Accordingly, without Fermi level pinning, the diode quality factor varies between 1 and 2 depending on the doping ratio and the activation energy of the J_0 is $E_{\mathrm{A}} = E_{\mathrm{g,IF}}$. The same situation applies for an exponential defect distribution. In case of a Fermi level pinning either above or below the middle of the interface band gap, the recombination will depend on the interface hole or electron concentration, respectively, and the diode quality factor becomes $A = 1$ as only the hole quasi Fermi level or electron quasi Fermi

level will move under applied bias with an activation energy being smaller than the interface band gap, $E_{\mathrm{A}} < E_{\mathrm{g,IF}}$.

The previous analysis is based on exhibiting a conduction band cliff between the absorber and buffer layers with $E_{\mathrm{g,IF}} < E_{\mathrm{g,abs}}$. However, when a conduction band spike is present with a highly nonsymmetric heterojunction, e.g., if $\varepsilon_{\mathrm{buffer}} N_{\mathrm{D,buffer}} >> \varepsilon_{\mathrm{abs}} N_{\mathrm{A,abs}}$, the activation energy for $\Delta E_{\mathrm{C}} > 0$ is $E_{\mathrm{g,abs}}$ which also equals the interface band gap and the diode factor is $A = 1$. In the case that $\varepsilon_{\mathrm{buffer}} N_{\mathrm{D,buffer}} = \varepsilon_{\mathrm{abs}} N_{\mathrm{A,abs}}$, the activation energy exceeds the absorber band gap and is given by $E_{\mathrm{g,abs}} + \Delta E_{\mathrm{C}}$ with a diode factor of $A = 2$ [17]. For devices with a dominant interface recombination, a front surface band gap grading can shift the recombination to a position within the bulk [17]. For a cell without interface recombination, the benefit of a front surface gradient will be small. A front surface band gap gradient increases the V_{oc} of the solar device due to the suppression of interface recombination without losses in J_{sc} [40].

A summary of the diode quality factors and activation energies for the main defect related recombination paths is listed in Table 2.1.

Table 2.1.: Compilation of the diode quality factors and activation energies for defect related recombination.

Recombination region	Condition	Diode factor (A)	Activation energy (E_{A})
SCR	Deep defect	2	$E_{\mathrm{g,abs}}$
	Shallow defect	1	
	Shallow + deep defect	2	
	E_{def} between $E_{\mathrm{g}}/2$ and $E_{\mathrm{C}}/E_{\mathrm{V}}$	1.1 - 1.8	
	Exp. defect distribution	1 - 2	
	Tunneling	> 2	
QNR	$d_{\mathrm{abs}} >> L_n$	1	$E_{\mathrm{g,abs}}$
IF ($\Delta E_{\mathrm{C}} < 0$)	No FLP	$1/(1-\theta) = 1-2$	$E_{\mathrm{g,IF}}$
	FLP	1	$< E_{\mathrm{g,IF}}$
	Exp. defect distribution	1 - 2	$E_{\mathrm{g,IF}}$
IF ($\Delta E_{\mathrm{C}} > 0$)	Highly nonsymmetric	1	$E_{\mathrm{g,abs}}$
	Symmetric	2	$E_{\mathrm{g,abs}} + \Delta E_{\mathrm{C}}$

The considerations of the electrical transport and recombination mechanisms presented in this chapter will serve as a basis for the interpretations of CIGSe solar cell examined in the following chapters.

2.4. Influence of alkali metals in CIGSe solar cells - Literature review

In recent years, the introduction of alkali fluoride post deposition treatments with heavy alkali elements (heavier than Na) has led to efficiency improvements of CIGSe solar cells. Initially, PDTs were introduced as a means to incorporate Na into CIGSe for flexible solar cells [42] after growing the absorber film without Na (also due to the absence of Na diffusing from the alkali-free substrate) for a better Ga diffusion and desired band gap profile. In 2013, PDT with KF was introduced [7] on low temperature co-evaporated CIGSe absorbers grown on flexible substrates with an efficiency of 20.4% - a record efficiency for flexible CIGSe cells at that time. Later on, a higher performance was accomplished by incorporating RbF into the absorber layer on glass substrates with a remarkable efficiency of 22.6% [11] and, in 2019 a record efficiency of 23.35% was achieved by incorporating CsF [8] in CdS-free solar cells. These records were obtained with different absorber techniques and without/with S in the absorber. Despite the numerous studies demonstrating such high efficiencies and the impact of using alkali metals post deposition treatments, the mechanisms behind the beneficial effects on CIGSe devices are still open to discussion.

Non-electronic effects of alkali fluoride PDT

Studies concerning the electronic structure of the CIGSe surface and CIGSe/CdS interface after alkali fluoride PDT resulted in a downward shift of the valence band maximum (VBM) at the absorber surface after PDT [43–45] using ultraviolet photoelectron spectroscopy (UPS), X-ray photoelectron spectroscopy (XPS) and inverse photoemission spectroscopy (IPES). Contradictory results were also reported; in the case of KF, an upward shift of the VBM [46] was derived from hard X-ray photoelectron spectroscopy (HAXPES). Similar discrepancy has also occurred when comparing the CBM between untreated/treated PDT samples [44, 45]. From this, either low-temperature absorbers [45, 47] or high-temperature absorbers [43] with alkali fluoride PDT have shown a band gap widening at the CIGSe surface, but also the case without significant band gap widening has been reported on RbF-PDT CIGSe absorbers prepared at high temperatures [44]. Moreover, XPS measurements detected the presence of heavy alkali metal content in the first few nanometers of the CIGSe surface, whereas no Na was detected. Such measurements have suggested that changes of the CIGSe surface chemical composition induced by PDT occur in a depth of less than 30 nm [7].

A VBM shift and/or band gap widening at the absorber surface could reduce the hole concentration at the interface, and a reduced carrier recombination near the absorber surface [41] has been assumed in previous studies [43, 45, 48, 49]. This can only be the case if there is actually substantial interface recombination in the device, which is

presumably not the case for high efficiency CIGSe devices [18, 50]. The downward shift of the VBM was considered as an outcome of the change of surface composition of the CIGS after PDT due to the formation of secondary alkali-In-Se_2 phases that were made responsible for the observed band gap widening [51, 52] with an increased $E_{g,IF} \approx 2.5$ eV [45, 53], and due to the Cu and Ga depletion in the near-surface region [48, 53–57] which was shown to lead to the formation of a so-called ordered vacancy compound (OVC) layer on the surface of Cu-poor CIGSe thin-films (see $CuInSe_2$ phase diagram in Reference [58], [59]).

Malitckaya et al. [60] investigated the segregation of a secondary phase at the CIGSe surface as a consequence of alkali fluorides during PDT based on density functional theory (DFT), finding that the formation of K-, Rb- and Cs-$InSe_2$ compounds is energetically favorable (and not in the cases of Li and Na), and therefore are expected to be found at the absorber surface after PDT. Hence, the CIGSe surface is depleted of Cu and Ga and enriched with Rb, K or Cs [54, 61], in particular, a K-, Rb-, Cs-$InSe_2$ is observed on top of the absorber [62, 63], varying its thickness with respect to the evaporation rate/deposition time during PDT [53]. Such alkali-In-Se_2 phase formation has been suggested to passivate the CIGSe surface [64]. Lepetit et al. [65] showed that a K-In-Se phase intentionally incorporated on the absorber surface results in similar effects to those by PDT. However, Larsson et al. and Siebentritt et al. [53, 66] reported that the K-, Rb- or Cs-$InSe_2$ rich surface phase in itself or any surface modification are not responsible for the enhancement performance of chalcopyrite devices, in contradiction to Ishizuka et al. [67] who suggest that such modification of the band diagram at the interface contributes to improvements in the V_{oc}. The model proposed by Kodalle et al. [68] suppose that the $RbInSe_2$ (RIS) layer acts as a barrier for the photocurrent and therefore lowers the FF if it becomes too thick.

A Cu-depleted surface facilitates the in-diffusion of Cd into copper vacancies during the chemical bath deposition (CBD) of the CdS buffer layer, as suggested in previous studies [7, 46, 51, 69]. The Cd in-diffusion further enhances the type inversion close to the CIGSe interface (forming a $p - n$ homojunction within the absorber). The created Cd_{Cu} donors push the Fermi level closer to the conduction band and reduce the recombination of electrons due to lower hole concentration at the interface [70]. Lepetit et al. [65, 71] also suggested that the alkali elements could be partially substituted by Cd during CdS CBD by converting the alkali-In-Se_2 phase into a $CdIn_2S_4$ interface layer in the beginning of the CdS CBD that would yield beneficial interface properties.

From the formation of a secondary phase and Cd in-diffusion into Cu vacancies at the CIGSe surface, the absorber surface is improved for a better coverage [7, 49, 72] and a better buffer growth allowing a reduction of the CdS layer thickness without losses in

photovoltaic parameters [73]. However, it has been reported that the main beneficial effects from PDT are not necessary associated with the CdS CBD [66].

Secondary-ion mass spectroscopy (SIMS) profiles have revealed a significant reduction of the Na content after PDT in the CIGSe bulk and a higher heavy alkali content compared with Na throughout the CIGSe absorber layer [7, 11, 51, 64], showing that PDT leads to a significant incorporation of the heavy alkali metal and removal of Na in the CIGSe layer which is commonly explained by an ion exchange mechanism [74, 75] that favors the presence of heavy alkali elements over Na. One hypothesis is that the main benefit of Rb, K or Cs is the passivation of defects at grain boundaries [55, 76, 77] in a similar way as for Na. All alkali elements tend to accumulate at the front and the back of the absorbers (surfaces and interfaces) [77], with lower concentrations within the bulk [78], and especially they segregate at the CIGSe grain boundaries [53, 79–84], where the lighter alkali elements are pushed into the grain interior with the presence of the heavy alkalis. Na is expected to be more present within the grains than K and Rb, however, K is also able to diffuse into the grain interior as well as to passivate defects at the grain boundaries, so K is found inside the grains in larger amount in contrast to Rb which is unlikely to diffuse into the grain interiors [60, 85, 86]. A larger concentration of the alkali elements close to the surface is expected due to the formation of secondary phases and also due to the presence of smaller grains (larger concentration of grain boundaries) [51].

Electronic effects of alkali fluoride PDT

As previously discussed, Rb, K and Cs are all known to enhance the performance of CIGSe devices in a similar way with comparable modifications in the composition of the absorber films and the impact on the chemical structure at the surface and interphases [11, 51]. Excessive amounts of heavy alkali metals result instead in degraded photovoltaic properties [48, 51]. Besides some results have suggested that the alkali effects on the CIGSe films and device properties depend on the group IIIA elemental composition in the CIGSe absorbers, i.e., effects of PDT strongly depends on the GGI [67] and the [Cu]/([Ga]+[In]) (CGI) ratio [57, 68] in the absorbers.

Regarding the electronic effects of alkali fluoride PDT on device parameters, an increase in the open-circuit voltage has been observed consistently, whereas short-circuit current and fill factor present an inconsistent trend in different contributions [8, 11, 48, 51, 66, 67, 78, 87, 88].

It has been assumed that the dominant recombination of CIGSe samples is at the interface, and upon PDT the recombination shifts to bulk recombination as the dominant mechanism. On this basis, since PDT has an impact on the CIGSe near-surface

properties and the V_{oc} is related to carrier recombination, the gain in V_{oc} has been explained through the assumption that PDT suppresses (but not eliminates) the interface recombination mechanism for small band gap [66,70,89] and wide band gap [87] CIGSe absorbers. Conversely, some other authors [49,53,84] have suggested a V_{oc} improvement due to an alkali treatment-induced suppression of merely bulk recombination, and particularly due to modifications of the grain boundaries. Furthermore, time-resolved photoluminiscence (TRPL) revealed an increase in the minority carrier lifetime τ_n after PDT [55,67,90], then resulting in the reduction of the photogenerated carrier recombination and the reason for improved V_{oc} [11,48,67,90,91]. Larsson et al. [66] showed that the beneficial effect on V_{oc} from the PDT is independent of the buffer layer material, while Nakamura et al. [8] by using a Zn-based double buffer layer enhanced V_{oc}, suggesting a modified band bending in the depletion region of the chalcopyrite absorber or less elemental diffusion from the buffers into the absorber, and so reducing the recombination rate.

Capacitance-voltage ($C-V$) measurements have been performed to investigate the hole concentration of the CIGSe thin film solar cells fabricated with and without PDT, showing an increase in the net doping concentration (N_{CV}) as reported by some authors [48,55,61,70,88,92], which could also explain the reason for the improved V_{oc}. Nevertheless, Pianezzi et al. [70] concluded that the addition of heavy alkali metals is less effective than Na to increase the hole concentration by PDT.

Concerning the FF, it has been assumed that a loss in FF is due to an interaction between the buffer layer and the alkali-rich surface modification created by PDT [66]. Some authors have reported that HCl etching prior the buffer layer deposition is needed to achieve competitive FF values [66,78] since as deposited or water-rinsed absorbers result in lower FF. Nakamura et al. [8] reported a gain in FF by depositing Zn-based buffer layers explained by a better coverage of the buffer which results in a better shunt resistance.

Some publications have reported the presence of a barrier for the diode current, resulting for instance in a roll-over of the current-voltage characteristics and a cross-over between dark and light $J-V$ curves after PDT [48,53,66,70,78,93,94] with an increasing blocking behavior (roll-over of the $J-V$s) when increasing the amount of the heavy alkali element incorporated into the solar cell device. Furthermore, a more expressed saturation of the V_{oc} at low temperatures has been observed for PDT samples [93].

Three possible origins of the $J-V$ roll-over have been suggested [17,95]: (1) back contact barrier located at CIGSe/Mo interface, (2) acceptor states located at the buffer/window interface, and (3) a large positive (cliff) conduction band offset at the buffer/window interface. Additionally, the CIGSe-surface layer has also been assumed to cause the barrier [78], where the alkali-In-Se phase has been interpreted as the layer

responsible for the blocking of the diode current, in contradiction to the findings of Siebentritt et al. [53], who concluded that the surface band gap widening does not lead to a transport barrier.

It has also been reported that a surface treatment either with H_2O [66] or HCl [53, 78] leads to a diode quality improvement by removing soluble salts from the surface and/or thinning the alkali-induced surface layer which might be the reason for a reduced blocking of the diode current, and therefore leading to an increased FF as previously mentioned.

Ishizuka et al. [94] have found that the buffer layer plays an important role in suppressing the emergence of the cross-over and the roll-over shapes in the $J-V$ curves after PDT, indicating the phenomenon is not an issue of the Mo/CIGSe interface. On the other hand, Pianezzi et al. [70] suggested the presence of a secondary diode at the back contact whose barrier is strongly influenced by Na and much less by heavier alkali metals, and from this point of view, the ion exchange of Na by the heavy alkali metals during PDT should be avoided [48, 96].

The following table (Table 2.2) summarizes the findings of the main effects caused by the introduction of alkali fluoride PDT in chalcopyrite thin-film solar cells:

Table 2.2.: Summary of the non-electronic and electronic effects of CIGSe solar cells caused by alkali fluoride PDT.

Non-electronic effects
Downward/upward shift of the VBM and/or CBM at the absorber surface
Cu and Ga depletion at the absorber surface
Surface improved for buffer layer growth
Reduction/substitution of Na in the CIGSe bulk
Heavy alkali metal enrichment in the CIGSe bulk
Segregation of alkali-In-Se phase at the CIGSe surface
Electronic effects
Enhancement in V_{oc}
Inconsistent trend in J_{sc}
Inconsistent trend in FF
Roll-over of $J-V$s
Cross-over of $J-V$s
V_{oc} saturation at low temperatures

Main findings of the CIGSe thin film solar cells fabricated at HZB

An extensive research has been previously performed by Kodalle [48, 49, 52, 68, 97] on the CIGSe thin-film solar cells prepared with RbF-PDT and fabricated at HZB

including some samples presented in this work.
Most of these results are in accordance with the main findings of the morphological and compositional changes induced by the RbF-PDT and its impact on the performance of solar devices described above.

Among the main findings are:

- An increasing V_{oc} and decreasing FF has been observed for longer PDT duration, which represents a higher amount of RbF deposited on the CIGSe absorber. The optimum deposition time of the PDT was 10 min.
- All PV parameters deteriorate for low Cu content (low CGI ratio) in the CIGSe absorber, with a gain in V_{oc} for CGI ≥ 0.8 and improved FF only for CGI $= 0.95$.
- Accumulation of Rb near the absorber surface and the back side of the absorber seen from elemental depth profiles of RbF-PDT (see Appendix A.2, Figure A.1).
- Segregation of Rb at the grain boundaries in the CIGSe bulk as observed in the energy-dispersive X-ray spectroscopy using a scanning transmission electron microscope (STEM-EDX) measurements, leading to a migration of Na to the CIGSe surface and into the gran interior. A Rb-Na exchange mechanism was apparently only valid in sample with high Cu content (CGI > 0.8).
- Cu and Ga depletion at the absorber surface after rinsing with ammonia solution.
- A (Rb,Na)-In_xSe_y secondary phase is formed at the absorber surface during the RbF-PDT based on scanning electron microscope (SEM), XPS and STEM analyses. After NH_3(aq) etching, traces of In-Se-O remain on the (Rb,Na)-In_xSe_y surface leaving a nanostructured surface layer. The most likely candidate for such secondary surface phase is the $RbInSe_2$ layer [63].
- An $E_g = 2.8 \pm 0.1$ eV was found for the grow high-quality n-doped $RbInSe_2$ layer determined by total reflectance (TR) and total transmission (TT) optical measurements and whose thickness is dependent on the CGI ratio.
- Better coverage of the CIGSe surface after RbF-PDT for the subsequent CdS deposition with a lower growth rate and shorter CBD duration (i.e. thinner CdS layers). Also the CdS growth led to a reduction of the amount of the so-called ordered defect compound (ODC), which is initially present at the surface of the absorber of Cu-poor films.
- Reduction of the Na content within the absorber for longer deposition times of Rb with a flatter Na distribution near the back contact. Na depth profiles of some of the samples studied in this work are shown in Appendix A.2, Figure A.1.

- Higher carrier concentration in the absorber layer for longer RbF-PDT duration ($t = 10$ min) due to a higher concentration of Na inside the grains. A short RbF-PDT ($t = 4$ min) led to a reduction of the carrier concentration as measured by $C-V$ profiling given in Appendix A.2, Figure A.1. RbF-PDT led to lower carrier concentration in samples with CGI < 0.8 and to a higher carrier concentration in samples with CGI ≥ 0.8 in comparison to samples without PDT as seen in Appendix A.2, Figure A.2.
- Blocking of the forward diode current (roll-over) of the dark $J-V$ curves after PDT.

These observations will be considered in the explanation of the experimental and numerical results given in Chapters 4 and 5 for the proposed models described in Chapter 6 in order to find the possible connections that will lead to the unknown origin of the non-ideal effects caused by the RbF-PDT.

3. Characterization and simulation details

The main characterization methods used in this work to study the behavior of the different CIGSe solar cells included in Chapter 4 are described here. Two different fitting programs were used extract the diode parameters of the dark and illuminated characteristics and the fitting procedure is given. At the end of this chapter, the reference model used in SCAPS-1D with the material and device parameters are listed. By using this model, variations of some of these parameters will be performed in order to find out which parameters may influence the $J-V$ behavior of the CIGSe solar cells after RbF-PDT.

3.1. Characterization techniques

Temperature-dependent current-voltage characterization

Measurements of the $J-V$ characteristics as a function of temperature and illumination were performed in an evacuated (to avoid water condensation inside the chamber) liquid N_2 cooled cryostat (CryoVac) using a Keithley 2601A source measure unit in four-point configuration and measuring in the range of -0.5 V to +1.5 V. The temperature range was varied from 320 K to 100 K with a step size of 10 K. A solar simulator (Oriel VeraSol) with light-emitting device (LED) light sources was used to simulate the AM1.5 solar spectrum. The light intensity (I) was varied from 100 mW/cm^2 to 0.1 mW/cm^2.

Current-voltage characterization

The main electrical parameters of the solar cells (J_{sc}, V_{oc}, FF and η) were determined by current-voltage measurements under standard test conditions (STC: AM1.5 spectrum, 100 mW/cm^2, 25 °C) using aWACOM A+ dual light source solar simulator equipped with a xenon and halogen lamp, and a Keithley source measure unit.

External quantum efficiency

The external quantum efficiency (EQE) measurements of the solar cells were performed without applied bias voltage (short-circuit conditions) and with a monochromator under chopped illumination over the wavelength range of 300 nm to 1400 nm with a step size of 10 nm, and using lock-in technique with white light bias. The minimum band gap energy ($E_{\mathrm{g,min}}$) of the solar cell was extracted from the maximum of the first-order derivative of the EQE, $\mathrm{d}(EQE)/\mathrm{d}(\lambda)$. The determination of the minimum band gap used in this work is merely an approximation since the double-graded band gap present in most of the absorbers would need a more complex analysis as described by Troviano et al. [98], who proposed an analytical model that considers both absorption and collection properties of the front and back grading of high-efficiency CIGSe solar cells in order to interpret the internal quantum efficiency (IQE) and extract parameters such as the Urbach energy of band tails and the minimum band gap.

Capacitance-voltage characterization

Capacitance-voltage measurements were performed using a self-built setup based on an Agilent 4284A LCR meter to determine the doping profiles of the absorber. The solar cells were relaxed in dark for 5 minutes before each measurement and measured at room temperature at a frequency of 100 kHz with DC bias voltages ranging from -0.5 V to +0.5 V.

3.2. Fitting procedure of the $J(V,T)$ − characteristics and diode equation

A large number of data files was obtained after performing JVT measurements of each sample. Each file contains the PV parameters (J_{sc}, V_{oc}, FF and η) and the corresponding current densities of the selected voltage range at different temperatures and light intensities I (evenly distributed along the curve: 100, 75, 50, 35, 25, 15, 10, 7, 5, 4, 3, 2, 1, 0.8, 0.6, 0.5, 0.4, 0.3, 0.2, 0.1 mW/cm^2). Dark measurements were also carried out at each temperature.

In order to determine the diode quality factors A, saturation current densities J_0, series and shunt resistance R_{s}, R_{sh} of the dark $J-V$ curves, each curve at each temperature was fitted with the two-diode model equation (see Equation 2.11). Previous comparisons between different software programs including MATLAB and Grace by using their non-linear least-squares fit solvers, and the software IGOR Pro by using the evaluation procedure PV-Evaluate 1.0.0 developed by Roland Mainz (HZB) [99] were done and thus obtaining with the latter program a higher accuracy of the fit. Two diode quality

factors A_1, A_2, and two saturation current densities $J_{0,1}$, $J_{0,2}$ were deduced and needed to reproduce the experimental curves. However, only the parameters corresponding to the main diode (A_1, $J_{0,1}$) were used in this work for recombination analysis. Dark $J-V$ curves that present a blocking of the forward diode current at forward bias do not correspond to the model and have therefore not been fitted.
Under illumination, since the voltage dependence of the photocurrent would lead to an incorrect determination of the diode parameters, a direct evaluation of the light $J-V$ characteristics is not feasible. Therefore, the diode parameters under illumination are determined from the J_{sc} vs V_{oc} plots. From the two-diode model equation (Equation 2.11), at V_{oc} there is no current flow, then $J=0$, and the curve is independent of the R_{s} since there is no voltage drop across it. Besides, the $J_{\mathrm{sc}}(V_{oc})$ data points are not typically in the regime of shunt, thus R_{sh} can be neglected[1]. The resulting two-diode model equation for the $J_{\mathrm{sc}}(V_{oc})$ curve results:

$$J_{\mathrm{sc}} = J_{0,1}\left[\exp\left(\frac{qV_{oc}}{A_1kT}\right)-1\right] + J_{0,2}\left[\exp\left(\frac{qV_{oc}}{A_2kT}\right)-1\right] \tag{3.1}$$

The $J_{\mathrm{sc}}(V_{oc})$ curves were fitted with Equation 3.1 and using the software Grace 2D graph plotting tool for Unix-like operating system[2]. The Equation 3.1 was modified in order to introduce the equation with Grace parameters as it is shown:

$$y = \frac{\mathrm{abs}\left(a0\left[\exp(a1*x)-1\right]+a2\left[\exp(a3*x)-1\right]\right)}{s0.y} \tag{3.2}$$

where:

$y=1$	$a0=J_{0,1}$	$a3=q/A_2kT$
$x=V_{oc}$	$a1=q/A_1kT$	
$s0.y=\mathrm{abs}(J_{\mathrm{sc}})$	$a2=J_{0,2}$	

Setting the equation equal to 1 on the left side of the equation and dividing then the right side of the equation by the J_{sc}, a more accurate fit of the curve was obtained.

[1] In some cases, the shunt resistance could not be neglected since the $J_{\mathrm{sc}}(V_{oc})$ points were positioned on the shunt region of the $J-V$ curves, and therefore R_{sh} was included in the fit equation.
[2] The few number of data points of the $J_{\mathrm{sc}}(V_{oc})$ curves did not allow the application of the same fit tool used for dark curves

3.3. Numerical simulation

In order to model the results obtained from the experimental measurements and to analyze the effects of material or electrical parameters such as conduction band offsets ΔE_{C}, thickness d, doping $N_{\mathrm{A,D}}$ and defect densities N_{def}, diffusion lengths L, mobilities μ, among others, influence the JVT behavior, numerical simulations of a CIGSe solar cell are conducted using SCAPS-1D.

SCAPS-1D is a one dimensional solar cell simulation program developed at the Department of Electronics and Information Systems (ELIS) of the University of Gent [100]. It was originally developed for $CuInSe_2$ and CdTe based solar cells, however its capabilities have been improved to be also applicable to crystalline Si and GaAs and amorphous a-Si devices. A solar device with up to seven semiconductor layers and its interfaces between the back and the front contact can be modeled by setting a large number of material and electrical parameters. SCAPS-1D finds numerical solutions by solving the basic semiconductor equations: Poisson equation, relating the charge to the electric potential (ϕ), transport equations and continuity equations for electrons and holes (equations can be found in Reference [101]). The total length of the solar cell is divided in N discrete intervals, and the value of ϕ_{i} and the electron and hole carrier densities (n_{i}, p_{i}) at each of the intervals constitute the unknowns of the problem that can be found by numerically solving a set of $5N$ non-linear equations with $5N$ variables. The basic equations are non-linear because the continuity equations contain a recombination term, which is non-linear for n and p. The boundary conditions at semiconductor-semiconductor interfaces assume that the transport mechanism across the heterojunctions is thermionic emission. Interface recombination can be treated by considering not only direct recombination where the electrons of a given semiconductor can only recombine with the holes of the same semiconductor, but also for cross recombination. The boundary conditions at metal-semiconductor interfaces assume a Schottky barrier, thermionic emission for the majority carriers and surface recombination for the minority carriers. A more detailed description of the program and its algorithm can also be found in [102–106].

3.3.1. Simple model of a CIGSe solar cell

The layer stack for the reference CIGSe solar cell consists of four layers: p-type electron mirror layer, non-graded p-type CIGSe absorber layer, n-type CdS buffer layer, and n-type ZnO window layer. Table 3.1 lists the input parameters set for each layer and contacts to represent a simple model with a non-graded absorber, a reasonably long diffusion length L_n and lifetime of charge carriers τ adjusted only by neutral mid-gap bulk defects N_{def} in each layer.

Table 3.1.: Device and layer properties for a simple CIGSe thin-film solar cell model used for simulations with SCAPS.

Contact Properties		
Parameter [units]	Back	Front
Surf. rec. vel. of electrons [cm·s^{-1}]	1×10^{7}	1×10^{7}
Surf. rec. vel. of holes [cm·s^{-1}]	1×10^{7}	1×10^{7}
Barrier height (rel. to E_{V}) [eV]	0	0
Reflectivity [1]	0.3	from file

Layer Properties				
Parameter [units]	p-e-mirror	p-CIGSe	n-CdS	n-ZnO
Thickness [μm]	0.1	2.4	0.06	0.15
Band gap [eV]	1.3	1.1	2.4	3.3
Electron affinity [eV]	4.2	4.4	4.3	4.45
Dielectric permittivity (rel.) [-]	13.6	13.6	10	9
CB effective DOS [cm^{-3}]	2.2×10^{18}	2.2×10^{18}	2.2×10^{18}	2.2×10^{18}
VB effective DOS [cm^{-3}]	1.8×10^{19}	1.8×10^{19}	1.8×10^{19}	1.8×10^{19}
Electron thermal velocity [cm·s^{-1}]	1×10^{7}	1×10^{7}	1×10^{7}	1×10^{7}
Hole thermal velocity [cm·s^{-1}]	1×10^{7}	1×10^{7}	1×10^{7}	1×10^{7}
Electron mobility [cm^2·V^{-1}·s^{-1}]	100	100	50	50
Hole mobility [cm^2·V^{-1}·s^{-1}]	25	25	25	25
Shallow unif. donor density N_{D} [cm^{-3}]	0	0	1×10^{16}	1×10^{19}
Shallow unif. acceptor density N_{A} [cm^{-3}]	2.5×10^{15}	2.5×10^{15}	0	0
Absorption constant B [eV$^{(1/2)}$cm^{-1}]	1×10^{5}	1×10^{5}	1×10^{5}	from file

Neutral Defect States				
Parameter [units]	p-e-mirror	p-CIGSe	n-CdS	n-ZnO
Cap. cross sec. of electrons [cm^{-2}]	1×10^{-15}	1×10^{-15}	1×10^{-13}	1×10^{-12}
Cap. cross sec. of holes [cm^{-2}]	1×10^{-15}	1×10^{-15}	1×10^{-13}	1×10^{-12}
Energetic distribution (above E_{V})	Single	Single	Gauss	Gauss
Energy level [eV]	mid-gap	mid-gap	mid-gap	mid-gap
Characteristic energy [eV]	-	-	0.1	0.1
Defect density [cm^{-3}]	5×10^{15}	5×10^{15}	1.8×10^{18}	1.8×10^{16}

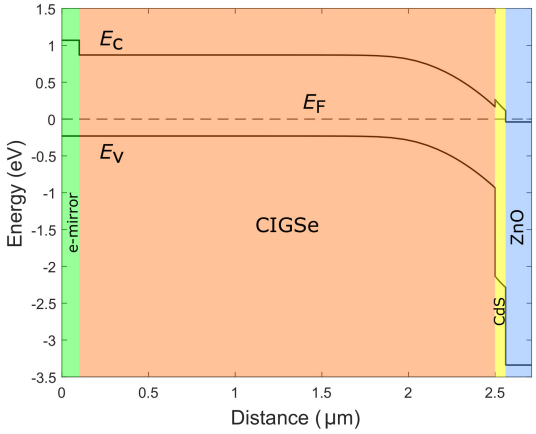

Figure 3.1.: Equilibrium band diagram of a e-mirror/CIGSe/CdS/ZnO thin-film solar cell.

In addition, no Fermi-level pinning and no interface defects were included in this model. The absorption coefficient of the ZnO was determined via reflectance and transmission measurements by UV-Vis as well as the reflectivity parameter of the front contact of the solar device once finished. The data corresponding to the dielectric permittivity ε, effective density of states $N_{\mathrm{C,V}}$, thermal velocities $v_{n,p}$ and mobilities $\mu_{n,p}$ were taken from the numerical modeling given in reference [107].

Conduction band offsets (ΔE_{C}) at the absorber/buffer and buffer/window interfaces are chosen to be a spike [108–110] and cliff [13, 110, 111] respectively, as can be seen in the equilibrium band diagram of Figure 3.1. The back contact is assumed to be ohmic (flat bands).

In CIGSe based solar cells, a high GGI content grading at the backside can reduce the surface recombination by acting as an electron mirror (also known as back surface field, BSF) [17]. Because of a long bulk diffusion length of the minority carrier electrons of the p-type absorber, an electron mirror has been included in the simple CIGSe model to assure bulk recombination as the dominant process.

In Chapter 5, the parameters of this model are modified to simulate the non-ideal effects caused by RbF-PDT in JVT measurements presented and described in Chapter 4. SCAPS version 3.3.05 is used to run the calculations without involving changes in the temperature and/or illumination parameters. Variations of these parameters are done using SCAPS version 3.2.01 due to small bugs existing in newer versions when temperature and light power are modified. To characterize a solar cell a voltage is applied to the left contact and the current is positive when entering the left contact. Power is generated by the solar cell ($P = -VJ$) with $J - V$ curves plotted in the fourth quadrant.

4. Evaluation of $J(V,T)$ − characteristics of CIGSe solar cells and the effects caused by RbF-PDT

In this chapter, temperature-dependent $J-V$ characteristics of a large set of CIGSe samples prepared by a multi-source evaporation process (known as physical vapor deposition, PVD) under different criteria such as absorber band gap grading, absorber Na and Cu content, PDT-duration and layer stack configuration of the device are presented to show typical cases of the JVT behavior of samples without and with RbF post deposition treatment. Evaluation of diode factors and activation energies is also given for this series of samples in order to describe the recombination and current transport mechanisms and the role that alkali fluorides by post deposition treatment play in CIGSe solar cells. In the final section of this chapter, JVT characteristics of samples in which RbF-PDT was deposited on CIGSe absorbers prepared by rapid thermal processing are also described.
Since most of the figures in this chapter correspond to JVT characteristics and to avoid a repetitive figure description, the JVT results will be displayed in the following way: JVT characteristics in dark (solid lines) and under illuminated conditions (square symbols) are plotted in semi-logarithmic scale in a temperature range from $T = 320$ K to $T = 100$ K with a step size of 10 K. The insets show the linear plot of the dark and light $J-V$ curves for three different temperatures: $T = 300$ K, 200 K and 100K.

4.1. Reference CIGSe solar cells − no RbF-PDT

4.1.1. CIGSe absorbers with graded band gap

CIGSe absorbers are prepared in a multi-source evaporation process. The decrease of the Cu content in the third stage by introducing In_2Se_3 and Ga_2Se_3 to reach the

desired CGI ratio results in a V-shape depth profile of the band gap energy, being useful to improve solar cell performance as described in Sections 2.3.3 and 2.3.4, with $E_{g,min}$ between 1.08-1.10 eV. In Section 4.2, band gap energies and EQE curves for each reference sample used in this work are given. The corresponding layer stack for the reference CIGSe solar cells consists of glass/Mo/CIGSe-PVD/CdS/i-ZnO/ZnO:Al. Deposition processes for these devices can be found in Appendix A.1. However, the reference CIGSe samples come from different "standards" since some deposition parameters have been slightly modified over time, changing the absorber thickness and the final CGI ratio from CGI = 0.90-0.95 in the earliest samples to CGI = 0.97 in the latest samples. CGI values and the STC electrical parameters for reference samples used in this work can be found in Section 4.2. Doping profiles derived from $C-V$ measurements can be seen in Appendix A.5, Figure A.12.

Figure 4.1 shows the JVT characteristics of a set of reference CIGSe solar cells. JVT results are displayed in chronological order from Reference 1 to Reference 6 according to the deposition date of the absorber. Typically, JVT results of the reference cells show no roll-over effect of the dark $J-V$ curves. Reference 2 and 4 present this characteristic over the entire temperature range from $T = 320$ K to $T = 100$ K. Reference CIGSe samples such as Reference 1, 3, 5, and 6 show a small roll-over effect only at lower temperatures as can also be clearly seen in the inset of each plot when $T = 100$ K.

No discrepancy between the $J_{sc}(V_{oc})$ data and the dark $J-V$ characteristics can be observed. In other words, the $J_{sc}(V_{oc})$ points follow the dark characteristics over the entire temperature range from $T = 320$ K to $T = 100$ K, with the exception of those samples where a small roll-over effect at low temperatures is present. For the latter case, the $J_{sc}(V_{oc})$ data appear to be positioned to the left of the dark $J-V$ curves as a consequence of the roll-over effect. Despite not significantly affecting the STC electrical parameters of the cell, the slight variations in the process parameters may lead to certain differences in the JVT characteristics of the reference cells.
At low temperatures, a slight cross-over effect between dark and light $J-V$ curves can be observed in the insets of the JVT characteristics of the reference CIGSe cells. Reference 4 is the cell in which all the non-idealities of a standard diode described above are missing, namely no roll-over, no discrepancy between dark $J-V$ and $J_{sc}(V_{oc})$ points and with an almost inappreciable cross-over effect at low temperatures.
$V_{oc}(T)$ behaviors of this set of reference CIGSe samples will be described in Section 4.2.

As described in Section 3.2, diode factors were extracted with the two-diode model equation (see Equation 2.11). The derived main diode factors of the set of reference CIGSe solar cells are displayed in Figure 4.2. In dark (Figure 4.2a) and under light conditions (Figure 4.2b),the different reference cells (Reference 1-6) have very similar

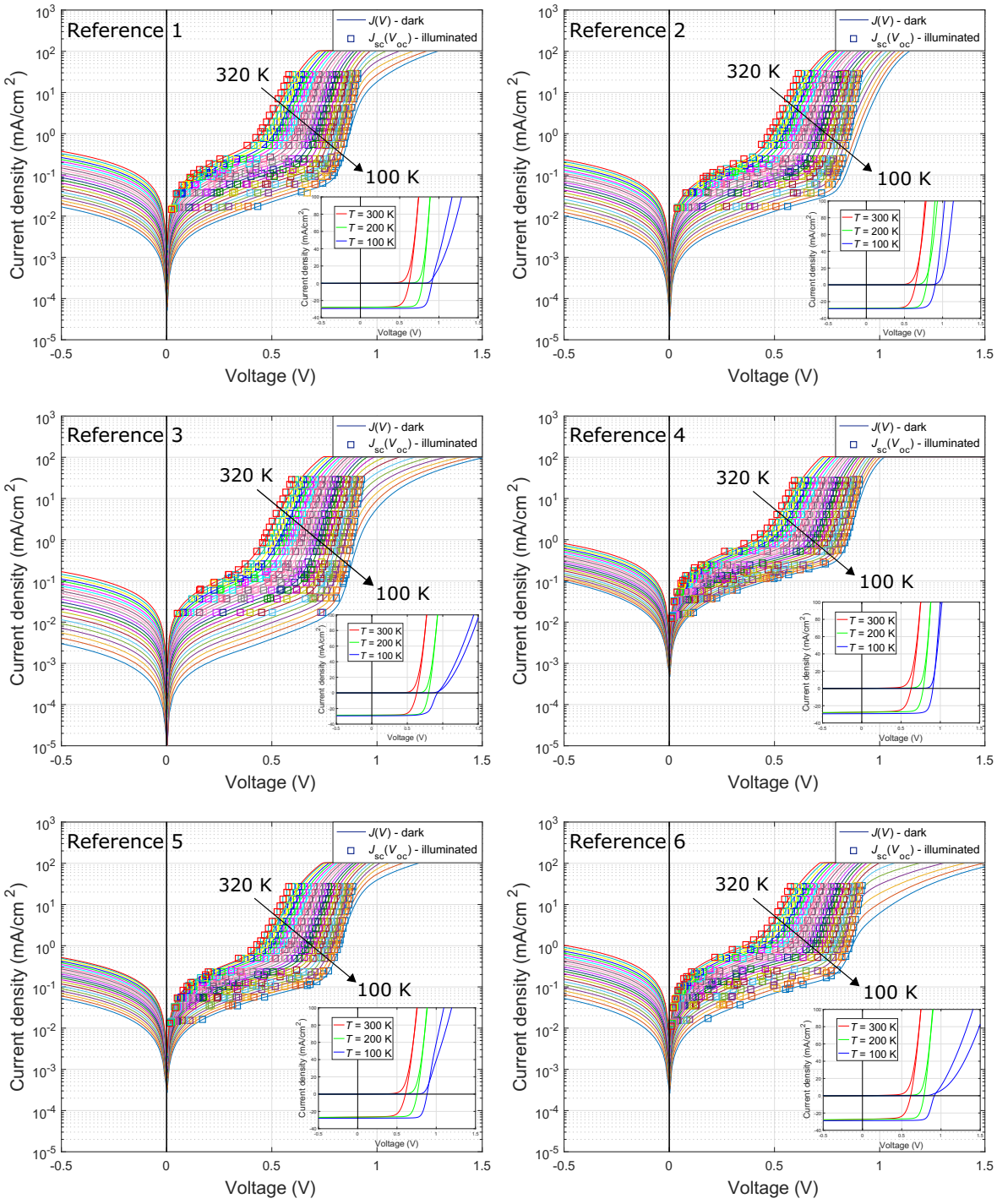

Figure 4.1.: *JVT* characteristics of a set of reference CIGSe solar cells numbered chronologically according to their deposition date (Reference 1-6).

diode factors under both conditions. Diode factors tend to increase while reducing the temperature (A is slightly temperature-dependent). Nevertheless, A_{dark} and A_{light} are mainly < 2 for the measured temperature range.
It was not possible to derive the diode factors in dark at low temperatures in many of the reference samples since the two-diode model equation did not fit properly in some of the dark $J - V$ curves.

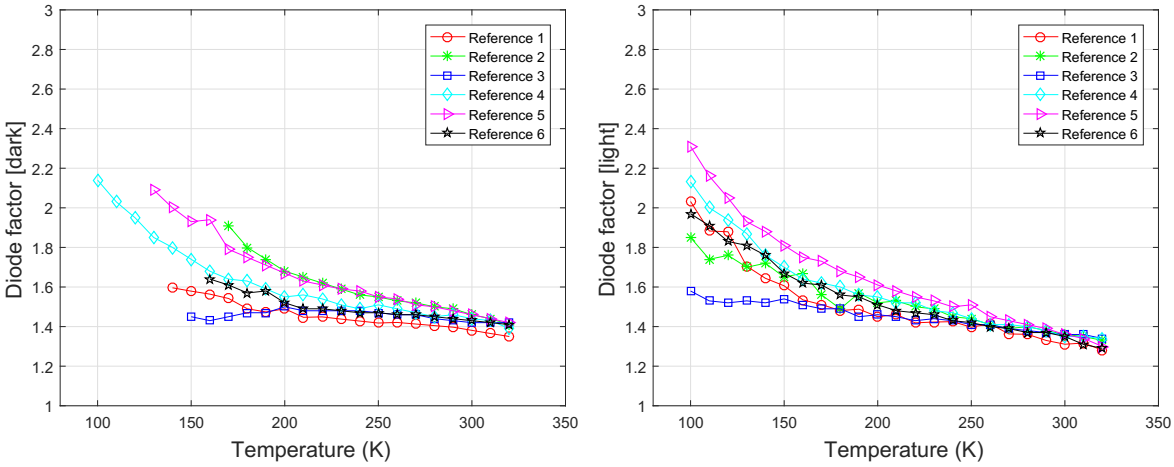

Figure 4.2.: Diode factors determined from a set of reference CIGSe solar cells as a function of the temperature (a) in dark and (b) under illumination. Each reference sample is represented by the same color/symbol in dark and light plots.

Hence, diode factors are consistent with Shockley-Read-Hall recombination in the SCR (see Section 2.3.1). This recombination model assumes a diode factor of $A = 2$ and independent of temperature, but a recombination due to a defect distribution may explain the temperature dependence of the diode factor (see Table 2.1). It can be deduced that the presence of a barrier at low temperatures in some of the $J - V$ curves of the reference samples lead to an incorrect fit of the two-diode model equation. It should be pointed out that even when the fit of the dark $J - V$ curves allowed to determine the dark diode factors, these may not reflect the actual recombination mechanism if such a barrier is present.

The main findings can be summarized as follows:

- Typically, the reference CIGSe solar cells do not show a roll-over or discrepancy between dark and light $J - V$ (assuming that the $J_{\text{sc}}(V_{oc})$ corresponds to the light $J - V$).
- Slight cross-over at low temperatures in some of the reference solar cells.
- A_{dark} and A_{light} are slightly temperature-dependent with values mainly < 2.

– V_{oc} saturation at low temperatures in the set of reference CIGSe cells (it will be described in Section 4.2).

4.1.2. CIGSe absorbers with constant band gap

CIGSe samples with constant (no grading) band gap were prepared by performing a one-stage process and calibrating the sources for the desired composition, so a multi-source evaporation of Cu, In, Ga and Se was done simultaneously, i.e., Cu, In, Ga and Se depth profiles are constant then resulting in a constant band gap energy of the absorber. Non-graded samples were prepared under the same layer stack as described in Section 4.1.1. Doping profiles of the measured CIGSe solar cells with constant band gap are given in Appendix A.5, Figure A.13.

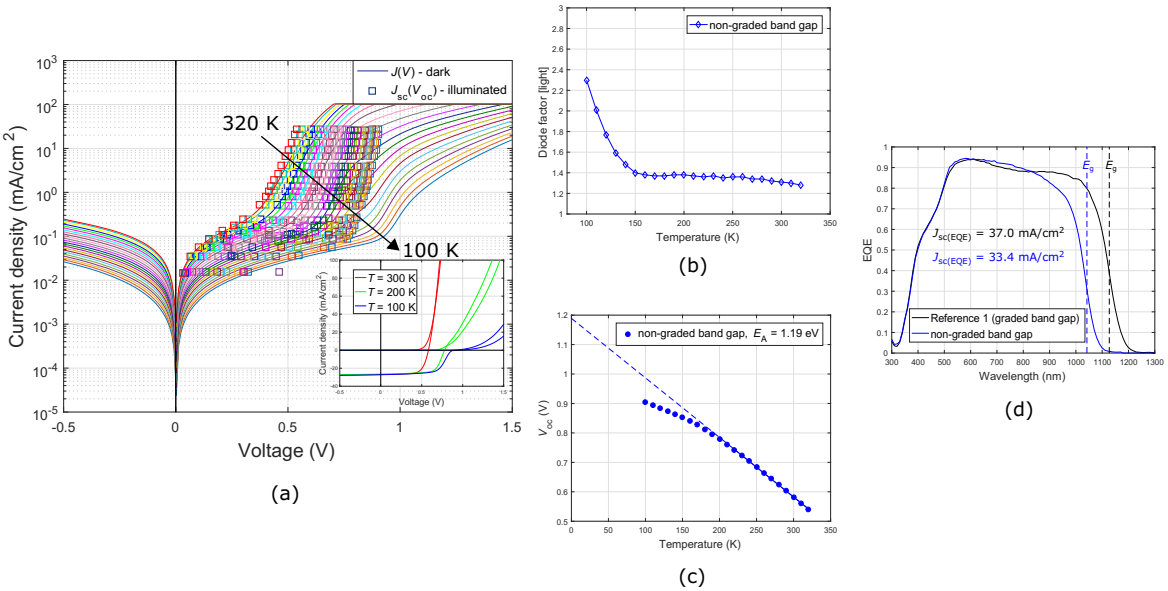

Figure 4.3.: Evaluation of a CIGSe solar cell with constant (non-graded) band gap: (a) JVT characteristics, (b) $A(T)$ plot under illumination, (c) $V_{oc}(T)$ plot and (d) EQE of Reference 1 with graded band gap and a CIGSe cell with non-graded band gap.

Figure 4.3a shows a reference CIGSe solar cell without a Ga grading into the absorber. Here, a blocking of the forward diode current occurs already at much higher temperatures and therefore a deviation of the $J_{\mathrm{sc}}(V_{oc})$ points with respect to the dark $J-V$ curves takes place. The linear plot in Figure 4.3a shows that the diode current is already limited at $T = 200$ K while in graded reference samples (see Figure 4.1) the diode current is not blocked at this temperature. Besides, at this temperature a slight cross-over between dark and light $J-V$ curves is present. Estimations of the diode factors under illumination are shown in Figure 4.3b. In a wide temperature range from $T = 320$ K to $T = 150$ K diode factors have a remarkable constant behavior with A_{light}

$\approx$ 1.4 independent of the temperature. At lower temperatures when $T < 150$ K, diode factors increases while decreasing the temperature until reaching values close to 2 as previously observed in reference CIGSe cells with graded band gap. Noted that the dark $J - V$ curves were not fitted because of the presence of the roll-over and thus the diode factors in dark A_{dark} were not determined. This practice will be repeated in further cases with a blocking behavior. In Figure 4.3c, the V_{oc} extrapolation to $T = 0$ K exhibits a saturation at low temperatures, a non-ideal characteristic equally observed in reference CIGSe devices with Ga grading which will be discussed in more detail in Section 4.2.

Moreover, from STC parameters, a reduced J_{sc} results for a non-graded CIGSe solar cell together with a slight loss in FF in comparison with reference cells with graded band gap, as can be seen in Table 4.2. Similarly, the integrated short-circuit current density calculated from EQE (Figure 4.3d) indicates a decrease of J_{sc} in the cell with constant band gap, $J_{\mathrm{sc}} \approx 37.0$ mA/cm^2 for graded absorbers and $J_{\mathrm{sc}} \approx 33.4$ mA/cm^2 for non-graded absorbers. The main reason of this decrease in photocurrent is the higher band gap obtained in samples with no Ga grading, $E_{\mathrm{g}} = 1.19$ eV (band gap estimation from EQE, see Figure 4.3d), thus reducing the absorption of photons of the energy of the solar spectrum compared to the graded absorber with a minimum band gap of $E_{\mathrm{g,min}} = 1.08$-$1.10$ eV. Additionally, a missing grading in the absorber and/or an influence of the back contact barrier as discussed in Section 2.3.3 may lead to a reduced J_{sc} and to an earlier blocking of the diode current in terms of temperature.

The main findings can be summarized as follows:

- The absence of a Ga grading into the absorber of CIGSe solar cells shows $J - V$ characteristics with a strong roll-over and hence a dark/light discrepancy at higher temperatures than with graded band gap.
- Slight cross-over at higher temperatures than with graded band gap.
- Typically, A_{light} is constant over a wide temperature range (150 K $\leq T <$ 320 K) but highly temperature-dependent at $T < 150$ K.
- V_{oc} saturation at low temperatures.

4.2. CIGSe solar cells with RbF-PDT

The graded absorbers prepared in HZB of the set of CIGSe samples shown in Figure 4.1 were treated with RbF *in situ* post deposition treatment and then the RbF-treated CIGSe solar cells were characterized by JVT measurements. Measured CGI ratios for the set of samples studied in Section 4.1 and 4.2 are given in Table 4.1. The optimum deposition time of RbF on the absorbers was $t = 10$ min [97] and was maintained for

the whole series of CIGSe samples with a constant substrate temperature of $T_{\text{sub}} = 280$ °C and depositicion rate of approximately 0.2 Å/s. Likewise as in Section 4.1.1, the absorber deposition for these samples was done on different dates. Details about the evaporation process of the absorber and the post deposition of the RbF can be found in Appendix A.1. Doping profiles of reference CIGSe samples with and without RbF are shown in Appendix A.5, Figure A.12.

Table 4.1.: CGI ratios of a set of CIGSe solar cells with and without RbF by PDT.

Cells	CGI ([Cu]/([Ga]+[In]))
Reference 1 (no PDT) (RbF-PDT)	0.90
Reference 2 (no PDT) (RbF-PDT)	0.95
Reference 3 (no PDT) (RbF-PDT)	0.90
Reference 4 (no PDT) (RbF-PDT)	0.95
Reference 5 (no PDT) (RbF-PDT)	0.97
Reference 6 (no PDT) (RbF-PDT)	0.97
non-graded band gap (no PDT)	unknown
from Halle (no PDT) (RbF-PDT)	unknown
from EMPA (RbF-PDT)	unknown
from ZSW (RbF-PDT)	0.92

A higher performance has been accomplished due to the alkali treatment by increasing the V_{oc} and η, whereas the J_{sc} and FF show an inconsistent trend in this series of treated samples as seen in Table 4.2.

The JVT characteristics of the set of RbF-treated samples are shown in Figure 4.4. Reference 1 + PDT to Reference 6 + PDT cells correspond to Reference 1 to 6 cells ordered chronologically in Figure 4.1. CIGSe samples treated with RbF exhibit non-ideal $J-V$ characteristics over a wide temperature range, but especially at lower temperatures. These include a roll-over effect, a discrepancy between dark $J-V$ curves and $J_{\text{sc}}(V_{oc})$ points, and a slight cross-over between dark and illuminated JV curves. This cross-over effect was also present in most of the samples without RbF treatment (see linear plots in Figure 4.1) especially at low temperatures.

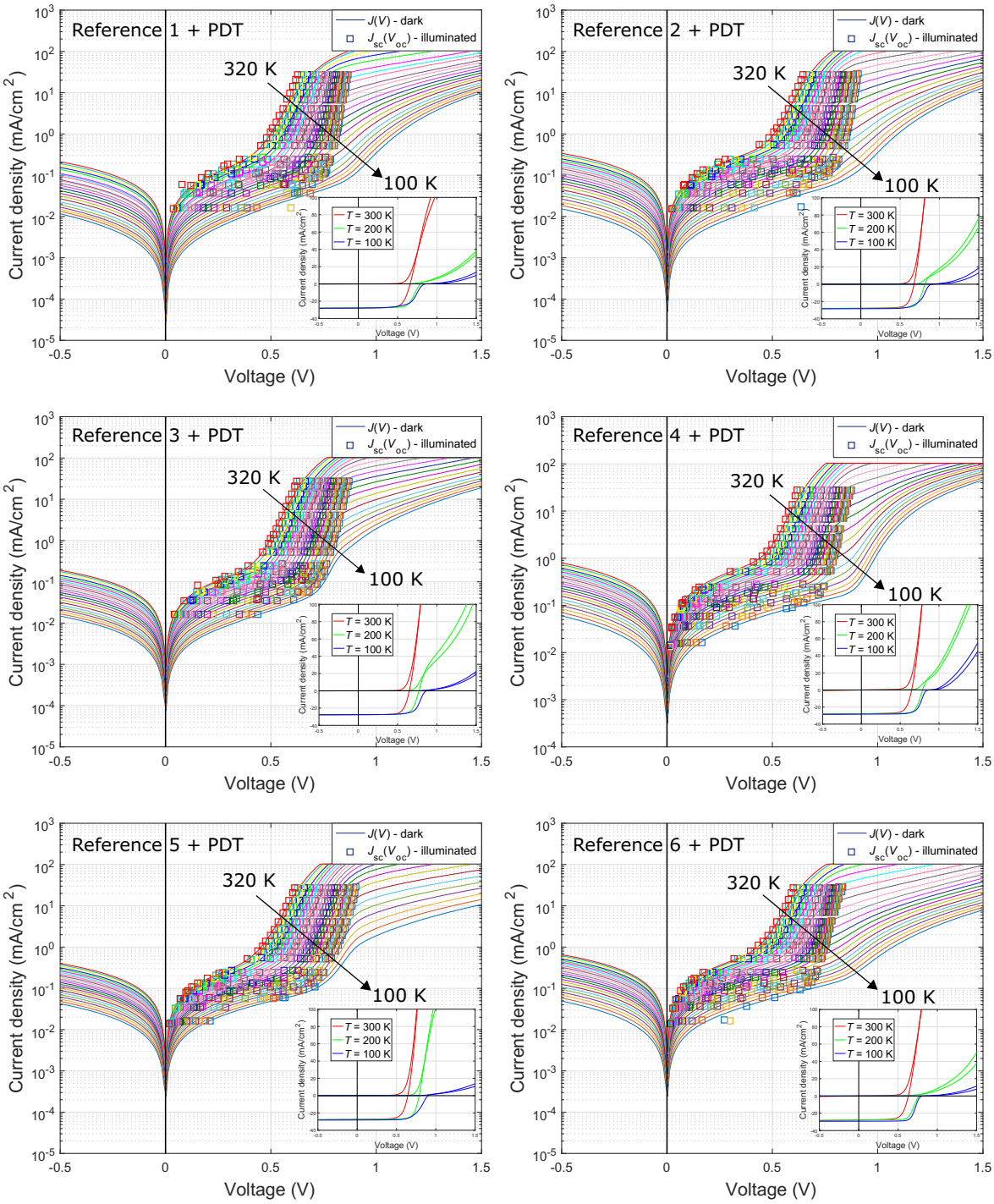

Figure 4.4.: JVT characteristics of a set of CIGSe solar cells with RbF-PDT.

Table 4.2.: STC parameters of a set of CIGSe solar cells with and without RbF by PDT.

Cells	J_{sc} (mA/cm^2)	V_{oc} (mV)	FF (%)	η (%)
Reference 1 (no PDT)	35.3	635	72.4	16.2
(RbF-PDT)	36.1	673	69.8	17.0
Reference 2 (no PDT)	34.3	656	72.8	16.4
(RbF-PDT)	34.1	683	74.2	17.3
Reference 3 (no PDT)	35.9	643	71.2	16.4
(RbF-PDT)	36.0	656	72.2	17.1
Reference 4 (no PDT)	35.2	638	71.6	16.1
(RbF-PDT)	35.3	656	72.6	16.8
Reference 5 (no PDT)	34.8	632	71.6	15.7
(RbF-PDT)	35.5	649	72.6	16.7
Reference 6 (no PDT)	35.8	629	71.1	16.0
(RbF-PDT)	36.4	645	71.5	16.8
non-graded band gap (no PDT)	31.1	599	70.0	13.0
from Halle (no PDT)	31.9	644	72.7	14.9
(RbF-PDT)	31.5	678	74.4	15.9
from EMPA (RbF-PDT)	36.8	720	72.0	19.1
from ZSW (RbF-PDT)	38.8	732	74.3	21.1

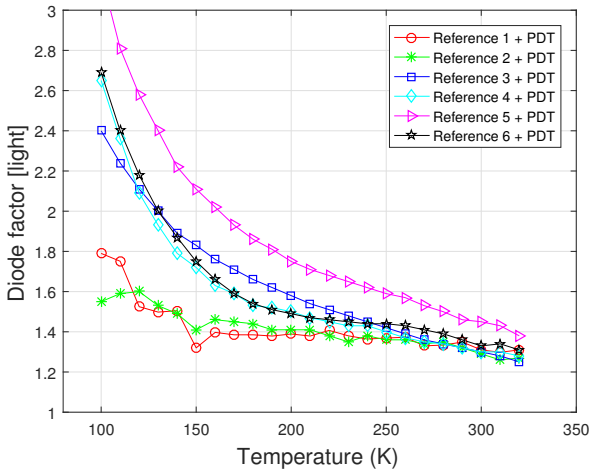

Figure 4.5.: Diode factors under illumination as a function of the temperature calculated from a set of CIGSe solar cells with RbF-PDT.

Diode factors obtained from the $J_{sc}(V_{oc})$ data are shown in Figure 4.5. A similar diode factor behavior with respect to untreated CIGSe solar cells with graded band gap is shown, but with a more significant temperature dependence in some cells with diode factors increasing as the temperature decreases and then obtaining for Reference 3 + PDT to Reference 6 + PDT diode factors in light conditions > 2 at lower temperatures. Because of the strong roll-over effect in most of the dark $J - V$ curves a fit using the two-diode model equation was not done.

A comparison of A_{light} between the six different set of CIGSe samples with and without RbF is shown in Figure 4.6. From this series of samples, there is no general agreement on the influence of alkali fluorides on the behavior of diode factors obtained from the $J_{sc}(V_{oc})$ data. Set 1, 2 and 4 show a decrease of A_{light} in samples treated with RbF over a wide or the entire temperature range. This tendency is only observed over a narrow range at high temperatures in Set 3. Conversely, Set 5 shows higher diode factors in the sample with RbF over the entire temperature range, while in Set 6 no change of A_{light} due to PDT was observed, except at low temperatures.

When CGI is closer to stoichiometry, i.e., samples from Set 5 and 6 with CGI = 0.97, larger or similar diode factors were calculated in RbF-treated samples compared to the untreated samples. Samples from Set 1 to 4 with lower Cu content, i.e., with CGI = 0.90-0.95, show a tendency to decrease diode factors when samples are treated with alkali fluorides (see Table 4.1 for CGI).

An important non-ideal diode behavior not observable in Figure 4.4 corresponds to the saturation of the V_{oc} in CIGSe solar cells with RbF-PDT. Figure 4.7 shows the behavior of the V_{oc} with respect to the temperature obtained from JVT measurements for each pair of reference cells (with/without RbF-PDT). All CIGSe cells present a V_{oc} saturation at lower temperatures with a more expressed effect in cells with RbF. Approximately above $T = 200$ K, V_{oc} decreases linearly with temperature.

Band gap energies were estimated from external quantum efficiency measurements (Figure 4.8) and are given in Table 4.3 together with the activation energies of the saturation current which were estimated from the V_{oc} extrapolation to $T = 0$ K. For most of the samples, there is a good agreement between the estimated E_g and E_A, where V_{oc} extrapolations are approximately equal to the band gap energies, i.e., $E_g \approx E_A$, regardless of whether the absorbers were treated with alkali fluorides or not. Exceptions are found in samples without PDT such as Reference 1, 3, and 6 where higher activation energies than band gap energies were estimated from EQE with $E_A \approx E_g$ + (60-70) meV.

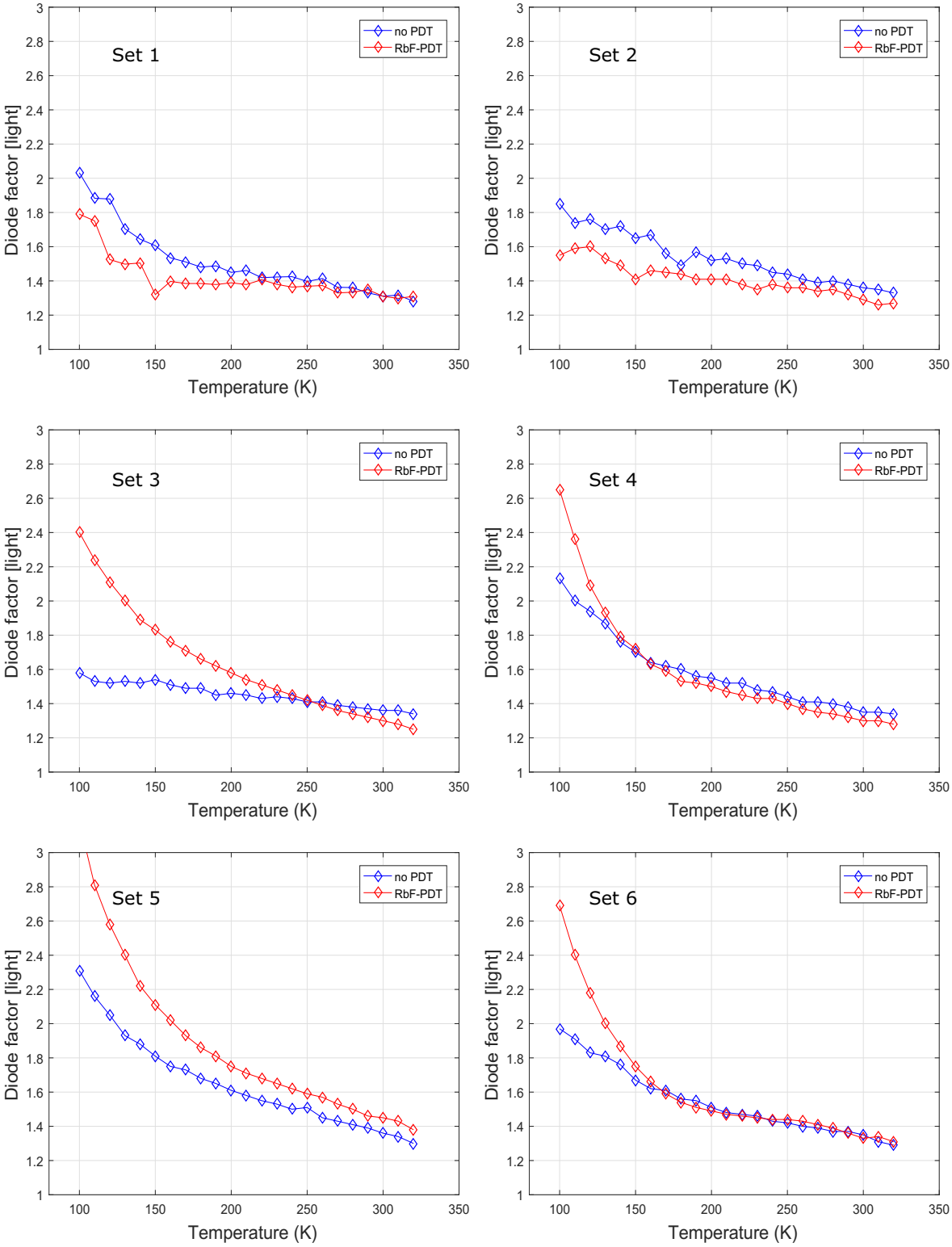

Figure 4.6.: Diode factors under illumination as a function of the temperature of a series of CIGSe samples with and without RbF-PDT.

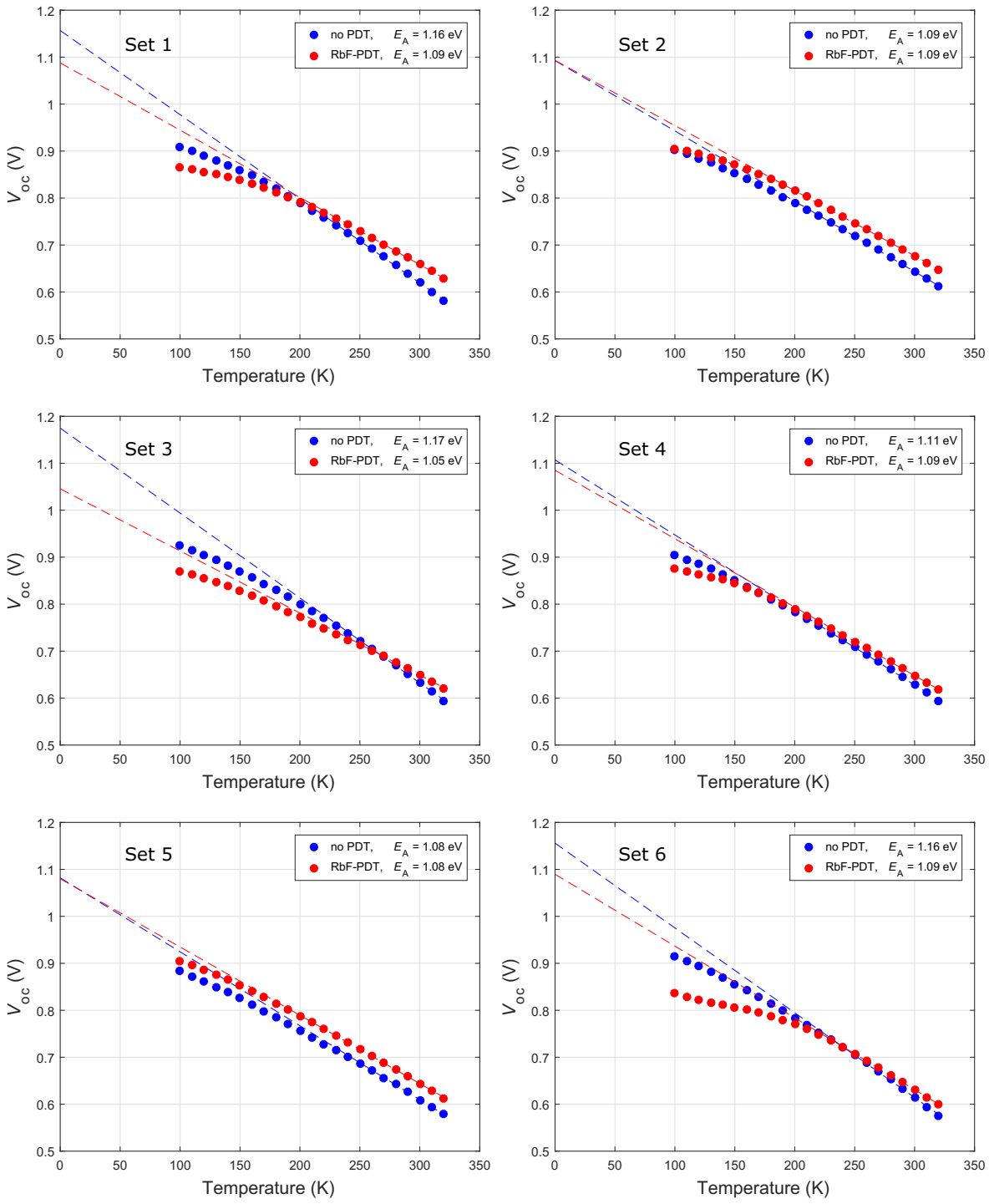

Figure 4.7.: V_{oc} as a function of the temperature of a series of CIGSe samples with and without RbF-PDT.

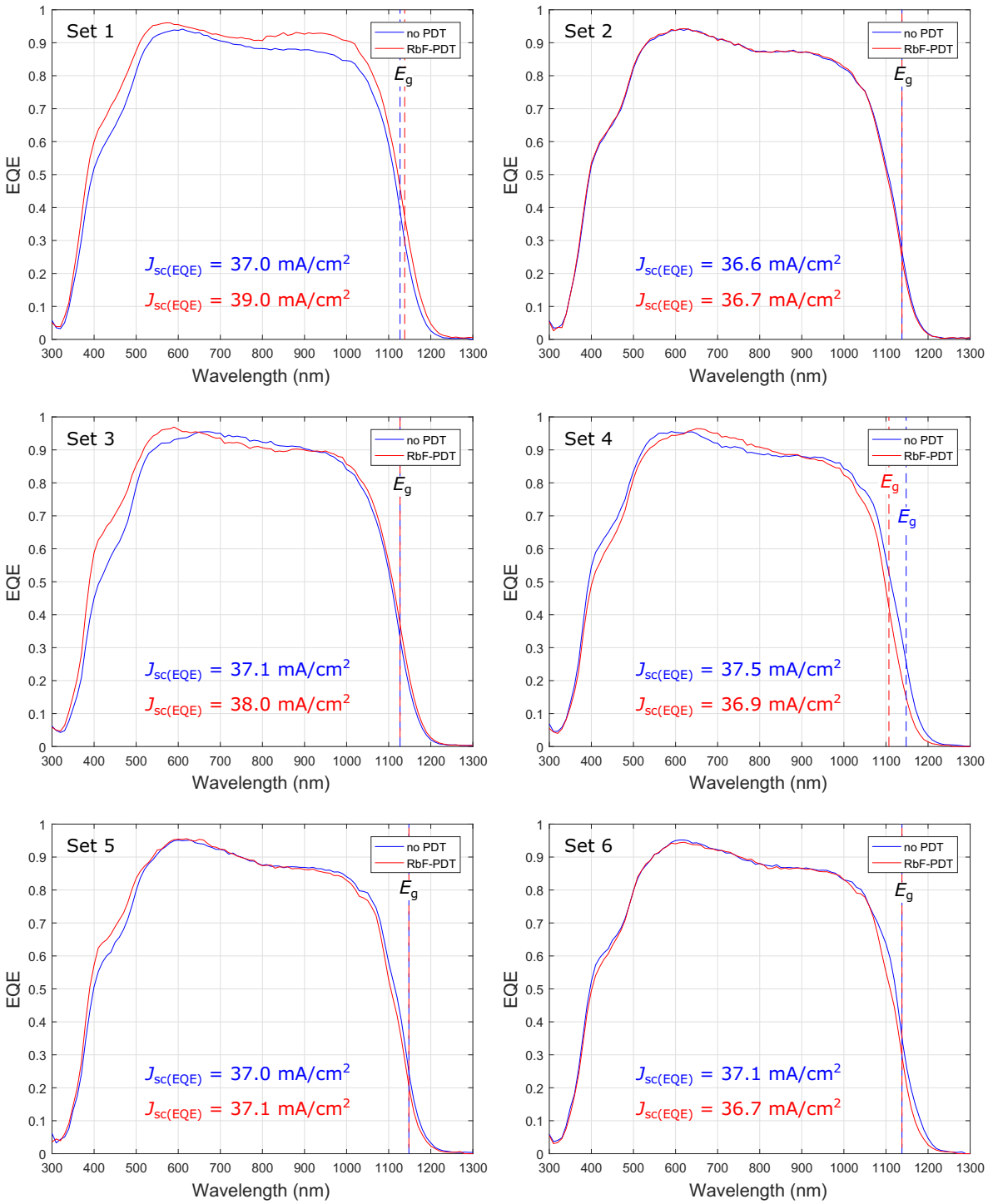

Figure 4.8.: External quantum efficiencies of a series of CIGSe samples with and without RbF-PDT.

Table 4.3.: Band gap energies from EQE measurements and activation energies from V_{oc} extrapolations to $T = 0$ K of the sets of CIGSe solar cells without/with RbF-PDT fabricated at HZB and external laboratories. The third column gives the activation energy obtained from the best linear dependence of the V_{oc} data at high temperatures. The fourth column gives the average activation energy with an estimated error range generated by varying the number of data points towards low temperature included in the linear regression.

Cells (no PDT)	$E_{g\ (EQE)}$ [eV]	$E_{A(V_{oc}(0\ K))}$ [eV]	$E_{A(V_{oc}(0\ K))}$ [eV]
Reference 1	1.10	1.16	1.165 ± 0.035
Reference 2	1.09	1.09	1.095 ± 0.025
Reference 3	1.10	1.17	1.170 ± 0.030
Reference 4	1.08	1.11	1.115 ± 0.025
Reference 5	1.08	1.08	1.065 ± 0.025
Reference 6	1.09	1.16	1.160 ± 0.040
non-graded band gap	1.19	1.19	1.190 ± 0.030
from Halle	1.14	1.14	1.140 ± 0.020
Cells (RbF-PDT)	$E_{g\ (EQE)}$ [eV]	$E_{A(V_{oc}(0\ K))}$ [eV]	$E_{A(V_{oc}(0\ K))}$ [eV]
Reference 1	1.09	1.09	1.090 ± 0.030
Reference 2	1.09	1.09	1.110 ± 0.020
Reference 3	1.10	1.05	1.045 ± 0.035
Reference 4	1.12	1.09	1.085 ± 0.015
Reference 5	1.08	1.08	1.080 ± 0.020
Reference 6	1.09	1.09	1.080 ± 0.020
from Halle	1.14	1.14	1.130 ± 0.020
from EMPA	1.16	1.14	1.190 ± 0.030
from ZSW	1.13	1.12	1.120 ± 0.020

The linear extrapolation of the V_{oc} is connected to an estimated error range generated by the number of data points taken from high temperatures towards low temperatures to be included in the linear regression. The fourth column in Table 4.3 includes the average activation energy with the estimated error range for each sample. Consequently, the accuracy of the determination of the activation energy from the $V_{oc}(T)$ extrapolation and/or the accuracy of the measurements carried out by the JVT/EQE setups may lead to a miscalculation and difference between E_g and E_A in some samples. Besides, the determination of E_g from EQE is also an approximation especially when the band gap is graded (see Section 3.1) and the determination of the dominant recombination mechanism is defined by the E_g where the Fermi level is at the mid-gap position rather than the $E_{g,min}$ of the graded absorber and/or a variation of the fundamental recombination theory as discussed in Section 2.2, may have a role on the proper estimation of the aforementioned parameters. Discussions will be further addressed in Chapter 6.

The main findings can be summarized as follows:

- CIGSe solar cells with RbF-PDT show a strong roll-over and a dark/light discrepancy over a wide temperature range, especially at lower temperatures.
- Slight cross-over, especially at lower temperatures.
- A_{light} is temperature-dependent with values < 2 and a higher dependence is exhibited at lower temperatures ($T < 150$ K) with values > 2 in some of the samples.
- V_{oc} saturation at low temperatures.

Non-idealities are observed in CIGSe solar cells with RbF-PDT in comparison to CIGSe cells without RbF-PDT with graded absorbers. Typically, A_{light} decreases with RbF, especially at high temperatures when CGI = 0.90-0.95. Typically, more expressed V_{oc} saturation at low temperaturatures in samples with RbF. Mostly, $E_g \approx E_A$ in solar cells with/without PDT with some exceptions in cells without PDT where $E_A > E_g$.

4.2.1. Evaluation of CIGSe solar cells with RbF-PDT from external laboratories

In order to evaluate the behavior of the RbF-PDT in different CIGSe solar cells produced in external laboratories, CIGSe devices from the Martin Luther University of Halle-Wittenberg (Figure 4.9), from the Swiss Federal Laboratories for Materials Science and Technology (EMPA), and from the Center for Solar Energy and Hydrogen Research Baden-Württemberg (ZSW) (Figure 4.10) were measured by JVT.
The same stack sequence in HZB samples described in Section 4.1.1 was used for Halle and EMPA samples in which a bilayer of i-ZnO/ZnO:Al was deposited as the window layer. However, in the sample given by ZSW, the window layer was deposited with a bilayer of (Zn,Mg)O/ZnO:Al. STC parameters can be found in Table 4.2.

CIGSe samples with RbF-PDT provided by the University of Halle show non-idealities similar to those seen in samples produced in HZB: a strong blocking of the forward diode current over a wide temperature range of the RbF-treated sample with a strong deviation of the $J_{\text{sc}}(V_{oc})$ points with respect to the dark $J-V$ curves along with a slight cross-over between dark and light JV characteristics (see Figure 4.9b), and a more expressed V_{oc} saturation of the RbF-treated sample at lower temperatures (see Figure 4.9c). The estimated diode factors under illumination from the sample treated with RbF show a clear decrease with respect to the sample without PDT, in accordance to HZB samples with CGI ratio between CGI = 0.90-0.95 (Set 1, 2 and 4 in Figure 4.6).

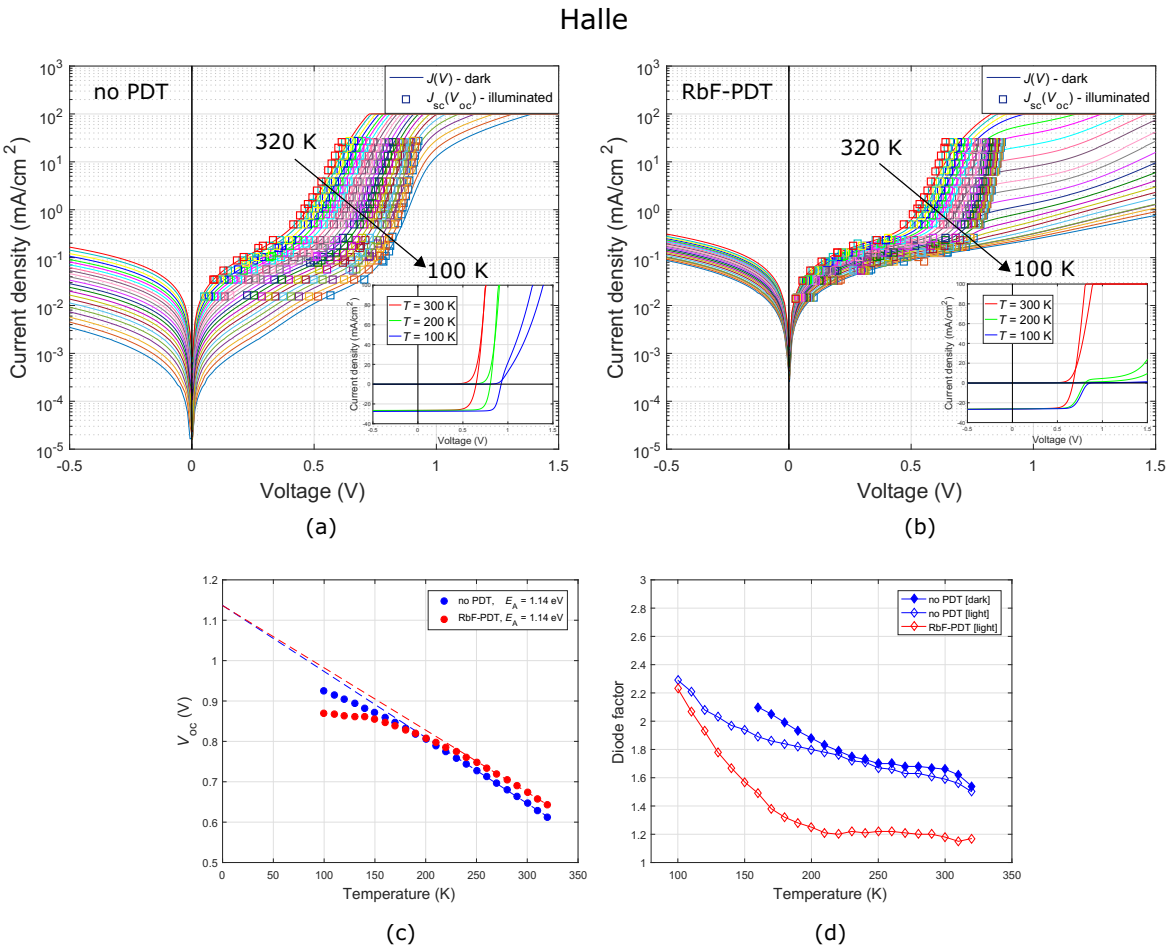

Figure 4.9.: JVT characteristics of (a) a reference CIGSe solar cell and (b) a CIGSe solar cell with RbF-PDT, (c) $V_{oc}(T)$ plot and (d) $A(T)$ plot of a cell with and without RbF. Samples provided by the Martin Luther University of Halle-Wittenberg.

A remarkable JVT behavior is observed in the RbF-treated sample provided by EMPA (see Figure 4.10a) with an efficiency of $\eta = 19.4\%$ which despite being treated with alkali fluorides presents no roll-over effect over the entire temperature range even not at lower temperatures, with no discrepancy between dark $J-V$ curves and $J_{\mathrm{sc}}(V_{oc})$ points. In this case, both diode factors in dark and light conditions were calculated (Figure 4.10b) since the absence of a roll-over effect allowed a good fit of the dark $J-V$ curves and the two-diode model equation and, then a correct determination and evaluation of the parameters extracted from the equation, obtaining equal diode factors in both conditions for temperatures above $T = 200$ K. Below this temperature, there is a small discrepancy with lower diode factors under illumination.
A CIGSe sample treated with RbF provided by ZSW with a higher efficiency of $\eta = 21.5\%$ with anti-reflective coating (ARC) presents a roll-over effect especially at low temperatures as can also be seen in our samples, along with a discrepancy between dark and $J_{\mathrm{sc}}(V_{oc})$ curves. Likewise, a V_{oc} saturation at low temperatures is observed

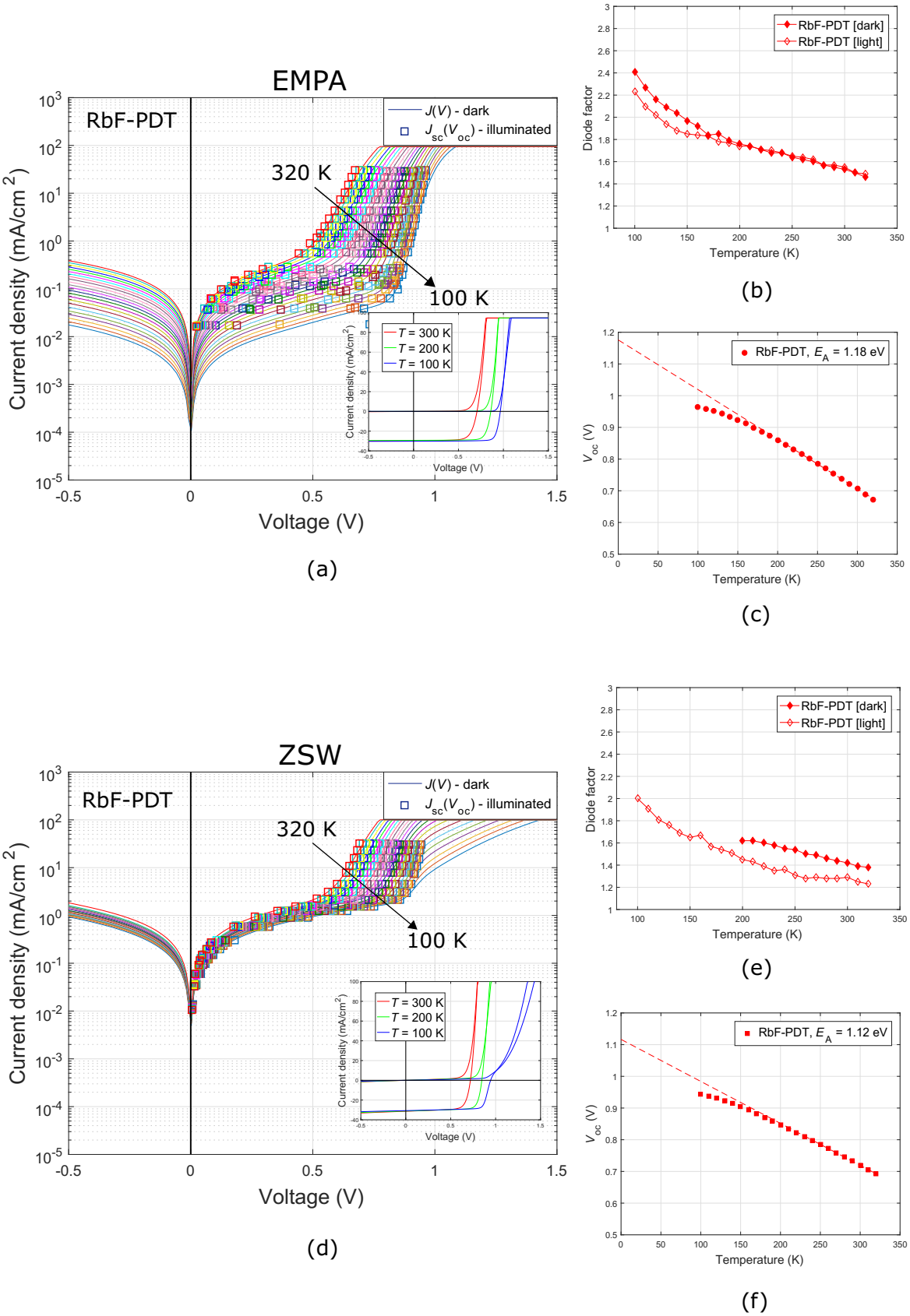

Figure 4.10.: (a) and (d) JVT characteristics of CIGSe solar cells with RbF-PDT, (b) and (e) $A(T)$ plots and, (c) and (f) $V_{oc}(T)$ plots of samples provided by EMPA and ZSW, respectively.

for the non-blocked (EMPA) and blocked (ZSW) solar cell.
In Table 4.3, the estimated E_g and E_A of Halle, EMPA and ZSW samples are also given, again with band gap energies approximately equal to the activation energies, i.e, $E_g \approx E_A$. *EQE* curves of external samples of this section can be found in the Appendix A.4, Figure A.5.

The main findings can be summarized as follows:

- Halle solar cells show a similar behavior as HZB solar cells either with or without RbF-PDT, including diode factors.
- EMPA solar cell with RbF-PDT does not show the non-idealities observed in HZB/Halle samples but only a small V_{oc} saturation at low temperatures. A_{dark} and A_{light} are slightly temperature-dependent with values mainly < 2 and $A_{dark} = A_{light}$ at $T \geq 200$ K.
- ZSW solar cell shows similar non-idealities than the HZB samples but with a less expressed roll-over at low temperatures. Also a similar behavior for the diode factors.
- For all the external CIGSe solar cells, $E_g \approx E_A$.

Note that regardless of the high efficiency achieved by the ZSW solar cell, non-ideal effects may occur in high efficiency devices. On the other hand, there are some treated CIGSe samples which do not show these effects. Preliminary, we conclude here that the positive and negative effects of alkali fluorides are not necessary linked to the same physical mechanism (see Section 2.3). Further discussions will be presented later on.

The previous two sections (Section 4.1 and 4.2) described the general observations seen in CIGSe samples with and without an alkali fluoride treatment such as RbF deposited on the absorber. The corresponding electrical characterizations and analysis were performed in CIGSe devices where the process parameters were optimized to produce highly efficient solar cells. In the following sections, variations of the process parameters will provide more insights about the JVT behavior and the current transport mechanism that deteriorates the diode current and induces non-idealities with respect to a standard diode especially at low temperatures of CIGSe solar cells with absorbers treated with RbF.

4.3. Deposition time of RbF on CIGSe absorbers

CIGSe samples were prepared with different amounts of RbF which is controllable by varying the deposition time of the PDT in order to analyze the effects of the alkali fluoride concentration deposited on CIGSe absorbers on the JVT characteristics. In this section, samples have a CGI ratio of CGI = 0.90 and two variations of the process

time of the RbF-PDT were measured by JVT: 4 min and 10 min of RbF-PDT. See Appendix A.1 and Reference [97] for sample details.

Figures 4.11a-c show the JVT results of a reference cell without any PDT (Reference 1, from the set in Section 4.1), a cell with 4 min-treated absorber and a cell with 10 min-treated absorber with RbF (Reference 1 + PDT, from the set in Section 4.4), respectively. It can be clearly seen how a higher amount of RbF deteriorates the $J-V$ curves especially at lower temperatures. The linear plots of PDT cells show a strong roll-over of the $J-V$ curves at low temperatures. This effect is more expressed when the sample is treated with a duration of 10 min of RbF. A discrepancy between dark JV curves and $J_{\mathrm{sc}}(V_{oc})$ points already exists in the cell with low RbF amount.

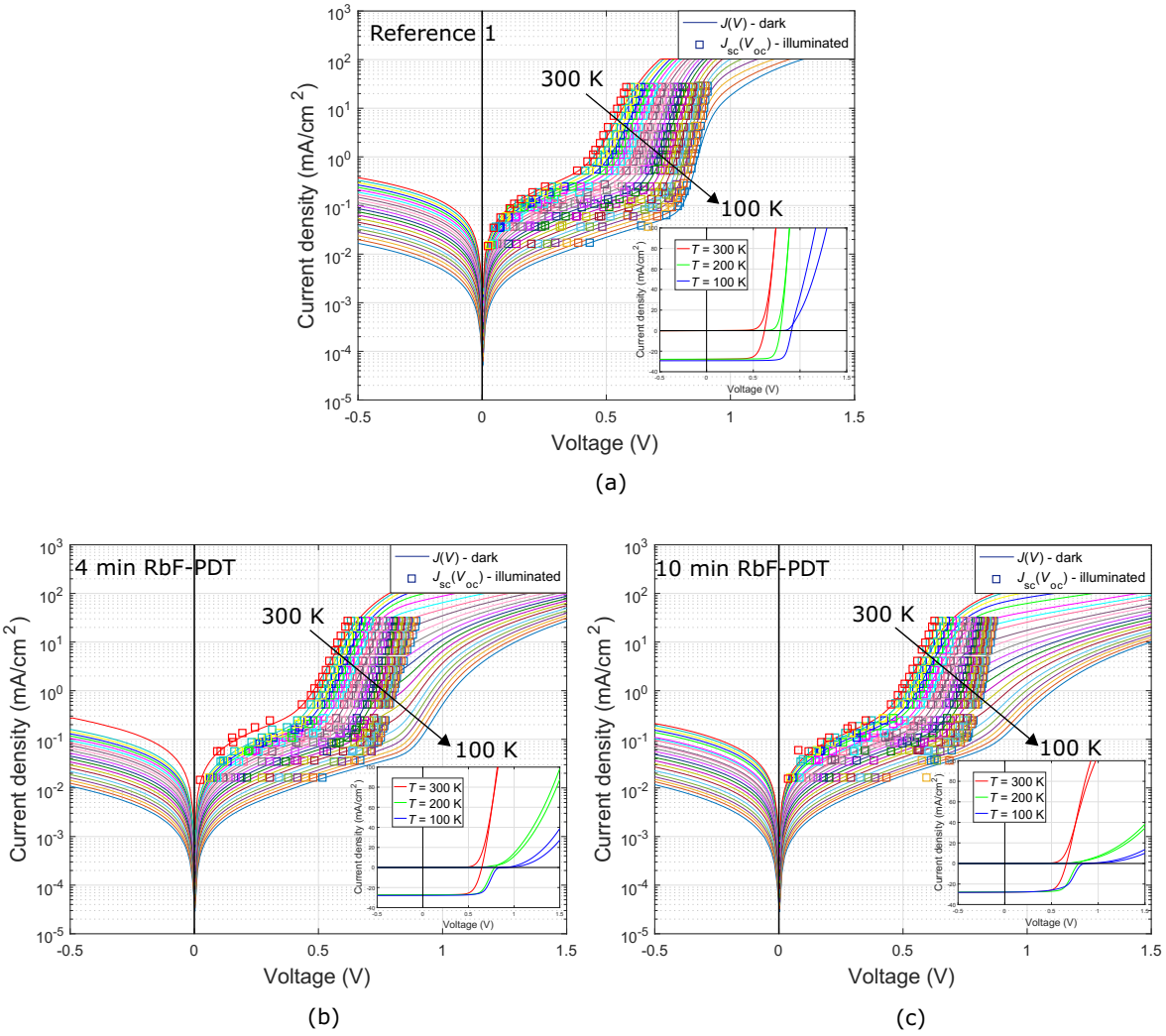

Figure 4.11.: Effects of the deposition time of RbF on the JVT characteristics: (a) reference CIGSe solar cell, (b) 4 min deposition of RbF-PDT and (c) 10 min deposition of RbF-PDT.

The diode factors under illumination are plotted in Figure 4.12a. The diode factors of the cell with 4 min RbF-PDT are higher than those of the reference cell whereas with 10 min RbF-PDT the diode factors are lower than the reference values.

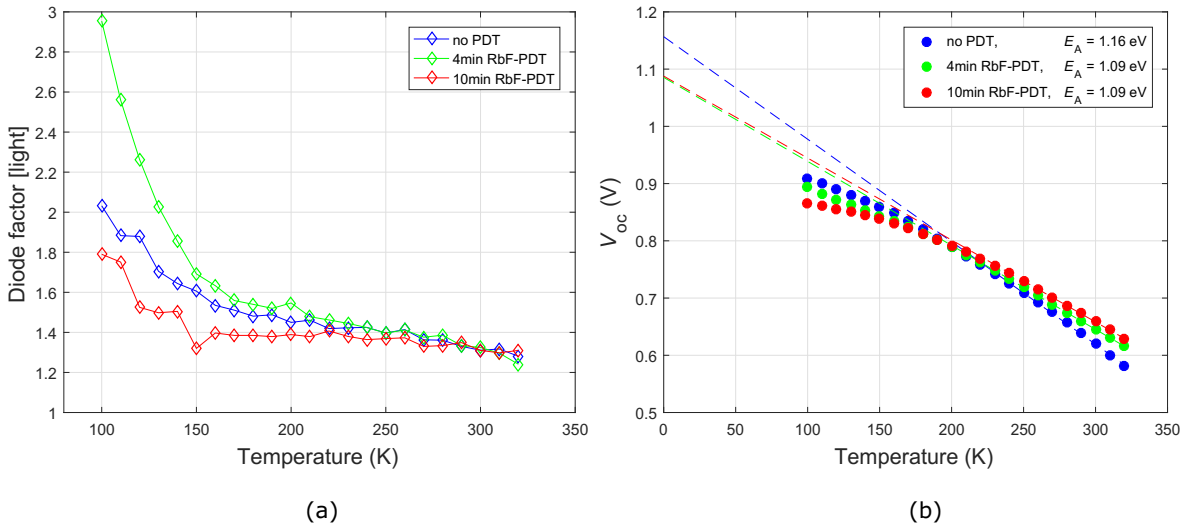

Figure 4.12.: (a) $A(T)$ under light and (b) $V_{oc}(T)$ plot of CIGSe samples with different amounts of RbF (deposition time).

The presence of a roll-over effect, enhanced with higher amount of RbF deposited is accompanied by a stronger saturation of the V_{oc} at low temperatures as seen in Figure 4.12b. Above $T = 200$ K, V_{oc} decreases linearly with temperature in all three cells. The gain in V_{oc} at room temperature is visible in the figure and directly linked to the increase of the deposition time of the RbF into the absorber. A clear trend of decreasing FF as process time of PDT increases can be seen in Table 4.4. The extrapolation of the V_{oc} to $T = 0$ K results in $E_{\mathrm{A}} = 1.09$ for both CIGSe solar cells with RbF-treated absorbers, which is in good agreement with the estimated band gap, $E_{\mathrm{g}} = 1.09$ (see EQE curves in Appendix A.4, Figure A.6).

Table 4.4.: STC parameters of a set of CIGSe solar cells with different amounts of RbF.

Cells	J_{sc} (mA/cm^2)	V_{oc} (mV)	FF (%)	η (%)
Reference 1 (no PDT)	35.3	635	72.4	16.2
4 min RbF-PDT	34.9	654	70.7	16.1
10 min RbF-PDT	36.1	673	69.8	17.0

The depth profiles of Na and Rb for this set of samples is given in Appendix A.2, Figure A.1. Measurements revealed a lower Na content within the absorber with larger deposition times of Rb and an almost flat Na distribution near the back contact. The severity of the non-ideal effects is directly connected to the amount of RbF deposited

onto the absorber. The non-ideal effects emerge already with low amounts of RbF. The sample with higher amount of RbF (10 min RbF-PDT) presents a higher Na content reduction especially at the back contact region than the sample treated with 4 min RbF-PDT. This correlates with stronger non-ideal effects such as a stronger roll-over in dark $J-V$ curves and V_{oc} saturation at lower temperatures. It should be noted that a certain saturation of the V_{oc} is already present in the sample without an alkali fluoride treatment (Figure 4.12b). Doping profiles showed that small amounts of Rb (4 min RbF-PDT) lead to a reduction of the carrier concentration N_{CV} compared to the cell without PDT, and N_{CV} is increased above the reference cell with higher RbF amount (10 min RbF-PDT). The increase of diode factors in the 4 min RbF cell may be a consequence of the lower carrier concentration within the absorber. Once the cell is treated with larger deposition times of PDT (10 min-PDT), the carrier concentration is recovered with higher values than measured in the reference cell and at the same time the diode factors are reduced with lower values than the ones calculated from the reference device.

The main findings can be summarized as follows:

- A higher amount of RbF enhances the roll-over of the $J-V$ curves.
- Compared to A_{light} of the reference cell: low amount of RbF increases A_{light} especially at low temperatures. A high amount of RbF decreases A_{light}.
- V_{oc} saturation at low temperatures is also enhanced with longer deposition times of RbF-PDT.
- V_{oc} tends to increase while FF decreases with increasing amount of RbF.

The severity of the non-idealities may be linked to the Na content within the absorber, since a higher Na content reduction correlates with the roll-over enhancement and stronger V_{oc} saturation. At this point, the A_{light} behavior correlates with the carrier concentration N_{CV}.

4.4. Influence of Na content in CIGSe absorbers

CIGSe samples were prepared under Na-free conditions where a SiO_xN_y diffusion barrier was deposited on a glass substrate and sputtered with Mo. The layer stack then follows the sequence of glass/SiO_xN_y/Mo/CIGSe-PVD/CdS/i-ZnO/ZnO:Al. For the sample treated with RbF-PDT, the optimum deposition time of 10 min PDT was set. A Na-barrier was also deposited on a CIGSe sample with constant band gap without PDT, preparation process previously described in Section 4.1.2, and its corresponding JVT and $A(T)$ plots can be found in Appendix A.3, Figure A.3.

Table 4.5.: STC parameters of a set of CIGSe solar cells including a Na-barrier at the back contact.

Cells	J_{sc} (mA/cm^2)	V_{oc} (mV)	FF (%)	η (%)
Na-barrier 1 (no PDT)	33.5	505	50.8	8.57
(RbF-PDT)	33.4	579	65.6	12.7
Na-barrier 2 (no PDT)	33.2	493	54.9	8.99
(RbF-PDT)	33.7	572	66.7	12.9
Na-barrier 3 (no PDT)	34.0	504	58.2	9.97
Na-barrier + non-graded band gap (no PDT)	31.0	513	54.1	8.6

Figure 4.13 shows the JVT characteristics of CIGSe solar cells with a Na-barrier at the back contact. The CIGSe cell without PDT in Figure 4.13a exhibits a strong roll-over effect even at high temperatures as can be seen in the linear plot at $T = 300$ K. For lower temperatures, the effect is very severe. This cell also exhibits the strongest cross-over effect between dark and light $J - V$ curves seen so far in CIGSe samples at any temperature.
In the CIGSe cell with Na-barrier and RbF-PDT of Figure 4.13b the roll-over effect is considerably reduced at high temperatures but still very expressed at low temperatures. Regarding the STC parameters in Table 4.5, there is a significant V_{oc} and FF gain for the Na-barrier cell with RbF.
A deviation of the $J_{sc}(V_{oc})$ data with respect to the dark $J - V$ curves is present in both solar cells with a Na-barrier.

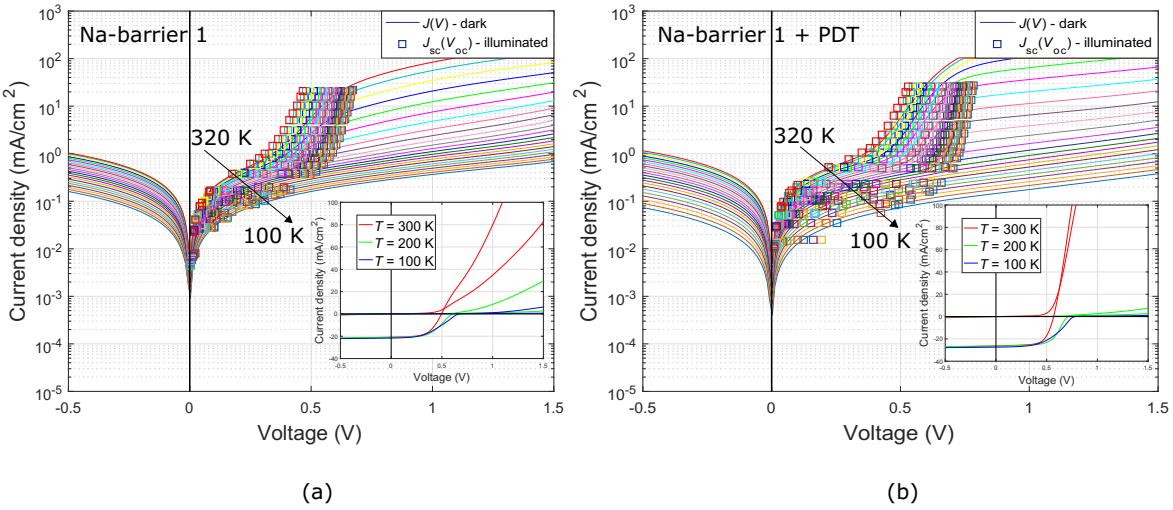

Figure 4.13.: JVT characteristics of a CIGSe solar cell including a Na-barrier (a) without PDT and (b) with RbF-PDT.

Additional CIGSe solar cells with Na-barrier, some of them prepared on different deposition dates, were measured and are included in this section for the evaluation of the estimated activation energies, band gap energies and diode factors and can be found in Figure 4.14 and in Table 4.6 (JVT characteristics of these additional cells are not shown in this work).

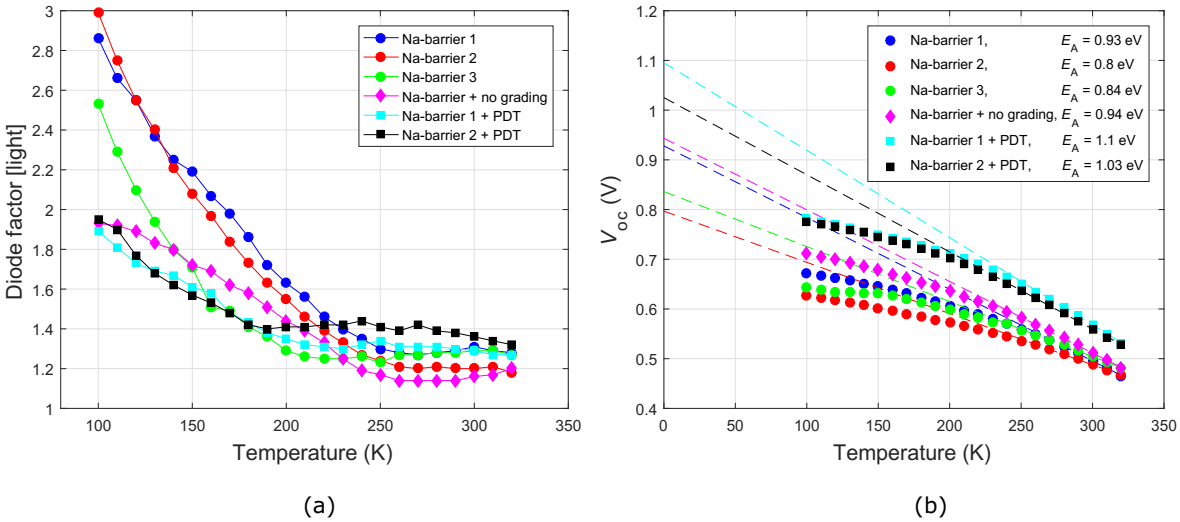

Figure 4.14.: (a) $A(T)$ plot under illumination, and (b) $V_{oc}(T)$ plot of a series of CIGSe solar cells with Na-barrier at the back contact with and without RbF-PDT.

Table 4.6.: Band gap energies from EQE measurements and activation energies from V_{oc} extrapolations to $T = 0$ K of a set of CIGSe solar cells with Na diffusion barrier. The third column gives the activation energy obtained from the best linear dependence of the V_{oc} data at high temperatures. The fourth column gives the average activation energy with an estimated error range in function of the number of V_{oc} data taken to extrapolate from high to low temperatures.

Cells (no PDT)	$E_{g\ (EQE)}$ [eV]	$E_{A(V_{oc}(0\ K))}$ [eV]	$E_{A(V_{oc}(0\ K))}$ [eV]
Na-barrier 1	1.13	0.93	0.93 ± 0.030
Na-barrier 2	1.13	0.80	0.80 ± 0.020
Na-barrier 3	1.13	0.83	0.845 ± 0.035
Na-barrier + non-graded band gap	1.19	0.96	0.965 ± 0.035
Cells (RbF-PDT)	$E_{g\ (EQE)}$ [eV]	$E_{A(V_{oc}(0\ K))}$ [eV]	$E_{A(V_{oc}(0\ K))}$ [eV]
Na-barrier 1	1.13	1.10	1.095 ± 0.035
Na-barrier 2	1.13	1.03	1.015 ± 0.015

As can be clearly seen in Table 4.6, the activation energies of the set of CIGSe cells with Na-barrier at the back contact are smaller than the band gap energies estimated from the EQE ($E_A \leq E_g$ - 200 meV). Once the cells "Na-barrier 1" and "Na-barrier 2" are treated with RbF, the activation energies increase towards the band gap energies. For

the cell "Na-barrier 2" there remains a small discrepancy between E_A and E_g ($E_A \approx E_g$ - 100 meV). *EQE* curves of this series of CIGSe cells are included in the Appendix A.4, Figure A.7.

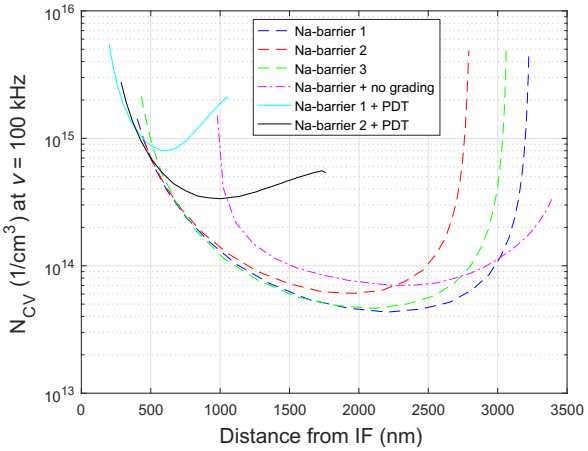

Figure 4.15.: N_{CV} profiles of a series of CIGSe solar cells with a Na-barrier at the back contact with or without RbF-PDT.

Doping profiles derived from $C-V$ measurements of the corresponding Na-barrier devices are shown in Figure 4.15. Here, the four CIGSe cells without any PDT exhibit almost one order of carrier concentration N_{CV} lower than the cells with RbF-PDT. At this point, a very low carrier concentration in the absorber correlates to smaller activation energies than band gap energies. When the CIGSe is treated with RbF, the carrier concentration in the absorber increases and the estimation of the activation energy becomes approximately equal to the band gap energy. It can also be observed that the "Na-barrier 2 + PDT" cell exhibits a lower N_{CV} than the "Na-barrier 1 + PDT" cell by almost a half order of magnitude and this behavior correlates with the small discrepancy between E_g and E_A in the "Na-barrier + PDT" cell. From this set of devices, with a higher carrier concentration, i.e., with $N_{CV} \geq 10^{15}$ cm^{-3}, the estimation of the activation energy approximately equals the band gap energy, as evidenced by the "Na-barrier 1 + PDT" cell.

The aforementioned behavior can be seen also in the CIGSe samples with and without RbF-PDT studied earlier in Sections 4.1 and 4.2. The corresponding doping profiles found in Appendix A.5, Figure A.12 show a carrier concentration N_{CV} larger than 10^{15} cm^{-3}, and for most of these cells in Table 4.3 the relation $E_g \approx E_A$ was obtained.

The derived diode factors under illumination are plotted in Figure 4.14a. CIGSe devices "Na-barrier 1" and "Na-barrier 2" present an almost constant behavior at high temperatures where $A_{light} \approx 1.2$-1.3. For $T < 250$ K, the diode factors are temperature-dependent and tend to increase to values above 2 as the temperatures decreases. A similar behavior is observed in the cell "Na-barrier 3" with constant diode factors A_{light}

≈ 1.3 above $T = 200$ K and becoming temperature-dependent at lower temperatures. Once the CIGSe is treated with RbF, cells "Na-barrier 1 + PDT" and "Na-barrier 2 + PDT" show almost constant diode factors $A_{\text{light}} \approx 1.3$-1.4 for $T > 200$ K, and once again increasing values at lower temperatures, in this case below 2. Therefore, PDT tends to decrease the diode factors at lower temperatures with $A_{\text{light}} < 2$.
However, an exception is observed in the cell "Na-barrier + no grading" without PDT where the diode factors stay below 2 at low temperatures contrary to the series of samples with Na-barrier and no PDT.

The main findings can be summarized as follows:

- CIGSe solar cells with Na-barrier at the back contact show all non-idealities with significant roll-over and cross-over over the full temperature range.
- RbF-PDT reduces the roll-over only at high temperatures and the cross-over effect.
- A stronger V_{oc} saturation is observed in the set of samples.
- Gain in V_{oc} and FF in samples with RbF-PDT.
- In samples without PDT: $E_{\text{A}} < E_{\text{g}}$. After RbF deposition, E_{A} increases trying to approximate to E_{g}.
- Typically, A_{light} is constant at high temperatures. At lower temperatures, A_{light} is highly temperature-dependent especially in samples without PDT with values > 2. RbF decreases A_{light} at low temperatures to values < 2.

Stronger non-idealities are shown in CIGSe solar cells with low Na concentration within the absorber in comparison to reference cells without/with PDT. A relation between the carrier concentration due to the Na content and the E_A can be observed: low Na content correlates with low E_A.

4.5. Influence of Cu concentration in CIGSe absorbers

Variations of the Cu content in CIGSe absorbers were done by varying the duration of the third stage of the multi-source evaporation process. As mentioned in [97], the absorber layers not only differ in CGI ratio and thickness but also the band gap grading as well as the position of the minimum band gap are affected. CIGSe samples with CGI = 0.30, 0.70, 0.80 and 0.99 were measured by JVT and are described in this section.

Table 4.7 gives the STC parameters of the corresponding set of CIGSe solar cells. For CGI < 0.80, RbF-PDT does not have a positive effect on V_{oc} but decreases the V_{oc}.

Table 4.7.: STC parameters of a set of CIGSe solar cells with different CGI ratio.

Cells	J_{sc} (mA/cm^2)	V_{oc} (mV)	FF (%)	η (%)
CGI = 0.30 (no PDT)	23.6	656	71.5	11.1
(RbF-PDT)	25.4	509	48.9	6.3
CGI = 0.70 (no PDT)	32.6	657	73.3	15.7
(RbF-PDT)	33.6	609	69.7	14.3
CGI = 0.80 (no PDT)	34.6	640	71.8	15.9
(RbF-PDT)	33.9	676	63.6	14.6
CGI = 0.99 (no PDT)	34.7	639	68.6	15.2
(RbF-PDT)	34.7	682	69.3	16.4

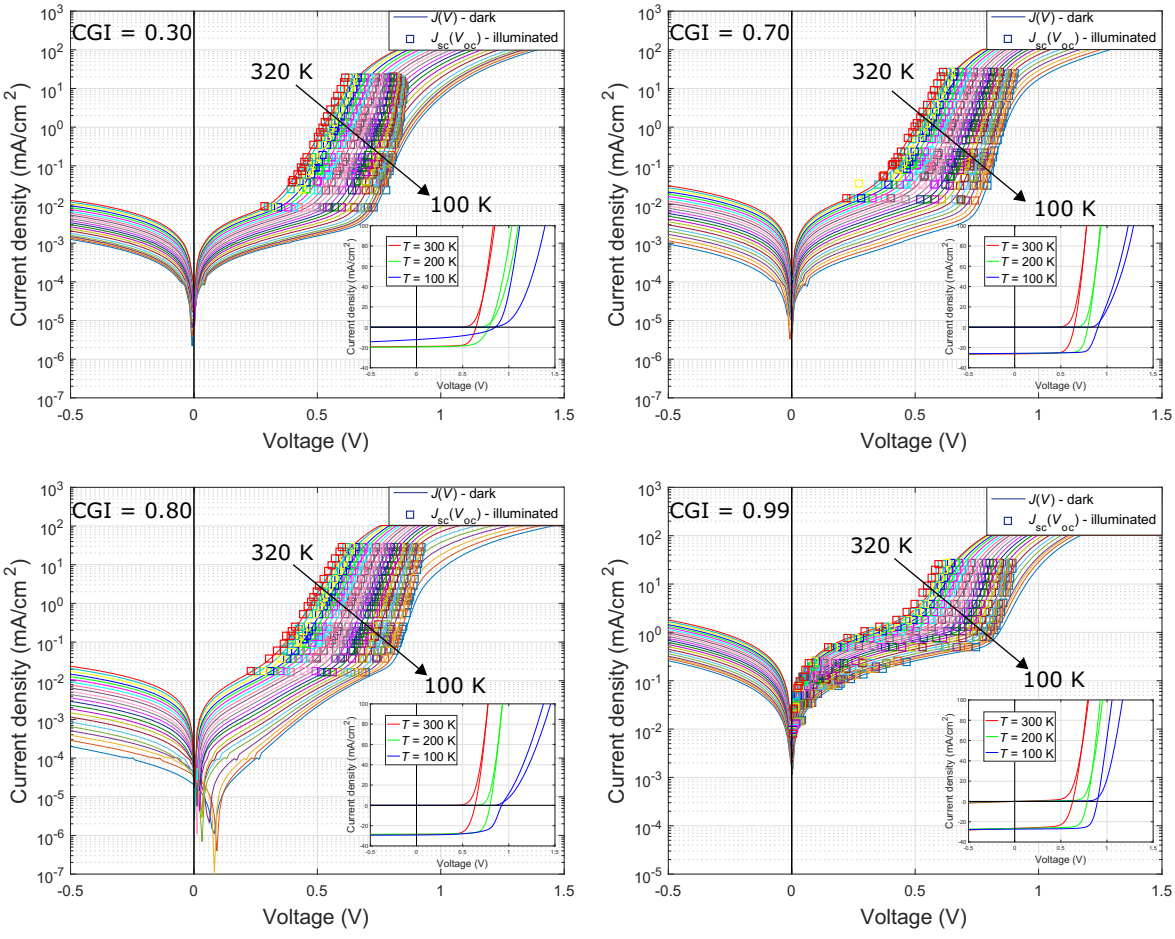

Figure 4.16.: JVT characteristics of a set of CIGSe solar cells without RbF and different CGI ratio: 0.30, 0.70, 0.80 and 0.99.

The low efficiency of the solar cell with CGI = 0.30 is not only affected by the large decrease of the V_{oc} after the deposition of RbF but also by the large loss in FF. The low J_{sc} achieved by the cell is independent of the RbF-PDT, it is rather a consequence of the large band gap shift as seen in Appendix A.4, Figure A.8.
For CGI > 0.80, there is a V_{oc} gain and only for samples grown at CGI > 0.90 (also see results of samples measured in Table 4.2) PDT leads to an improved FF.

The JVT curves of the set of CIGSe cells without RbF-PDT can be seen in Figure 4.16. Here, the roll-over effect of the dark $J-V$ curves is only slightly present in some of the devices at low temperatures. A small discrepancy between the $J_{sc}(V_{oc})$ data and dark $J-V$ curves can hardly be seen in the cells more affected by the roll-over at low temperatures. A special case is observed in the cell with CGI = 0.30 where the $J_{sc}(V_{oc})$ data show more deviation to the left due to the $J_{sc}(V_{oc})$ saturation at higher light intensities and lower temperatures. The $J_{sc}(V_{oc})$ points are not positioned on the non-blocked dark $J-V$ curves.

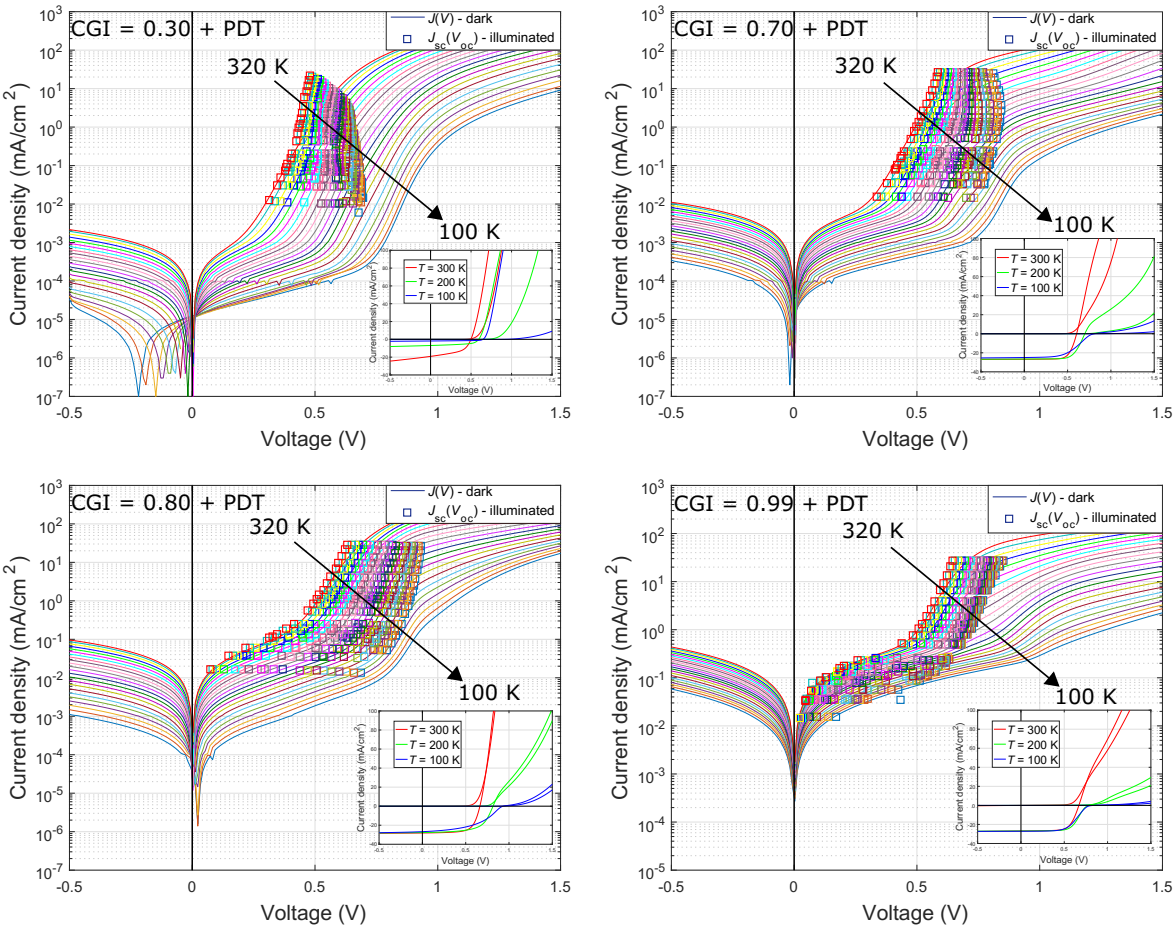

Figure 4.17.: JVT characteristics of a set of CIGSe solar cells with RbF-PDT and different CGI ratio: 0.30, 0.70, 0.80 and 0.99.

The linear plots of the cells in Figure 4.16 exhibit a slight cross-over effect between dark and light $J-V$ curves at lower temperatures when CGI $\geq$ 0.70, for CGI = 0.30 this effect is more significant.

In Figure 4.17, it can be observed that the post deposition of RbF on CIGSe leads again to JVT characteristics with much stronger non-ideal effects: a strong roll-over of the dark $J-V$ curves over the entire temperature range, a strong deviation of the $J_{\mathrm{sc}}(V_{oc})$ data with respect to the dark $J-V$ curves and a cross-over between dark and light $J-V$ curves which is more expressed for CGI $\leq$ 0.70. The low-efficiency CIGSe cell when CGI = 0.30 did not allow a good JVT measurement as can be seen in the behavior of the dark $J-V$ curves in negative bias at lower temperatures.
The additional deviation of the $J_{\mathrm{sc}}(V_{oc})$ data points observed previously in Figure 4.16 for CGI = 0.30 without PDT becomes even more significant with RbF-PDT, occurring already at much higher temperatures and lower light intensities. Here, the $J_{\mathrm{sc}}(V_{oc})$ points are not only clamped but take a reverse direction where the V_{oc} is deteriorated. Same applies for the $J_{\mathrm{sc}}(V_{oc})$ data points of CGI = 0.70 + PDT.

Figure 4.18 shows the V_{oc} saturation at lower temperatures that this set of CIGSe solar cells exhibits when measured at full illumination. This saturation is more expressed when the Cu content is either too low or too high (CGI = 0.30 and 0.99). For CGI = 0.70 and 0.80, the V_{oc} saturation is minimized and for CGI = 0.70 + PDT, the V_{oc} follows the linear extrapolation to T = 0 K, decreasing linearly with temperature. The beneficial effect of the RbF can be clearly seen for the treated sample once the CGI is above 0.80.
The E_{A} extracted from the V_{oc} extrapolations of Figure 4.18 are given and compared with the E_{g} from EQE curves (included in Appendix A.4, Figure A.8) in Table 4.8.

The relation $E_{\mathrm{A}} < E_{\mathrm{g}}$ holds for CGI = 0.30 with and without RbF and for CGI = 0.70 with RbF-PDT, with a difference of 240 meV or more ($E_{\mathrm{A}} \leq E_{\mathrm{g}}$ - 240 meV). For the rest of the cells, activation energies are approximately equal to the band gap energies ($E_{\mathrm{g}} \approx E_{\mathrm{A}}$), except when PDT is applied for high Cu concentration (CGI = 0.99) where there is still a small difference between the estimated energies ($E_{\mathrm{A}} \approx E_{\mathrm{g}}$- 90 meV). In Section 4.4, it was observed that the carrier concentration N_{CV} played a role in the activation energy of the series of samples with Na-barrier. Previously, it was discussed that a low carrier concentration in the absorber, i.e., when $N_{\mathrm{CV}} < 10^{15}$ cm^{-3}, correlates to lower activation energies and, thus to the relation $E_{\mathrm{A}} < E_{\mathrm{g}}$. Nevertheless, the doping profiles for the set samples with diverse CGI ratios shown in Figure 4.19 does not correspond to the same conclusion. Only for CGI = 0.30 + PDT, the low carrier concentration in the absorber results in a lower E_{A} than E_{g}, as estimated by the V_{oc} extrapolation.

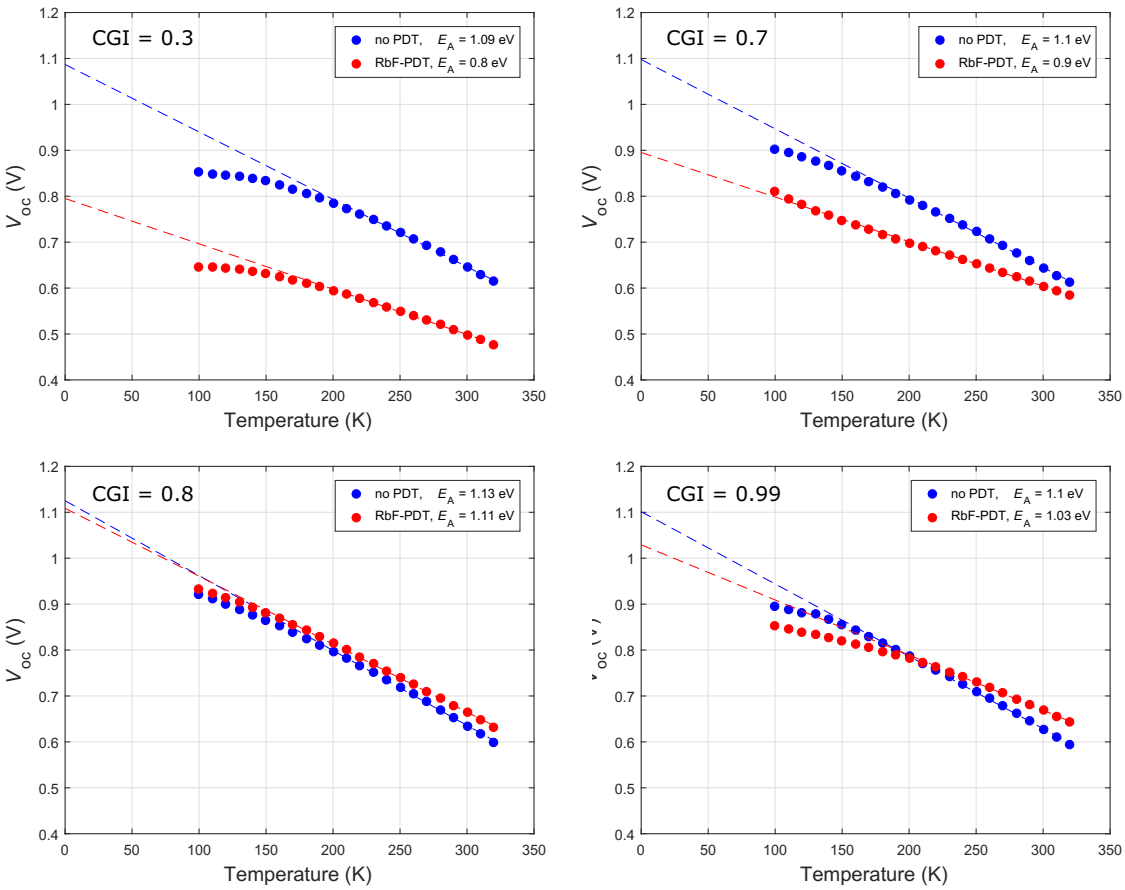

Figure 4.18.: V_{oc} as a function of the temperature of a series of CIGSe samples with and without RbF-PDT and different CGI ratio.

Table 4.8.: Band gap energies from *EQE* measurements and activation energies from V_{oc} extrapolations to $T = 0$ K of a set of CIGSe solar cells with different CGI ratio. The third column gives the activation energy obtained from the best linear dependence of the V_{oc} data at high temperatures. The fourth column gives the average activation energy with an estimated error range in function of the number of V_{oc} data taken to extrapolate from high to low temperatures.

Cells (no PDT)	$E_{g\ (EQE)}$ [eV]	$E_{A(V_{oc}(0\ K))}$ [eV]	$E_{A(V_{oc}(0\ K))}$ [eV]
CGI = 0.30	1.36	1.09	1.095 ± 0.025
CGI = 0.70	1.14	1.10	1.105 ± 0.025
CGI = 0.80	1.11	1.13	1.135 ± 0.025
CGI = 0.99	1.09	1.10	1.120 ± 0.030
Cells (RbF-PDT)	$E_{g\ (EQE)}$ [eV]	$E_{A(V_{oc}(0\ K))}$ [eV]	$E_{A(V_{oc}(0\ K))}$ [eV]
CGI = 0.30	1.30	0.80	0.80 ± 0.02
CGI = 0.70	1.14	0.90	0.90 ± 0.01
CGI = 0.80	1.10	1.11	1.12 ± 0.01
CGI = 0.99	1.12	1.03	1.03 ± 0.02

However, for CGI = 0.30 (no PDT) and for CGI = 0.70 + PDT which also resulted in $E_A < E_g$, the corresponding carrier concentrations are approximately $N_{CV} \geq 10^{15}$ cm^{-3} so the previous assumption is not fulfilled.
The loss in V_{oc} (see Table 4.7) after PDT for CGI = 0.30 and 0.70 may be a consequence of the reduction of the carrier concentration once the samples are treated with RbF as can be seen in the respective doping profiles.

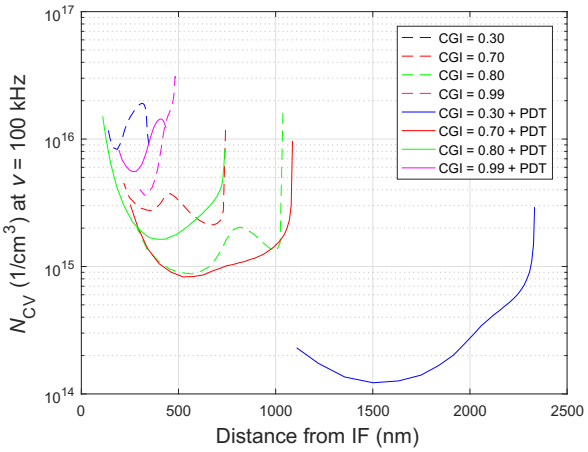

Figure 4.19.: N_{CV} profiles of a series of CIGSe solar cells with or without RbF-PDT and different CGI ratio.

The extraction of the diode factors under dark and/or illumination were done in samples affected neither by the blocking of the forward diode current nor by the deviation of the $J_{sc}(V_{oc})$ data points with respect to the non-blocked dark $J-V$ curves. The results are given in Figure 4.20. For CGI = 0.70, the determination of the diode factors were done in dark and under illumination. Here, no change exists in both conditions since the diode factors show almost identical values and a similar temperature-dependent trend where the diode factor increases as the temperature decreases. For CGI = 0.80, the calculations done with and without PDT under illumination show lower diode factors for CIGSe treated with RbF in comparison to the non-treated absorber, as previously observed in solar cells with CGI = 0.90-0.95 (see Figure 4.6). Finally, for CGI = 0.99, highly temperature-dependent diode factors were calculated with values above 2 at lower temperatures for dark (no PDT) and light (with PDT), whereas for a non-treated CIGSe the diode factors under illumination are smaller than those calculated in dark, a different behavior observed for lower CGI ratio (CGI = 0.70). It should be noted that, the large diode factors at lower temperatures may indicate the influence of a blocking and the incorrect determination and evaluation of the diode factors extracted from the fit.

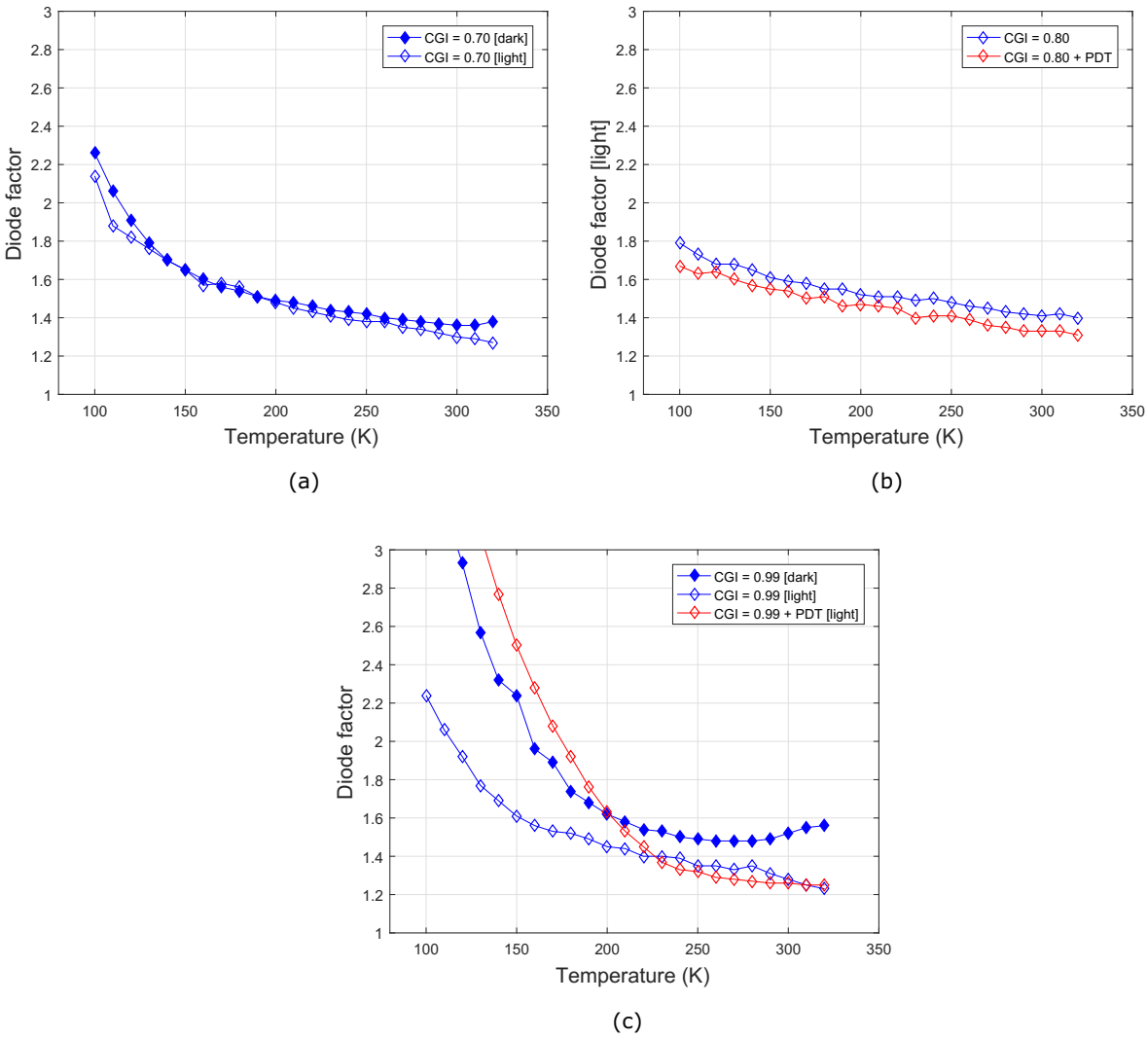

Figure 4.20.: $A(T)$ plots of CIGSe solar cells for (a) CGI = 0.70 (no PDT), (b) for CGI = 0.80 (with and without PDT) and (c) CGI = 0.99 (with and without PDT).

The main findings can be summarized as follows:

- The beneficial behavior of RbF (gain in V_{oc}) is only achieved in CIGSe solar cells with CGI $\geq$ 0.8. An increase in FF is only obtained for high Cu content with CGI = 0.99.
- Typically, the set of CIGSe solar cells without PDT do not show a roll-over or dark/light discrepancy, unlike solar cells with RbF-PDT that show significant non-idealities.
- Severe cross-over in cells with CGI = 0.30 (with/without PDT) and CGI = 0.70 (with PDT).
- The V_{oc} saturation at low temperatures is more significant for too low Cu (CGI = 0.30) and too high Cu (CGI = 0.99) content.

- $E_A < E_g$ for CGI = 0.30 (with/without PDT), CGI = 0.70 (with PDT) and CGI = 0.99 (with RbF), the latter with less difference.
- A_{dark} and/or A_{light} is slightly temperature-dependent and mainly < 2, except for too high Cu content (CGI = 0.99) which is highly temperature-dependent especially at lower temperatures.
- A_{light} decreases with RbF only when CGI = 0.80, similarly as observed in Section 4.2 for CGI = 0.90-0.95.

The non-idealities are independent of the Cu content, since a similar behavior to the reference CIGSe solar cells with and without RbF was observed. The decrease in carrier concentration after PDT correlates with the lower V_{oc} in cells with low Cu content. However, the carrier concentration due to the Cu content does not show a relation with the lower E_A than the E_g contrary to that observed in Section 4.4 due to the Na content.

4.6. Variations of the layer stack of the standard CIGSe solar cell structure

In this section, the standard layer stack of the CIGSe device described in Section 4.1.1 is modified by changing the type of deposition and materials of the buffer and window layers in order to study how the JVT characteristics behave by varying the heterojuntion and/or the heterointerfaces of a standard CIGSe solar cell.

Table 4.9.: STC parameters of a set of CIGSe solar cells with a different layer stack of the standard device.

Cells	J_{sc} (mA/cm^2)	V_{oc} (mV)	FF (%)	η (%)
-/i-ZnO/AZO (no PDT)	34.2	366	49.5	6.2
(RbF-PDT)	35.3	313	44.8	4.9
CdS/-/AZO (no PDT)	37.5	622	68.0	15.8
(RbF-PDT)	36.2	635	68.8	15.8
CdS/ZnOS/AZO (no PDT)	35.3	619	69.8	15.3
(RbF-PDT)	36.0	647	70.1	16.3
ZnOS/i-ZnO/AZO (no PDT)	31.5	526	62.6	10.4
(RbF-PDT)	33.3	551	60.4	11.1
ZnOS/ZnMgO/AZO (no PDT)	33.5	532	63.7	11.4
(RbF-PDT)	32.8	553	60.0	10.9
ZnOS/ZnMgO/i-ZnO/AZO (no PDT)	34.6	550	66.4	12.6
(RbF-PDT)	35.0	595	61.9	12.9

In Table 4.9, the STC parameters of the measured and studied solar cells are given. *EQE* curves of this series of samples can be found in Appendix A.4, Figure A.9.

4.6.1. No deposition of the CdS buffer layer

The cell structure of a CIGSe solar cell without a buffer layer results in glass/Mo/CIGSe-PVD/-/i-ZnO/ZnO:Al. As seen in Table 4.9 and compared to cells with buffer layer, lower V_{oc} at STC is obtained for these samples as a consequence for a reduced barrier for recombination (see below).

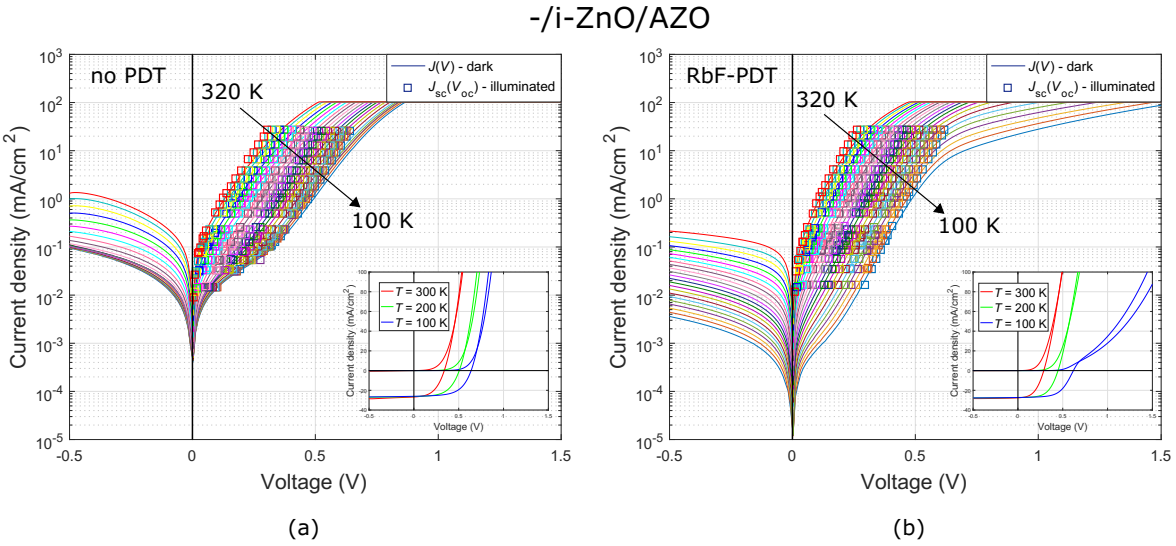

Figure 4.21.: *JVT* characteristics of a CIGSe solar cell with no CdS buffer layer: (a) without RbF-PDT and (b) with RbF-PDT.

Figure 4.21 shows the *JVT* characteristics of a solar cell with no CdS layer and without/with RbF, where the non-idealities caused by the PDT are much less significant than the ones observed in samples with the standard cell structure. A roll-over at low temperatures is present in the cell with RbF-PDT (see Figure 4.21b) as well as a slight cross-over effect that can be seen in the linear plot of the figure inset. No important deviation of the $J_{\mathrm{sc}}(V_{oc})$ data points with respect to the dark $J-V$ curves is observed in any case. However, even when no visible blocking of the forward diode current is observed in the cell without PDT (see Figure 4.21a), the CIGSe cell without a buffer layer between the absorber and the window film does not obey correctly the diode model equation since a good fit of the $J-V$ curves using a single or a two-diode model was not achieved for dark or illuminated conditions.

Figure 4.22 shows the V_{oc} plot as a function of the temperature where a slight V_{oc} saturation is only exhibited at very low temperatures ($T < 130$ K) in the cell without RbF-PDT. Once the absorber is treated with RbF, the V_{oc} values seem no longer be

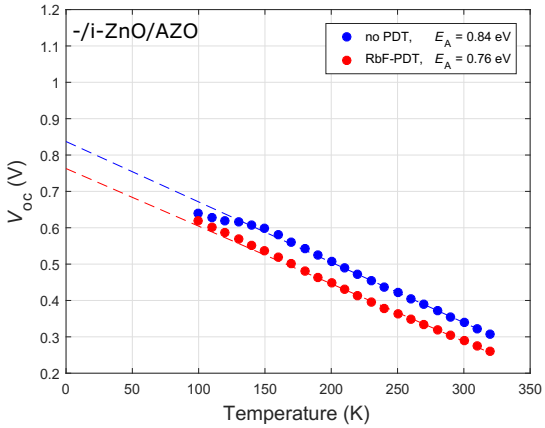

Figure 4.22.: V_{oc} as a function of the temperature of a CIGSe solar cell (without/with RbF-PDT) with no CdS buffer layer.

saturated at low temperatures, following closely the linear extrapolation to $T = 0$ K. Nevertheless, the post deposition treatment of the RbF leads to a V_{oc} loss in the full range of temperature (see also V_{oc} at STC in Table 4.9).

The estimation of the activation energies can be found in Table 4.10. In both cases, with and without RbF-PDT, lower E_A are determined compared to the EQE values, so $E_A < E_g$. Previous studies [112] demonstrated that a conduction band cliff between the absorber and the next layer in the direction of the front contact leads to a reduced barrier for recombination. Consequently, if $E_A < E_g$ as resulted in this case, the cells without a CdS buffer layer, assuming then a conduction band cliff between the absorber and the i-ZnO layer, are limited by interface recombination (see Section 2.3.4) which is also the reason for the low V_{oc} at STC. Doping profiles of this set (included in Appendix A.5, Figure A.14) show a high doping in the CIGSe absorber with $N_{CV} \approx 10^{15}$ cm^{-3}, therefore the estimation of the activation energy does not correlate with the carrier concentration in the absorber unlike the samples with a diffusion barrier at the back contact described in Section 4.4.

The main findings can be summarized as follows:

- A CIGSe solar cell without CdS buffer layer does not exhibit significant non-idealities after RbF-PDT such as roll-over, dark/light discrepancy and V_{oc} saturation in comparison to standard CIGSe solar cells with buffer layer.
- Loss in V_{oc} after RbF-PDT.
- The absence of a buffer layer leads to $E_A < E_g$ with/without PDT.

In this case, a relation between the carrier concentration and the value of the E_A cannot be found since the band line-up is the main responsible for a lower activation energy than the band gap due to the dominant interface recombination in this cell structure.

Table 4.10.: Band gap energies from EQE measurements and activation energies from V_{oc} extrapolations to $T = 0$ K of a set of CIGSe solar cells under different cell structures. The third column gives the activation energy obtained from the best linear dependence of the V_{oc} data at high temperatures. The fourth column gives the average activation energy with an estimated error range in function of the number of V_{oc} data taken to extrapolate from high to low temperatures.

Cells (no PDT)	$E_{\mathrm{g\ (EQE)}}$ [eV]	$E_{\mathrm{A}(V_{oc}(0\ \mathrm{K}))}$ [eV]	$E_{\mathrm{A}(V_{oc}(0\ \mathrm{K}))}$ [eV]
-/i-ZnO/AZO	1.09	0.84	0.840 ± 0.010
CdS/-/AZO	1.09	1.09	1.090 ± 0.020
CdS/ZnOS/AZO	1.11	1.05	1.045 ± 0.015
ZnOS/i-ZnO/AZO	1.10	0.97	0.975 ± 0.015
ZnOS/ZnMgO/AZO	1.10	0.96	0.965 ± 0.035
ZnOS/ZnMgO/i-ZnO/AZO	1.11	1.16	1.160 ± 0.010
Cells (RbF-PDT)	$E_{\mathrm{g\ (EQE)}}$ [eV]	$E_{\mathrm{A}(V_{oc}(0\ \mathrm{K}))}$ [eV]	$E_{\mathrm{A}(V_{oc}(0\ \mathrm{K}))}$ [eV]
-/i-ZnO/AZO	1.10	0.76	0.740 ± 0.040
CdS/-/AZO	1.10	1.10	1.100 ± 0.030
CdS/ZnOS/AZO	1.10	0.97	0.950 ± 0.020
ZnOS/i-ZnO/AZO	1.09	1.15	1.155 ± 0.045
ZnOS/ZnMgO/AZO	1.09	1.05	1.030 ± 0.030
ZnOS/ZnMgO/i-ZnO/AZO	1.10	0.97	0.970 ± 0.010

4.6.2. No deposition of the i-ZnO window layer

The cell structure of a CIGSe solar cell without the deposition of the highly resistive i-ZnO window layer results in glass/Mo/CIGSe-PVD/CdS/-/ZnO:Al.

The JVT characteristics in Figure 4.23 exhibit the non-idealities such as a roll-over, slight cross-over effect at lower temperatures and the discrepancy between the $J_{\mathrm{sc}}(V_{oc})$ data and the dark $J - V$ curves, being much more expressed in the CIGSe cell with RbF-PDT as previously observed for treated absorbers.

The corresponding cells also exhibit a V_{oc} saturation at lower temperatures as can be seen in Figure 4.24a, however the estimations of the activation energies are equal to the band gap energies $E_{\mathrm{g}} = E_{\mathrm{A}}$ (Table 4.10), a good agreement between both energies. From these observations, solar cells with the absence of the highly resistive i-ZnO of the window bilayer still have a good performance with efficiencies of approximately 16% (see Table 4.9) and with dominant recombination in the bulk obtained from the relation $E_{\mathrm{g}} = E_{\mathrm{A}}$. Besides, a similar JVT and $V_{oc}(T)$ behavior is observed in comparison with reference devices described in Sections 4.1 and 4.2. However, a poor V_{oc} gain results for the cell with RbF-PDT without any improvement in the performance due to the post deposition treatment because of the reduction in the J_{sc}.

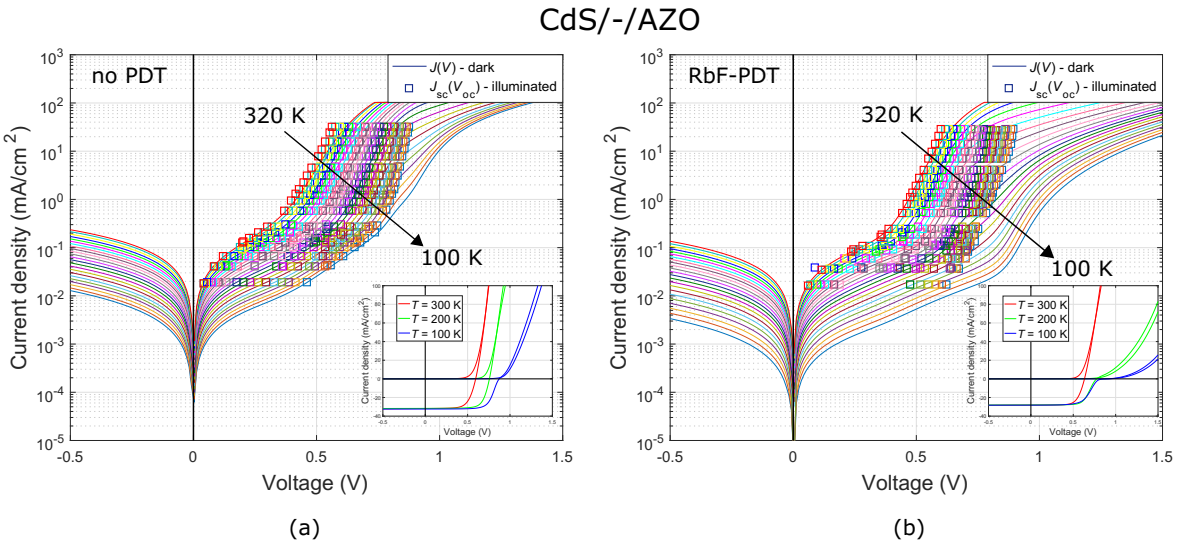

Figure 4.23.: JVT characteristics of a CIGSe solar cell without i-ZnO layer: (a) without RbF-PDT and (b) with RbF-PDT.

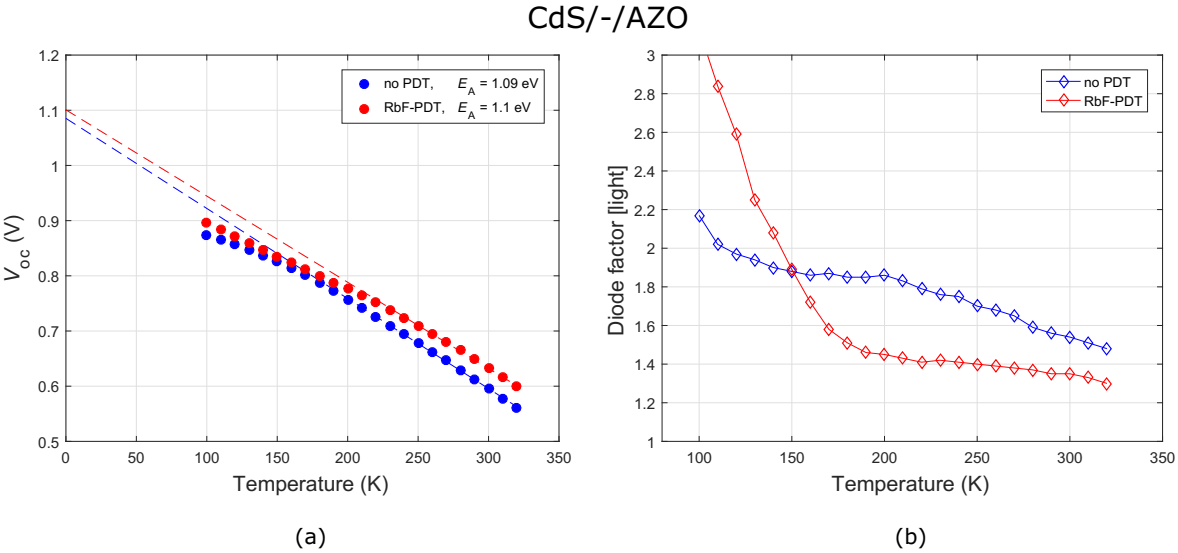

Figure 4.24.: (a) $V_{oc}(T)$ plot and (b) $A(T)$ plot under illumination of a CIGSe solar cell (without/with RbF-PDT) with no i-ZnO layer.

The $A(T)$ plot under illumination in Figure 4.24b gives lower diode factors at higher temperatures for the cell with RbF-PDT with respect to the cell without PDT. For temperatures below $T < 200$ K, the derived diode factors for the cell with treated absorber begin to increase as the temperature decreases to values for above 2. Once again, PDT reduces the diode factors as observed for cells with CGI = 0.90-0.95 in Figure 4.6.

The main findings can be summarized as follows:

- A CIGSe solar cell without i-ZnO layer presents a similar behavior than a standard CIGSe cell with/without RbF-PDT including the V_{oc} saturation at low temperatures and A_{light} behavior.
- Poor V_{oc} gain with RbF-PDT.

The main difference with respect to standard CIGSe cell structures is the poor gain in V_{oc} obtained after PDT. This structures is not beneficial for RbF.

4.6.3. Deposition of Zn(O,S) as a window layer

The substitution of the highly resistive part of the window layer was done by replacing the i-ZnO with a Zn(O,S) layer. The cell structure follows the layer stack glass/Mo/CIGSe-PVD/CdS/Zn(O,S)/ZnO:Al. The deposition of the Zn(O,S) was conducted by RF-sputtering (see Appendix A.1).

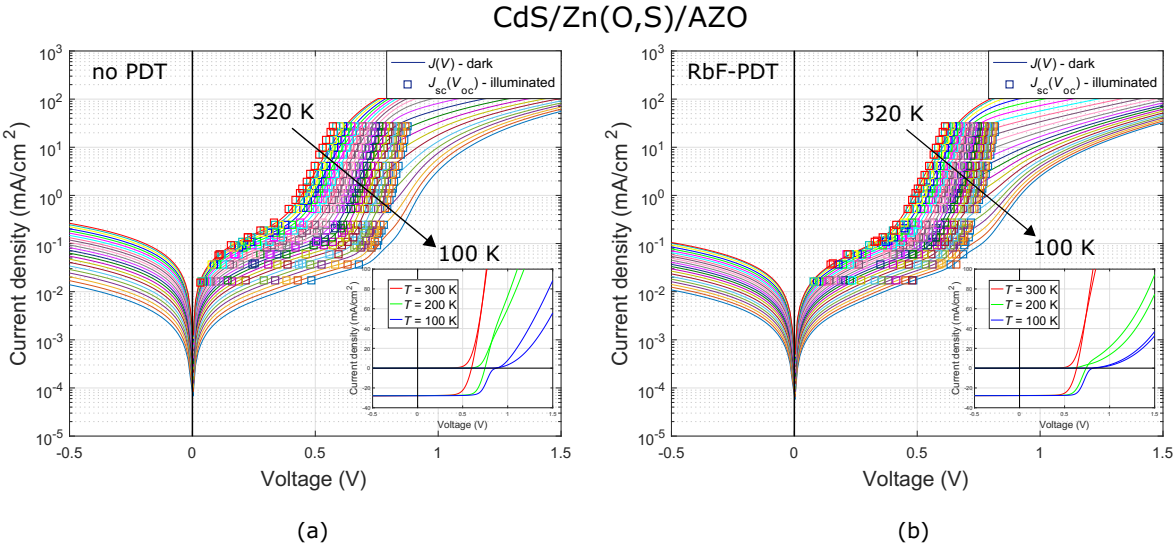

Figure 4.25.: *JVT* characteristics of a CIGSe solar cell with Zn(O,S) as a window layer: (a) without RbF-PDT and (b) with RbF-PDT.

Non-idealities with respect to a standard diode are shown in both devices with and without RbF as can be seen in Figure 4.25, again the roll-over and the discrepancy between the $J_{\text{sc}}(V_{oc})$ data and the dark $J-V$ curves are more significant in the cell with PDT. A slight cross-over effect between dark and light curves is also observed in the linear plot in both devices.

The non-ideal effect of the PDT in CIGSe solar cells is once again observed in a more significant saturation of the V_{oc} with respect to the temperature in Figure 4.26a. However, despite exhibiting the non-idealities after PDT in a similar way to the reference

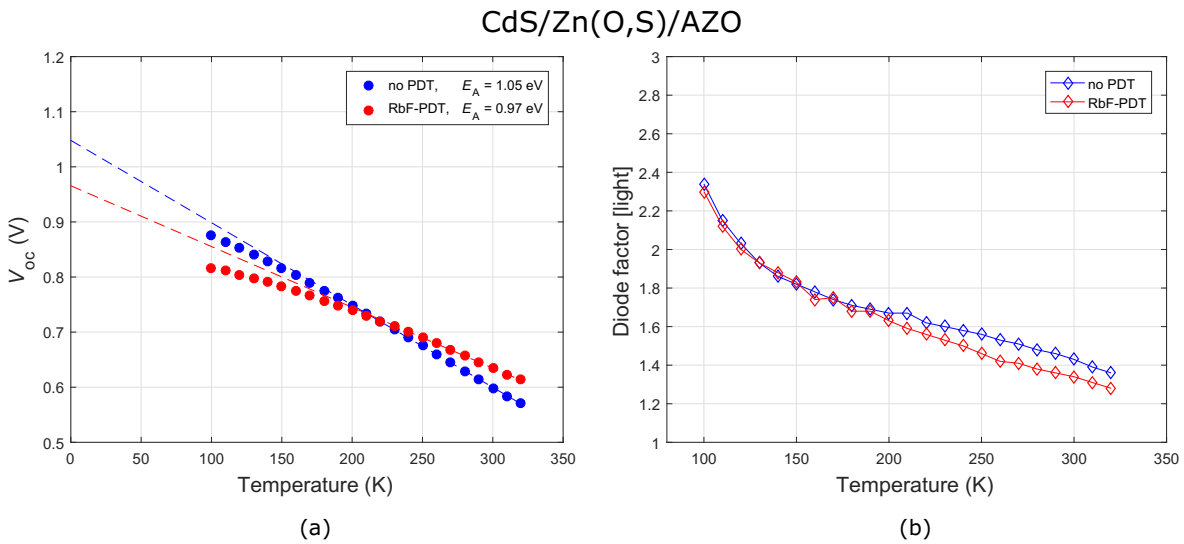

Figure 4.26.: (a) $V_{oc}(T)$ plot and (b) $A(T)$ plot under illumination of a CIGSe solar cell (without/with RbF-PDT) with Zn(O,S) as a window layer.

samples with i-ZnO window layer, the estimations of the activation energies give more discrepancy when comparing to their respective band gap energies given in Table 4.10. For the solar cell without RbF the activation energy is slightly lower than its band gap, $E_A < E_g$ ($E_A \approx E_g$- 60 meV) and this discrepancy becomes more important for a cell with RbF-PDT ($E_A \approx E_g$- 130 meV).
The above notwithstanding, the derived diode factors under illumination of both cells follow a similar trend with lower diode factors for the treated absorber at higher temperatures and increasing values with decreasing temperatures. At the lower temperatures, diode factors are matched and reach values close to 2.

The main findings can be summarized as follows:

- The non-ideal effects are present in both conditions, being much more expressed with RbF, including the V_{oc} saturation at low temperatures.
- The substitution of the i-ZnO layer leads to $E_A < E_g$ with a higher difference in the case with PDT.
- A_{light} presents a similar trend than standard solar cells.

The main difference of using a Zn(O,S) layer instead of the standard i-ZnO is the lower E_A than E_g especially when the absorber is treated with RbF. RbF-PDT is beneficial for this structure.

4.6.4. Deposition of Zn(O,S) as a buffer and (Zn,Mg)O as a window layer

In the first instance, the CdS layer was replaced by the Zn(O,S) to act as a buffer layer of the CIGSe device structure: glass/Mo/CIGSe-PVD/Zn(O,S)/i-ZnO/ZnO:Al. Afterwards, the highly resistive i-ZnO layer was replaced by the deposition of the (Zn,Mg)O to act as a part of the window bilayer, resulting in the cell structure as follows: glass/Mo/CIGSe-PVD/Zn(O,S)/(Zn,Mg)O/ZnO:Al. One more sample was produced as in the latter case except that, erroneously the i-ZnO layer was also deposited after the deposition of the (Zn,Mg)O on a different deposition date. Consequently, the three samples with the Zn(O,S) buffer layer as a common characteristic were measured by JVT. The deposition of the Zn(O,S) and (Zn,Mg)O was conducted by RF-sputtering (see Appendix A.1). The corresponding plots for the three-layer window device are found in the Appendix A.3, Figure A.4.

The corresponding JVT characteristics can be seen in Figure 4.27 where for the two different layer stacks where the Zn(O,S) is used as a buffer layer, the non-idealities are present in the cells with RbF-PDT such as a roll-over over the entire temperature range or at lower temperatures and a deviation of the $J_{\mathrm{sc}}(V_{oc})$ points with respect the dark $J-V$ curves. The CIGSe solar cells without RbF-PDT do not exhibit the effects mentioned above and behave without any visible blocking over the entire temperature range. Just a slight cross-over effect between the dark and light $J-V$ curves is present in one of the samples especially at lower temperatures for the untreated absorbers and at higher temperatures for the treated CIGSe.

$V_{oc}(T)$ plots of this set of solar cells are shown in Figure 4.28 where the estimated E_{A} obtained from the V_{oc} extrapolations to $T=0$ are given in Table 4.10. From this, the cells with structures consisting of Zn(O,S)/i-ZnO/ZnO:Al and Zn(O,S)/(Zn,Mg)O/ZnO:Al have lower activation energies than band gap energies, i.e., $E_{\mathrm{A}} < E_{\mathrm{g}}$. Once the absorber of these cells is treated with RbF, the activation energies approach the band gap, for the Zn(O,S)/i-ZnO/AZO cell structure the activation energy exceeds the band gap energy ($E_{\mathrm{A}} \approx E_{\mathrm{g}} + 60$ meV), while for the Zn(O,S)/(Zn,Mg)O/AZO cell structure the activation energy is slightly lower than the band gap ($E_{\mathrm{A}} \approx E_{\mathrm{g}}$-40 meV).

From the $V_{oc}(T)$ plots in Figure 4.28, the V_{oc} saturation at lower temperatures usually observed in most of the CIGSe cells either with or without RbF-PDT is not observed in the solar cells without PDT where the Zn(O,S) act as a buffer layer. Conversely, in solar cells with treated absorbers the saturation of the V_{oc} at lower temperatures takes place.

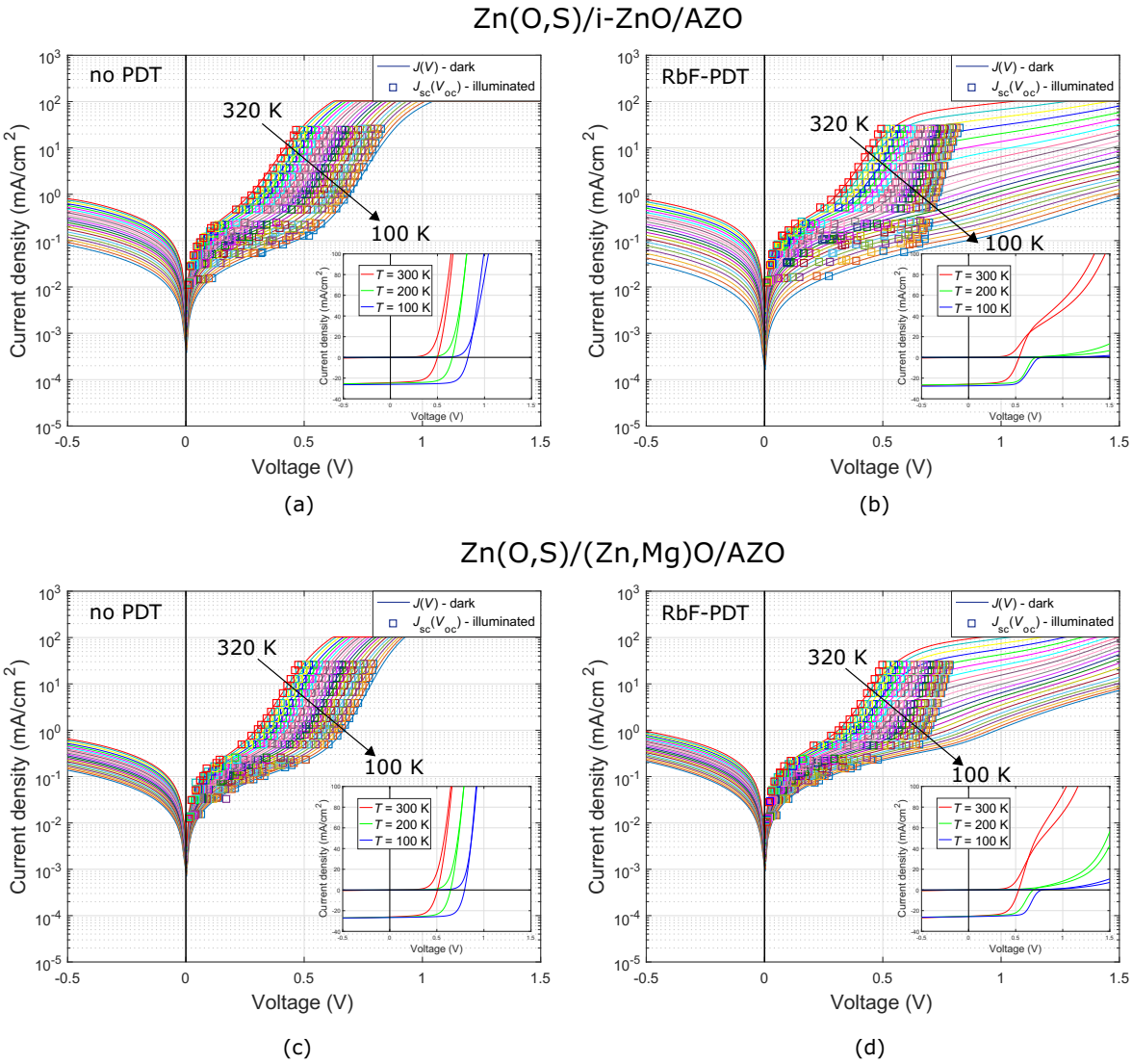

Figure 4.27.: JVT characteristics of a CIGSe solar cell with two different layer stacks above the absorber: Zn(O,S)/i-ZnO/AZO and Zn(O,S)/(Zn,Mg)O/AZO (a) and (c) without RbF-PDT, and (b) and (d) with RbF-PDT, respectively.

A general conclusion from the $A(T)$ plots in Figure 4.28 can not be described since diode factors even above 3 were derived in most of the fits. Nevertheless, for the Zn(O,S)/i-ZnO/ZnO:Al and Zn(O,S)/(Zn,Mg)O/ZnO:Al cell structures, diode factors in dark and under illumination of the solar cells without PDT show similar values and a similar trend with highly temperature-dependent diode factors increasing while decreasing the temperature. As a consequence of the RbF-PDT, the diode factors under illumination are lowered over the full temperature range.

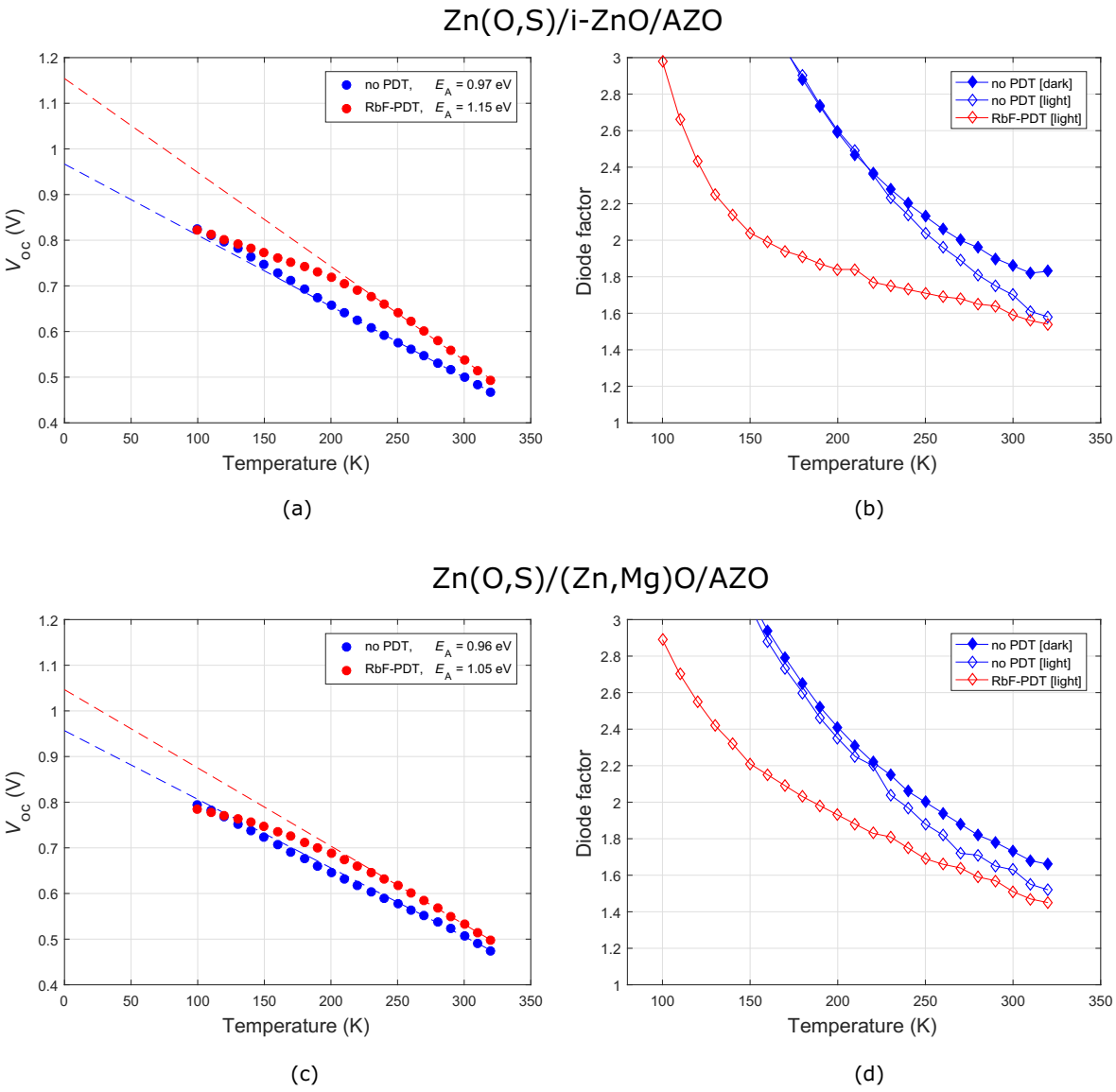

Figure 4.28.: (a) and (c) $V_{oc}(T)$ plot, and (b) and (d) $A(T)$ plot of a CIGSe solar cell (without/with RbF-PDT) with two different layer stacks above the absorber: Zn(O,S)/i-ZnO/AZO and Zn(O,S)/(Zn,Mg)O/AZO, respectively.

The main findings can be summarized as follows:

- When using Zn(O,S) as a buffer layer with/without (Zn,Mg)O as part of the window, the roll-over and dark/light discrepancy are only exhibited in samples with RbF-PDT over the full temperature range, even at room temperature, including the cross-over of the $J-V$s.
- In solar cells without RbF, $E_\mathrm{A} < E_\mathrm{g}$. After PDT, the E_A tries to approximate to the band gap.
- V_{oc} saturation is not observed at low temperatures in samples without PDT but emerges once the absorber is treated with RbF.

- A_{light} is highly temperature-dependent (with/without PDT) over the entire temperature range with values > 2 especially at lower temperatures. A_{light} decreases after the deposition of RbF.
- These structures with PTD leads to a V_{oc} gain but also to a loss in FF such as the standard cells.

Even when the V_{oc} increases with RbF-PDT, the FF is further reduced by using Zn(O,S) instead of CdS as a buffer layer with/without (Zn,Mg)O as part of the window, with more expressed non-idealities once the RbF is deposited on the absorber. In this experiment, the substitution of CdS by Zn(O,S) and the use of (Zn,Mg)O as a window layer do not improve the performance of the device.

4.7. Deposition of a secondary phase on CIGSe surface: $RbInSe_2$ layer

In Section 2.4, some studies indicate a formation of a secondary phase at the top of the CIGSe absorber, most likely a $RbInSe_2$ compound. For this reason, JVT characteristics of a reference CIGSe solar cell with CGI = 0.95 are compared with cells where a $RbInSe_2$ layer was grown onto the CIGSe surface. The layer stack follows the sequence of glass/Mo/CIGSe-PVD/$RbInSe_2$/CdS/i-ZnO/ZnO:Al. The $RbInSe_2$ thin film was deposited using a one-stage multi-source evaporation of In, Se and RbF and the deposition times of the $RbInSe_2$ layer were 1 min (with a thickness of 5 nm) and 4 min (with a thickness of 20 nm) for the measured samples. The increase of the deposition time is directly connected to the increase of the $RbInSe_2$ layer thickness. Process details of these samples can be found in Appendix A.1. EQE curves and N_{CV} profiles derived from $C-V$ measurements are given in Appendix A.4 and A.5.

Table 4.11.: STC parameters of a set of CIGSe solar cells with a $RbInSe_2$ thin-film onto the absorber.

Cells	J_{sc} (mA/cm^2)	V_{oc} (mV)	FF (%)	η (%)
no RIS	37.2	655	73.4	17.9
1 min RIS	35.7	670	73.3	17.5
4 min RIS	35.9	684	71.2	17.5

The STC parameters of this set of devices in Table 4.11 show an increase of the V_{oc} but a steady decrease in FF with higher deposition times of the $RbInSe_2$ layer, a similar trend as observed for samples prepared with RbF-PDT (see Section 4.2), but here without any improvement in the efficiency of the device.

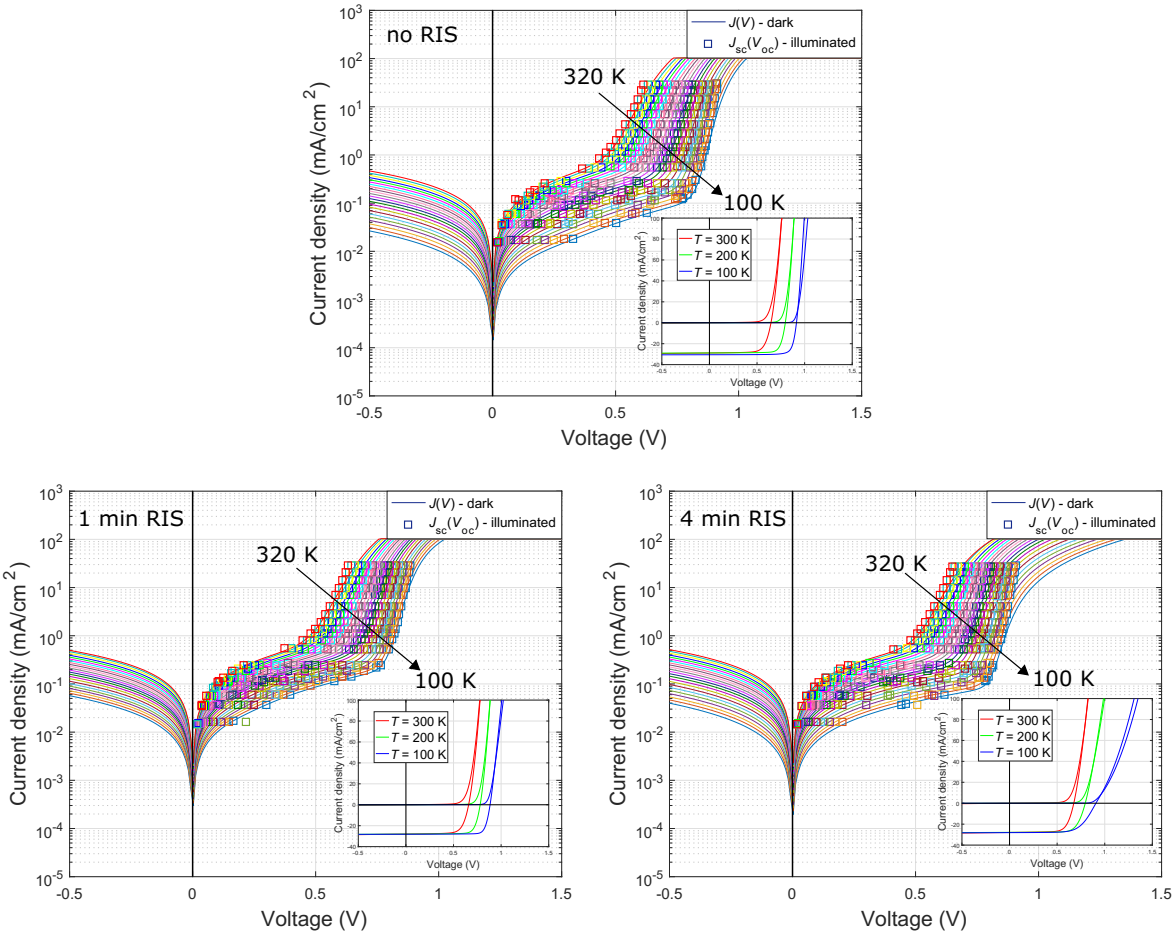

Figure 4.29.: JVT characteristics of a reference CIGSe solar cell and two cells with different deposition times of a $RbInSe_2$ thin film onto the absorber.

The JVT measurements of the corresponding set of solar cells are displayed in Figure 4.29. As previously observed in Section 4.1.1, the reference solar cell does not exhibit non-idealities with respect to a standard diode, i.e., there is no blocking of the forward diode current over the entire temperature range and the $J_{sc}(V_{oc})$ data follow the dark $J-V$ curves at high and low temperatures. When a 1 min $RbInSe_2$ layer is then deposited, there is no change in the JVT characteristics, showing again an ideal diode behavior. A very slight roll-over at low temperatures appears when a 4 min $RbInSe_2$ layer is deposited onto the absorber. Even when the Rb concentration incorporated into the bulk after the 4 min $RbInSe_2$ deposition is higher than the Rb content within the absorber after 10 min PDT (see Appendix A.2, Figure A.1), the strong non-idealities observed in Section 4.2 do not occur.

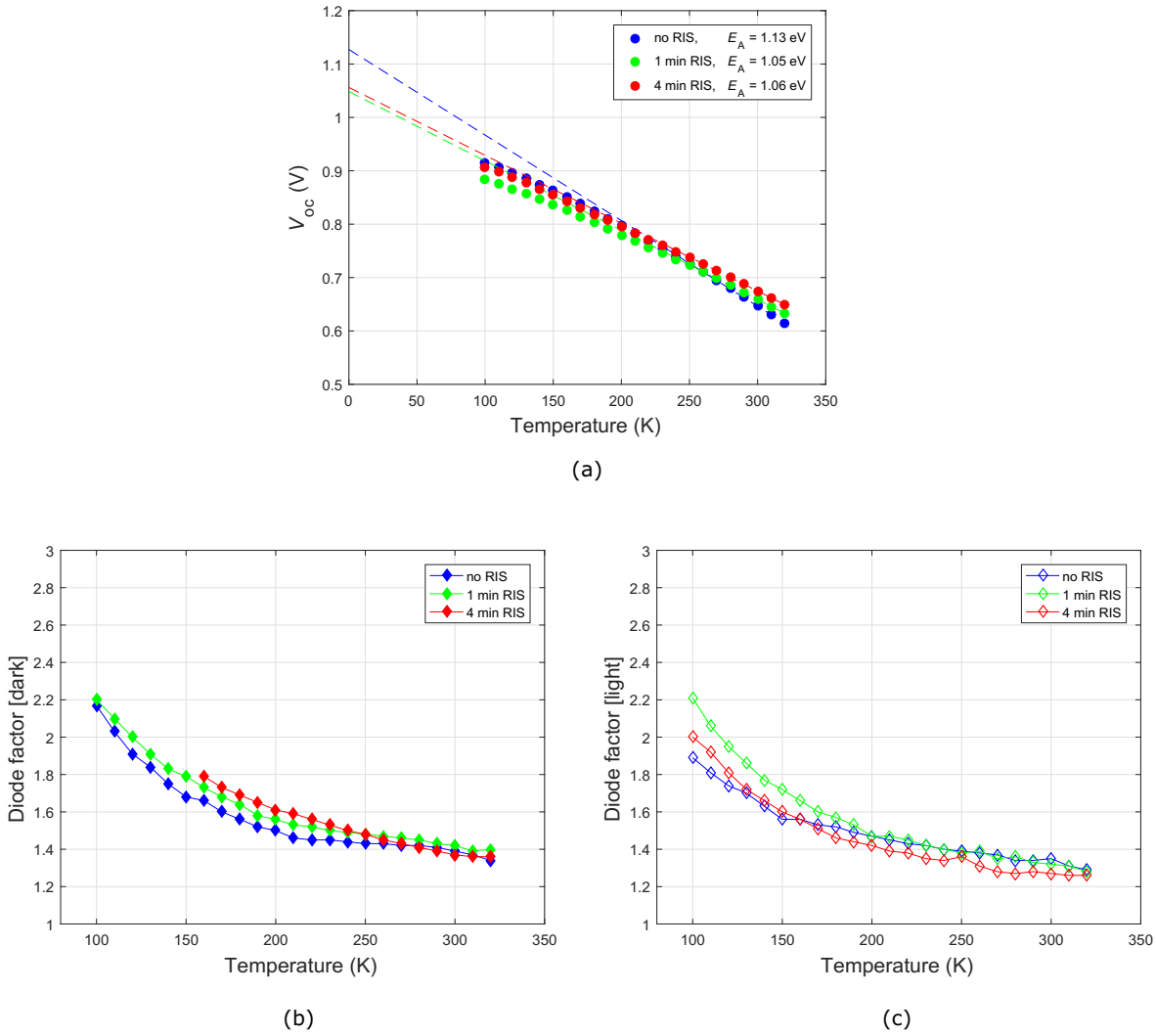

Figure 4.30.: (a) $V_{oc}(T)$ plot, and $A(T)$ plot in (b) dark and (c) under illumination of a reference CIGSe solar cell and two cells with different deposition times of a $RbInSe_2$ thin film onto the absorber.

Nevertheless, the saturation of the V_{oc} at low temperatures is present in this set of solar cells as seen in Figure 4.30 especially for the reference and the 1 min $RbInSe_2$ layer, while for the 4 min $RbInSe_2$ the saturation is less pronounced. The estimations of the E_A and the E_g are given in Table 4.12. The comparison results in a small difference of 40-50 meV between both energies (a possible miscalculation as briefly discussed at the end of Section 4.2) but $E_A \approx E_g$.

Since the JVT curves show no roll-over or a significant roll-over effect only at low temperatures, the determination of the diode factors of this set was done in dark (Figure 4.30b) and under illumination (Figure 4.30c), showing a similar behavior as the reference CIGSe samples with RbF-PDT where the diode factors are slightly temperature-dependent and increase as the temperature decreases, stay mainly < 2

Table 4.12.: Band gap energies from *EQE* measurements and activation energies from V_{oc} extrapolations to $T = 0$ K of a set of CIGSe solar cells with a $RbInSe_2$ thin-film onto the absorber. The third column gives the activation energy obtained from the best linear dependence of the V_{oc} data at high temperatures. The fourth column gives the average activation energy with an estimated error range in function of the number of V_{oc} data taken to extrapolate from high to low temperatures.

Cells	$E_{g\ (EQE)}$ [eV]	$E_{A(V_{oc}(0\ K))}$ [eV]	$E_{A(V_{oc}(0\ K))}$ [eV]
no RIS	1.09	1.13	1.115 ± 0.025
1 min RIS	1.10	1.05	1.040 ± 0.020
4 min RIS	1.10	1.06	1.050 ± 0.020

and have $A_{dark} \approx A_{light}$. There is no clear trend between the diode factors and the deposition times of the $RbInSe_2$ thin film. At higher temperatures, the lowest diode factors are obtained from the 4 min $RbInSe_2$, while at the lowest temperatures the diode factors increase with the deposition of the $RbInSe_2$ with the highest values for the 1 min deposition time. Besides, doping profiles given in Appendix A.5, Figure A.15 show higher N_{CV} for the 1 min $RbInSe_2$ in comparison with the 4 min $RbInSe_2$ and the reference cell, respectively. From this, higher N_{CV} corresponds to higher diode factors at lower temperatures, an opposite trend with respect to the samples with RbF-PDT.

The main findings can be summarized as follows:

- The deposition of a RIS layer shows similarities of the STC parameters with respect to RbF-PDT CIGSe solar cells: V_{oc} gain and FF loss.
- RIS samples do not show a roll-over or dark/light discrepancy.
- V_{oc} saturation at low temperatures, being less pronounced in the 4 min RIS solar cell.
- Diode factors behave as the deduced diode factors from the reference cells.

The formation of a RIS layer on the absorber surface is not responsible of the non-ideal effects observed after PDT.

4.8. Deposition of RbF-PDT on CIGSSe absorbers prepared by Rapid Thermal Processing

Up to this point, CIGSe absorbers had been prepared by multi-source evaporation. The set of samples presented in this section comes from $Cu(In,Ga)(S,Se)_2$ (CIGSSe) absorbers prepared by rapid thermal processing (RTP) described in Appendix A.1. The

cell structure of these samples follows the sequence of glass/SiO_xN_y/Mo/MoNa/Mo/CIGSSe-RTP/CdS/i-ZnO/ZnO:Al. One reference sample, one sample with RbF-PDT and one sample with NaF+RbF-PDT were processed and measured by JVT. EQE curves and N_{CV} profiles are included in the Appendix A.4 and A.5.

Table 4.13.: STC parameters of a set of CIGSSe solar cells prepared by RTP.

Cells	J_{sc} (mA/cm^2)	V_{oc} (mV)	FF (%)	η (%)
no PDT	38.5	547	69.0	14.5
RbF-PDT	38.6	580	64.7	14.5
NaF + RbF-PDT	38.0	596	69.2	15.7

The STC parameters are given in Table 4.13 and show an increase in V_{oc} in the samples with PDT, with a higher V_{oc} gain where NaF+RbF-PDT was deposited on the absorber. Samples with RbF-PDT undergo a loss in FF but it is recovered when NaF is deposited by PDT with the highest beneficial performance due to the PDT.

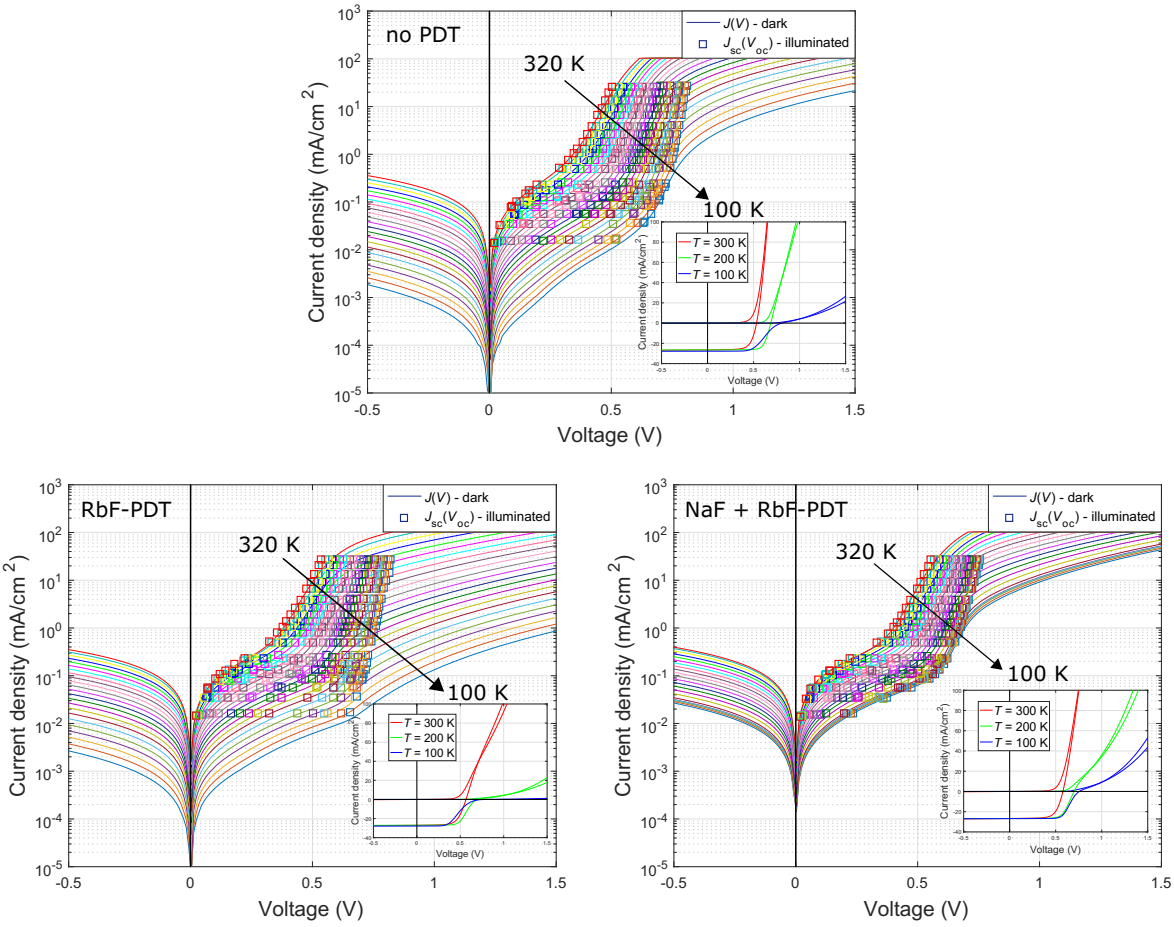

Figure 4.31.: JVT characteristics of a set of CIGSSe solar cells prepared by RTP.

Non-idealities with respect to a standard diode are present even in the reference CIGSSe solar cell at lower temperatures: roll-over effect, discrepancy between $J_{sc}(V_{oc})$ data and dark $J-V$ curves and slight cross-over effect, as can be seen in Figure 4.31. For the RbF-PDT solar cell, the non-ideal effects extend to higher temperatures. When the PDT includes Na, the non-idealities are reduced.

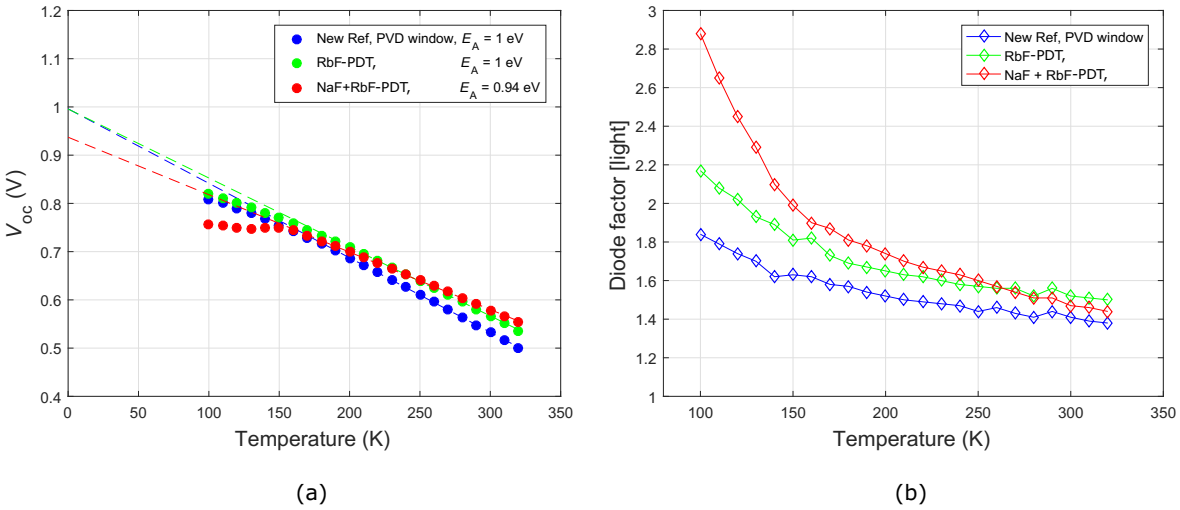

Figure 4.32.: (a) $V_{oc}(T)$ plot, and (b) $A(T)$ plot of a set of CIGSSe solar cells prepared by RTP.

The V_{oc} saturation is exhibited at lower temperatures and very expressed for the NaF+RbF-PDT solar cell as can be observed in Figure 4.32a, and also for this case, the estimation of E_{A} is slightly smaller than the estimation of the E_{g}, obtaining $E_{\mathrm{A}} \approx E_{\mathrm{g}}$- 60 meV (see Table 4.14). For the reference and RbF-PDT solar cell, the activation energies precisely equal the band gap energy, $E_{\mathrm{g}} = E_{\mathrm{A}}$.
As seen in the doping profiles given in Appendix A.5, Figure A.16, the PDT causes a reduction of the carrier concentration N_{CV}, whereas typically for absorbers prepared by PVD, the N_{CV} is increased for larger deposition times (see Appendix A.2, Figure A.1).

In Figure 4.32b, an increase of the slightly temperature-dependent diode factors for PDT solar cells with respect to the reference cell is observed, obtaining the highest values for the NaR+RbF-PDT cell with A_{light} close to 3 at lower temperatures. In Section 4.2, compared to the CIGSe reference samples, the results at higher temperatures mostly showed a decrease of the diode factors when PDT was applied to the CIGSe absorber for CGI = 0.90-9.95 (see Figure 4.6). However, in some cells, A_{light} also showed an increasing trend as the temperature decreases.

Table 4.14.: Band gap energies from EQE measurements and activation energies from V_{oc} extrapolations to $T = 0$ K of a set of CIGSSe solar cells prepared by RTP. The third column gives the activation energy obtained from the best linear dependence of the V_{oc} data at high temperatures. The fourth column gives the average activation energy with an estimated error range in function of the number of V_{oc} data taken to extrapolate from high to low temperatures.

Cells	$E_{\mathrm{g\ (EQE)}}$ [eV]	$E_{\mathrm{A}(V_{oc}(0\ \mathrm{K}))}$ [eV]	$E_{\mathrm{A}(V_{oc}(0\ \mathrm{K}))}$ [eV]
no PDT	1.0	1.0	1.000 ± 0.010
RbF-PDT	1.0	1.0	1.000 ± 0.010
NaF + RbF-PDT	1.0	0.94	0.945 ± 0.015

The main findings can be summarized as follows:

- CIGSSe solar cells prepared by RTP show an increase of V_{oc} after PDT with a loss in FF when RbF is only deposited.
- The set of CIGSSe cells exhibit non-ideal effects over a wide temperature range especially at low temperatures, including the cell without PDT, being much more expressed in the cell with only RbF.
- More significant V_{oc} saturation at lower temperatures for the NaF+RbF-PDT cell with $E_{\mathrm{A}} < E_{\mathrm{g}}$, even when the roll-over and dark/light discrepancy is reduced when NaF is deposited.
- Reduction of the N_{CV} after PDT in contrast to samples prepared by PVD.
- A_{light} are temperature-dependent with values increasing in a higher rate at low temperatures, especially for the NaF+RbF-PDT cell.

RTP CIGSSe solar cells show certain similarities with PVD CIGSe solar cells after PDT, mainly the gain in V_{oc} and efficiency as the positive effect of PDT. For the RTP cells, NaF plays an important role since it reduces the roll-over and the FF loss due to RbF-PDT. However, this causes a reduction of the E_A and V_{oc} saturation at low temperatures not present in the cell without PDT or RbF-PDT cell. Compared to PVD devices, the main difference lies on the reduction of the N_{CV} and increase of A_{light} after PDT.

4.9. Summary of the non-idealities of CIGSe thin-film solar cells

This chapter presented the main characteristics that CIGSe solar cells exhibit after the absorber is treated with RbF and/or NaF+RbF by post deposition treatment. In most of the cells, PDT induces non-ideal effects with respect to a standard diode especially

at low temperatures: roll-over of the $J-V$ characteristics, discrepancy between the $J_{\mathrm{sc}}(V_{oc})$ data points and the dark $J-V$ curves, V_{oc} saturation and cross-over between the dark and illuminated $J-V$ curves.

The roll-over of the forward diode current, usually accompanied by the discrepancy between the $J_{\mathrm{sc}}(V_{oc})$ data and dark $J-V$ curves, is enhanced with higher amounts of Rb which also leads to a lower Na content within the absorber. In high-efficient CIGSe solar cells from external laboratories, the roll-over is shown in the sample with the highest efficiency measured so far in this work, however, the effect on the ZSW cell that presents a different layer structure that includes a (Zn,Mg)O layer instead of the i-ZnO as part of the window bilayer is less expressed than in the samples prepared at HZB. In samples without a RbF treatment, the roll-over is also present when the sample has no Ga grading (constant E_{g}), when the i-ZnO is replaced by a Zn(O,S) layer as part of the window bilayer, with the presence of a Na-barrier at the back side of the absorber at full temperature range and finally in RTP CIGSe solar cells.

A slight cross-over effect between dark and light $J-V$ curves is typically present in most of the CIGSe solar cells at low temperatures but ocurring earlier in temperature with RbF-PDT. The more severe cross-over effect is shown in the samples with low Cu content and in samples with a Na-barrier at the back contact.

Similarly, a saturation of the V_{oc} at low temperatures is typically exhibited in most of the CIGSe devices, being more expressed in samples with RbF-PDT which leads to a lower Na content than the reference CIGSe cells, in samples with too low or too high Cu content (CGI = 0.30 and CGI = 0.99) in comparison to $0.7 < \mathrm{CGI} < 0.8$ samples, and with the most severe saturation in the samples with a Na-barrier at the back contact. A reduced V_{oc} saturation is mainly observed in samples with a different layer structure than the standard device, e.g., when Zn(O,S) is used as a window layer or as a buffer layer with/without a (Zn,Mg)O as a window layer, or without CdS layer. Much less expressed V_{oc} saturation is achieved for the latter cases either before or after PDT. The same applies when a 4 min RIS layer is deposited on the absorber. In RTP cells, a saturation of the V_{oc} is more expressed in the sample treated with NaF+RbF.

From the evaluation of the activation energies and band gap energies, typically $E_{\mathrm{A}} \approx E_{\mathrm{g}}$ in most of the CIGSe solar cells. As discussed in Chapter 2, recombination in the bulk is assumed to be the dominant recombination mechanism in high-efficient CIGSe thin-film solar cells. However, there are cases where $E_{\mathrm{A}} < E_{\mathrm{g}}$. This is found is samples with Na-barrier at the back contact in which after PDT, Rb helps to increase the E_{A}. A relation between the low E_{A} and the low N_{CV} due to the Na content was observed. Another situation is present in samples with different CGI ratio, especially in samples with low Cu content (CGI = 0.30) and when the sample is treated with RbF at CGI = 0.7 and CGI = 0.99. Varying the layer structure of the device, the relation $E_{\mathrm{A}} < E_{\mathrm{g}}$ is

shown in the sample without a CdS buffer layer, when Zn(O,S) is used as a part of the window bilayer and when Zn(O,S) is used as a buffer layer, in which for the latter, Rb increases E_{A} approaching the band gap. In RTP, a lower activation energy than the band gap was found in the samples with the highest gain in V_{oc}, namely, the sample with NaF+RbF-PDT.

The determination of the diode factors in dark (if possible) and under illumination showed a slightly temperature dependence with diode factors mainly < 2 and with a decreasing trend especially at high temperatures once the RbF is deposited on the absorber in samples with a CGI range between CGI = 0.8-0.95. At low temperatures, it was usually observed a higher temperature dependence of the diode factors with larger A_{light} for low Rb content (4 min RbF-PDT) and lower A_{light} for high Rb content (10 min RbF-PDT), which also led to a lower and higher N_{CV}, respectively, compared to the ones deduced from the reference cells without PDT. A decreased of the diode factors after PDT was also observed at low temperatures in samples with Na-barrier at the back contact. However, an opposite trend was observed in CIGSe solar cells prepared by RTP with increased diode factor after PDT over the full temperature range. It is worth mentioning that RTP samples present a similar behavior in A_{light} and N_{CV} when comparing with PVD samples with short Rb deposition time. A high temperature dependence of the diode factors was obtained in samples with too high Cu content (CGI = 0.99) and when CdS was replaced by the Zn(O,S) buffer. A non-temperature-dependent A_{light} behavior was observed in the sample with a constant band gap in the absorber with almost constant diode factors at $T \geq 150$ K.

As previously described in Chapter 2, one of the main beneficial effects of the RbF-PDT is the increase of the V_{oc}, an effect mostly observed in the samples with absorbers prepared by PVD and RTP studied in this work. A V_{oc} increase was observed with longer RbF deposition times and longer deposition time of the RIS layer on the absorber in samples with CGI ≥ 0.80. CIGSe solar cells without CdS buffer layer and cells with low Cu content did not show an increase in the open-circuit voltage which correlates with the significant limitation by the interface recombination and the low carrier concentration N_{CV} in the absorber after PDT, respectively. Finally, PDT led to a FF loss for samples with higher Rb amount, higher deposition time of the RIS layer and with low Cu content. A decrease in FF was also observed in samples without CdS and when it was replaced by Zn(O,S) as a buffer.

The aforementioned findings obtained from experimental measurements will be described in more detail in Chapter 6 in connection with the results of the numerical simulations presented in the following chapter in order to explain the physical, recom-

bination and transport mechanisms behind the non-idealities of the previous CIGSe thin-film solar cells without and with RbF-PDT.

5. Numerical modeling: Study of current limitation

In this chapter, the limitations of the current flow across the heterojunction in CIGSe-based thin film solar cells are modeled using SCAPS-1D simulations. Non-idealities with respect to a standard diode are observed especially at low temperatures in temperature-dependent $J-V$ measurements of CIGS solar cells prepared with PDT as seen in Chapter 4. These include: blocking of the forward diode current, saturation of the open-circuit voltage with respect to temperature, a discrepancy between dark and $J_{\mathrm{sc}}(V_{oc})$ characteristics, and a crossover between dark and light $J-V$ curves. Supposed beneficial effects that could result from the PDT deposition such as the increase in the carrier concentration and/or increased carrier lifetime in the absorber were neglected in the numerical simulations. However, such material parameters were included in the analysis of the back contact barrier model in order to know to what extent they affect the resuting $J-V$ characteristics.

In Chapter 3 the device and material properties of a simple CIGSe model were listed. Figure 5.1 shows the results for the simulated $J-V$ curves in linear scale, the semi-logarithmic dark $J-V$ curves including the $J_{\mathrm{sc}}(V_{oc})$ data points at different light intensities from 100 mW/cm^2 to 0.1 mW/cm^2 and the V_{oc} as a function of the temperature from 400 K to 100 K, respectively, in order to reproduce the experimental characteristics already observed and described for reference CIGSe solar cells in Chapter 4.

The reference model already presents some non-ideal behavior at the lowest temperature (T = 100 K), and this will be a subject of study included in Section 5.1.1. The corresponding V_{oc} extrapolation to $T = 0$ K shown in Figure 5.1c, results in a E_{A} above the value of the E_{g} of the absorber set in the SCAPS model ($E_{\mathrm{A}} = E_{\mathrm{g}}$ + 90 meV). As mentioned in Reference [17], device simulation programs may use temperature-dependent material parameters such as the lifetime of electrons and holes $\tau_{n,p}$ and the effective density of states in the conduction and the valence band of the absorber $N_{\mathrm{C,V}}$, which increase the slope of the $V_{oc}(T)$ curve by about $3kT_{300} \approx 78$ meV in the case of the SCR and QNR recombination.

Since the reference model presents SCR recombination as the dominant recombination in the absorber, the material parameters mentioned above may be considered and may increase the activation energy above the band gap energy of 1.1 eV.

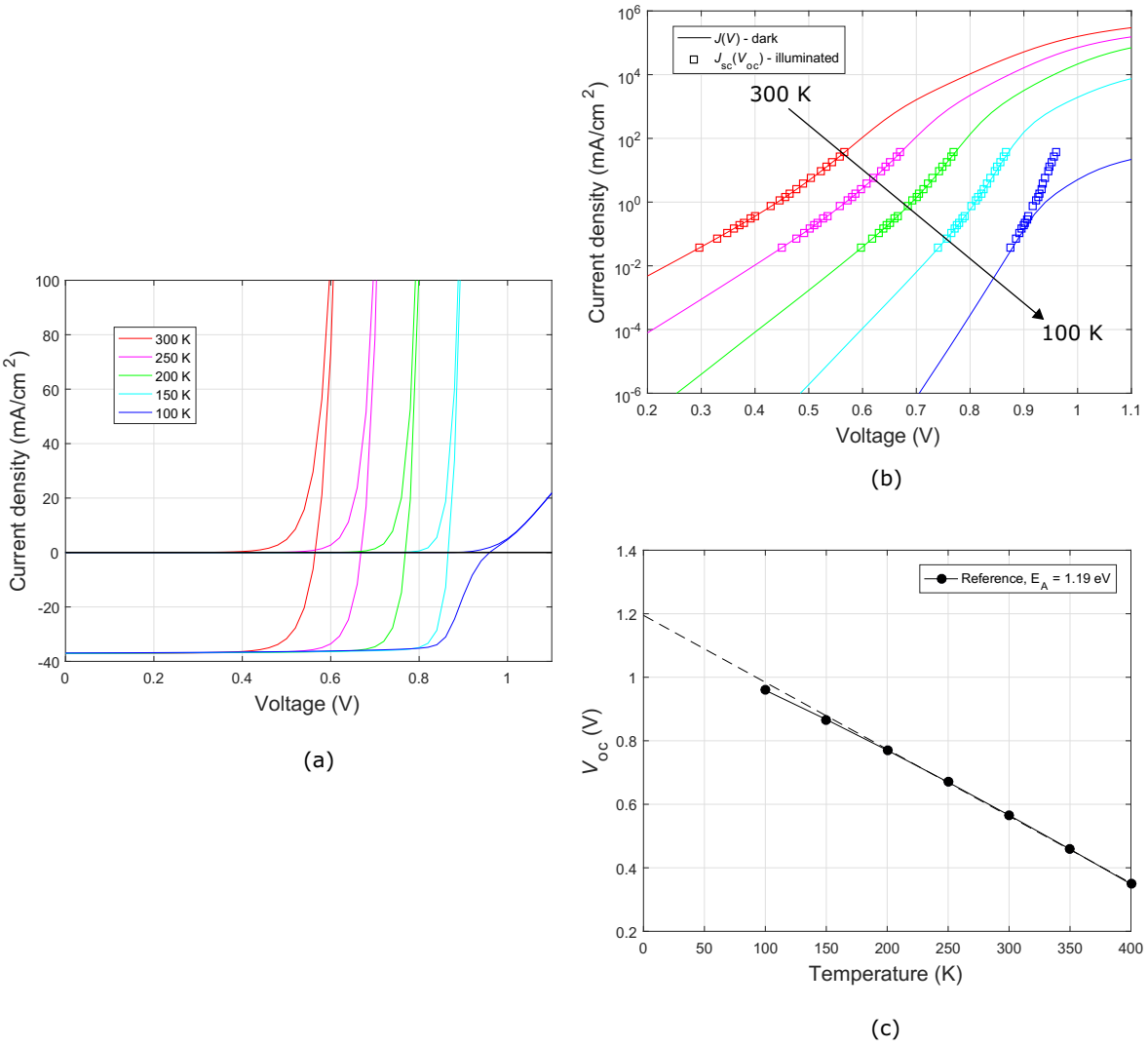

Figure 5.1.: Simulation of the reference device: (a) $J-V$ curves in linear scale, (b) $J-V$ characteristics in semi-logarithmic scale from $T = 300$ K to $T = 100$ K where the square symbols represent the $J_{\mathrm{sc}}(V_{oc})$ data points for intensities of 100 mW/cm^2 - 0.1 mW/cm^2, and (c) $V_{oc}(T)$ plot including the V_{oc} extrapolation to $T = 0$ K (dashed line).

Table 5.1.: STC parameters of the reference CIGSe numerical model for different doping densities and carrier lifetimes within the absorber.

$N_{\mathrm{A,CIGSe}}$ (cm^{-3})	τ (ns)	J_{sc} ($\mathrm{mA/cm}^2$)	V_{oc} (mV)	FF (%)	η (%)
2.5×10^{15}	20	37.1	565	77.4	16.2
	100	37.3	609	80.6	18.3
	200	37.3	628	81.3	19.1
6×10^{15}	20	36.7	588	78.0	16.9
	100	37.2	630	81.3	19.1
	200	37.3	648	82.1	19.9
1×10^{16}	20	36.5	601	78.3	17.2
	100	37.2	643	81.6	19.5
	200	37.3	661	82.4	20.3

Table 5.1 lists the STC parameters of the reference CIGSe model for different doping densities and carrier lifetimes within the absorber. The reference parameter set results in low open-circuit voltage due to a low doping density and carrier lifetime within the absorber ($N_{\mathrm{A,CIGSe}} = 2.5\times10^{15}$ cm^{-3} and $\tau = 20$ ns), considering that real CIGSe devices show a $V_{oc} \approx$ 635-640 meV without any absorber treatment. It is clear that higher doping densities and/or carrier lifetimes would lead to an increased V_{oc} and efficiencies as seen in Table 5.1. However, improving the carrier lifetime may also result in an increased effect of the recombination outside the SCR, i.e., recombination in the QNR that departs from the traditional analytical models presented in Chapter 2 where the dominant recombination is assumed to take place in the SCR. The chosen reference parameters also ensure good convergence of the numerical algorithm at low temperatures, and because the study of $J-V$ behaviors at low temperatures is an important task in this work, low material parameters were kept in the model for the following sections if not mentioned otherwise.

The calculations of the recombination rate displayed in Figure 5.2 show that the dominance of the total recombination within the SCR of the absorber is only valid for a certain voltage range, especially at low voltage, e.g., $V = 0.3$ V. When the voltage increases further and around V_{oc}, the recombination begins to also take place in the QNR of the absorber as shown for $V = 0.6$ V. A band gap grading in the absorber suppresses the recombination in the QNR (see Apendix A.17) and the recombination in the SCR stays dominant for larger bias voltages since a wider band gap outside the SCR will cause lower recombination rate in this region.

From this, especial attention needs to be paid to the estimation of the diode factors of the simulated dark $J-V$ curves and the $J_{\mathrm{sc}}(V_{oc})$ data points since two types of recombination mechanisms may be present when fitting the corresponding SCAPS $J-V$ curves. Fits by using the two-diode model and the method used for the experimental

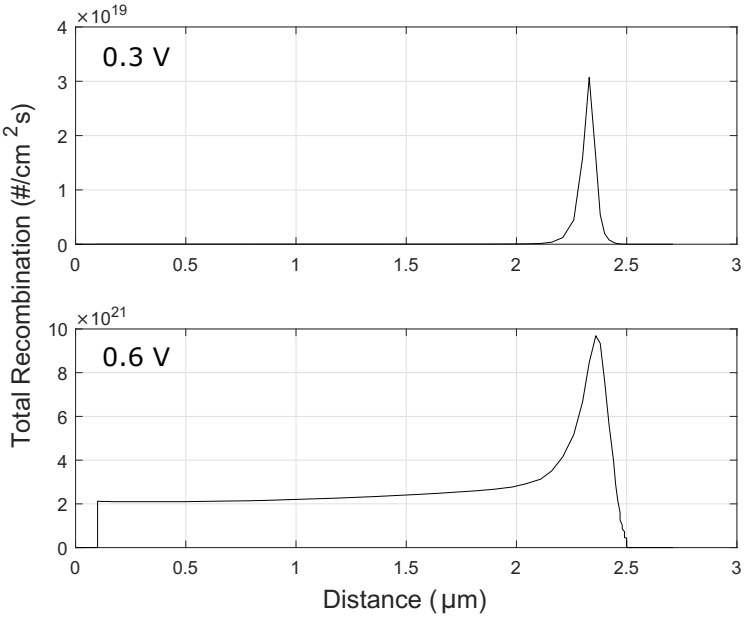

Figure 5.2.: Total recombination rate of the reference CIGSe model.

curves described in Section 3.2 at different temperatures determine the diode factors which are given in Table 5.2. Likewise, the diode factors of the experimental JVT characteristics already given in Chapter 4 were estimated using the two-diode model. As described in Section 2.2, the second diode of the equation with very high values of the diode factor (parasitic diode) determines the current at low voltages. The main diode controls the current at high voltage up to where the series resistance becomes relevant. It defines the open-circuit voltage and its underlying recombination mechanism is therefore the one that needs to be deduced. SCAPS $J-V$ curves include neither the shunt nor the series resistance and the parasitic diode. Instead, the first diode of the diode equation fit returns values close to 1 while the second diode of the equation returns values close to 2, and both slightly increase as the temperature decreases for the dark $J-V$ curves.

Table 5.2.: Estimated diode factors of the simulated dark $J-V$ curves and $J_{\mathrm{sc}}(V_{oc})$ data for different temperatures of the reference CIGSe numerical model.

	Dark $J-V$		$J_{\mathrm{sc}}(V_{oc})$ data	
T(K)	A_1	A_2	A_1	A_2
300	1.09	1.90	1.05	1.86
250	1.1	1.91	1.04	1.86
200	1.14	1.93	1.03	1.82
150	1.2	1.95	1.04	1.83
100	-	-	1.0	1.84

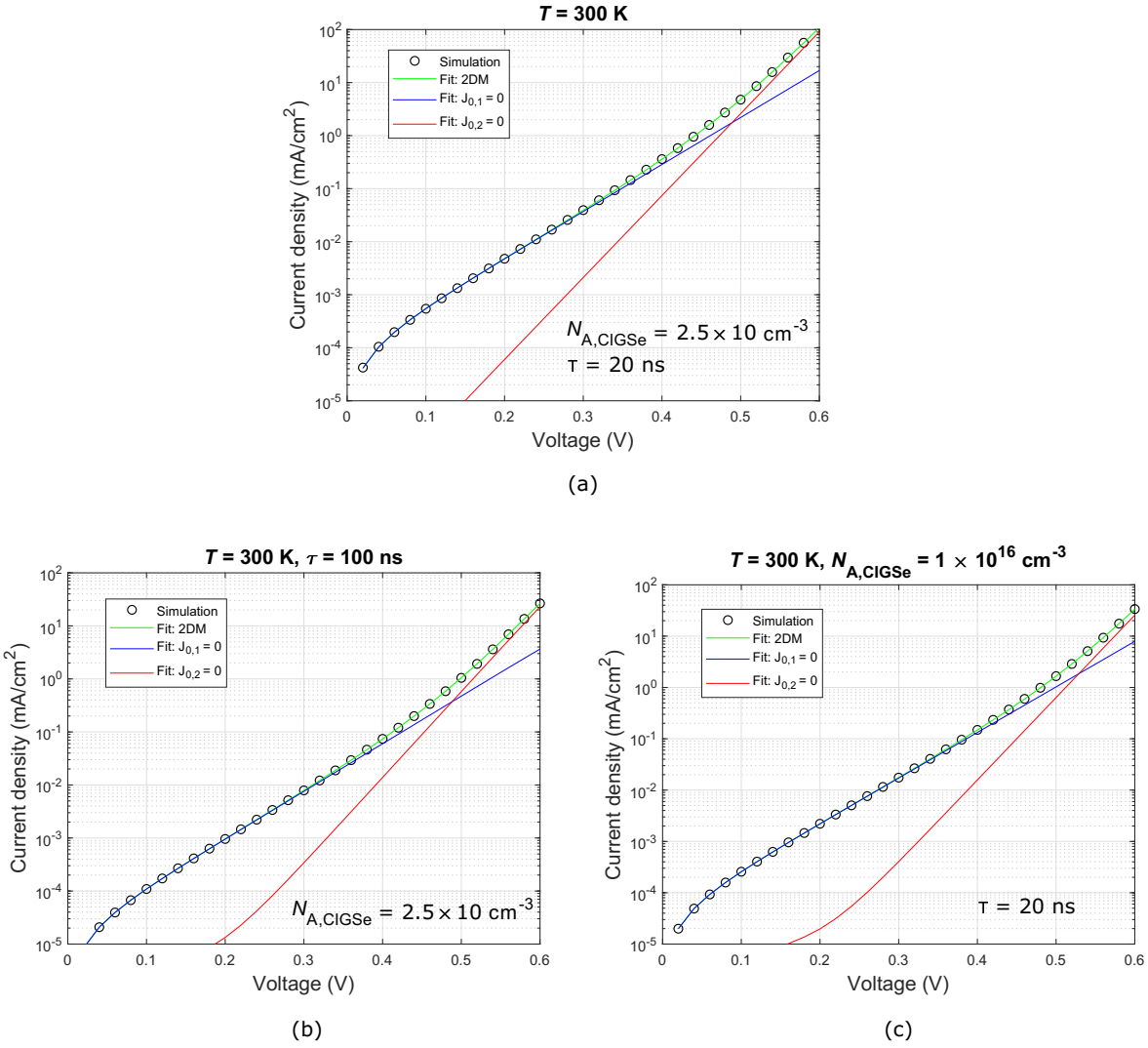

Figure 5.3.: Fits of the simulated dark $J-V$ curves at $T = 300$ K in semi-logarithmic scale, of the reference CIGSe model (a) with low doping density and carrier lifetime ($N_{\mathrm{A,CIGSe}} = 2.5{\times}10^{15}$ cm^{-3} and $\tau = 20$ ns), (b) with low doping density and high carrier lifetime ($N_{\mathrm{A,CIGSe}} = 2.5{\times}10^{15}$ cm^{-3} and $\tau = 100$ ns), and (c) with high doping density and low carrier lifetime ($N_{\mathrm{A,CIGSe}} = 1{\times}10^{16}$ cm^{-3} and $\tau = 20$ ns).

In Figure 5.3a, the simulated dark $J-V$ curve of the reference CIGSe model is fitted using the two-diode model. In order to see the contribution of the two diodes in the curve, the recombination current density of the first diode (A_1) is set to $J_{0,1} = 0$, then the curve only shows the result of the second diode of the equation (A_2). Likewise, the same procedure applies for the recombination current density of only the first diode, $J_{0,2} = 0$. The corresponding values are those listed in Table 5.2 for $T = 300$K, resulting A_2 (when $J_{0,1} = 0$) close to 2 and A_1 (when $J_{0,2} = 0$) close to 1.

It can be observed that at low bias voltages the recombination is dominant in the SCR where $A = 2$. At higher bias voltages, the curve begins to deviate from the A_2 fit

curve and the diode factor changes from 2 to 1. In this case, the injection into the bulk of the absorber is more significant and the recombination begins to take place not only in the SCR but also in the QNR, as previously observed in the plots of the total recombination in Figure 5.2. A dependency with respect to the absorber doping density is present as seen in Figure 5.3c, here the dominant recombination of the device stays longer in the SCR while for a higher carrier lifetime (Figure 5.3b) no significant change is observed.

In the following sections, the non-ideal behaviors are evaluated according to the barriers occurring at the heterointerfaces and/or the back contact of the device model.

5.1. Interface barriers

5.1.1. Conduction band offset

The electrical properties of the devices are dependent on the electronic matching of the interfaces, i.e., band line-ups. Valence and conduction band offsets are important parameters which characterize a heterojuntion. The transport properties are strongly influenced by band discontinuities, interface states, and potential barrier height. As previously described in Section 3.3.1, the conduction band offsets of the CIGSe model were chosen to be a spike between the absorber/buffer layers ($\Delta E_C = 0.10$ eV) and a cliff between the buffer/window layers ($\Delta E_C = 0.15$ eV).

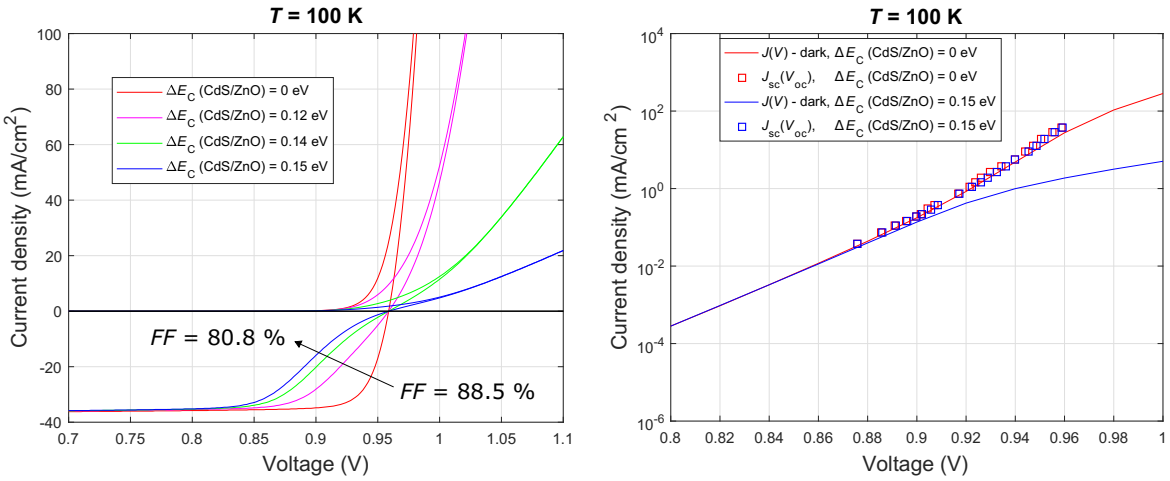

Figure 5.4.: Simulation at $T = 100$ K of: (a) $J - V$ curves for different conduction band cliffs at the buffer/window interface, and (b) $J - V$ curves in semi-logarithmic scale for $\Delta E_C = 0$ eV and $\Delta E_C = 0.15$ eV where the square symbols represent the $J_{sc}(V_{oc})$ data points for intensities of 100 mW/cm^2 - 0.1 mW/cm^2.

At the beginning of this chapter, Figure 5.1 showed the $J-V$ characteristics which resulted from the reference model. At $T = 100$ K, the $J-V$ curve already exhibited a roll-over effect and a discrepancy between the dark $J-V$ curve and the $J_{\mathrm{sc}}(V_{oc})$ data points.

Figure 5.4a shows how the $J-V$ curves at $T = 100$ K are less influenced by the blocking when reducing the cliff at the CdS/ZnO interface, accompanied by an improvement in the FF. The $J_{\mathrm{sc}}(V_{oc})$ points for the corresponding limited-current curve are positioned on the non-blocked dark curve (see Figure 5.4b).

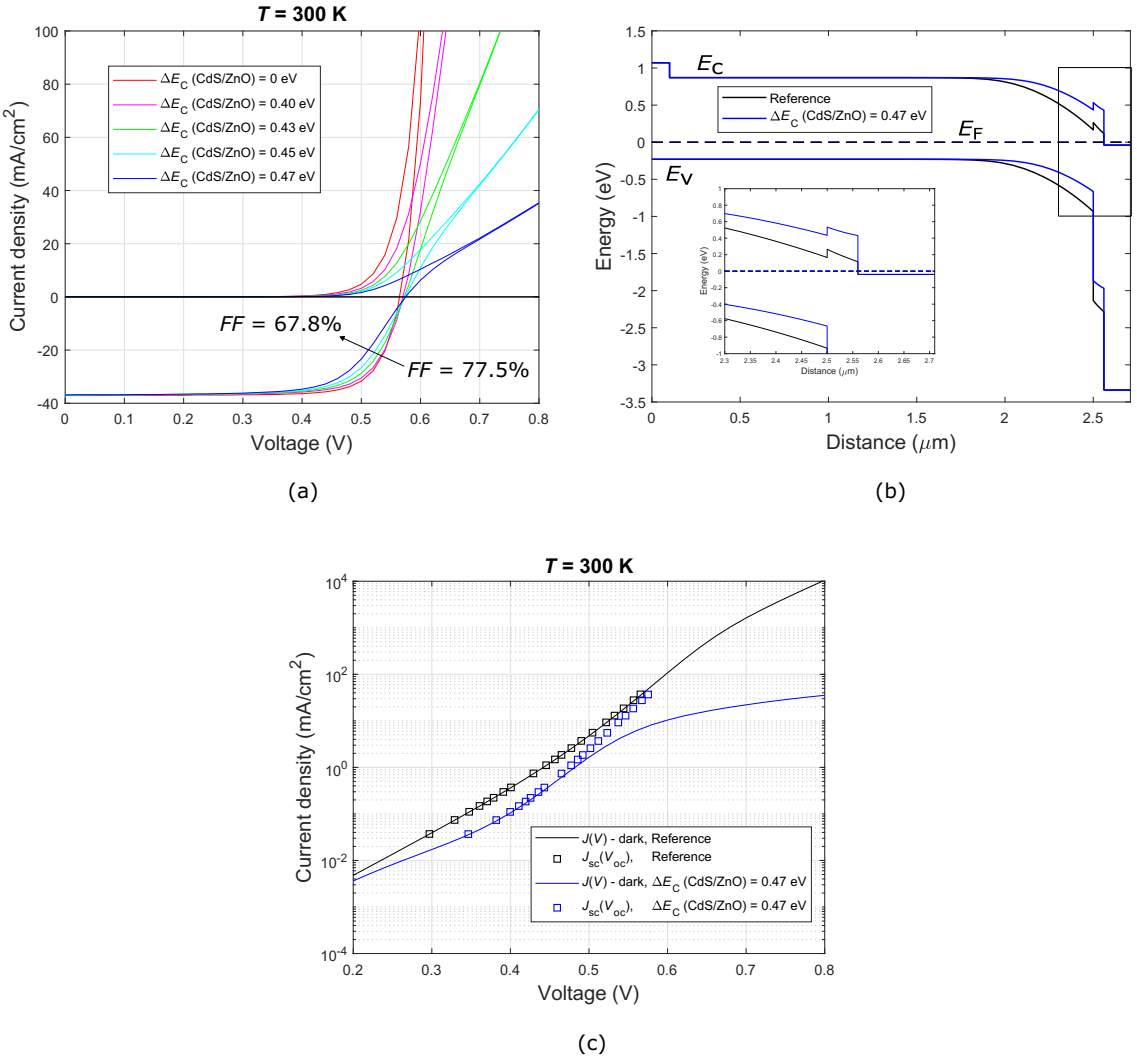

Figure 5.5.: (a) Simulated $J-V$ curves for different conduction band cliffs at the buffer-/window interface, (b) equilibrium band diagram of the reference and the model where a large cliff at the buffer/window interface has been introduced ($\Delta E_{\mathrm{C}} = 0.47$ eV), and (c) $J-V$ characteristics in semi-logarithmic scale of the models presented in the band diagrams where the square symbols represent the $J_{\mathrm{sc}}(V_{oc})$ data points for intensities of 100 mW/cm^2 - 0.1 mW/cm^2.

The roll-over effect of the diode current for conduction band offsets below 0.12 eV is not significant or is barely observed, however, the FF is still affected by the cliff. A band alignment ($\Delta E_C = 0$ eV) gets rid of the roll-over effect and also the discrepancy between the dark $J-V$ curve and the $J_{sc}(V_{oc})$ data existing with higher conduction band offsets, as seen in Figure 5.4b.

To study the current limitation of the diode current at high bias voltage and at high temperatures, larger conduction band cliffs at the CdS/ZnO interface were introduced in the model (Figure 5.5). To considerably limit the diode current, conduction band cliffs above 0.40 eV are needed to cause a roll-over and a loss in FF. In forward current, a large cliff, as seen in the equilibrium band diagram of Figure 5.5b, acts as a barrier to the flow of electrons from the window side to the absorber, i.e., the flow of electrons faces a spike, thus limiting the diode current at high bias voltages, above V_{oc} [113]. The transport of electrons over the barrier can be described by the thermionic emission theory [53, 114].
The comparison of Figures 5.4b (small cliff, low temperature) and 5.5c (large cliff, room temperature) shows a small difference as in the the latter case the bucking current at low voltage is reduced by the barrier. Consequently, the $J_{sc}(V_{oc})$ points at low intensities do not follow the non-blocked dark $J-V$. Nevertheless, they still deviate from the blocked dark $J-V$ towards the non-blocked dark $J-V$ at higher intensities. The gain in open-circuit voltage at low photocurrent densities does not necessarily imply a better solar cell because the relevant number is the voltage at the maximum power point.

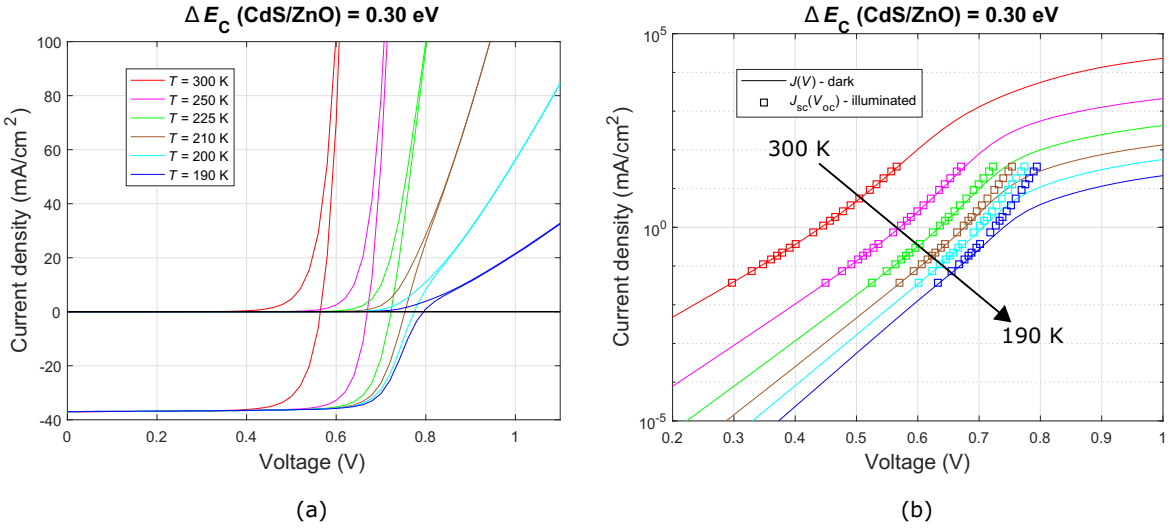

Figure 5.6.: (a) Simulated $J-V$ curves for different temperatures and constant conduction band cliff (ΔE_C(CdS/ZnO)= 0.30 eV), and (b) $J-V$ characteristics in semi-logarithmic scale when ΔE_C(CdS/ZnO)= 0.30 eV for different temperatures where the square symbols represent the $J_{sc}(V_{oc})$ data points for intensities of 100 mW/cm^2 - 0.1 mW/cm^2.

It is clear from the above that moderate cliffs do not block the current at higher temperatures but will do so at lower temperatures. To further illustrate this, we show the case where $\Delta E_C = 0.30$ eV at different temperatures in Figure 5.6, observing how the blocking of the forward diode current and the discrepancy between the $J_{sc}(V_{oc})$ points and the dark $J-V$ curves begin to take place when decreasing the temperature. The colormap in Figure 5.7b shows the PV parameters for different conduction band offsets and temperatures and the threshold region where the FF begins to decay and consequently where the roll-over begins to emerge (fading of red color) with increasing conduction band offsets and decreasing temperatures.

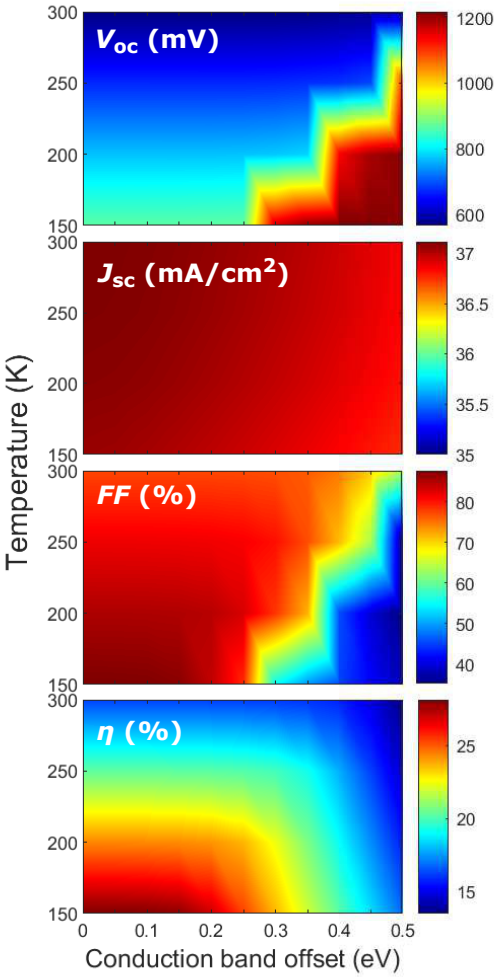

Figure 5.7.: PV parameters versus temperature and conduction band offset at the CdS/ZnO interface displayed on colormaps.

For the colormaps presented here and in subsequent sections, it should be noted that the open-circuit voltage of strongly blocked devices is somewhat arbitrary and difficult to precisely calculate because the current densities in a wide interval around V_{oc} are

extremely low so that even a small variation in current will cause a large change of the open-circuit voltage. The uncertainty in open-circuit voltage also affects the fill factor calculation.
So far, the saturation of the V_{oc} at lower temperatures seems to be an effect independent from the blocking of the diode current caused by the conduction band cliff at the CdS/ZnO interface since it was not observed for the simulations previously described.

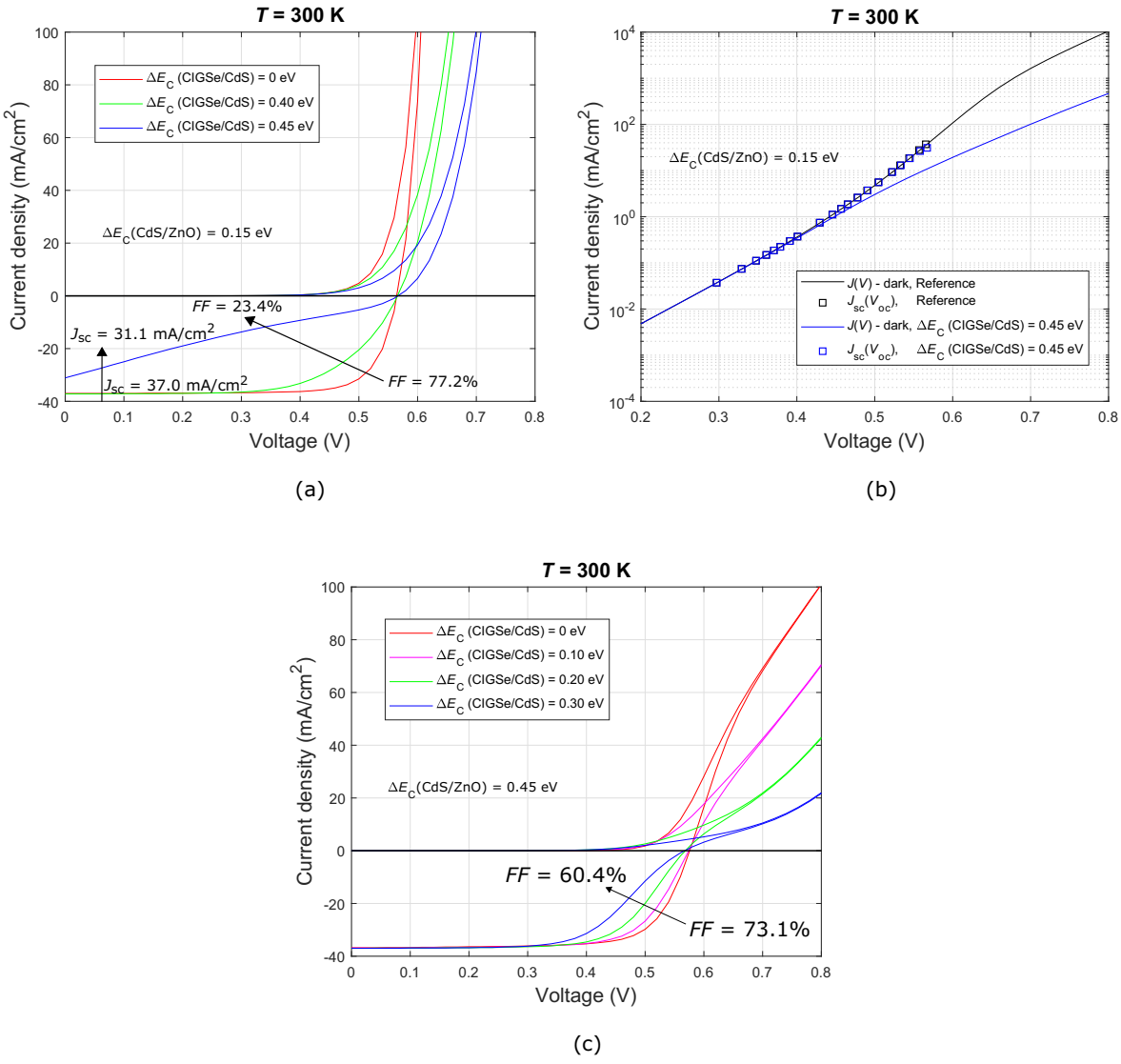

Figure 5.8.: Simulated (a) $J-V$ curves with different conduction band spikes at the absorber/buffer interface for $\Delta E_{\mathrm{C}}(\mathrm{CdS/ZnO}) = 0.15$ eV, (b) $J-V$ characteristics in semi-logarithmic scale of the reference model ($\Delta E_{\mathrm{C}}(\mathrm{CIGSe/CdS}) = 0.10$ eV) and when $\Delta E_{\mathrm{C}}(\mathrm{CIGSe/CdS}) = 0.45$ eV, where the square symbols represent the $J_{\mathrm{sc}}(V_{oc})$ data points for intensities of 100 mW/cm^2 - 0.1 mW/cm^2, and (c) $J-V$ curves with different conduction band spikes at the absorber/buffer interface for $\Delta E_{\mathrm{C}}(\mathrm{CdS/ZnO}) = 0.45$ eV.

In the case of a spike at the absorber/buffer interface (with a small cliff of $\Delta E_{\mathrm{C}}(\mathrm{CdS/ZnO})$ = 0.15 eV), only larger conduction band offsets above 0.40 eV cause a change of shape

in the $J-V$ characteristics mainly at low bias voltages, i.e., for V < Voc, with losses in the photocurrent, while the diode current remains exponential as can be observed in Figure 5.8a. A higher spike causes a reduction in the short-circuit current by creating a barrier for the transport of photo generated carriers leaving the absorber through the interface, as reported in previous studies [53, 113, 115]. The barrier should be smaller than $\Delta E_{\mathrm{C}} = 0.40$ eV to avoid losses in FF and J_{sc}. Zhang et al. [115] also reported that if the electron carrier concentration in the near-interface region of the buffer layer is increased, the J_{sc} is not affected even if a large conduction band spike is introduced. Here, the $J_{\mathrm{sc}}(V_{oc})$ data points in the semi-logarithmic plot for a large spike in Figure 5.8b are again positioned on the reference dark curve.

Figure 5.8c shows the variations of the spike at the absorber/buffer interface with a large constant cliff at the buffer/window interface ($\Delta E_{\mathrm{C}} = 0.45$ eV). As the spike increases, the kink effect is enhanced and accompanied by a loss in FF. In this combination of band offsets, the influence of the spike is noticeable earlier than in the case where only the spike is present with only a small cliff at the buffer/window interface.

5.1.2. p^+ layer at the CIGSe surface

Previous studies [116] have reported that a highly doped p^+ layer at the absorber surface may be responsible for kinks present in the $J-V$ curves. In order to analyze the possible effects caused by the introduction of a p^+ layer, Figure 5.9a shows the band diagram of the reference model including a 50 nm layer with a high acceptor (p-type) doping density at the absorber surface ($N_{\mathrm{A},p^+\ \mathrm{layer}} = 2.0{\times}10^{17}$ cm^{-3}).

It can be shown that the p^+ layer mainly affects the photocurrent collection, which can explain the loss in FF and the reduction of the J_{sc} for bias voltages below V_{oc} when high doping concentrations above 2.0×10^{17} cm^{-3} are introduced but not the blocking of the dark or bucking current, as observed in Figure 5.9b. The photocurrent collection becomes very voltage-dependent. A high p-type doping at the absorber surface will cause an approach of the E_{V} to the Fermi level and simultaneously a distancing of the E_{C} due to the constant band gap. This will cause a barrier that the electron flow needs to overcome resulting in a reduced J_{sc} due to the incomplete collection of carriers. Even when a large spike at the absorber/buffer interface also leads to a reduction of the photocurrent as seen in Section 5.1.1, the semi-logarithmic plots of these two models behave differently. A highly doped p-type layer at the surface of the CIGSe entails a gain in V_{oc} due to the shrinking of the SCR. The lower the temperature, the larger discrepancy between the $J_{\mathrm{sc}}(V_{oc})$ data and the dark $J-V$ characteristics without any diode current limitation.

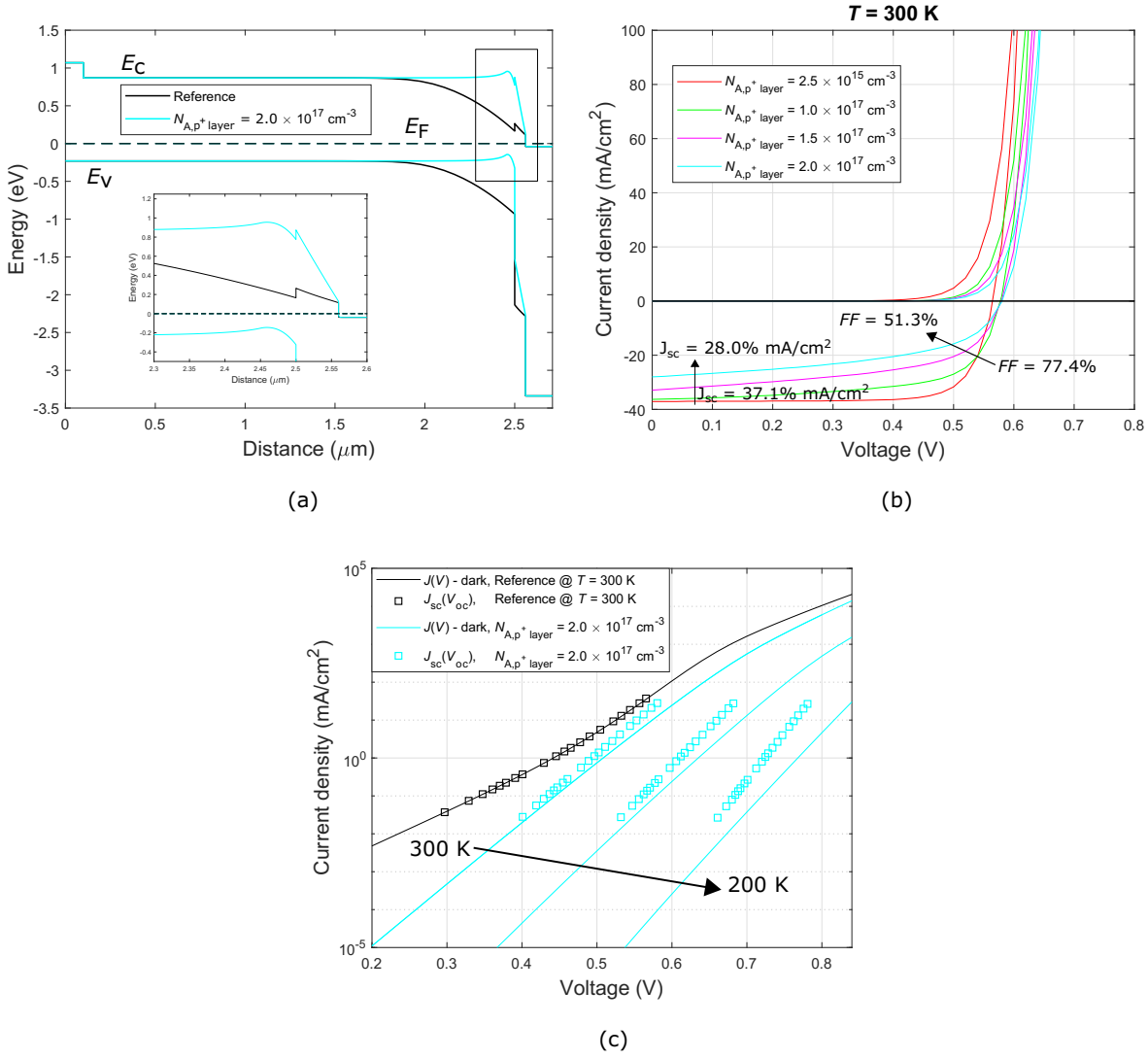

Figure 5.9.: (a) Equilibrium band diagram of the reference CIGSe model and including a highly doped p-type layer at the absorber surface, (b) simulated $J-V$ characteristics for different doping densities of the p^+ layer, and (c) $J-V$ characteristics in semi-logarithmic scale of the reference model ($T = 300$ K) and including a p^+ layer at the absorber surface for different temperatures where the square symbols represent the $J_{sc}(V_{oc})$ data points for intensities of 100 mW/cm^2 - 0.1 mW/cm^2.

5.1.3. Buried $p-n$ junction in the absorber

The influence of a buried $p-n$ junction within the CIGSe absorber has been evaluated and discussed in Reference [117]. An n-doped region near the absorber surface leads to a $p-n$ junction that is buried inside the absorber, resulting in reduced open-circuit voltage and photocurrent. This is also demonstrated in the model given in Figure 5.10.

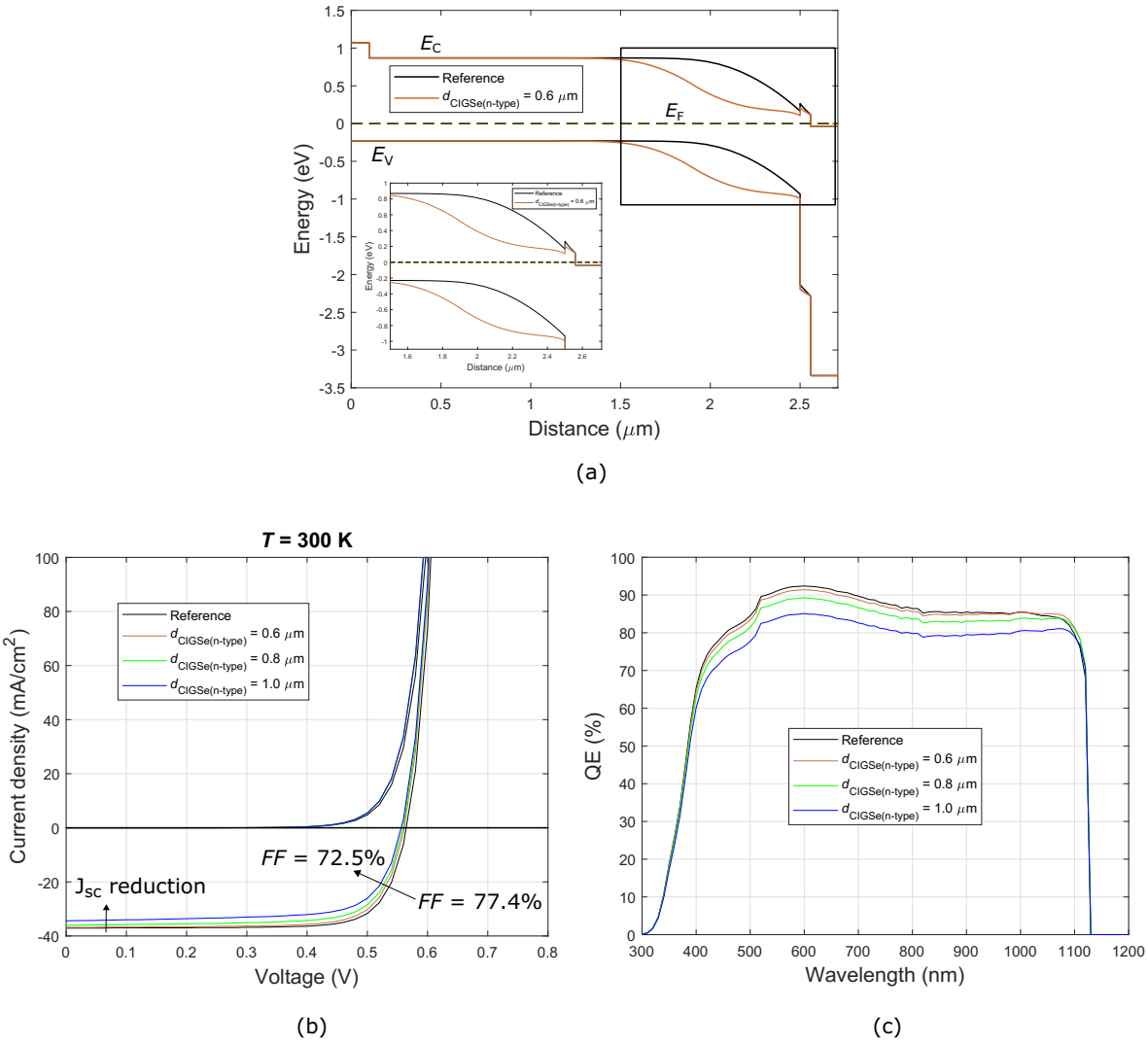

Figure 5.10.: (a) Equilibrium band diagram of the reference CIGSe model compared to a buried $p-n$ junction near the absorber surface, (b) simulated $J-V$ characteristics for different thicknesses of the n-type region of the CIGSe absorber, and (c) the quantum efficiencies for different thicknesses of the n-type region of the CIGSe absorber.

The $J-V$ characteristics for different depths of the n-type region in the absorber maintaining the same doping concentration, i.e., with $N_{\mathrm{D}} = N_{\mathrm{A}}$ are shown in Figure 5.10b with an increase in the loss of FF and J_{sc} with increasing depths, doping

concentrations and/or diffusion lengths (the latter two absorber parameters are not shown here). No non-ideal effect (kink, roll-over) is exhibited even for very large n-type region depths within the absorber.

The quantum efficiencies given in Figure 5.10c show the decrease in the blue range of the spectrum when the $p-n$ junction is shifted deeper into the absorber which causes the decrease of the J_{sc}. The band bending of the band diagram shown in Figure 5.10a is shifted more into the absorber in comparison to the band bending of the reference model. In both models the maximum recombination point is positioned within the CIGSe absorber and not directly at the interface, so a higher performance is not guaranteed for the buried $p-n$ junction. Pistor et al. also discussed the low contribution of the minority carriers in the n-type region of the absorber to the photocurrent that results in a lower blue response.

5.1.4. Doping concentrations in the window and buffer layer

Variations of the doping concentrations N_{D} will be carried out to study the possible non-idealities with respect to a standard diode induced by lower doping concentrations in the window and buffer layer.
In terms of doping, the ZnO layer in the SCAPS model represents the i-ZnO layer in the actual device where it is located between the buffer and the highly doped ZnO:Al. The doping of the i-ZnO layer depends strongly on preparation conditions such as the oxygen partial pressure [118] during sputtering. The high doping in ZnO:Al is needed to lower the total sheet resistance but is not relevant for the current transport across the junction.

Figure 5.11a shows the $J-V$ characteristics for various doping concentrations of the ZnO layer. A strong roll-over behavior for very low doping densities is notable accompanied by an important loss in FF. However, the formation of the kink effect due to the ZnO doping emerges only when the conduction band cliff at the CdS/ZnO interface is considerable, e.g., when $\Delta E_{\mathrm{C}} = 0.40$ eV in the given example. The band diagram for $N_{\mathrm{D,ZnO}} = 5.0 \times 10^{17}$ cm^{-3} can be seen in Figure 5.11b. For this case, the semi-logarithmic plot shows the discrepancy of the $J_{\mathrm{sc}}(V_{oc})$ points with respect to the dark curve at high illumination intensities usually exhibited in the presence of a barrier blocking of the diode current.

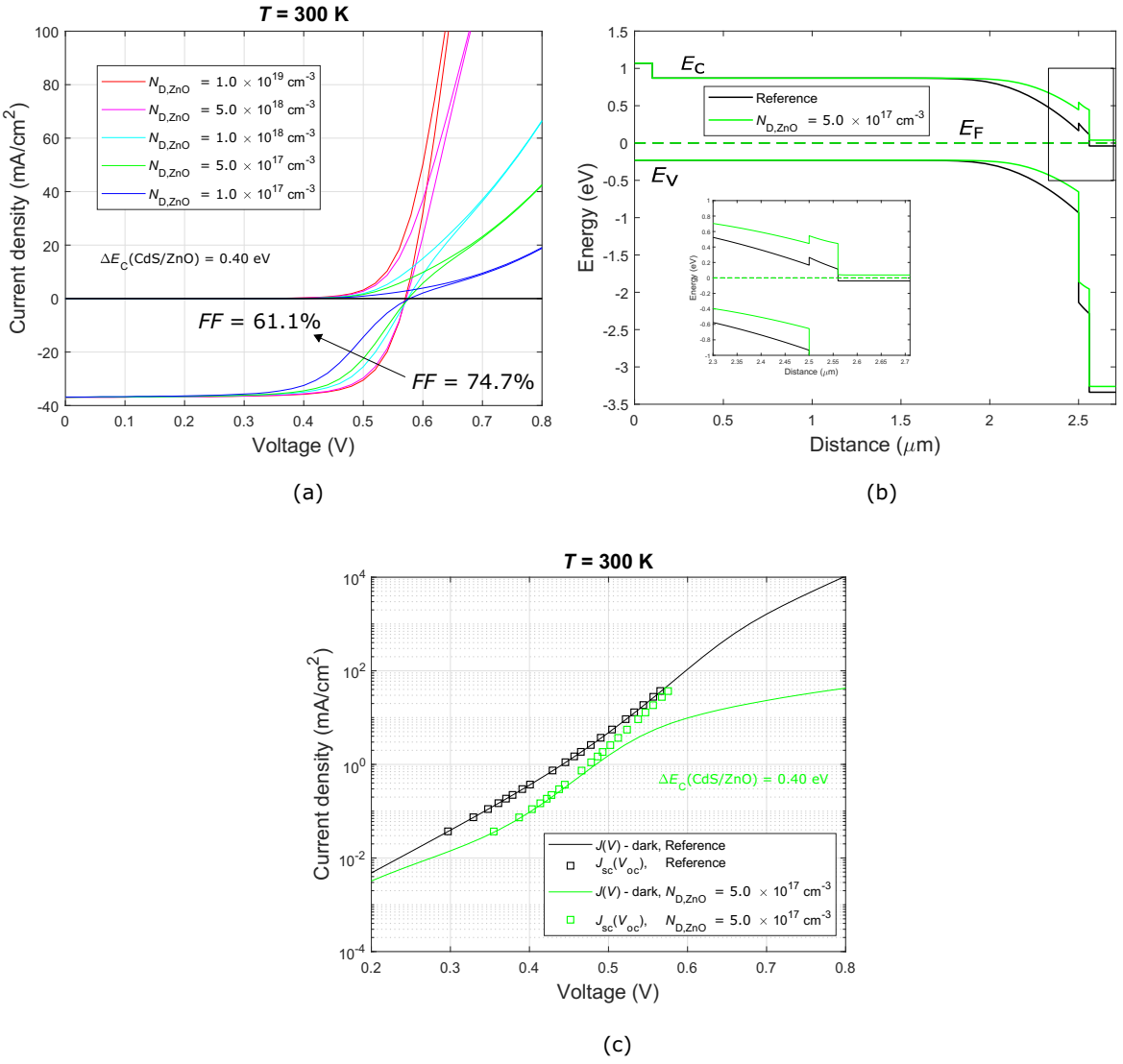

Figure 5.11.: (a) Simulated $J-V$ characteristics for various doping densities in the window layer when $\Delta E_{\mathrm{C}} = 0.40$ eV, (b) equilibrium band diagram of the reference model and the low-doped ZnO window layer model, and (c) $J-V$ characteristics in semi-logarithmic scale of the reference and low-doped ZnO curve when $\Delta E_{\mathrm{C}} = 0.40$ eV where the square symbols represent the $J_{\mathrm{sc}}(V_{oc})$ data points for intensities of 100 mW/cm^2 - 0.1 mW/cm^2.

The trend of the $J-V$ characteristics with decreasing temperature is illustrated in Figure 5.12. For a high ZnO doping (see Figure 5.12a), the roll-over emerges only when decreasing temperature, since at $T = 300$ K no blocking occurs. For a lower ZnO doping (see Figure5.12b), the roll-over arises earlier and more expressed, even at room temperature.

Lowering the doping concentration in the CdS buffer layer alone does not have any influence on the non-idealities or the PV parameters for the reference model. Nevertheless, a low-doped CdS layer enhances the barrier effects for larger conduction band offsets and lower ZnO doping densities (Figure 5.12).

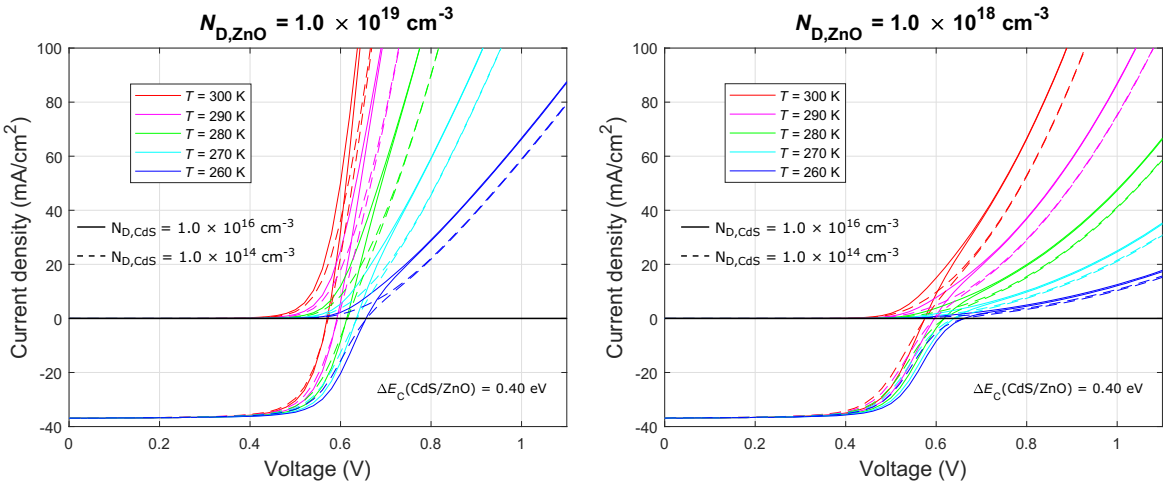

Figure 5.12.: Simulated $J-V$ characteristics for different temperatures when $\Delta E_{\mathrm{C}}(\mathrm{CdS/ZnO}) = 0.40$ eV with high CdS doping (solid lines) and low CdS doping (dashed lines) for (a) $N_{\mathrm{D,ZnO}} = 1.0 \times 10^{19}$ cm^{-3}, and (b) $N_{\mathrm{D,ZnO}} = 1.0 \times 10^{18}$ cm^{-3}.

The colormap in Figure 5.13a shows the threshold region where the FF begins to decay with increasing band offset and decreasing ZnO doping. As an example in semi-logarithmic scale, the model with a low-doped ZnO layer of $N_{\mathrm{D,ZnO}} = 1.0 \times 10^{18}$ cm^{-3} when $\Delta E_{\mathrm{C}}(\mathrm{CdS/ZnO}) = 0.40$ eV is shown in Figure 5.13b for different temperatures. The arrow indicates the area where these parameters are located in the colormap. The discrepancy between the $J_{\mathrm{sc}}(V_{oc})$ points and the dark $J-V$ curve is present when $T = 300$ K and becomes more noticeable as the temperature decreases.

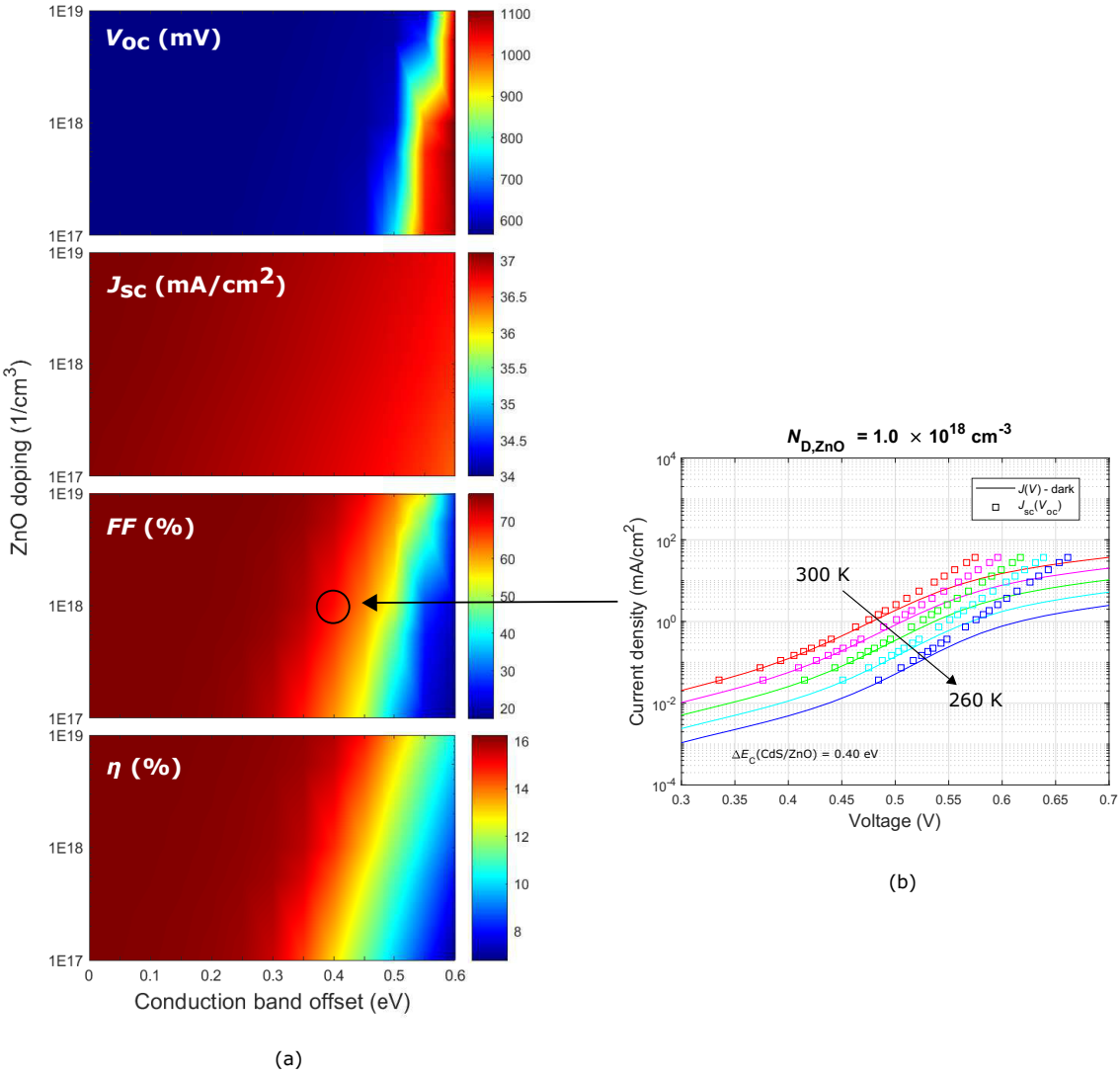

Figure 5.13.: (a) Calculated PV parameters versus ZnO doping and conduction band offset at the CdS/ZnO interface displayed on colormaps, and (b) $J-V$ characteristics in semi-logarithmic scale of the model with a low-doped ZnO ($N_{\mathrm{D,ZnO}} = 1.0 \times 10^{18}$ cm^{-3}) when $\Delta E_{\mathrm{C}} = 0.40$ eV where the square symbols represent the $J_{\mathrm{sc}}(V_{oc})$ data points for intensities of 100 mW/cm^2 - 0.1 mW/cm^2.

5.1.5. Acceptor defects at the buffer/window interface

In this section, the introduction of interface defects that could explain some of the non-idealities of the $J-V$ characteristics is studied. The presence of acceptor defects at the heterointerface in superstrate devices was discussed in reference [119]. Furthermore, Hölscher et al. [120] discussed the presence of interface defects (acceptor or donor not specified) at the heterointerface detected by admittance spectroscopy due to the impact of the air-light exposure of the bare absorbers. However, the introduction of such interface defects at the heterointerface of the absorber/buffer layers do not reproduce the non-idealities searched in this work. The presence of neutral and donor defects at the CIGSe/CdS interface only result in a reduced V_{oc} and negligible loss in FF. Acceptor defects at this heterointerface result in a more significant loss of the PV parameters, including a loss in the photocurrent. For the latter cases, the degree of loss is dependent on the doping densities and the level of energy with respect to the reference.

Thus, especial attention is focused on the incorporation of acceptor defects at the heterointerface between the CdS/ZnO layers.

The model presented in Figures 5.14b and c consists of various acceptor defects densities at the CdS/ZnO interface at the energetic position of $E_{\mathrm{def}} = 0.3$ eV and $E_{\mathrm{def}} = 0.6$ eV above the E_{V} of the buffer layer, respectively, which lead to a roll-over effect of the diode current and FF loss with increasing defect densities in the order of magnitud of $\sim 10^{12}$ cm^{-2}. At higher bias voltages and higher doping concentrations, a cross-over between the dark and light$J-V$ curves is exhibited, being more significant for deeper defects. The equilibrium band diagram of the model including acceptor defects with N_{A}(CdS/ZnO)$= 5.5 \times 10^{12}$ cm^{-2} in comparison to the reference model is given in Figure 5.14a.

Some other non-ideal effects are exhibited and presented in Figure 5.15. The discrepancy between the $J_{\mathrm{sc}}(V_{oc})$ data and the blocked dark $J-V$ curve occur at high intensities as seen in the semi-logarithmic plot with a slight V_{oc} gain (Figure 5.15a). Here, the SCAPS evaluation of the V_{oc} with respect to the temperature was possible, then obtaining a saturation of the V_{oc} at low temperatures and an activation energy approximately equal to the one obtained from the reference model (see Figure 5.15b).

Figure 5.16 illustrates the linear and the semi-logarithmic plot for different temperatures. Simulations were performed for lower defect densities and as can be seen such low densities do not caused a roll-over or cross-over at high temperatures but are sufficient to cause a blocking of the diode current, a cross-over between dark and light curves and a discrepancy of the $J_{\mathrm{sc}}(V_{oc})$ data points when decreasing the temperature.

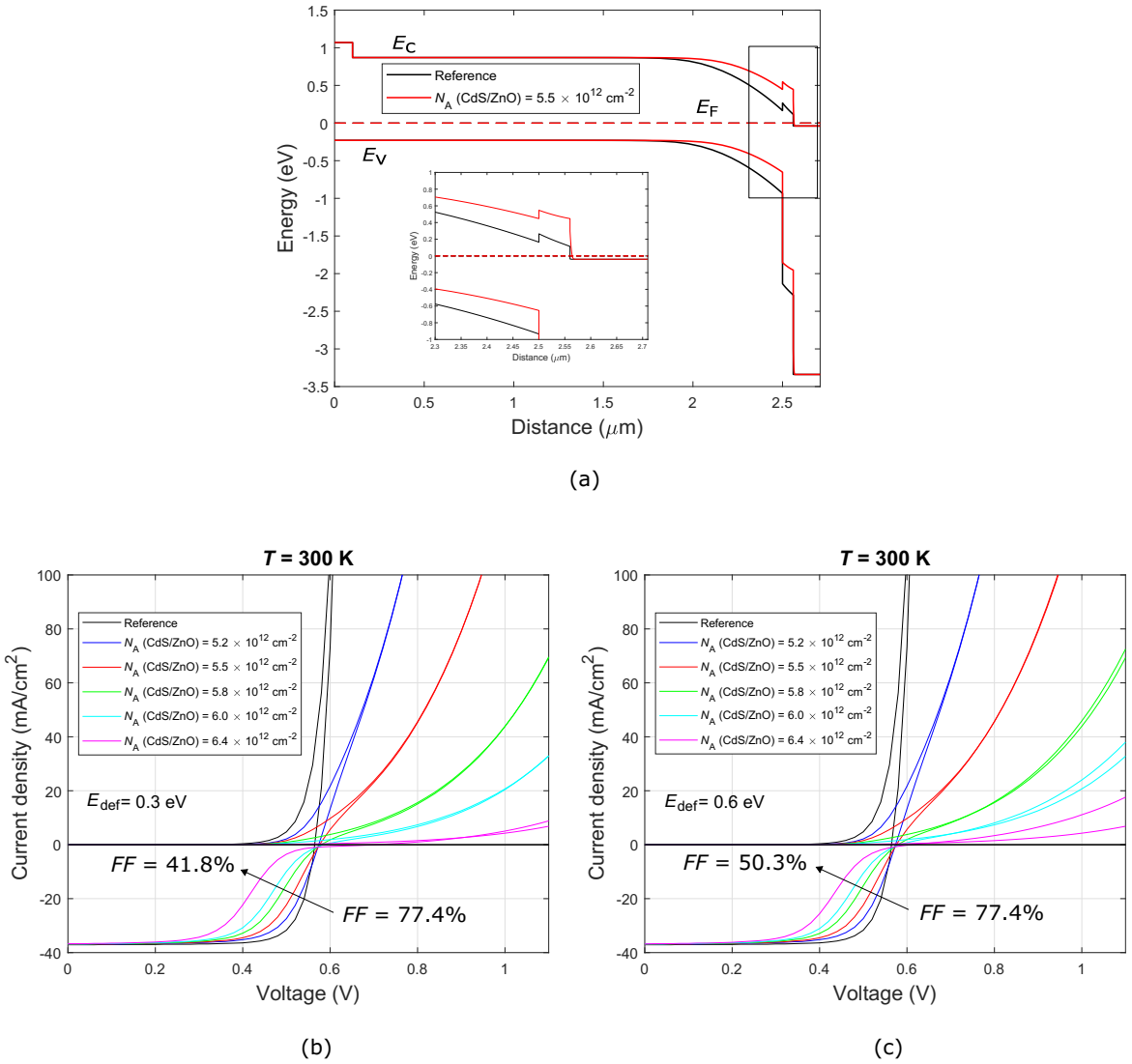

Figure 5.14.: (a) Equilibrium band diagram of the reference and the model including acceptor defects with $N_{\mathrm{A}}(\mathrm{CdS/ZnO})= 5.5 \times 10^{12}$ cm^{-2}, and (b)-(c) simulated $J-V$ characteristics for different acceptor defect densities at the buffer/window interface, for $E_{\mathrm{def}} = 0.3$ eV and $E_{\mathrm{def}} = 0.6$ eV, respectively.

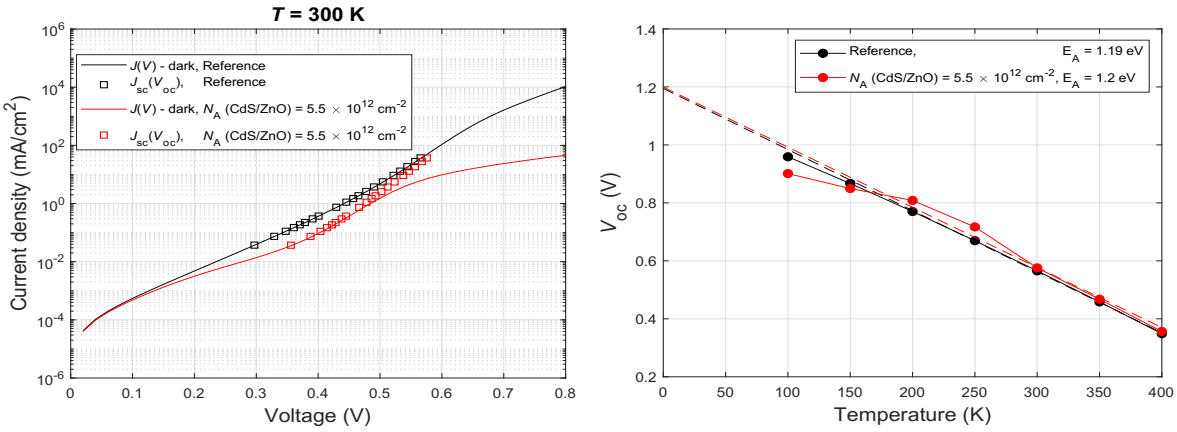

(a) (b)

Figure 5.15.: Simulation of the reference model and the model including acceptor defects with $N_{\mathrm{A}}(\mathrm{CdS/ZnO})= 5.5 \times 10^{12}$ cm^{-2}: (a) $J-V$ characteristics in semi-logarithmic scale where the square symbols represent the $J_{\mathrm{sc}}(V_{oc})$ data points for intensities of 100 mW/cm^2 - 0.1 mW/cm^2, and (b) the $V_{oc}(T)$ plot including the V_{oc} extrapolation to $T = 0$ K (dashed lines).

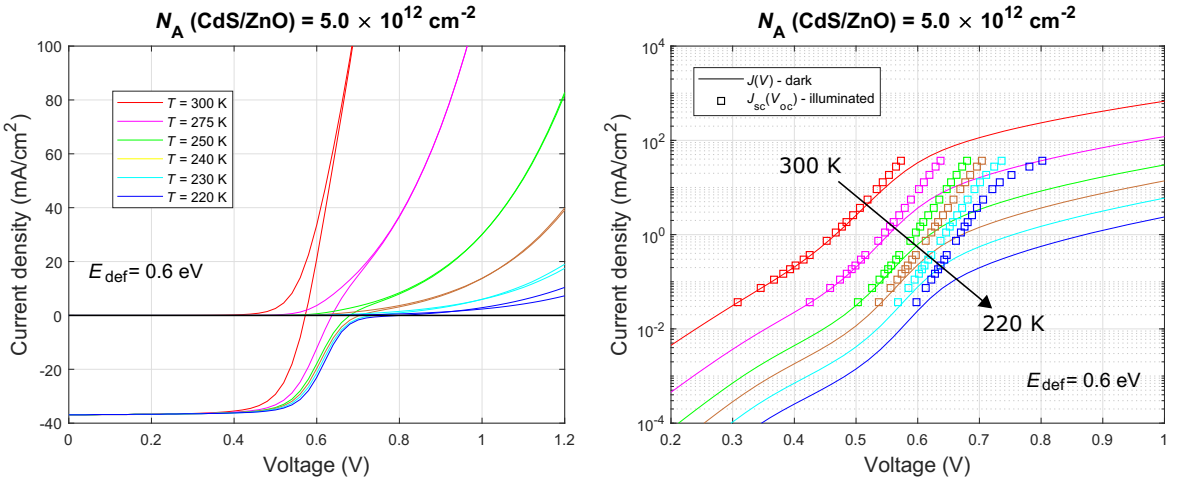

(a) (b)

Figure 5.16.: Simulations of the $J-V$ characteristics for different temperatures when $N_{\mathrm{A}}(\mathrm{CdS/ZnO})= 5.0 \times 10^{12}$ cm^{-2} in (a) linear scale, and (b) semi-logarithmic scale where the square symbols represent the $J_{\mathrm{sc}}(V_{oc})$ data points for intensities of 100 mW/cm^2 - 0.1 mW/cm^2.

5.2. Back contact barrier

As the emphasis in Section 5.1 was on understanding transport across the heterojuntion, the models presented assumed and were restricted to ideal back contact properties. However, such a back contact barrier may be needed to completely reproduce measured $J-V$ curves in numerical calculations. In numerous publications there are indications that a barrier at the back contact at least contributes to the limitation of the current transport in actual devices [95, 121–124].

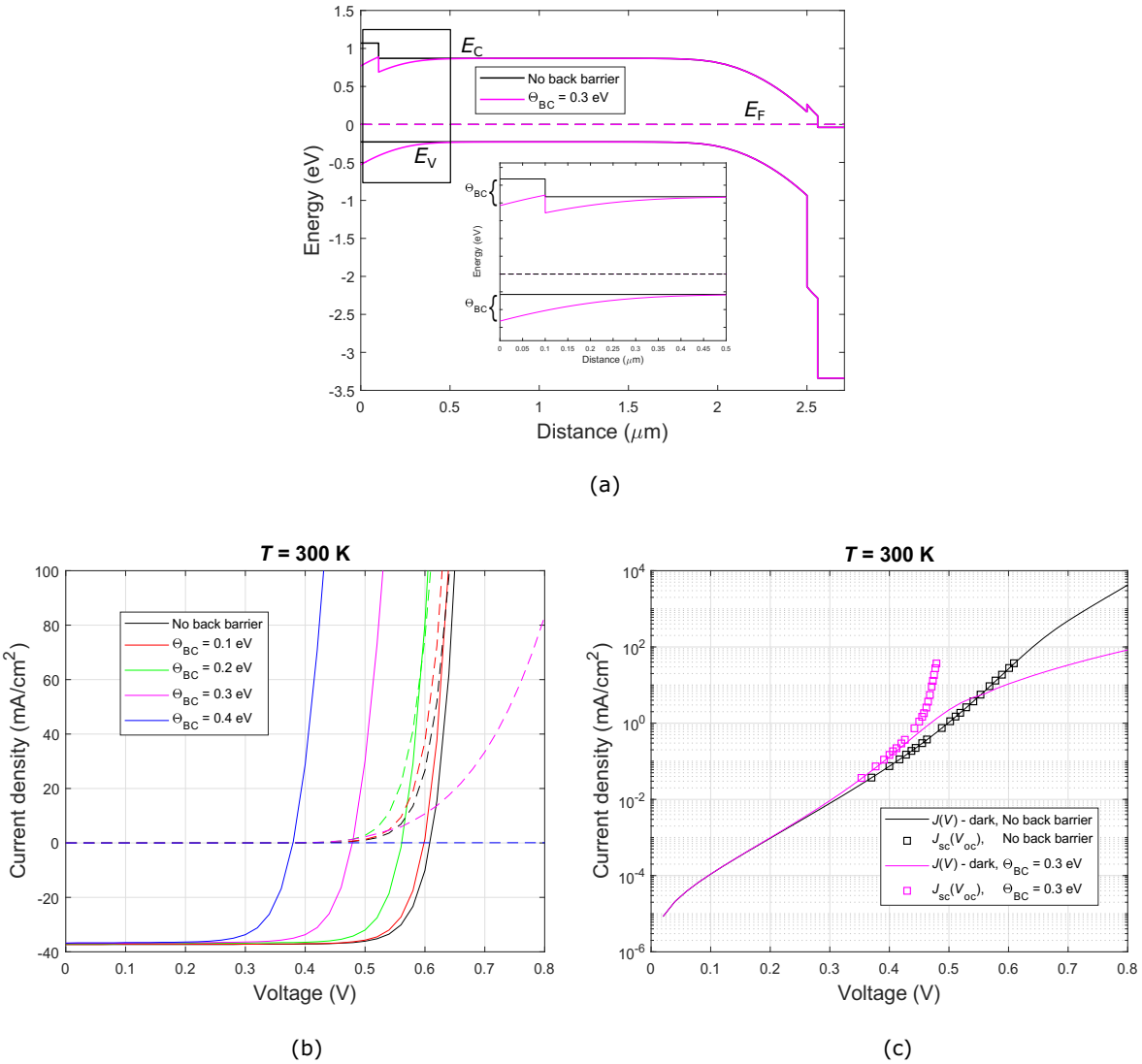

Figure 5.17.: (a) Equilibrium band diagram of the reference model and the model including a back contact barrier, (b) $J-V$ characteristics for varied back barrier heights, and (c) $J-V$ characteristics in semi-logarithmic scale of the model without back barrier and the model including a barrier height of 0.3 eV where the square symbols represent the $J_{\mathrm{sc}}(V_{oc})$ data points for intensities of 100 mW/cm^2 - 0.1 mW/cm^2.

The model presented in this section keeps the material and device parameters given in Table 3.1 but introduces a back barrier as seen in the band diagram in Figure 5.17a. For convergence purposes, a higher carrier lifetime/longer diffusion length in the CIGSe absorber was set in the model with neutral mid-gap defects of $N_{\mathrm{def}} = 1 \times 10^{15}$ cm^{-3}.

The corresponding $J - V$ curves for a varied back contact barrier height (Θ_{BC}) are shown in Figure 5.17b in comparison to the curve without any back barrier. The blocking of the diode current is more expressed as the back barrier height increases for the dark $J - V$ curves with the curve completely lying on the x-axis when $\Theta_{\mathrm{BC}} = 0.4$ eV. The light characteristics are not affected by the back barrier since they follow an exponential diode current behavior for any barrier height. The calculations show a significant V_{oc} reduction when the back barrier is introduced as well as a cross-over between the dark and the illuminated characteristics. The semi-logarithmic plot of the back barrier model exhibits an expressed discrepancy of the $J_{\mathrm{sc}}(V_{oc})$ data points with respect to the dark $J - V$ curve with the points deviating to the left of the dark blocked curve as can be observed in Figure 5.17c.

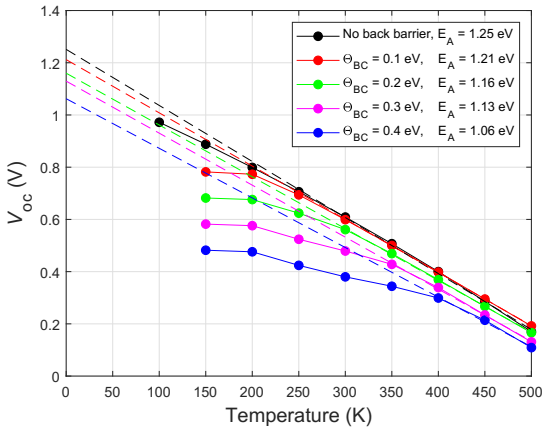

Figure 5.18.: $V_{oc}(T)$ plot including the V_{oc} extrapolation to $T = 0$ K (dashed lines) for different back barrier heights.

The V_{oc} extrapolations to $T = 0$ K for the varied back barrier heights are given in Figure 5.18. Besides the reduced open-circuit voltage as a consequence of the introduced back barrier, the latter also leads to a reduced value of the apparent activation energy as deduced from the extrapolation of the V_{oc} to $T = 0$ K. At lower temperatures, a saturation of the V_{oc} becomes more significant and it shows earlier for larger barrier heights.

Material parameters of the CIGSe absorber such as the thickness d, doping density N_{A}, and neutral mid-gap defects N_{def} (determining the diffusion lengths L_n, a concept used hereafter for behavior descriptions) together with the back barrier height Θ_{BC} lead to differences in the recombination and/or the transport mechanisms, and therefore

the resulting PV parameters. The corresponding STC parameters by varying such aforementioned settings in the model illustrated in the band diagram of Figure 5.17a can be found in Appendix A.7, Figure A.19. In order to purely describe and observe the back barrier effects, such variations were performed in the model without an electron mirror, also known as back surface field (BSF), at the back side and are given in Figure 5.19.

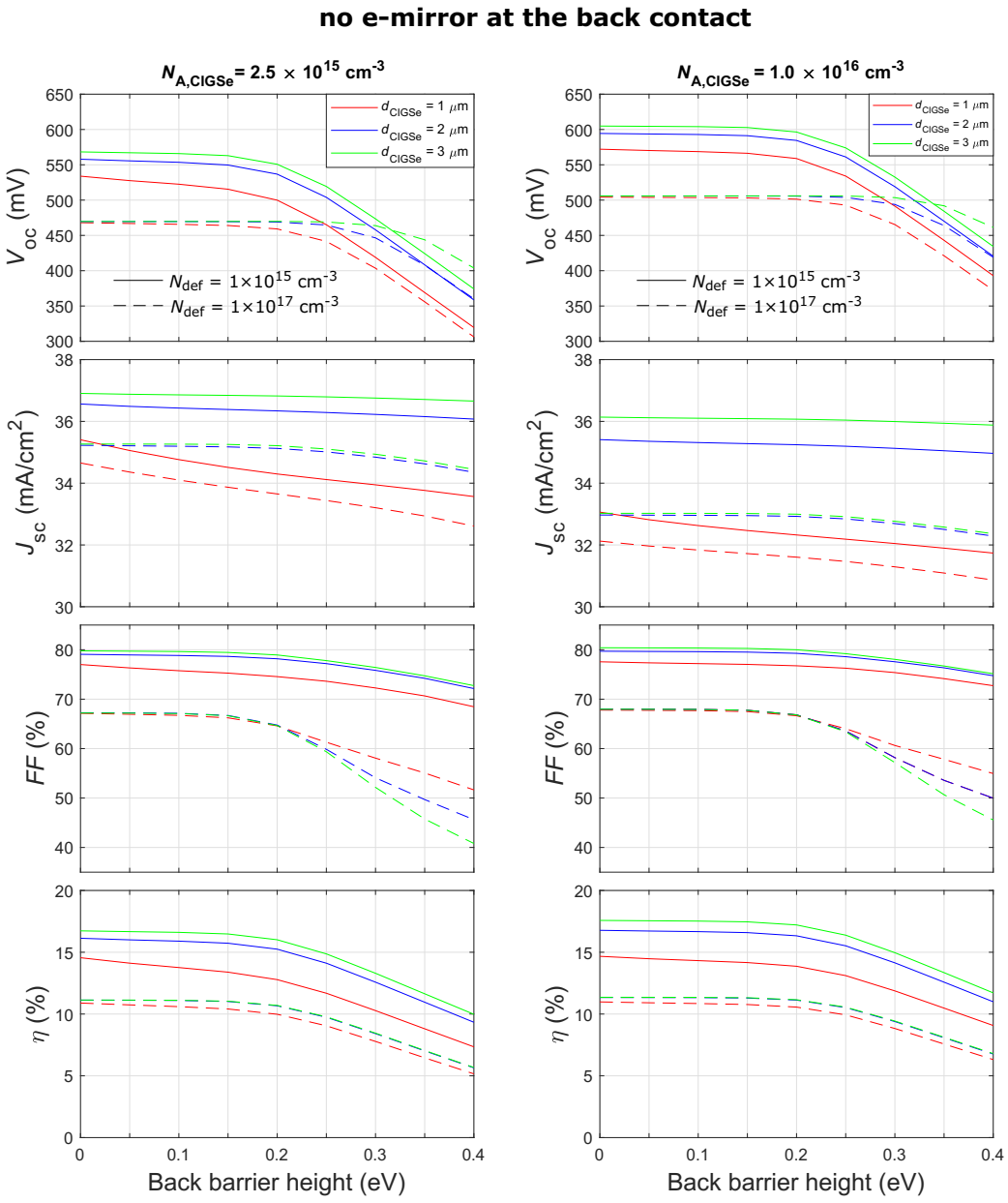

Figure 5.19.: PV parameters as a function of the back barrier height Θ_{BC}, absorber thickness d_{CIGSe}, doping density $N_{\mathrm{A,CIGSe}}$, and neutral mid-gap defect density N_{def} in the absorber of the model without an electron mirror (back surface field) at the back contact.

Without a back barrier ($\Theta_{\mathrm{BC}} = 0$ eV), V_{oc} and FF increase for longer diffusion lengths (low neutral defect density, $N_{\mathrm{def}} = 1 \times 10^{15}$ cm^{-3}) and thicker absorbers while for shorter diffusion lengths (high neutral defect density, $N_{\mathrm{def}} = 1 \times 10^{17}$ cm^{-3}) is independent of the absorber thickness. Moreover, interface recombination emerges as the dominant recombination for longer diffusion lengths (from the SCAPS recombination profiles not shown here) as a consequence of the absence of an electron mirror at the back side.

With the introduction of a back barrier, e.g., $\Theta_{\mathrm{BC}} = 0.3$ eV, the high loss in V_{oc} for shorter diffusion lengths without any back barrier is reduced but still with a slight V_{oc} decrease for shorter diffusion lengths and thinner absorbers. However when $\Theta_{\mathrm{BC}} > 0.3$ eV, a different behavior results for thicker absorbers ($d_{\mathrm{CIGSe}} > 2$ μm) with higher V_{oc} for shorter diffusion lengths. Also for large back barrier heights, FF decreases for shorter diffusion lengths and thicker absorbers while for longer diffusion lengths a gain results for thicker absorbers. Besides, interface recombination stays dominant for longer diffusion lengths with the introduction of a back barrier.

In comparison to the model with an electron mirror (see Appendix A.7, Figure A.19), here the open-circuit voltage stays constant for larger back barrier heights ($\Theta_{\mathrm{BC}} \leq 0.2$ eV) in the case when $N_{\mathrm{def}} = 1 \times 10^{15}$ cm^{-3}. Conversely, an earlier reduction of the V_{oc} occurs for shorter diffusion lengths without an electron mirror, 0.5 eV of barrier height below the model with an electron mirror. A higher change in FF occurs for shorter diffusion lengths when larger barrier heights are introduced ($\Theta_{\mathrm{BC}} > 0.25$ eV).

In addition to all the above, the same trend is observed for higher doping densities but leading to higher open-circuit voltages over all.

To illustrate the $J - V$ characteristics under different absorber and back barrier parameters as described in the plots above, Figure 5.20 shows the behavior of the light and dark $J - V$ curves by varying the back barrier height Θ_{BC}, the absorber thickness d_{CIGSe}, and neutral mid-gap defect density N_{def}. It should be mentioned that for convergence purposes, the simulated characteristics shown in the following figures are taken from the model without an electron mirror at the back side of the absorber, nonetheless the $J-V$ behavior of both models are alike. For high carrier lifetimes/long diffusion lengths (with $N_{\mathrm{def}} = 1 \times 10^{15}$ cm^{-3}) the roll-over in the dark curve begins to occur as the back barrier increases (above $\Theta_{\mathrm{BC}} = 0.25$ eV) and becomes slightly more significant for thicker absorbers. However, the light curves do not experience any blocking of the diode current as already seen in Figure 5.17b. For low carrier lifetimes/short diffusion lengths (with $N_{\mathrm{def}} = 1 \times 10^{17}$ cm^{-3}), conversely, the blocking of the diode current occurs earlier in both light and dark curves and enhanced to a greater extent for higher back barrier heights and thicker absorbers.

A visible cross-over between the dark and light curves takes place with the presence of a back contact barrier, and in terms of diffusion lengths L_n, a greater loss in FF and V_{oc} for shorter diffusion lengths.

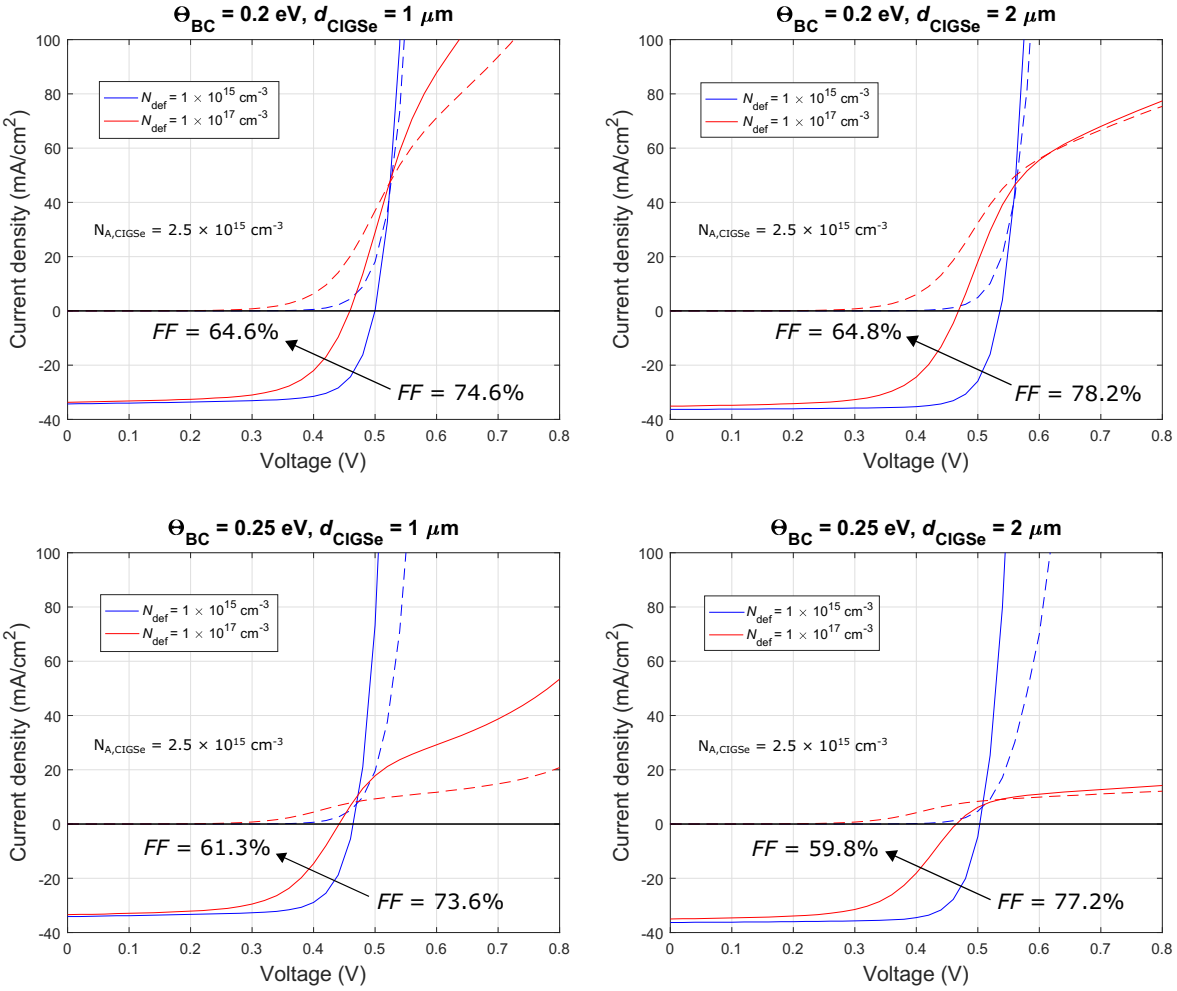

Figure 5.20.: Simulated $J-V$ characteristics of the model (without an e-mirror and low doping density in the absorber) including a back contact barrier with variations in the back barrier height Θ_{BC}, absorber thickness d_{CIGSe}, and neutral mid-gap defect density N_{def} in the absorber.

In order to investigate the effects of the back surface recombination velocity in CIGSe solar cells together with a back contact barrier, Figure 5.21 illustrates the $J-V$ characteristics obtained for variations of the surface recombination velocity S, absorber thickness d_{CIGSe}, and doping density $N_{\mathrm{A,CIGSe}}$ with a constant back barrier height of $\Theta_{\mathrm{BC}} = 0.2$ eV and a neutral mid-gap defect density of $N_{\mathrm{def}} = 1 \times 10^{17}$ cm^{-3}. It can be seen that lower recombination velocities lead to a stronger blocking effect of the diode current and is enhanced for thicker absorbers. With a higher doping density and a high recombination velocity ($S = 1 \times 10^{7}$ cm/s) the $J-V$ curves are no longer blocked, however as the recombination velocity decreases the roll-over develops once again.

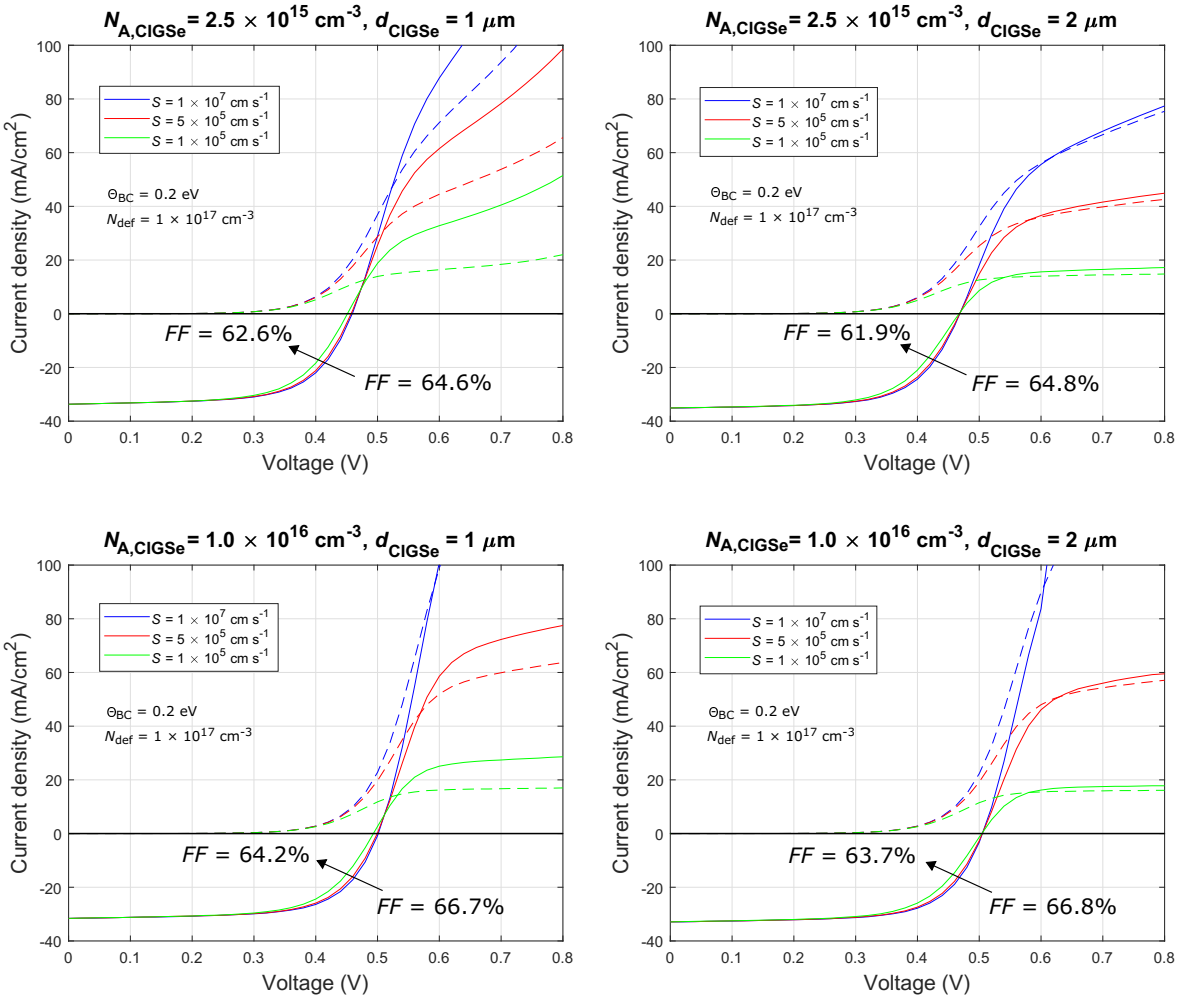

Figure 5.21.: Simulated $J-V$ characteristics of the model (without an e-mirror and short diffusion length) including a back contact barrier of $\Theta_{\mathrm{BC}} = 0.2$ eV with variations in the absorber doping density $N_{\mathrm{A,CIGSe}}$, thickness d_{CIGSe}, and surface recombination velocity S at the back contact.

The cross-over effect is reduced when increasing the thickness of the absorber as also seen in the resulting $J-V$ curves of Figure 5.20 for a shorter diffusion length.
The V_{oc} is not affected and the FF slightly deteriorates by decreasing the recombination velocity.
As previously observed for long carrier diffusion lengths, the dark $J-V$ curves are the only ones affected by the decrease of the back surface recombination velocity (see Apendix A.7, Figure A.20).

Since the evaluation of the JVT characteristics is one of the main tasks in this work to study such non-ideal effects, simulations of the temperature-dependent current-voltage characteristics including a back contact barrier are performed and given in Figure 5.22 keeping a constant back barrier height of $\Theta_{\mathrm{BC}} = 0.2$ eV, high back recombination velocity, short diffusion length and low doping density in the absorber.

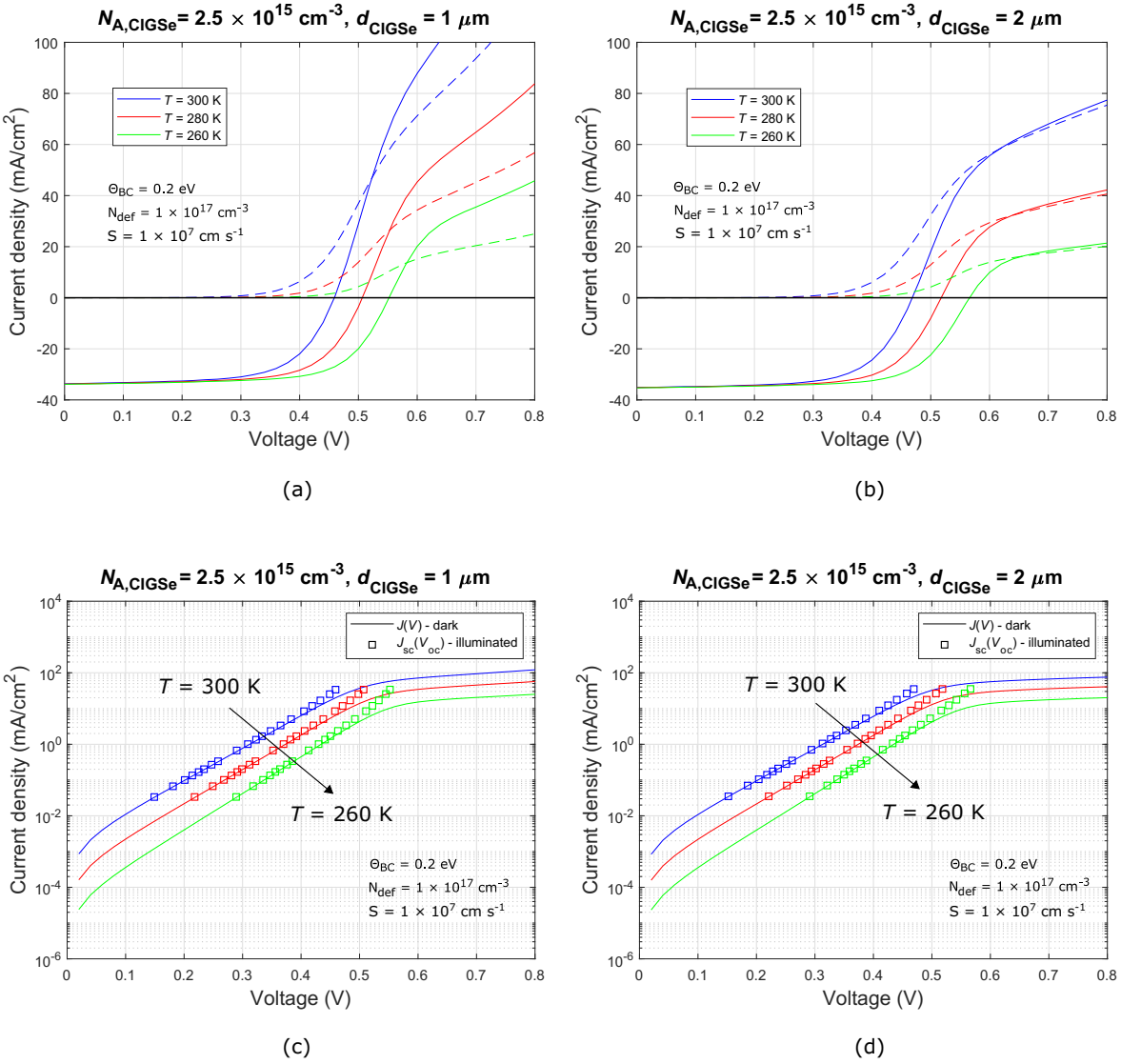

Figure 5.22.: Simulated $J-V$ characteristics of the reference model (without an e-mirror, low doping density, short diffusion length and high back surface recombination velocity) including a back contact barrier of $\Theta_{\mathrm{BC}} = 0.2$ eV with variations in the temperature T and the absorber thickness d_{CIGSe}: (a)-(b) linear plot, and (c)-(d) semi-logaritmic plot where the square symbols represent the $J_{\mathrm{sc}}(V_{oc})$ data points for intensities of 100 mW/cm^2 - 0.1 mW/cm^2.

A similar trend was obtained either by varying the recombination velocity or the temperature. As the temperature decreases, the kink is more expressed and especially for thicker absorbers since the blocking of the light curve gets more pronounced and the cross-over between the dark and light curve is minimized. The semi-logarithmic plots in Figures 5.22c-d also shows the discrepancy of the $J_{\mathrm{sc}}(V_{oc})$ data points with respect to the dark $J-V$ curve with decreasing temperature, a non-ideality usually observed in Chapter 4.

5.3. Summary of barrier models

In this chapter, the evaluation of those effects potentially responsible for degrading the idealities of the diode and photovoltaic performance has been carried out.

According to the models presented, neither a highly doped p^+ layer nor the formation of a buried homojunction are likely to contribute to the diode current limitations similar to those seen in the experiment (Chapter 4), but will mainly affect the photocurrent collection and FF. A surface band gap widening of the CIGSe (not shown here) by an OVC/ODC compound on the surface of the absorber has been a topic of discussion by some authors [125, 126] which lead to a new model for chalcopyrite-based heterojunctions. Numerical simulations showed that such model does not involve a limitation of the current or a deterioration of the PV parameters no matter if the OVC/ODC layer is a p-type or n-type compound with a constant electron affinity with respect to the absorber layer.

On the other hand, it has been shown above that a large band offset at the CdS/ZnO interface (Section 5.1.1), low ZnO doping (Section 5.1.4), and acceptor defects at the CdS/ZnO interface (Section 5.1.5) can all contribute to lower FF, kinked $J-V$ characteristics, and a discrepancy between dark and $J_{\mathrm{sc}}(V_{oc})$ characteristics. These three cases lead to similar band diagrams and non-ideal $J-V$ characteristics as shown in Figure 5.23 [93]. This suggests that the three cases share a common mechanism which impedes the current flow.

The main effect is the limitation of the forward diode current through the buffer layer and a poor FF, effects caused by the large separation between the CdS conduction band and the Fermi level. The current transport through the CdS layer depends on the carrier density in the buffer layer. By increasing the band offset at the CdS/ZnO interface the distance between the CdS conduction band and the Fermi level increases, resulting in a low charge carrier density (despite the relatively high doping, Table 3.1) in the buffer layer.
With a low-doped ZnO layer, its conduction band is positioned above the Fermi level in the equilibrium band diagram pushing again the CdS conduction band farther away from the Fermi-level. However, the formation of the roll-over effect due to the ZnO doping emerges only when the conduction band offset at the CdS/ZnO interface is still considerable, as observed in the colormap of Figure 5.13, e.g., when ΔE_{C}(CdS/ZnO) = 0.40 eV in the given example.
And finally, a similar roll-over effect together with a loss in FF occurs when adding acceptor defects at the CdS/ZnO interface to the reference model. The SCR in the ZnO generated by the defects at the interface again pushes up the conduction band of the buffer layer, as can be seen in Figure 5.23a.

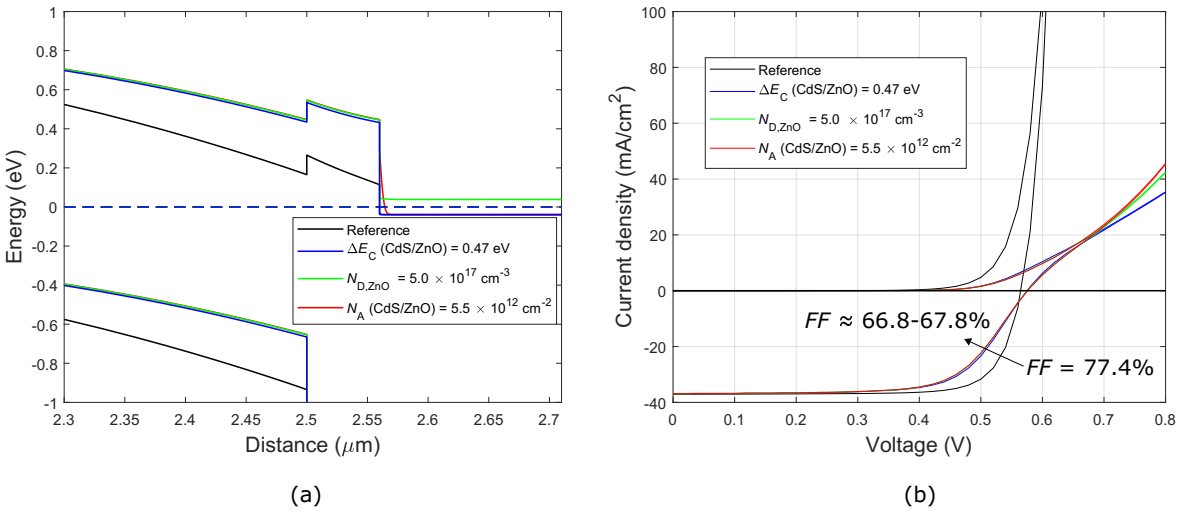

Figure 5.23.: Comparison of the (a) equilibrium band diagrams and (b) the simulated $J-V$ characteristics between the reference model (no barrier effect) and the electronic material parameters modified: high band offset at the CdS/ZnO interface (with $\Delta E_{\mathrm{C}}(\mathrm{CdS/ZnO}) = 0.47$ eV), low-doped ZnO window layer ($N_{\mathrm{D,ZnO}} = 5.0 \times 10^{17}$ cm^{-3} with $\Delta E_{\mathrm{C}}(\mathrm{CdS/ZnO}) = 0.40$ eV) and acceptor defects at the CdS/ZnO interface ($N_{\mathrm{A}}(\mathrm{CdS/ZnO}) = 5.5 \times 10^{12}$ cm^{-2} with $\Delta E_{\mathrm{C}}(\mathrm{CdS/ZnO}) = 0.15$ eV).

In addition to the current limitation of the forward diode current as a result of a low charge carrier density of the CdS layer, a deviation at high bias voltage between the $J_{\mathrm{sc}}(V_{oc})$ values at different illumination intensities and the dark $J-V$ curves was observed in all three cases. Due to unreliable V_{oc} values at low temperatures given by the numerical calculations for the large band offset at the CdS/ZnO interface and low-doped ZnO model, the $V_{oc}(T)$ plot was only shown for the case of defects at the interface (see Figure 5.15b) which showed a saturation of the open-circuit voltage at low temperatures. Since the effect of the current limitation is similar in all three cases, it might be expected to also have a similar behavior for the V_{oc} as a function of the temperature for the other cases.

The assumption that a common underlying mechanism is the limitation of the current by the transport through the buffer layer is strengthened by considering the carrier mobility in the buffer. Because of the low carrier density in the buffer layer, the electron mobility (μ_n) in the CdS significantly influences the current transport, as shown in Figure 5.24 (here it is shown the model with a large cliff at the CdS/ZnO interface of $\Delta E_{\mathrm{C}}(\mathrm{CdS/ZnO}) = 0.40$ eV, however the same effect occurs in the described models). While reducing the electron mobility, the barrier effect is enhanced because the transport through the CdS begins to dominate and the current scales linearly with the electron mobility when the bias voltage is greater than ~ 0.6 eV. Thus, a low mobility of electrons in the buffer amplifies all non-ideal effects.

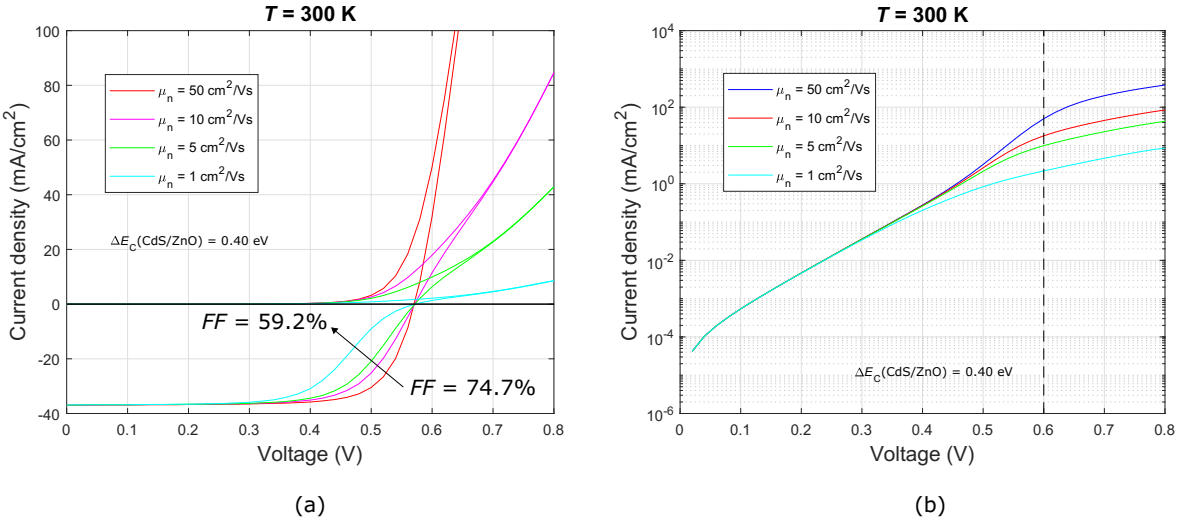

Figure 5.24.: Simulations of the $J-V$ characteristics as a function of the electron mobility μ_{n} of the CdS buffer layer with a constant cliff of $\Delta E_{\mathrm{C}}(\mathrm{CdS/ZnO}) = 0.40$ eV: (a) illuminated and dark curves in linear scale, and (b) dark curves in semi-logarithmic scale.

A low-doped CdS buffer layer enhances the kink effects as a result of large conduction band cliffs at the buffer/window interface and low doping in the window layer. It was also noticeable that even a small change in the spike at the CIGSe/CdS interface, when combined with the CdS/ZnO cliff, can also significantly affect the current transport. The spike at the absorber/buffer interface also influences the depletion but as it is by itself a barrier to the flow of electrons, it modifies the $J-V$ characteristics in a slightly different way.

Besides, in combination with the cases previously described in Figure 5.23, models such as the introduction of a p^{+} layer at the absorber surface, defects at the CIGSe/CdS interface, buried $p-n$ junction and/or the increase of the conduction band spike at the CIGSe/CdS interface will lead to a more severe influence and enhancement on the FF loss.

The introduction of a barrier at the back contact also contributes to a non-ideal behavior of the $J-V$ characteristics, such behavior being strongly dependent on absorber parameters and contact properties.

For a better and clear understanding, all these observations are summarized in Table 5.3. Here, the different models evaluated in this chapter are listed as well as the non-idealities and the positive or negative effects caused in the PV parameters.

Table 5.3.: Summary of interface and back contact barriers. The dots indicate the presence of the corresponding effect, the crosses indicate the absence of it. In certain models, the evaluation of the $V_{oc}(T)$ plot was not determined, then in such cases a dash is given. No change is indicated by n/c. The model/experiment comparison is done in Chapter 6.

	Non-idealities with respect to a standard diode							
Model	Roll-over	Cross-over	Discrepancy (dark vs $J_{sc}(V_{oc})$)	V_{oc} sat.	FF	V_{oc}	J_{sc}	Remarks
Cliff CdS/ZnO	•	×	•	–	loss	gain	n/c	Cliff above 0.40 eV is needed to cause such effects at $T = 300$ K. Smaller ΔE_C will do so at lower temperatures.
Spike CIGSe/CdS	×	×	•	–	loss	n/c	loss	Spike above 0.40 eV is needed to cause such effects at $T = 300$ K. Smaller spikes in combination with large cliffs increase the non-idealities.
p^+ layer	×	×	•	×	loss	gain	loss	In combination with the models described, a higher loss in FF occurs.
Buried $p-n$ junction	×	×	×	×	loss	loss	loss	In combination with the models described, FF may be slightly influenced.
E_g widening	×	×	×	×	n/c	n/c	n/c	No influence was observed in any case.
Low-doped ZnO	•	×	•	–	loss	gain	n/c	Cliff above 0.40 eV is needed to cause such effects at $T = 300$ K. In combination with a low-doped CdS, the effects are enhanced.
Defects at CIGSe/CdS	×	×	×	×	loss	loss	loss	To a greater or lesser extent, neutral, donors or acceptors contribute to a reduced device performance.
Acceptor defects at CdS/ZnO	•	•	•	•	loss	gain	n/c	Cross-over is more significant for deep defects.
Back contact barrier:								
-long diffusion length	• (only dark)	•	•	•	loss	loss	n/c	Only dark curves are influenced by the back barrier. Material parameters affect to a different extent.
-short diffusion length	•	•	•	•	loss	loss	n/c	Both dark and light curves are influenced by the back barrier. Material parameters affect to a different extent.

From the semi-logarithmic plots of the blocked models studied in Figure 5.23, it was observed that under dark conditions the current at low bias was also influenced by the blocking of the diode current. It is evident that in such cases, in the same manner as the experimental measurements shown in Chapter 4, it is not appropriate to deduce the diode factors from the dark $J-V$ curves to gain information on the recombination mechanisms. Furthermore, it may be challenging to align the determination of the diode factors obtained from the numerical simulations with the experimental results.

In contrast to the established analytical models (see Section 2.3), in SCAPS the reference model around V_{oc} is not only limited by the SCR recombination but is also influenced by the QNR recombination. For the blocked models, such QNR recombination becomes much more dominant (see Appendix A.6, Figure A.18).

This adds to the difficulty of assigning the observed diode factors. Experimental curves typically show diode behaviors with very large diode factors at low bias which is included neither in the analytical nor in the SCAPS model. On the other hand, due to the change in dominant recombination from the SCR to QNR the curves calculated by SCAPS can also show a two diode behavior. Therefore, assigning the different sections of the experimental curves to corresponding sections of the numerically calculates curves cannot be done with certainty.

6. Influence of RbF on the electrical characteristics of CIGSe thin-film devices

In the present chapter, the influence of RbF treatment on the electrical characteristics of CIGSe thin-film solar cells is examined. An extensive study of several series of samples was given and described in Chapter 4. CIGSe solar cells with and without RbF-PDT were prepared under different conditions and characterized by temperature-dependent $J-V$ measurements. The evaluation of CIGSe devices with absorbers treated with RbF-PDT typically showed the emergence of non-ideal effects especially at low temperatures: a blocking of the forward diode current (roll-over of the $J-V$s), a discrepancy between dark and the $J_{\mathrm{sc}}(V_{oc})$ characteristics, a cross-over between dark and light $J-V$ curves and a saturation of the V_{oc} with respect to temperature.
Chapter 5 included an extensive analysis of numerical models that could mainly explain the limitation of the current transport observed in CIGSe samples with RbF-PDT. Here, possible connections of the main RbF-PDT effects on CIGSe cells including the evaluation of the recombination parameters such as the activation energies of the saturation current density and the diode factors obtained from the previous chapters with the non-electronic findings reported from the literature and the fundamental recombination and transport theory are made.

6.1. Positive and negative consequences of RbF-PDT

While the post deposition treatment with RbF in CIGSe solar cells typically shows beneficial effects, mainly an increase in the open-circuit voltage (universally observed here either in PVD or RTP solar cells), simultaneously, non-ideal effects have also been observed in most of the samples. However, both effects may have different underlying reasons. One clear example corresponds to the EMPA sample in Figure 4.10 which introduces minor non-idealities even though it shows the benefits that PDT entails.

Typically, the recombination mechanism and its underlying parameters are responsible for the V_{oc} increase (except where the V_{oc} is not determined by recombination, e.g., when having a V_{oc} clamping according to the phototransistor model [121, 124, 127], also see Section 5.2).

On the other hand, the non-ideal effects originate from the carrier transport mechanisms other than the recombination. Their relevance for STC device performance lies in the lowering of the FF, especially observed in samples with increasing Rb concentration with CGI = 0.90 (in Section 4.3) and increasing deposition times of the RIS layer on the absorber (in Section 4.7). One of the main non-ideal effects corresponds to the blocking of the forward current that can be grouped into: (1) blocking of the photocurrent, e.g., the model of a p^+ layer at the absorber surface (Section 5.1.2) and buried $p-n$ juntion in the absorber (Section 5.1.3), and (2) blocking of the diode current, e.g., interface barrier from band alignment, doping concentration, interface defects, and from the back barrier model (see Chapter 5). While the latter models also reduce the photocurrent in the active quadrant, it can be shown that the blocked $J-V$ curve from the back barrier model corresponds to a series connection of the main diode of the solar cell and the Schottky diode at the back side of the absorber, i.e., both junctions can be calculated separately and the addition of their individual $J-V$ curves is equal to the $J-V$ curve of the complete device. This is only valid if phototransistor effects are still negligible. So, the apparent loss in photocurrent is just the current limitation introduced by the Schottky diode.

If the phototransistor effects are not negligible (even observed in CIGSe cells without PDT), saturation (clamping) of the open-circuit voltage can develop to a larger extend as another negative effect of PDT either observable only at low temperatures (V_{oc} extrapolates to E_g if only taking the points at high temperature and extrapolates to the reduced activation energy $E_\mathrm{g} - \Theta_\mathrm{BC}$ when taking points at lower temperature) or even at higher temperatures (V_{oc} no longer extrapolates to E_g even when only taking higher temperature points). The latter effect may be difficult to separate from interface recombination where V_{oc} also extrapolates to an activation energy $E_\mathrm{A} < E_\mathrm{g}$. Both, current blocking and V_{oc} clamping contribute to the discrepancy between dark $J-V$ and $J_\mathrm{sc}(V_{oc})$ (see below).

The corresponding topics of the recombination mechanisms as well as the non-idealities from the transport mechanisms of the measured samples in this thesis will be treated again in more detail in Section 6.2 and Section 6.3, respectively.

6.2. Recombination mechanisms in CIGSe solar cells

Based on temperature-dependent $J-V$ measurements performed and described in Chapter 4, there is no indication of a fundamental change in recombination mechanism in most of the CIGSe solar cells regardless if they have been treated with RbF-PDT. The dominant recombination mechanism in the bulk appears to typically be the same without/with PDT [128], in contrast to some earlier works that postulate a transition from interface to bulk recombination [90, 129, 130] mainly due to the modifications made on the absorber surface for which the PDT is responsible (see also Section 2.4). However, a dominant bulk recombination in CIGSe solar cells (without/with PDT) is in agreement with more recent and detailed literature [53]: (1) the determination of the activation energies from the V_{oc} extrapolation to $T = 0$ K and the band gap energies extracted from EQE measurements of a large set of samples without/with RbF-PDT characterized in Chapter 4 typically resulted in $E_{\mathrm{A}} \approx E_{\mathrm{g}}$ (unless V_{oc} is saturated at low temperatures), e.g., for reference PVD samples without/with RbF-PDT (see Table 4.3) and some RTP cells (see Table 4.14), and (2) the diode quality factors are typically mildly temperature-dependent and mostly $A < 2$ as seen in Figures 4.2, 4.5 and 4.32b. The corresponding increase with PDT and with the deposition of the RIS layer at the absorber surface in the open-circuit voltage is mainly due to two parameters [48] of bulk recombination: increase in the carrier lifetime τ that leads to a reduction of the SRH recombination rate (also a reduction of the Urbach energy values has been reported, i.e., suppression of tail states due to alkali treatments [53]) and increase of doping concentration.

In some of the reference samples without PDT, the activation energy was higher than the band gap energy $E_{\mathrm{A}} > E_{\mathrm{g}}$ about +(60-70) meV (see Table 4.3). Scheer et al. [17] mentioned that some temperature terms might be involved besides the thermally activated carrier density [131]. Therefore, in his evaluation the extrapolation of V_{oc} to $T = 0$ K equals $E_{\mathrm{g}} + 75$ meV, which is in accordance to the excess of the activation energy estimated ($E_{\mathrm{A}} \approx E_{\mathrm{g}}$ + (60-70) meV). Also, in a graded absorber the situation where $E_{\mathrm{A}} > E_{\mathrm{g}}$ may occur when the dominant recombination is shifted away from the location whose band gap determines the EQE cut-off [132].

On the other hand, some measured CIGSe cells showed $E_{\mathrm{A}} < E_{\mathrm{g}}$. In the cell without CdS buffer layer in Section 4.6.1 a lower activation energy than the band gap might truly indicate a recombination at the interface between the CIGSe absorber and ZnO layer as demonstrated with numerical simulations performed by Klenk et al. [112] due to a reduced barrier for recombination. In the same category, samples using Zn(O,S) as a buffer without PDT (see Section 4.6.4) also showed this relation. One characteristic

that the previous samples share in common is that the V_{oc} decreases linearly with increasing temperature in the full temperature range and therefore showing no (or insignificant) saturation of the open-circuit voltage as observed in Figures 4.22 and 4.28. Thus, a variation at the absorber/buffer interface in these samples results in the dominance of the interface recombination and thereby also in the decrease of the FF with RbF. Additionally, a CIGSe cell with PDT and CGI = 0.70 in Section 4.5 can also be included in this group of cells.

In some other cases, however, it may not be the recombination mechanism that determines the V_{oc} as stated above. CIGSe samples with a Na-barrier at the back contact without PDT characterized in Section 4.4 might be one case with V_{oc} clamping even at higher temperatures as a consequence of the phototransistor effect due to the low Na content especially at the back contact and doping concentration as seen in the doping profiles in Figure 4.15, and thus V_{oc} extrapolating to lower activation energies than they should. Other authors [133] have also found a connection between the activation energy and the Na content in the absorber. RTP cells with NaF+RbF PDT also showed $E_{\mathrm{A}} < E_{\mathrm{g}}$ with only a mild V_{oc} clamping at high temperatures but stronger at lower temperatures (see Figure 4.32a). From the GD-OES depth profile of this cell [134] it was observed that not only Rb but also Na are strongly segregated at the back side of the absorber. Besides, CIGSe cells with too low Cu content (CGI = 0.30) in the absorber characterized in Section 4.5 also showed $E_{\mathrm{A}} < E_{\mathrm{g}}$ and a saturation of the open-circuit voltage at low temperatures even when the doping concentration N_{A} in the cell without PDT is high (close to 10^{16} cm^{-3}). By introducing a Zn(O,S) layer as a part of the window bilayer of the cell with RbF-PDT in Section 4.6.3, the sample followed the same trend of the samples stated above and being less significant before PDT. However, in some cases, Rb was helpful to increase the activation energies and to approach the band gap energies, thus reducing the V_{oc} clamping at higher temperatures but exhibiting the saturation of the V_{oc} at low temperatures and therefore following the same trend as well-behaved CIGSe solar cells. The latter trend was presented in samples previously described with Na-barrier at the back contact and in samples with Zn(O,S) as a buffer.

In general, it is sometimes challenging to judge/determine the recombination mechanism, e.g., in dark $J-V$ characteristics it may be that the current is determined by blocking and under illumination the V_{oc} may be determined by the phototransistor effect rather than recombination.

As stated above, another indication to determine the recombination path is the behavior of the diode quality factor and in most of the CIGSe solar cells it was found to be slightly temperature-dependent with values $A < 2$ along almost all measured temperatures, and therefore indicating a dominant recombination in the bulk with a most likely

exponential defect distribution as seen in the summary of the fundamental theory of the different recombination regions given in Table 2.1. The effect of RbF, particularly at higher temperatures, in CIGSe devices (except when N_{CV} is too low, e.g., when a back Na-barrier is introduced) is to decrease the diode factors in samples with $0.80 \leq$ CGI ≤ 0.95 as seen in Figure 4.6 which also showed the beneficial effects of RbF-PDT in terms of V_{oc} and FF in absorbers with high Cu content. This A decrease is also visible in samples with a RIS layer on top of the absorber (see Figure 4.30c). The lowering of the diode factors at higher temperatures may be an indication of a transition towards recombination in the QNR. Additionally, the dominance of the recombination in the QNR with a blocking of the forward diode current as a consequence of the PDT has been observed from the recombination profiles obtained by SCAPS simulations in Figure A.18 in comparison to the reference model without any blocking in Figure 5.2, which also supports this assumption. On the other hand, an inconsistent trend is observed at lower temperatures with a higher temperature dependence and higher values of the diode factors. Measurements performed in Section 4.3 showed a clear dependence of the diode factors at low temperatures with the Rb amount deposited on the PVD-absorbers and the doping density. This finding suggests that higher amounts of RbF (longer deposition times) might be needed in RTP-absorbers in Section 4.8 in order to increase the doping concentration and therefore to decrease the diode factors over the entire temperature range. Further measurements need to be carried out.
When recombination occurs in the SCR both, the exponential defect distribution and tunneling assistance, will the A to increase with decreasing temperature. As studied in the fundamental theory of Section 2.3.1, if the recombination is dominant in the SCR, the diode quality factor is $A = 2$. With recombination over an exponential defect distribution, the diode factor is reduced from the standard value ($A = 2$) and that reduction is more expressed at higher temperatures, whereas with recombination with a tunneling assistance the diode factor is increased from the standard value and that increase is more expressed at lower temperatures [18]. The higher temperature dependence of the diode quality factors observed either only at low temperatures (in most of the CIGSe cells) or over the full temperature range (as in the case of samples with Zn(O,S) buffer layer in Section 4.6.4) might be an indication of a transition towards tunneling assisted recombination with A reaching values above 3 (see Table 2.1) as the temperature decreases especially when $T < 150$ K.

As seen in Figure 4.3, with a constant band gap in the absorber, the diode factors are temperature-independent over a wide range at high temperatures. Without the band gap grading, it is more likely that the dominant recombination occurs in the QNR (as shown in the SCAPS calculations given in Chapter 5) which could affect the temperature behavior of the diode factors in this sample, in contrast to samples with graded absorbers (see Figure 4.5) where the recombination in the QNR is suppressed

or reduced and where therefore the recombination in the SCR becomes dominant with slightly temperature-dependent diode factors.

6.3. Non-idealities of CIGSe solar cells with RbF-PDT

6.3.1. Discrepancy between dark $J-V$ and $J_{\mathbf{sc}}(V_{oc})$

One of the most consistent observations in CIGSe cell with Rbf-PDT is the discrepancy between the dark $J-V$ curves and the $J_{\mathrm{sc}}(V_{oc})$ data points (see Figure 4.4), a non-ideal effect hardly mentioned in literature. Three effects could lead to a similar picture and are discussed below.

1. A previous model described by Hengel et al. [135, 136] postulated a change in recombination mechanism under illumination, from tunneling into interface states in the dark to a thermally activated process under illumination. However, this model implies a change of the diode quality factor and its temperature dependence with illumination that was not usually seen here in the results or at least there is no considerable change with illumination in contrast to Hengel's results when comparing (if possible) the deduced diode factors under both conditions.

2. A shifting of the $J_{\mathrm{sc}}(V_{oc})$ characteristic to the left in the case where the V_{oc} is not determined by recombination but the dark current is. The V_{oc} is lower than it should be as an outcome of a saturation of the V_{oc} (phototransistor effect). This may be valid for some of the measured samples at high temperatures, e.g., samples with Na-barrier at the back contact, and also for some other samples which present a V_{oc} saturation at lower temperatures.

3. A shifting of the dark $J-V$ curve to the right where the $J_{\mathrm{sc}}(V_{oc})$ points are determined by recombination (and stay where they should be) but the dark current is not, but in rather it is reduced due to blocking. This condition is typical for well-behaved CIGSe solar cells with RbF-PDT.

Effects 2 and 3 are more likely to happen in the measured cells because they are supported by additionally observed effects as a consequence of the barrier such as a kink and roll-over that a change in recombination mechanism would not cause.

6.3.2. Cross-over between dark and light $J-V$ curves

A very typical non-ideal effect observed in characterized CIGSe thin-film solar cells in Chapter 4 is the cross-over between the dark and light $J-V$ curves mildly visible at low temperatures. After RbF-PDT, the cross-over occurs already at higher temperature. Two of the models studied in Chapter 5 can be responsible for such effect: acceptor defects at the CdS/ZnO interface (Section 5.1.5) and back contact barrier (Section 5.2).

Among all the samples measured, two set of samples clearly showed a significant cross-over. These samples correspond to CIGSe devices with a Na-barrier at the back side of the absorber (see Figure 4.13) and devices with low Cu content in the absorber (see Figures 4.16 and 4.17) and, as discussed in Section 6.2, these were referred to samples affected by the phototransistor effect which also correlates with the numerical simulations performed with a barrier at the back contact and the derivation of such a cross-over effect.

For all the remaining samples with a slight cross-over at lower temperatures, the model of acceptor states at the buffer/window interface correlates with the presence of such a non-ideal effect. In the work of Lauermann et al. [137], Na was found to be mobile before/during/after buffer layer deposition so we cannot exclude the possible Na diffusion from the absorber/buffer interface to the buffer/window interface with an enhanced density of acceptor states when Rb is deposited. The numerical simulations in Section 5.1.5 showed that with increasing doping densities of the acceptor defects at the buffer/window interface, among other non-idealities, the cross-over is developed and arises at higher temperatures for deeper defect levels.

6.3.3. Limitation of the diode current and its connection to alkali fluoride PDT

In Chapter 5, numerical calculations showed that lowering the ZnO doping, introducing acceptor defects at the CdS/ZnO interface, and/or creating a higher band offset at this interface, illustrated in Figure 5.23, lead to similar non-ideal $J-V$ characteristics typically observed in CIGSe solar cells with RbF-PDT presented in Section 4.2 such as a roll-over of the $J-V$s and a discrepancy between dark and $J_{\mathrm{sc}}(V_{oc})$ characteristics, as well as a lower FF. This model suggests that the limitation of the diode current results as a consequence of a low carrier density in the buffer layer where any mechanism that moves the conduction band of the buffer away from the Fermi level will lead to similar effects. From this, possible connections between the introduction of the heavy alkalis

and these electronic parameters of layers deposited after the PDT treatment can be suggested following the literature.

The diffusion of alkali elements has been seen in model experiments, e.g., the mobility of Na from the absorber into the buffer [137]. Some authors [138, 139] have reported the in-diffusion of elements from group-I (Li, Na and K) into n-type ZnO substrates. It has been demonstrated that substitutional group-I elements introduce shallow acceptor states [138] either by diffusion or *in situ* during ZnO growth [139]. Based on these observations, low ZnO doping could be a consequence of Rb in-diffusion during ZnO deposition. In addition, Heinemann et al. [140] demonstrated that if Na is present at the heterointerface between ZnO and CIGS in superstrate solar cells, the high density of deep acceptor states at the heterointerface lowers the FF, and therefore the device performance. Notwithstanding the different preparation sequences in our substrate cells, a similar situation may nevertheless arise [48]. Thus, introducing acceptor states at the CdS/ZnO interface induced by Rb migration could explain some of the non-idealities presented in RbF-treated samples within the scope of our numerical simulations. Another consequence of alkalis and fluoride present at this interface could be the formation of dipoles and corresponding modification of the band line-up [141]. The possible diffusion of Na before/during/after the buffer deposition within the fabrication process of some of the reference samples without any RbF-PDT might lead in such cases to the blocking of the diode current and discrepancy between light and dark curves visible at low temperatures (Reference 1, 3, 5 and 6 of Figure 4.1) as a consequence of the different mechanisms stated above and enhanced with RbF-PDT (Figure 4.4).

The numerical simulations in Figure 5.8c, by slightly varying the conduction band spike at the absorber/buffer interface in combination with a large conduction band cliff at the buffer/window interface, also demonstrated the enhancement of the diode current blocking at forward bias. Thus, the accumulation of heavy alkali metals, in this case Rb, and fluoride at the absorber surface reported by numerous authors and reviewed in Section 2.4 in this work could also change this band line-up via the formation of dipoles. However, this high Rb concentration and/or a formation of a $RbInSe_2$ layer at the surface of the absorber after PDT is not considered by itself responsible for the blocking of the diode current in accordance to the numerical calculations given in Section 5.1.2 and 5.1.3 for a p^+ layer and an n-doped region at the CIGSe surface (considering that the RIS layer is an n-type compound), respectively. Despite not having performed dedicated numerical calculations including an n-type layer on the absorber surface with $E_{g,RIS} > E_{g,CIGSe}$ which are the parameters known so far for this phase, the aforementioned simple device models together with the evaluation of the band gap widening at the surface of the absorber briefly discussed in Section 5.3, with variations of the layer thickness and doping density, are in accordance with the

simulations of a sample based on a CIGSe/$RbInSe_2$ stack performed by Kodalle et al. [97, 142, 143] which lead to a photocurrent barrier at the heterointerface under forward bias, decreasing the FF which is influenced by the band line-up, conductivity and thickness of the RIS layer. Kodalle proposed that the RIS layer acts as a barrier for the photocurrent, thus lowering the FF. These numerical calculations are supported by the JVT characteristics measured in Section 4.7 for a set of samples with varied RIS deposition times deposited on the CIGSe surface.
For the negative effect of the lowering of the FF, Kodalle et al. [68] also suggested the dependence of the FF on the CGI ratio where the PDT only acts beneficially on both V_{oc} and FF at high Cu content (see Table 4.7). An increase in the carrier concentration due to the Rb-Na exchange mechanism is only feasible if the availability of Cu vacancies is limited and only beneficial on samples with CGI ≥ 0.8, thus leading to an improved V_{oc}. For a better FF, a high CGI ratio leads to a lower amount of the ODC and then a thinner secondary phase at the absorber surface when CGI ≈ 0.95.
The severity of the blocking of the diode current with higher concentrations of RbF-PDT observed in Section 4.3 is correlated with the concentration of donors in the ZnO window layer, the concentration of acceptor states at the buffer/window interface, and the conduction band offset at such interface, presented in Section 5.1, where the roll-over of the $J-V$s and the discrepancy between dark and $J_{\mathrm{sc}}(V_{oc})$ characteristics are enhanced with decreasing temperatures.

Following the case of the ZnO doping density, it was expected to reduce the blocking having a higher ZnO doping than the reference cell. This was attempted to be achieved by going directly into the highly doped ZnO:Al layer after the CdS buffer layer, omitting the i-ZnO layer in the device structure. However, JVT measurements performed in Section 4.6.2 in a cell without i-ZnO did not show any diode current improvement at forward bias.
On the other hand, a reduced conduction band offset at the buffer/window interface by replacing the i-ZnO film with a semiconductor with a higher band gap and/or electron affinity was suggested to reduce the current limitation developed by this barrier. Using Zn(O,S) and (Zn,Mg)O as a part of the window bilayer, which can offer a greater range of E_{g} than the undoped ZnO from 3.2-3.26 up to 3.6-3.73 eV, respectively [144, 145]. Some HZB solar cells were prepared with such layer structures and characterized as seen in Section 4.6.3 and 4.6.4. However, an expected improvement of the the JVT characteristics was not shown. Since the value of the band gap energy and electron affinity are controlled by the oxygen-to-sulfur ratio ([O]/[S]+[O]) in Zn(O,S) and by the Mg content in (Zn,Mg)O, a more extensive survey might be needed in order to find an adequate ratio/content of the ZnO to effectively move the conduction band up to reduce the cliff. Nevertheless, the highly-efficient ZSW solar cell produced with a window bilayer of (Zn,Mg)O/ZnO:Al (Figure 4.10d) only showed a weak roll-over of

the $J-V$ curves at lower temperatures. As briefly discussed at the end of Section 4.2, the high performance of a CIGSe device seems to be independent of the non-idealities such as the roll-over of the $J-V$ curves and thus putting into consideration the reduced limitation of the current due to the window layer stack including the (Zn,Mg)O semiconductor.

Kodalle et al. [48] mentioned that a pronounced roll-over of the $J-V$ curve could indicate the presence of a barrier at the back contact. From the GD-OES profiles of Na (see Appendix A.2, Figure A.1), Rb appears to drive out Na, also at the back contact, which leads to a low local doping and a non-ohmic back contact. Thus, a blocking of the current at the back interface might be observed due to the low Na content and therefore worsening the back barrier with higher Rb concentrations [142, 143, 146]. As observed in the SCAPS simulations in Section 5.2, the introduction of a back barrier at the back side of the absorber layer leads to a roll-over of the $J-V$ curves and loss in FF and worsen the effects with higher barrier heights. Such numerical simulations are supported with the JVT measurements performed in CIGSe cell with a Na barrier at the back contact in Section 4.4 where the Na content within the absorber was studied to see the effects of a low Na doping.

In practice, both blocking mechanisms may be present at the same time [97]. If the blocking goes along with a stronger V_{oc} saturation it is likely that the back barrier is involved. From the $V_{oc}(T)$ measurements (see Figure 4.14b) and simulations (see Figure 5.18), it has been seen how the V_{oc} with respect to the temperature is highly influenced by the back barrier (low Na content) with higher saturation at lower temperatures when increasing the barrier height. Concerning the V_{oc} saturation with a front barrier, such effect was not very clear from the SCAPS simulations due to convergence complications to gather information about the V_{oc} at low temperatures but, if existing, presumably it is much less expressed than the phototransistor model at the back contact and only comes into play at low temperatures. The contribution rate of each blocking mechanism in a CIGSe solar cells with alkali fluoride PDT might be difficult to determine but it is more likely to suggest that the back contact barrier model is more appropriate to describe the blocking of the diode current when a strong saturation of the V_{oc} at low temperatures simultaneously exists.

7. Summary and conclusions

Post deposition treatments of chalcopyrite absorbers with RbF have contributed to improving the efficiency of CIGSe thin-film solar cell devices, mainly due to the increase in the open-circuit voltage. Various studies and some of the interpretations on the incorporation of heavy alkalis can already be found in literature but refer to a limited number of samples, whereas in this work a large set of CIGSe solar cells under different deposition conditions have been analyzed. In order to study the effects of RbF on the performance of a CIGSe solar cell, temperature-dependent $J-V$ measurements have been performed to give a set of measurements data to explain the multitude of those effects of RbF-PDT reported in literature.

Notwithstanding the typically improved efficiency, CIGSe thin-film solar cells prepared with RbF-PDT tend to exhibit non-ideal $J-V$ characteristics especially at low temperatures: blocking of the forward diode current (roll-over effect), saturation of the open-circuit voltage with respect to temperature, a cross-over between dark and light $J-V$ curves and a discrepancy between dark and $J_{\mathrm{sc}}(V_{oc})$ characteristics. The latter effect is very seldom reported but very consistent in RbF-PDT cells and assessed here for the first time. These non-idealities are typical observations in CIGSe cells prepared at HBZ by PDV or RTP, and also if the samples are prepared in other laboratories.
A discrepancy between the dark $J-V$ curves and the $J_{\mathrm{sc}}(V_{oc})$ characteristics exists if the V_{oc} is affected by the phototransistor effect, where the low V_{oc} obtained for the different light intensities at each measured temperature does not follow the dark $J-V$ curves. However, the dark curves can also be responsible for the discrepancy when the diode current is reduced due to the blocking present at the interface or back contact barrier.
The beneficial effects of RbF-PDT and the non-idealities observed in $J-V$ characteristics are not necessarily connected since without V_{oc} clamping, recombination mechanisms are typically responsible for the gain in V_{oc} after PDT while the forward current transport mechanisms are responsible for the non-ideal effects observed in JVT measurements.
The determination of E_{A} by the extrapolation of the V_{oc} to $T=0$ showed no evidence for a fundamental change in recombination mechanism with or without RbF-PDT. $E_{\mathrm{A}} \approx E_{\mathrm{g}}$ for typical CIGSe solar cells measured in this work. However, some cells

showed $E_A < E_g$ due to variations in the buffer layer clearly attributed to interface recombination, while in some other cells $E_A < E_g$ was attributed to phototransistor effects in the back barrier model. If the phototransistor effects cannot be neglected, the saturation of the V_{oc} develops either only at low temperatures or even at high temperature (especially when there is a low Na content within the bulk).

According to numerical simulations and the behavior of the diode quality factors, recombination in the SCR is dominant in samples without any PDT. After PDT, a lowering of A_{light} was observed from $A(T)$ plots in typical samples especially when $0.80 \leq CGI \leq 0.95$ and, in accordance to SCAPS, recombination in the SCR is reduced and a transition towards recombination in the QNR occurs.
An extensive modeling using SCAPS-1D of several proposed diode current limiting electronic effects of RbF-PDT has been performed. Although not completely conclusive, some hypotheses for the physical effects of RbF-PDT can be ruled out by comparing the modeled effect to JVT data whereas for other effects, model and experimental data are in accordance. Based on numerical simulations, the unification of several front barrier mechanisms into a single model was shown [93]: a low-doped ZnO window layer, acceptor defects at the CdS/ZnO interface, or a high band offset at that interface lead to similar non-ideal $J-V$ characteristics, where the current flowing through the solar cell is limited by the transport across the buffer layer and its interfaces. The density of carriers that is available for transport in the buffer depends on the distance between the CBM of the buffer and the Fermi level. This distance can be varied by changing the ZnO doping density, the band offset at the CdS/ZnO interface or by including acceptor defects at that interface. Connections between PDT and current transport limitations have been suggested due to the migration of alkali metals. Previous studies concerning alkali PDT in CIGS solar cells have reported the in-diffusion of Rb into the ZnO window layer and at the heterointerfaces. Thus, a low-doped ZnO layer and acceptor defects at the CdS/ZnO layer might be a consequence of the alkali diffusion. A formation of interface dipoles due to alkali metals and fluoride may result in a change in the band alignment. The formation of a secondary phase such as a $RbInSe_2$ layer at the absorber surface after the PDT blocks the photocurrent and only contributes to the lowering of the FF.

The models presented in this thesis allow to clarify the fundamental mechanisms and the parameters that have an influence on the recombination and transport mechanisms that affect the performance of chalcopyrite thin-film solar cells, especially when alkalis are deposited. These findings should give some insights to be applicable to multi-source evaporated as well as sequentially prepared CIGSSe thin-films where such non-ideal effects can be reduced by taking into consideration the electronic model of the device.

A. Appendix

A.1. Preparation of CIGSe solar cells

For solar cell fabrication, clean glass substrates with a thickness of 2 mm were coated with 800nm-thick molybdenum by DC-sputtering followed by the deposition of the CIGS absorbers. For the samples without a Na-barrier deposited on the glass, it was allowed the Na diffusion from the glass substrate into the CIGSe absorber. CIGS layers were prepared with and without RbF-PDT. PDT was done in situ without breaking the vacuum, which means that the samples without RbF have to be prepared in a separate evaporation run (using the same process parameters). Subsequently, a 60nm-thick CdS buffer layer was deposited by CBD and 40nm-thick i-ZnO and 140 nm ZnO:Al window layers were deposited by radio frequency (RF) sputtering. However, the samples presented in Section 4.6.3 and 4.6.4 used alternative buffer/window layers using Zn(O,S) as a buffer and window and (Zn,Mg)O as a window layer. The deposition of the alternative buffer/window layers were done by RF magnetron sputtering in the inline sputtering tool Von Ardenne Anlagentechnik VISS300. Finally, Ni-Al-Ni finger grids were deposited by electron beam evaporation onto the ZnO without ARC.

Most of the absorbers were prepared by three-stage-based evaporation and the samples discussed at the end of the Chapter 4, Section 4.8 were prepared by rapid thermal processing (RTP). A brief description of the deposition processes are described below. However, a more detailed description of the PVD and RIS samples can be found in the thesis by Kodalle [97], whereas for the RTP cells, further details on the sequencial preparation can be found in the work by Schmidt et al. [147].

Multi-source evaporation process (PVD)

The physical vapor deposition (PVD) is a vacuum deposition method that allows a good control of the elemental composition of the deposited thin-films. In the first stage of the process, In-Ga-Se precursors are deposited at a substrate temperature of $T_{\mathrm{sub}} = 300$ °C forming two layers of Ga_2Se_3 and In_2Se_3. During the second stage, the substrate temperature is increased up to $T_{\mathrm{sub}} = 530$ °C and, then the Cu-Se precursors are evaporated. As a result of this, the CGI steadily increases and at the end of the second stage the CGI reaches a value of CGI = 1.03 for RbF-PDT samples and CGI =

1.05 for RIS samples. Finally, in the third stage, In-Ga-Se precursors are evaporated and the In_2Se_3 and Ga_2Se_3 are then deposited and the CGI steadily decreases to reach the final Cu-poor composition of the absorbers. Hence, the CGI ratio of the samples is controlled by adjusting the duration of the third stage of the evaporation process. After finishing the CIGSe growth for samples without RbF-PDT, the Se rate is reduced and the substrate is cooled down.

Rapid thermal processing (RTP)

For the sequentially prepared Cu(In,Ga)(S,Se)2 (CIGSSe) thin-films using fast atmospheric pressure chalcogenization of sputtered precursors, soda-lime glass substrates were coated with a sputtered SiO_xN_y Na diffusion layer followed by a Mo/Mo:Na/Mo layer stack. The In and Cu-Ga precursors were then deposited by dynamic DC sputtering to obtain a GGI ratio of ∼0.27 and a CGI ratio of ∼0.87. The substrates were placed in a SMIT Thermal Solutions in-line vacuum-free RTP tool for the sulfurization-after-selenization (SAS) process with elemental Se and H_2S sources. The chalcogenization of the metallic precursos was done in approximately 16 min and at chamber temperatures between 580 °C and 600 °C.

Post deposition treatment of RbF

After CIGSe growth, the Se rate is reduced to less than 0.1 Å/s and the substrate temperature is decreased to T_{sub} = 280 °C where the RbF is evaporated with a deposition rate of 0.2 Å/s. The optimal duration time was set to 10 min. After finishing the PDT, the Se supply is cut off and the substrates are cooled down to room temperature.

For the RIS samples discussed in Section 4.7 as a substitution of the RbF-PDT and before cutting off the Se supply and cooling down to room temperature, the $RbInSe_2$ layer was deposited after the absorber growth keeping the substrate temperature of the third stage of T_{sub} = 530 °C using a one-stage multi source evaporation of In, Se and RbF. After the deposition process of the RIS layer, the samples were rinsed in diluted ammonia to wash off the excess of Rb and residual fluorine.

A.2. Complementary measurements of RbF-PDT

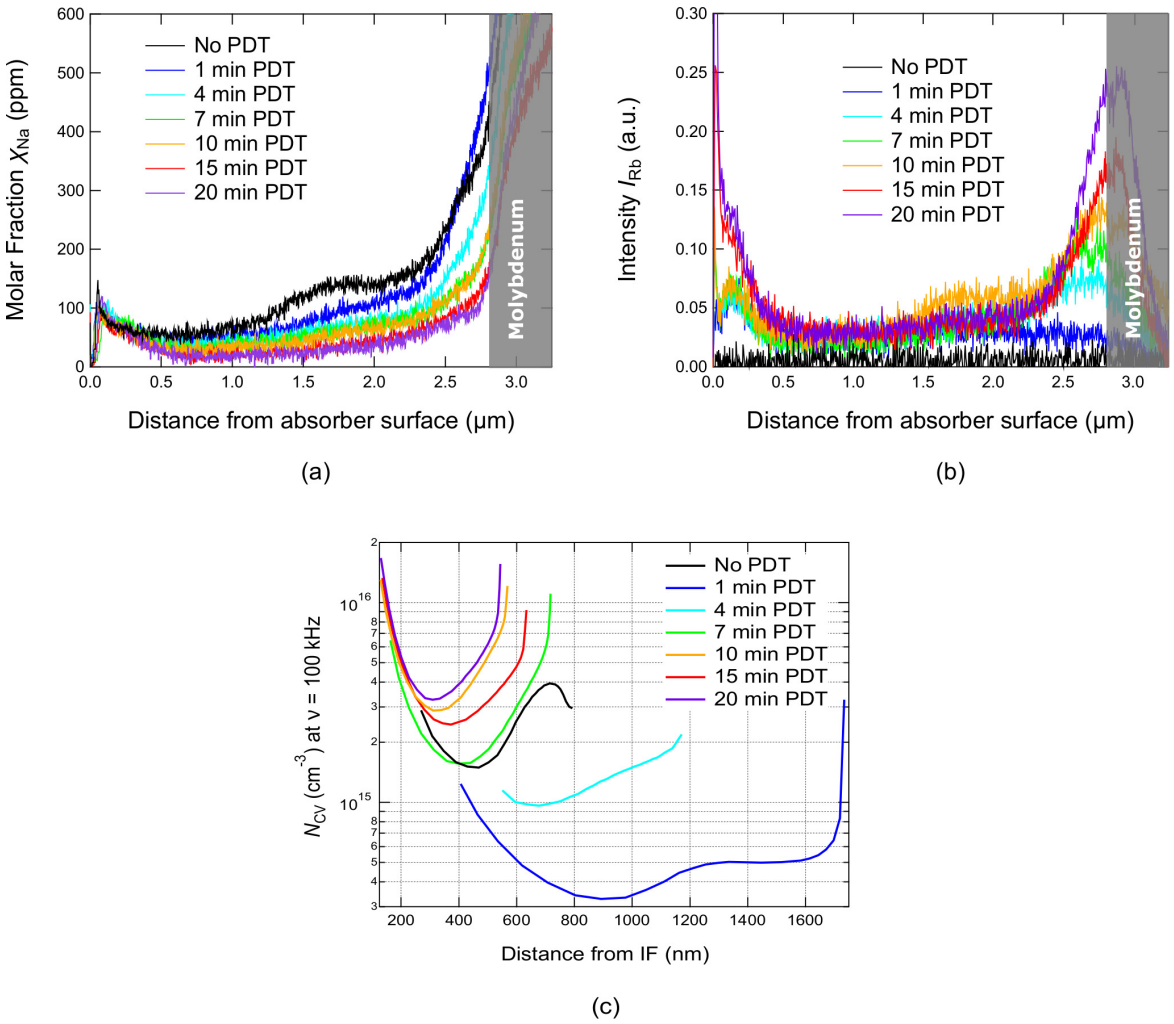

Figure A.1.: Set of CIGSe samples with varied deposition times of RbF-PDT onto the absorber: (a) GD-OES depth profiles of Na, (b) depth profiles of the Rb signal as measured by GD-OES (unquantified intensities), and (c) N_{CV} profiles derived from the $C-V$ curves. Plots taken from References [48, 97].

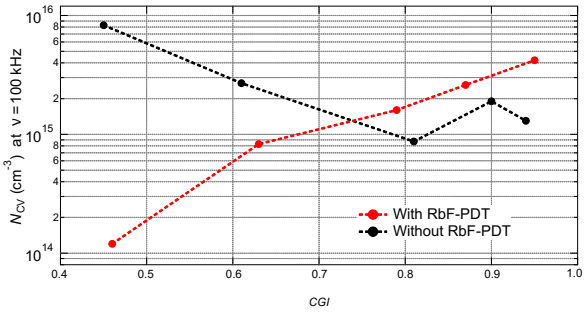

Figure A.2.: Evolution of the N_{CV} with CGI as measured by $C-V$ profiling of CIGSe solar cells with/without RbF-PDT. Plot taken from References [68, 97].

A.3. Additional results from JVT measurements of CIGSe solar cells

In Section 4.1.2 where CIGSe samples were produced with no diffusion barrier, it was seen that in samples with constant band gap a blocking of the forward diode current is present already at much higher temperatures than in samples with Ga grading. Figure A.3a shows the JVT characteristics of a CIGSe cell with constant band gap and a Na-barrier at the back contact. Here, the roll-over intensely affects the diode current even at room temperature. There is again a slight J_{sc} loss (see Table 4.5) in comparison to samples with graded band gap studied in Section 4.1.2. The cross-over effect and discrepancy between dark $J-V$ curves and $J_{\mathrm{sc}}(V_{oc})$ data are very prominent.
Figure A.3b shows the behavior of the diode factors under illumination of a CIGSe solar cell with constant (no grading) band gap previously described in Section 4.1.2 in comparison to the solar cell with constant band gap and a Na-barrier at the back contact. The main difference is the significant constant behavior over a wide temperature range for $T > 150$ K in the cell where Na diffuses from the glass substrate into the absorber, while the cell with a diffusion barrier shows a visible temperature dependence of the diode factors at higher temperatures with a slight constant behavior only at temperatures above 250 K. At the lowest temperatures, both samples with constant band gap reach values close to 2.

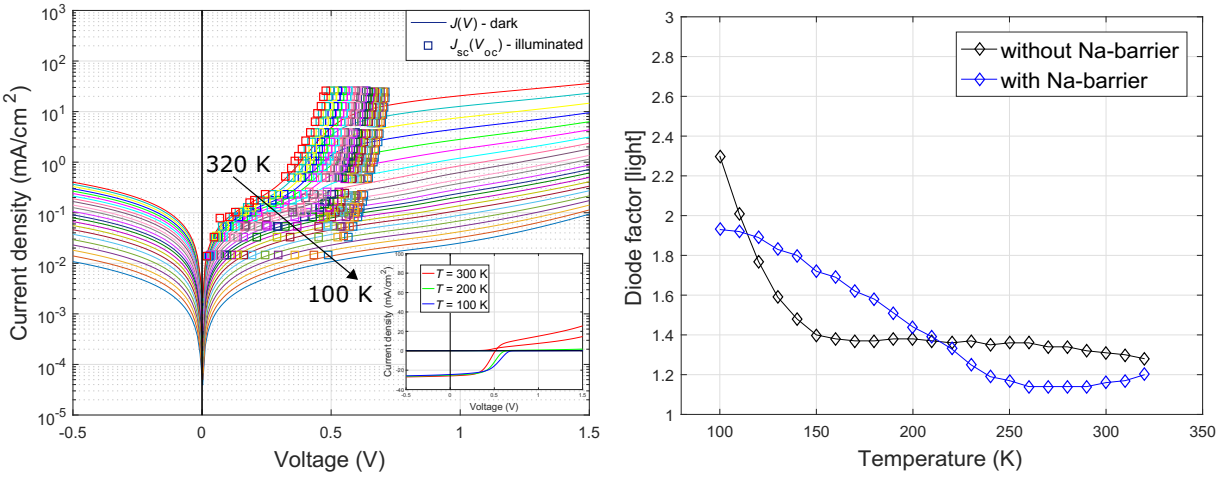

Figure A.3.: Evaluation of CIGSe solar cells with constant band gap: (a) *JVT* characteristics of a CIGSe solar cell including a Na-barrier and without PDT, and (b) diode factors under illumination of CIGSe solar cells with and without the deposition of a Na-barrier at the back contact.

The cell structure consisting of Zn(O,S)/(Zn,Mg)O/i-ZnO/ZnO:Al in Figure A.4 presents a blocking behavior at lower temperatures with RbF-PDT and a slight cross-over at low temperatures is exhibited with and without PDT. The post deposition of the RbF reduces the activation energy, putting it off from the band gap energy, i.e., $E_A < E_g$ (given in Table 4.10). For both cells, the V_{oc} decreases linearly within the full temperature range and the V_{oc} gain after PDT at higher temperatures is higher in comparison with the two structures discussed in Section 4.6.4. As a consequence of the RbF-PDT, the diode factors under illumination present a stronger temperature dependence than the diode factors without PDT and are lowered only at higher temperatures.

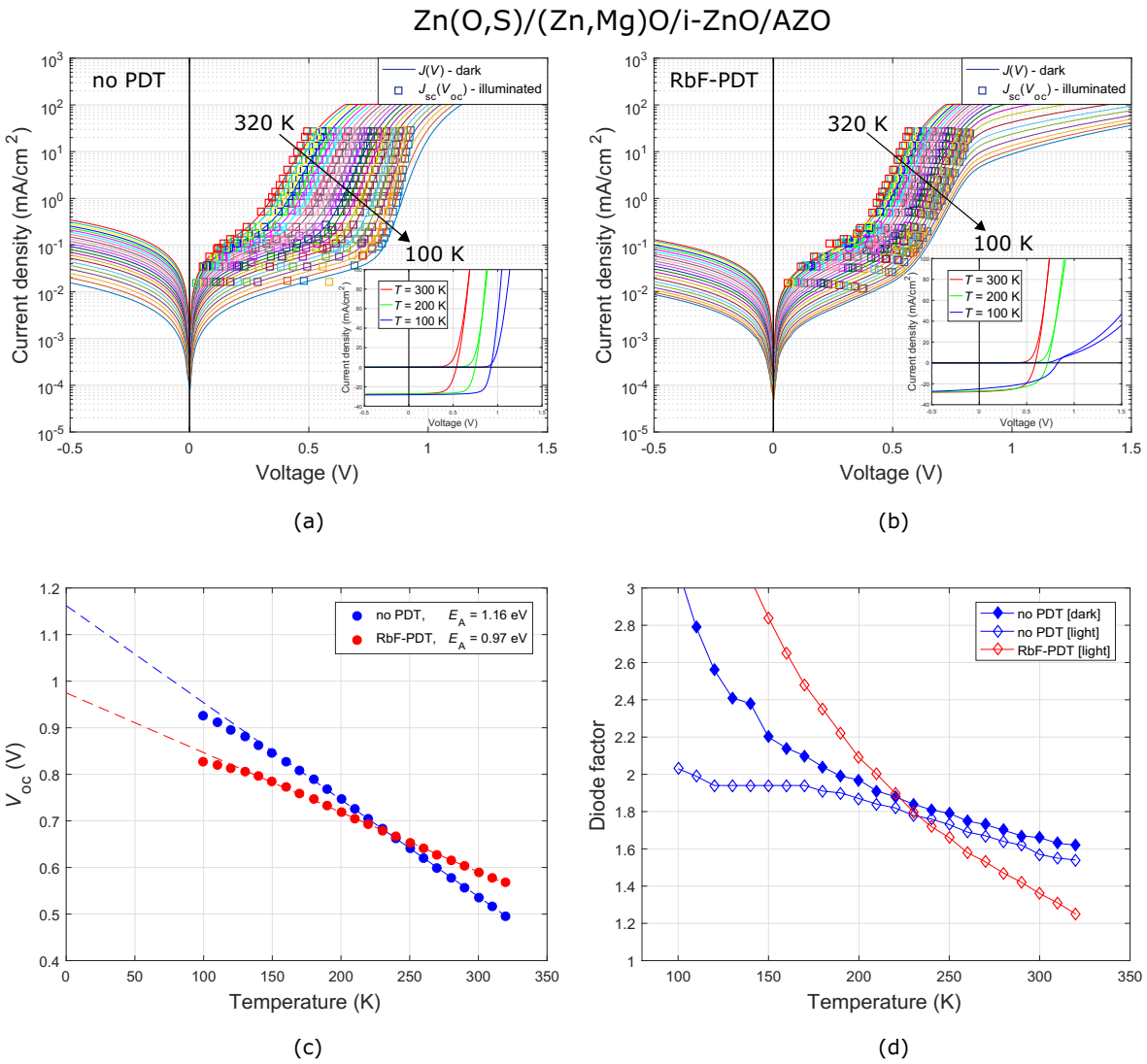

Figure A.4.: Evaluation of a CIGSe solar cell with a three-layer window: Zn(O,S)/(Zn,Mg)O/i-ZnO/AZO. (a) - (b) *JVT* characteristics of the cell without RbF and with RbF-PDT, respectively, (c) V_{oc} as a function of the temperature, and (d) diode factors as a function of the temperature.

A.4. Additional EQE measurements

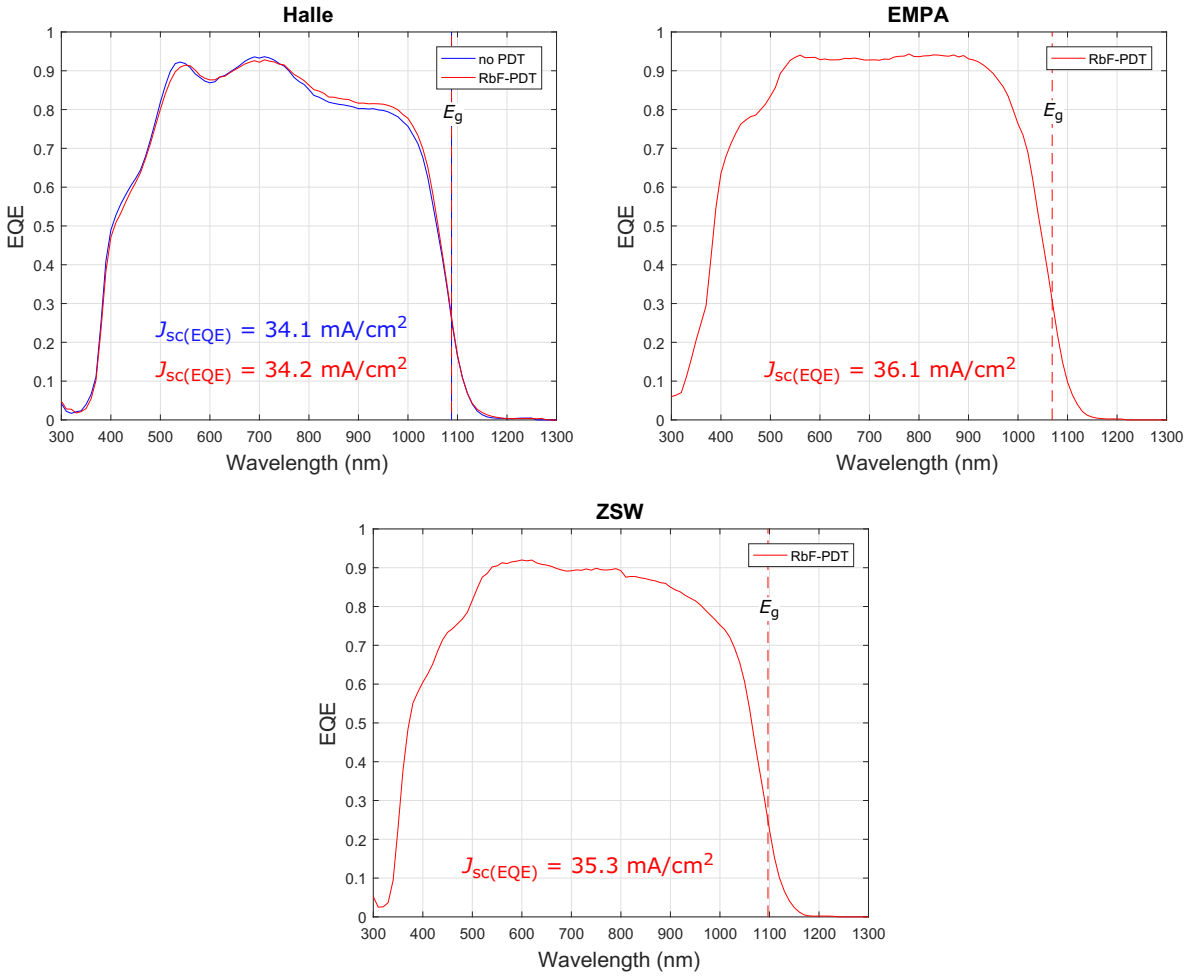

Figure A.5.: External quantum efficiencies of the set of CIGSe solar cells provided by external laboratories: Halle, EMPA and ZSW.

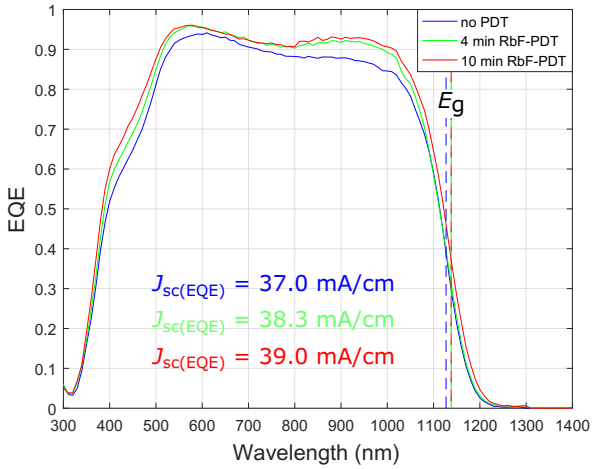

Figure A.6.: External quantum efficiencies of the set of CIGSe solar cells with different amounts of RbF.

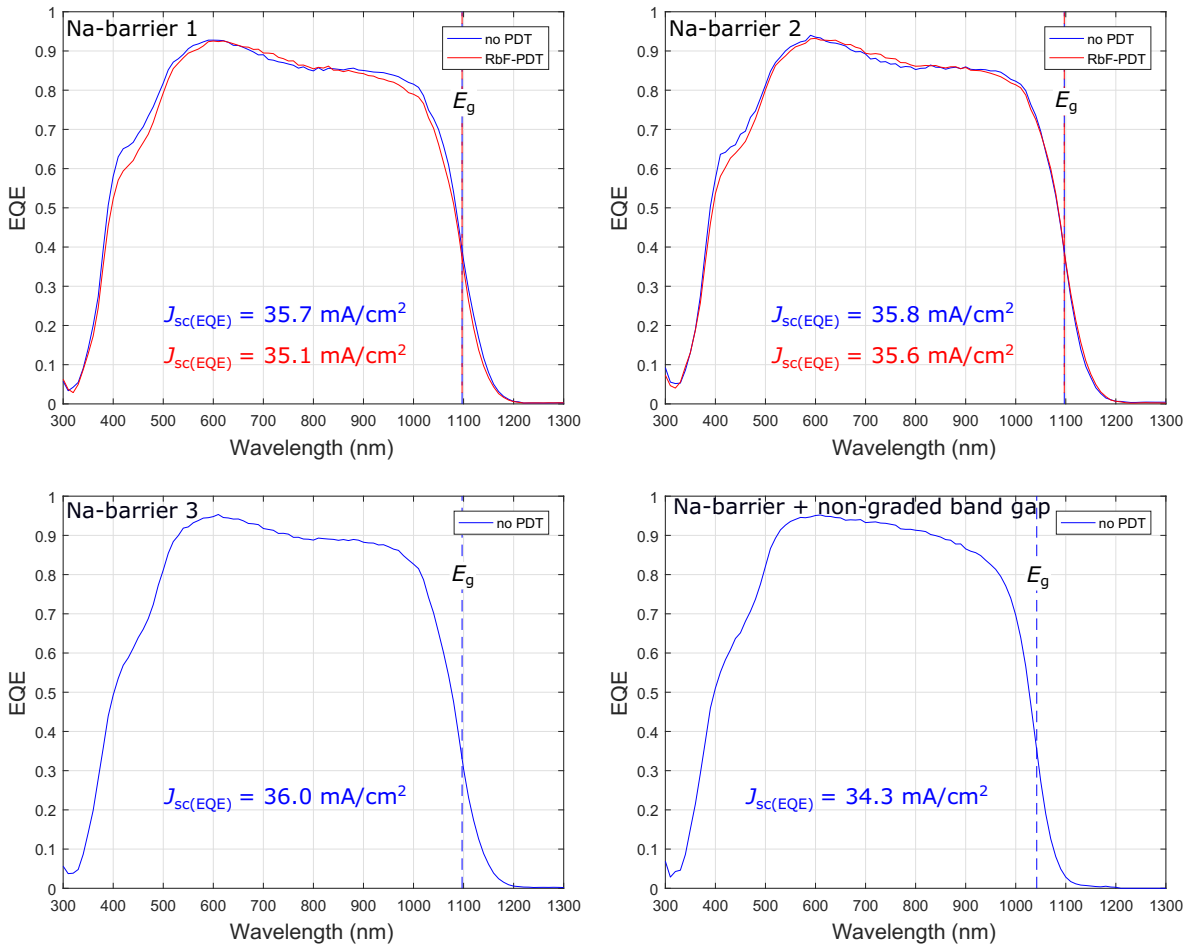

Figure A.7.: External quantum efficiencies of the set of CIGSe solar cells with a Na-barrier at the back contact.

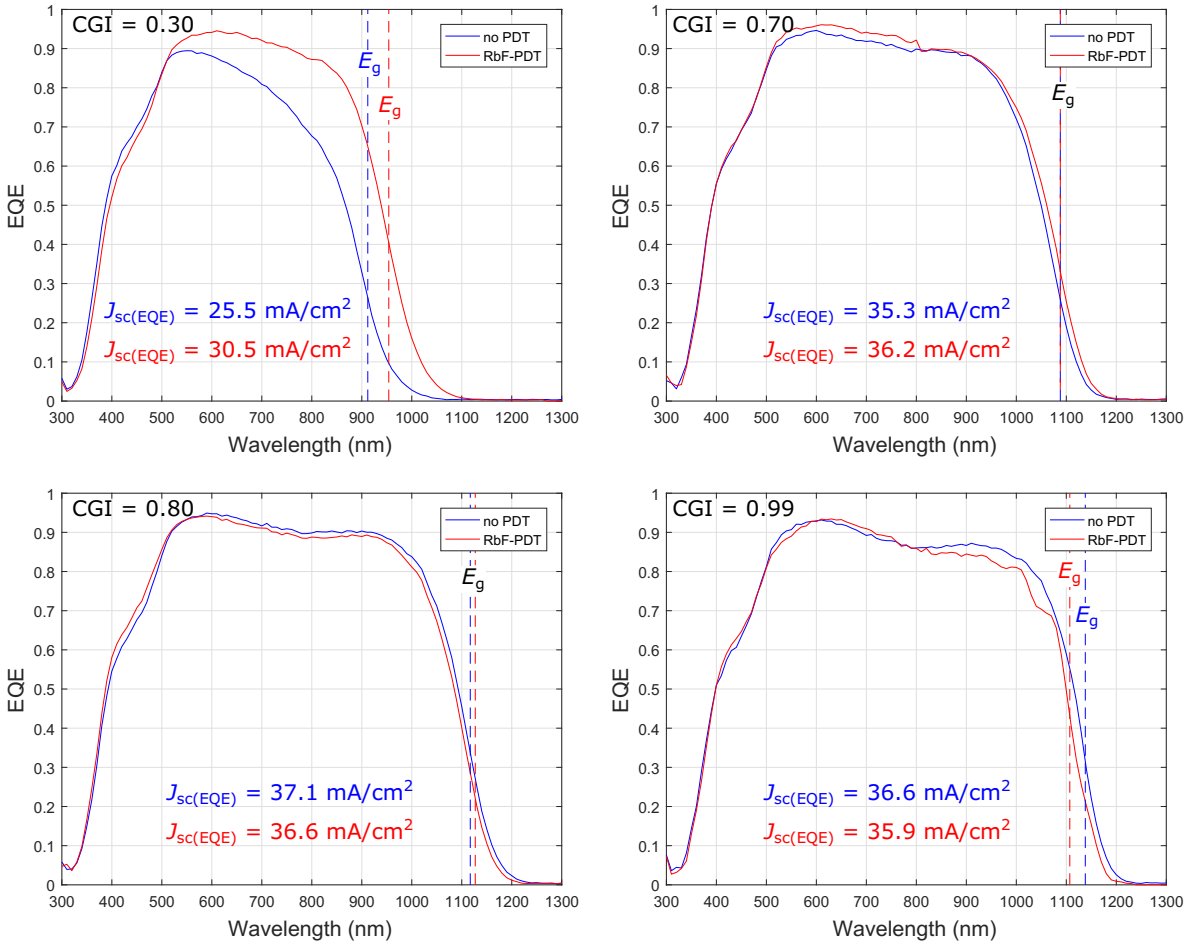

Figure A.8.: External quantum efficiencies of the set of CIGSe solar cells with variations in the CGI ratio.

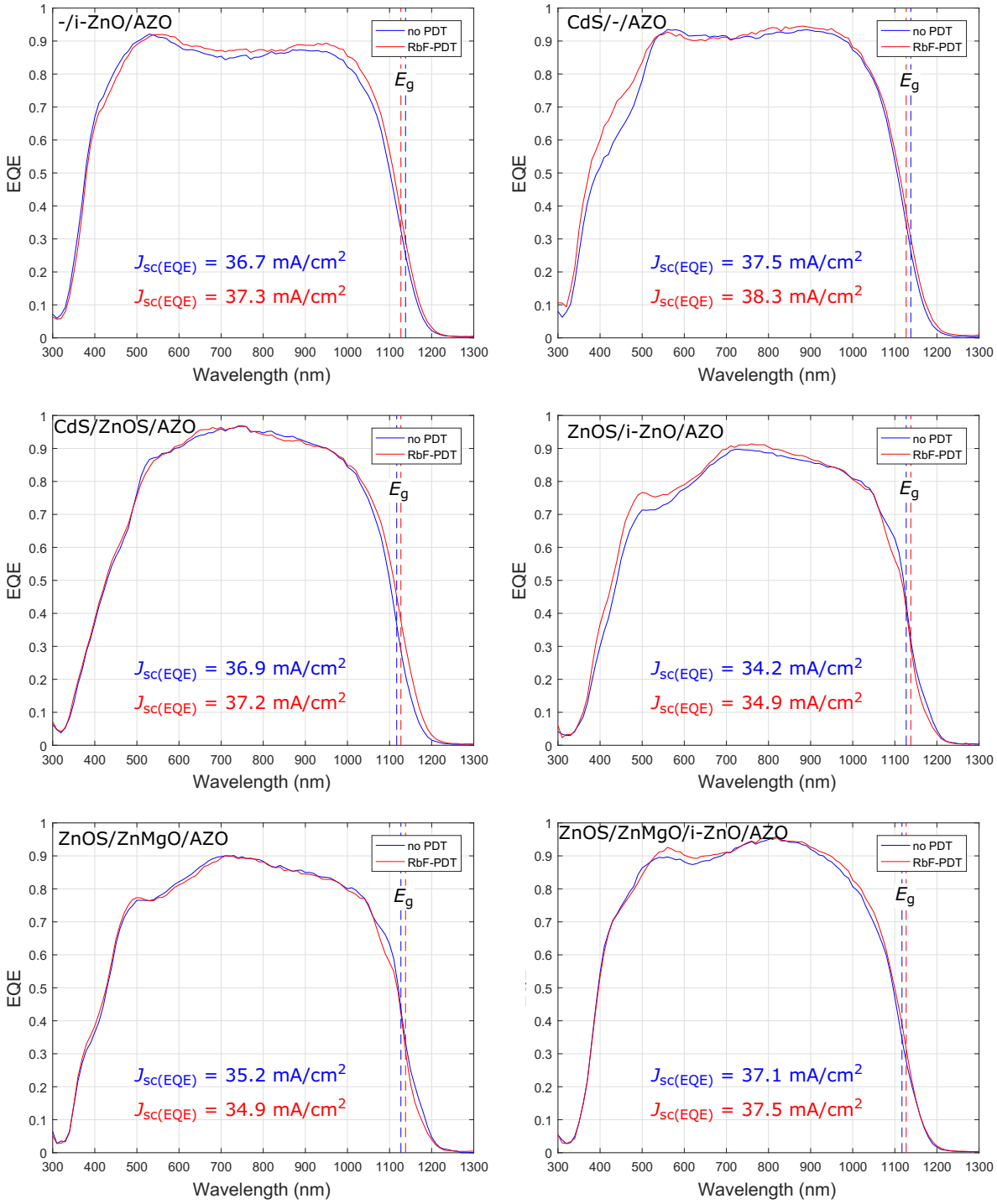

Figure A.9.: External quantum efficiencies of the set of CIGSe solar cells with variations in the layer stack of the device.

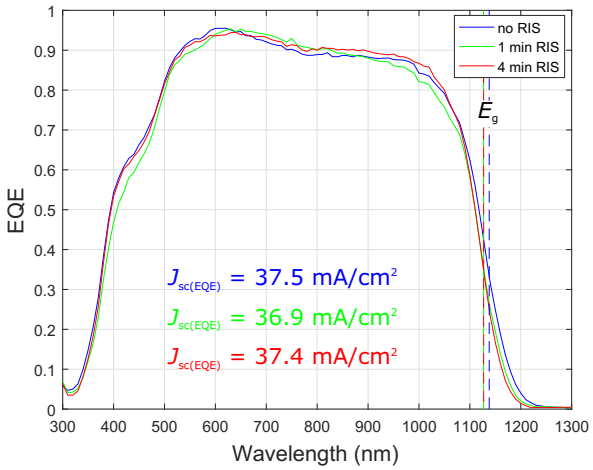

Figure A.10.: External quantum efficiencies of a set of CIGSe solar cells under different deposition times of a secondary phase: $RbInSe_2$ layer.

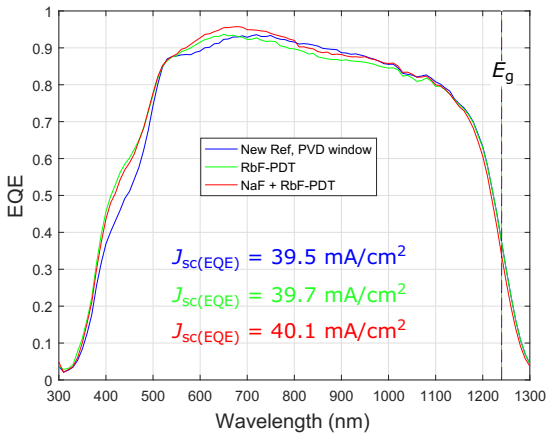

Figure A.11.: External quantum efficiencies of a set of CIGSe solar cells prepared by RTP.

A.5. Additional N_{CV} profiles

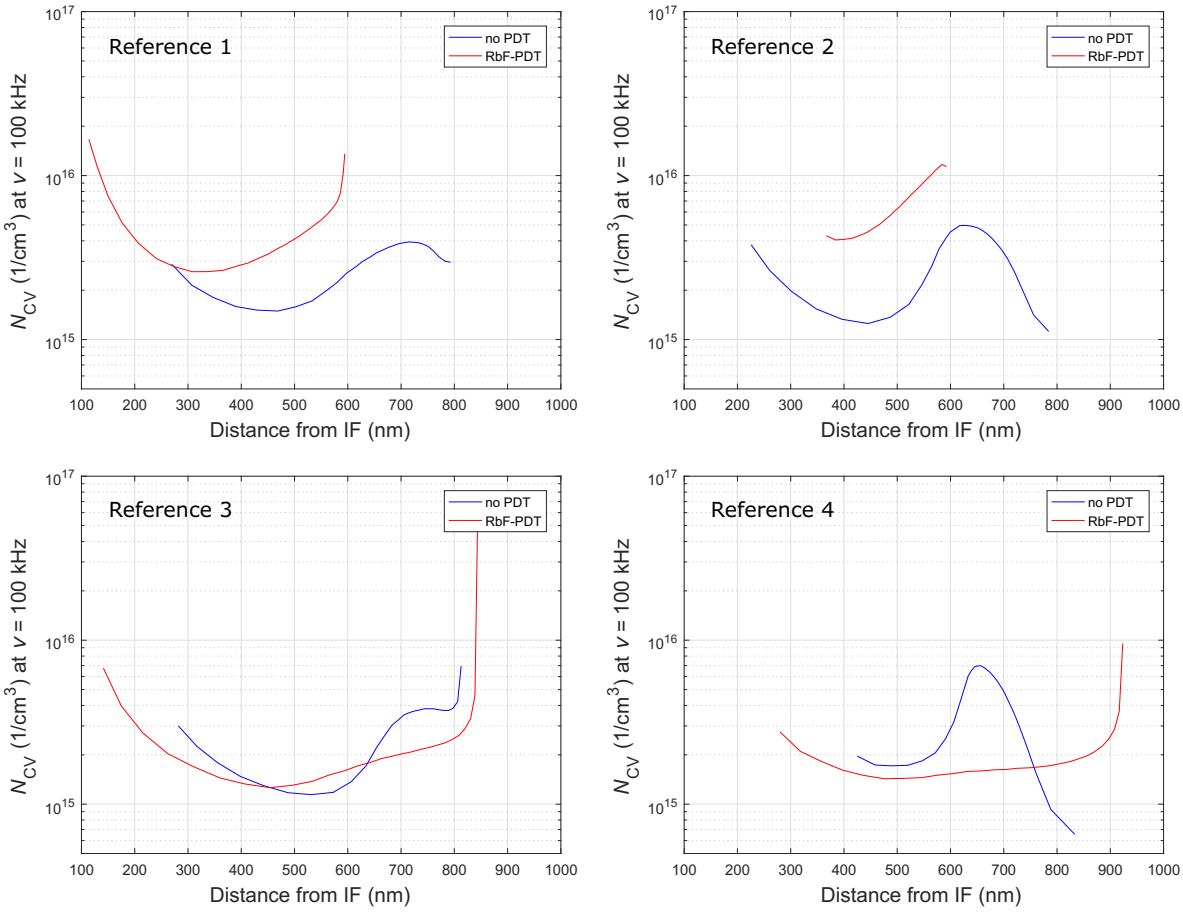

Figure A.12.: N_{CV} profiles of a series of CIGSe solar cells with and without RbF-PDT.

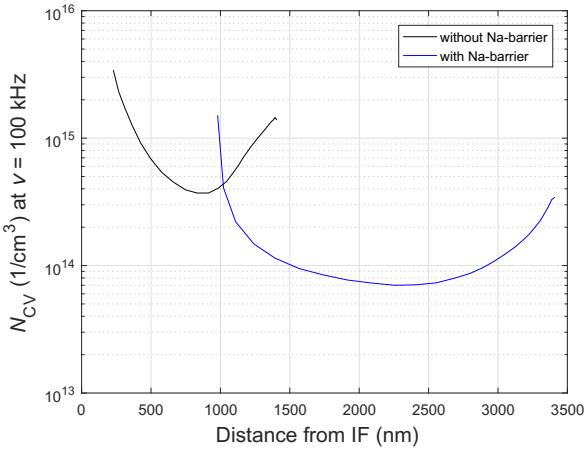

Figure A.13.: N_{CV} profiles of CIGSe solar cells with constant band gap.

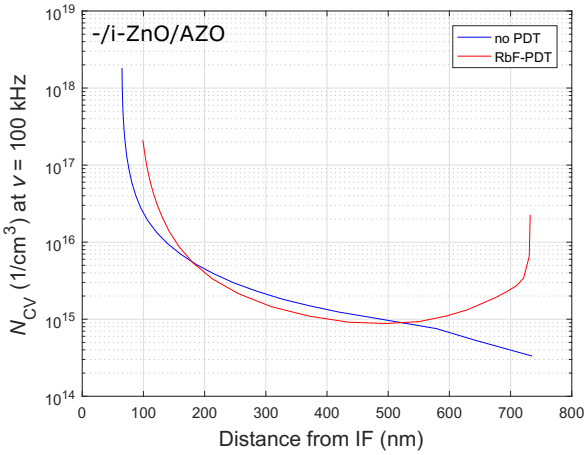

Figure A.14.: N_{CV} profiles of CIGSe solar cells without a CdS buffer layer.

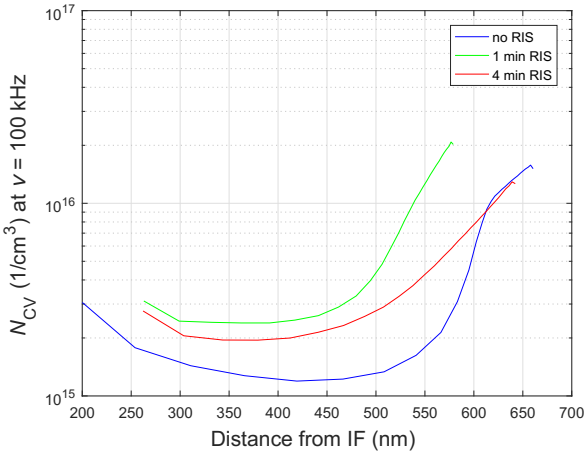

Figure A.15.: N_{CV} profiles of a set of CIGSe solar cells under different deposition times of a secondary phase: $RbInSe_2$ layer.

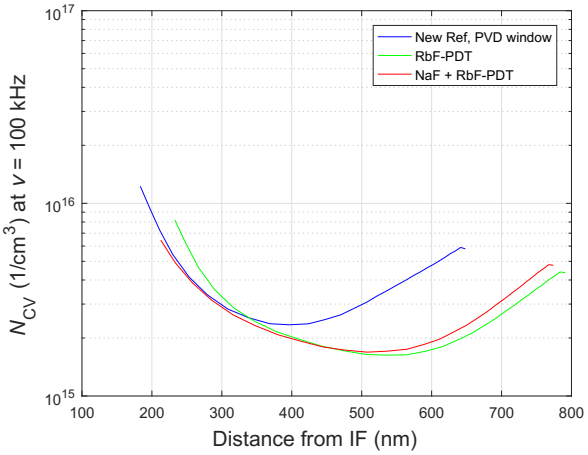

Figure A.16.: N_{CV} profiles of a set of CIGSe solar cells prepared by RTP.

A.6. Recombination rates

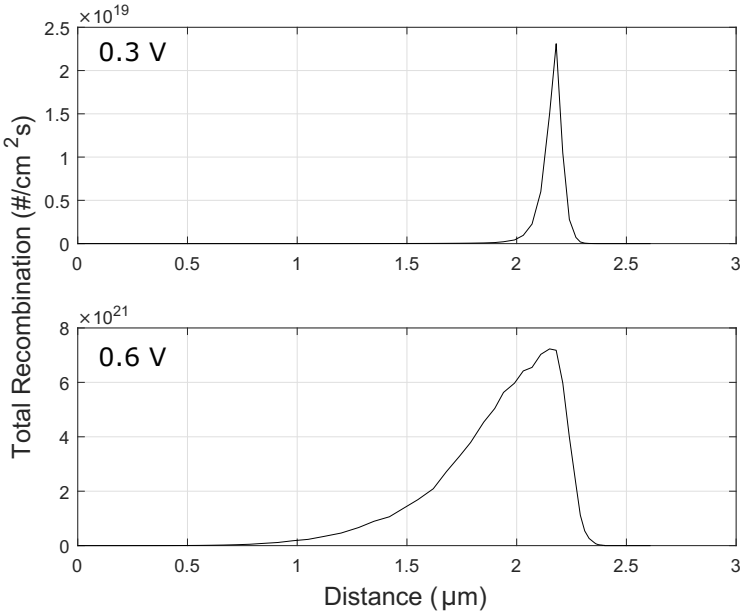

Figure A.17.: Total recombination rate of the reference CIGSe model with absorber with graded band gap (parabolic profile with $E_{\mathrm{g,min}}$ positioned in the SCR, close to 2 μm in the absorber layer).

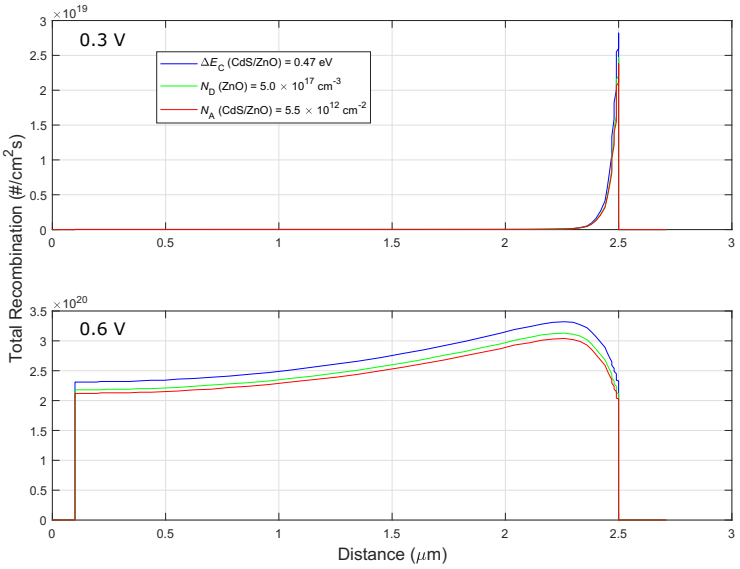

Figure A.18.: Total recombination rate of the blocked models: high band offset at the CdS/ZnO interface (with $\Delta E_{\mathrm{C}}(\mathrm{CdS/ZnO}) = 0.47$ eV), low-doped ZnO window layer ($N_{\mathrm{D,ZnO}} = 5.0 \times 10^{17}$ cm^{-3} with $\Delta E_{\mathrm{C}}(\mathrm{CdS/ZnO}) = 0.40$ eV) and acceptor defects at the CdS/ZnO interface ($N_{\mathrm{A}}(\mathrm{CdS/ZnO}) = 5.5 \times 10^{12}$ cm^{-2} with $\Delta E_{\mathrm{C}}(\mathrm{CdS/ZnO}) = 0.15$ eV).

A.7. Additional STC parameters of the back contact barrier

Back contact barrier model including an electron mirror at the back side

When no back barrier is introduced in the model (Figure A.19), i.e., $\Theta_{\mathrm{BC}} = 0$ eV, V_{oc} decreases for shorter diffusion lengths (high neutral defect density) and is independent of the absorber thickness while for longer diffusion lengths (low neutral defect density) the V_{oc} tends to decrease for thicker absorbers. A reduced FF results for shorter diffusion lengths with a constant value for any absorber thickness and defect density. Bulk recombination is always dominant in all of the cases (from the SCAPS recombination profiles not shown here) since the electron mirror (back surface field) at the back contact helps to avoid the flow of electrons to the back side specially for longer carrier diffusion lengths and thinner absorbers.

When introducing a back barrier, e.g., $\Theta_{\mathrm{BC}} = 0.3$ eV, the large difference in V_{oc} for shorter diffusion lengths without any back barrier is reduced but still with a slight V_{oc} decrease for shorter diffusion lengths and thinner absorbers. However when $\Theta_{\mathrm{BC}} > 0.3$

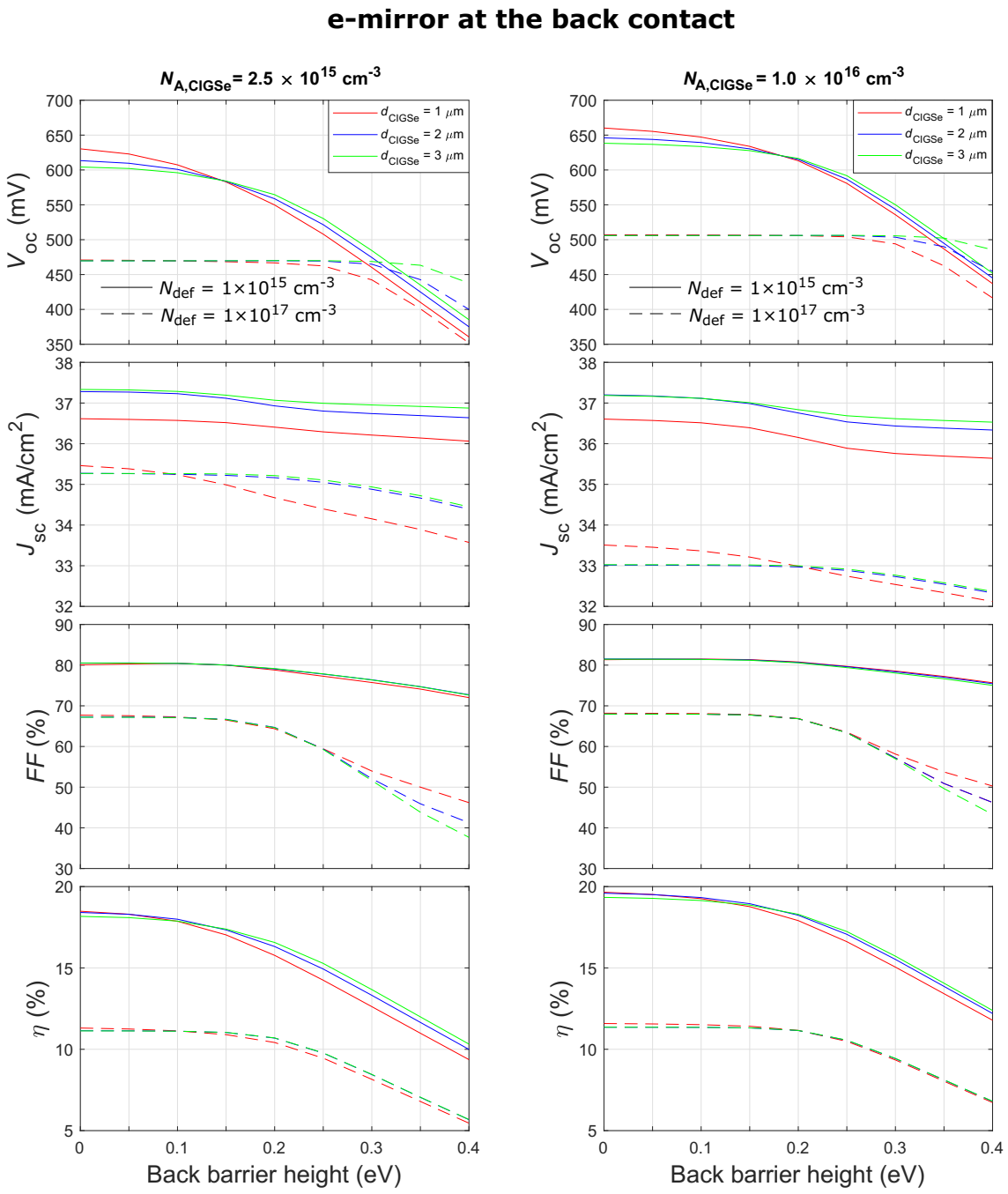

Figure A.19.: PV parameters as a function of the back barrier height Θ_{BC}, absorber thickness d_{CIGSe}, doping density $N_{\mathrm{A,CIGSe}}$, and neutral mid-gap defect density N_{def} in the absorber of the model including an electron mirror (back surface field) at the back contact.

eV, a different behavior results for thicker absorbers ($d_{\mathrm{CIGSe}} > 2\ \mu$m) with higher V_{oc} for shorter diffusion lengths. Also for large back barrier heights, FF decreases for shorter diffusion lengths and in this case a lower FF results for thicker absorbers. No change in FF with respect to the thickness results for longer diffusion lengths. With the introduction of a back barrier, the interface recombination begins to become dominant only for longer diffusion lengths.

There is a more significant effect and drastic reduction in V_{oc} for longer diffusion lengths when a back barrier is introduced in the model. Namely, for $N_{\mathrm{def}} = 1 \times 10^{15}$ cm^{-3} the reduction in V_{oc} starts to take place when $\Theta_{\mathrm{BC}} \approx 0.1$ eV whereas for $N_{\mathrm{def}} = 1 \times 10^{17}$ cm^{-3} V_{oc} keeps constant for a larger barrier height range ($\Theta_{\mathrm{BC}} < 0.25$ eV). Conversely, there is a higher change in FF for shorter diffusion lengths when larger barrier heights are introduced ($\Theta_{\mathrm{BC}} > 0.25$ eV).

In addition to all the above, the same trend is observed for higher doping densities but leading to higher open-circuit voltages over all.

For long carrier diffusion lengths, the dark $J - V$ curves are the only ones affected by the decrease of the back surface recombination velocity and with a loss in the open-circuit voltage (Figure A.20). The kink effect for both light and dark $J - V$ curves can only be seen for short diffusion lengths regardless of some other material parameters or contact properties.

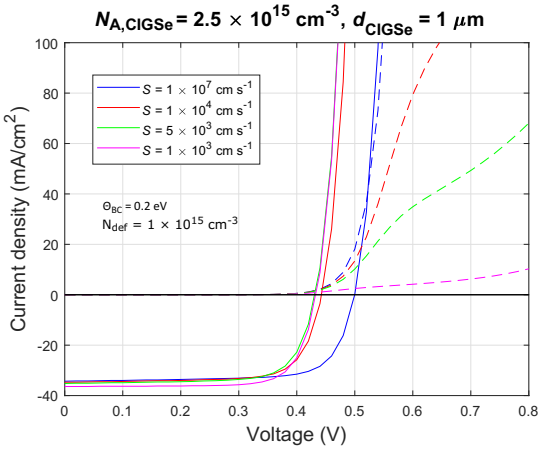

Figure A.20.: Simulated $J - V$ characteristics of the model (without an e-mirror, low doping density, long diffusion length and thinner absorber) including a back contact barrier of $\Theta_{\mathrm{BC}} = 0.2$ eV with variations in the surface recombination velocity S at the back contact.

Bibliography

[1] GISS Surface Temperature Analysis (v4). https://data.giss.nasa.gov/gistemp/graphs/. Accessed: 07.10.2020.

[2] Global Climate Report - August 2020. https://www.ncdc.noaa.gov/sotc/global/202008. Accessed: 07.10.2020.

[3] Just how much is the earth heating up?. https://www.weforum.org/agenda/2020/10/earth-global-warming-nasa-natural-disasters/. Accessed: 07.10.2020.

[4] H. Ritchie and M. Roser. CO_2 emissions. https://ourworldindata.org/co2-emissions#:~:text=Since%201751%20the%20world%20has,needs%20to%20urgently%20reduce%20emissions. Accessed: 07.10.2020.

[5] Y. Liu, Y. Li, Y. Wu, G. Yang, L. Mazzarella, P. Procel-Moya, A. C. Tamboli, K. Weber, M. Boccard, O. Isabella, et al. High-Efficiency Silicon Heterojunction Solar Cells: Materials, Devices and Applications. *Materials Science and Engineering: R: Reports*, 142:100579, 2020.

[6] J. Palm, H. Schneider, K. Kushiya, L. Stolt, A. N. Tiwari, E. Niemi, E. Jaremalm, M. Beck, C. Eberspacher, P. Wohlfart, M. Fischer, A. Bayman, U. Schoop, B. Wieting, K. Ramanathan, B. Dimmler, et al. White paper for CIGS thin-film solar cell technology. https://cigs-pv.net/. Accessed: 07.10.2020.

[7] A. Chirilă, P. Reinhard, F. Pianezzi, P. Bloesch, A. R. Uhl, C. Fella, L. Kranz, D. Keller, C. Gretener, H. Hagendorfer, D. Jaeger, R. Erni, S. Nishiwaki, S. Buecheler, and A. N. Tiwari. Potassium-induced surface modification of $Cu(In,Ga)Se_2$ thin films for high-efficiency solar cells. *Nature Materials*, 12(12):1107–1111, 2013.

[8] M. Nakamura, K. Yamaguchi, Y. Kimoto, Y. Yasaki, T. Kato, and H. Sugimoto. Cd-Free $Cu(In,Ga)(Se,S)_2$ Thin-Film Solar Cell With Record Efficiency of 23.35%. *IEEE Journal of Photovoltaics*, 9(6):1863–1867, 2019.

[9] S. Wagner, J. L. Shay, P. Migliorato, and H. M. Kasper. $CuInSe_2$/CdS heterojunction photovoltaic detectors. *Applied Physics Letters*, 25(8):434–435, 1974.

[10] J. L. Shay, S. Wagner, and H. M. Kasper. Efficient $CuInSe_2$/CdS solar cells. *Applied Physics Letters*, 27(2):89–90, 1975.

[11] P. Jackson, R. Wuerz, D. Hariskos, E. Lotter, W. Witte, and M. Powalla. Effects of heavy alkali elements in Cu(In,Ga)Se_2 solar cells with efficiencies up to 22.6%. *physica status solidi (RRL) - Rapid Research Letters*, 10(8):583–586, 2016.

[12] B. Dimmler, H. Dittrich, R. Menner, and H.-W. Schock. Performance and optimization of heterojunctions based on Cu(In,Ga)Se_2. In *Proceedings of the 19th Photovoltaic Specialist Conference (PVSC)*, page 1454. IEEE, 1987.

[13] M. Ruckh, D. Schmid, and H.-W. Schock. Photoemission studies of the ZnO/CdS interface. *Journal of Applied Physics*, 76(10):5945–5948, 1994.

[14] A. Oliva, O. Solís-Canto, R. Castro-Rodríguez, and P. Quintana. Formation of the band gap energy on CdS thin films growth by two different techniques. *Thin Solid Films*, 391(1):28–35, 2001.

[15] D. Kieven, A. Grimm, I. Lauermann, T. Rissom, and R. Klenk. Band alignment at Sb2S3/Cu(In,Ga)Se_2 heterojunctions and electronic characteristics of solar cell devices based on them. *Applied Physics Letters*, 96(26):262101, 2010.

[16] P. Würfel. *Physik der Solarzellen*. volume 2. Spektrum Akademische Verlag, Heidelberg-Berlin, 2000.

[17] R. Scheer and H.-W. Schock. *Chalcogenide photovoltaics: physics, technologies, and thin film devices*. John Wiley & Sons, 2011.

[18] U. Rau and H.-W. Schock. Electronic properties of Cu(In,Ga)Se_2 heterojunction solar cells-recent achievements, current understanding, and future challenges. *Applied Physics A: Materials Science & Processing*, 69(2):131–147, 1999.

[19] U. Malm, J. Malmström, C. Platzer-Björkman, and L. Stolt. Determination of dominant recombination paths in Cu(In,Ga)Se_2 thin-film solar cells with ALD-ZnO buffer layers. *Thin Solid Films*, 480-481:208–212, 2005.

[20] U. Rau. Tunneling-enhanced recombination in Cu(In,Ga)Se_2 heterojunction solar cells. *Applied Physics Letters*, 74(1):111–113, 1999.

[21] J. Reiß. *Generation un Rekombination von Ladungsträgern in $CuInS_2$-basierten Dünnschicht-Solarzellen*. PhD thesis, Free University of Berlin, 2002.

[22] W. Shockley and H. J. Queisser. Detailed Balance Limit of Efficiency of p-n Junction Solar Cells. *Journal of applied physics*, 32(3):510–519, 1961.

[23] M. J. Kerr and A. Cuevas. General parameterization of Auger recombination in crystalline silicon. *Journal of Applied Physics*, 91(4):2473–2480, 2002.

[24] L. Huldt. Band-to-band auger recombination in indirect gap semiconductors. *Physica Status Solidi (a)*, 8(1):173–187, 1971.

[25] M. Green. Limits on the open-circuit voltage and efficiency of silicon solar cells imposed by intrinsic Auger processes. *IEEE Transactions on Electron Devices*, 31(5):671–678, 1984.

[26] A. Richter, S. W. Glunz, F. Werner, J. Schmidt, and A. Cuevas. Improved quantitative description of Auger recombination in crystalline silicon. *Physical Review B*, 86(16):165202, 2012.

[27] M. Jošt, L. Kegelmann, L. Korte, and S. Albrecht. Monolithic Perovskite Tandem Solar Cells: A Review of the Present Status and Advanced Characterization Methods Toward 30% Efficiency. *Advanced Energy Materials*, 10(26):1904102, 2020.

[28] K. Yoshikawa, W. Yoshida, T. Irie, H. Kawasaki, K. Konishi, H. Ishibashi, T. Asatani, D. Adachi, M. Kanematsu, H. Uzu, and K. Yamamoto. Exceeding conversion efficiency of 26% by heterojunction interdigitated back contact solar cell with thin film Si technology. *Solar Energy Materials and Solar Cells*, 173:37–42, 2017.

[29] V. Nadenau, U. Rau, A. Jasenek, and H.-W. Schock. Electronic properties of $CuGaSe_2$-based heterojunction solar cells. Part I. Transport analysis. *Journal of Applied Physics*, 87(1):584–593, 2000.

[30] W. Shockley and W. T. Read. Statistics of the Recombinations of Holes and Electrons. *Physical Review*, 87(5):835–842, 1952.

[31] R. N. Hall. Electron-Hole Recombination in Germanium. *Physical Review*, 87(2):387–387, 1952.

[32] T. Walter, R. Herberholz, C. Müller, and H.-W. Schock. Determination of defect distributions from admittance measurements and application to Cu(In,Ga)Se_2 based heterojunctions. *Journal of Applied Physics*, 80(8):4411–4420, 1996.

[33] T. Walter. *Herstellung und optoelektronische Charakterisierung polykristalliner I-III-VI_2-Verbindungshalbleiter und darauf basierender Heteroübergänge für Dünnschichtsolarzellen*. PhD thesis, University of Stuttgart, 1994.

[34] P. Casper, R. Hünig, G. Gomard, O. Kiowski, C. Reitz, U. Lemmer, M. Powalla, and M. Hetterich. Optoelectrical improvement of ultra-thin Cu(In,Ga)Se_2 solar cells through microstructured MgF_2 and Al_2O_3 back contact passivation layer. *physica status solidi (RRL) - Rapid Research Letters*, 10(5):376–380, 2016.

[35] J. Kessler, M. Bodegård, J. Hedström, and L. Stolt. Baseline Cu(In,Ga)Se_2 device production: control and statistical significance. *Solar Energy Materials and Solar Cells*, 67(1-4):67–76, 2001.

[36] M. Gloeckler and J. Sites. Band-gap grading in Cu(In,Ga)Se2 solar cells. *Journal of Physics and Chemistry of Solids*, 66(11):1891–1894, 2005.

[37] O. Lundberg, M. Edoff, and L. Stolt. The effect of Ga-grading in CIGS thin film solar cells. *Thin Solid Films*, 480-481:520–525, 2005.

[38] M. Topič, F. Smole, and J. Furlan. Band-gap engineering in CdS/Cu(In,Ga)Se_2 solar cells. *Journal of Applied Physics*, 79(11):8537–8540, 1996.

[39] T. Dullweber, O. Lundberg, J. Malmström, M. Bodegård, L. Stolt, U. Rau, H.-W. Schock, and J. H. Werner. Back surface band gap gradings inCu(In,Ga)Se_2 solar cells. *Thin Solid Films*, 387(1-2):11–13, 2001.

[40] J. Song, S. S. Li, C. Huang, O. Crisalle, and T. Anderson. Device modeling and simulation of the performance of Cu(In_{1-x},Ga_x)Se_2 solar cells. *Solid-State Electronics*, 48(1):73–79, 2004.

[41] R. Scheer. Activation energy of heterojunction diode currents in the limit of interface recombination. *Journal of Applied Physics*, 105(10):104505, 2009.

[42] D. Rudmann, D. Brémaud, H. Zogg, and A. N. Tiwari. Na incorporation into Cu(In,Ga)Se_2 for high-efficiency flexible solar cells on polymer foils. *Journal of Applied Physics*, 97(8):084903, 2005.

[43] P. Pistor, D. Greiner, C. A. Kaufmann, S. Brunken, M. Gorgoi, A. Steigert, W. Calvet, I. Lauermann, R. Klenk, T. Unold, and M.-C. Lux-Steiner. Experimental indication for band gap widening of chalcopyrite solar cell absorbers after potassium fluoride treatment. *Applied Physics Letters*, 105(6):063901, 2014.

[44] D. Hauschild, D. Kreikemeyer-Lorenzo, P. Jackson, T. M. Friedlmeier, D. Hariskos, F. Reinert, M. Powalla, C. Heske, and L. Weinhardt. Impact of a RbF Post-deposition Treatment on the Electronic Structure of the CdS/Cu(In,Ga)Se_2 Heterojunction in High-Efficiency Thin-Film Solar Cells. *ACS Energy Letters*, 2(10):2383–2387, 2017.

[45] E. Handick, P. Reinhard, J.-H. Alsmeier, L. Köhler, F. Pianezzi, S. Krause, M. Gorgoi, E. Ikenaga, N. Koch, R. G. Wilks, S. Buecheler, A. N. Tiwari, and M. Bär. Potassium Postdeposition Treatment-Induced Band Gap Widening at Cu(In,Ga)Se_2 Surfaces − Reason for Performance Leap?. *ACS Applied Materials & Interfaces*, 7(49):27414–27420, 2015.

[46] B. Ümsür, W. Calvet, A. Steigert, I. Lauermann, M. Gorgoi, K. Prietzel, D. Greiner, C. A. Kaufmann, T. Unold, and M. C. Lux-Steiner. Investigation of the potassium fluoride post deposition treatment on the CIGSe/CdS interface using hard X-ray photoemission spectroscopy − a comparative study. *Physical Chemistry Chemical Physics*, 18(20):14129–14138, 2016.

[47] J. Bombsch, E. Avancini, R. Carron, E. Handick, R. Garcia-Diez, C. Hartmann, R. Félix, S. Ueda, R. G. Wilks, and M. Bär. NaF/RbF-Treated Cu(In,Ga)Se_2 Thin-Film Solar Cell Absorbers: Distinct Surface Modifications Caused by Two Different Types of Rubidium Chemistry. *ACS Applied Materials & Interfaces*, 12(31):34941–34948, 2020.

[48] T. Kodalle, M. D. Heinemann, D. Greiner, H. A. Yetkin, M. Klupsch, C. Li, P. A. van Aken, I. Lauermann, R. Schlatmann, and C. A. Kaufmann. Elucidating the Mechanism of an RbF Post Deposition Treatment in CIGS Thin Film Solar Cells. *Solar RRL*, 2(9):1800156, 2018.

[49] T. Kodalle, L. Choubrac, L. Arzel, R. Schlatmann, N. Barreau, and C. A. Kaufmann. Effects of KF and RbF post deposition treatments on the growth of the CdS buffer layer on CIGS thin films - a comparative study. *Solar Energy Materials and Solar Cells*, 200:109997, 2019.

[50] T. Walter, R. Herberholz, and H.-W. Schock. Distribution of Defects in Polycrytalline Chalcopyrite Thin Films. *Solid State Phenomena*, 51-52:309–316, 1996.

[51] E. Avancini, R. Carron, T. P. Weiss, C. Andres, M. Bürki, C. Schreiner, R. Figi, Y. E. Romanyuk, S. Buecheler, and A. N. Tiwari. Effects of Rubidium Fluoride and Potassium Fluoride Postdeposition Treatments on Cu(In,Ga)Se_2 Thin Films and Solar Cell Performance. *Chemistry of Materials*, 29(22):9695–9704, 2017.

[52] T. Kodalle, R. Kormath Madam Raghupathy, T. Bertram, N. Maticiuc, H. A. Yetkin, R. Gunder, R. Schlatmann, T. D. Kühne, C. A. Kaufmann, and H. Mirhosseini. Properties of Co-Evaporated $RbInSe_2$ Thin Films. *physica status solidi (RRL) - Rapid Research Letters*, page 1800564, 2018.

[53] S. Siebentritt, E. Avancini, M. Bär, J. Bombsch, E. Bourgeois, S. Buecheler, R. Carron, C. Castro, S. Duguay, R. Félix, et al. Heavy Alkali Treatment

of Cu(In,Ga)Se_2 Solar Cells: Surface versus Bulk Effects. *Advanced Energy Materials*, 10(8):1903752, 2020.

[54] E. Handick, P. Reinhard, R. G. Wilks, F. Pianezzi, T. Kunze, D. Kreikemeyer-Lorenzo, L. Weinhardt, M. Blum, W. Yang, M. Gorgoi, E. Ikenaga, D. Gerlach, S. Ueda, Y. Yamashita, T. Chikyow, C. Heske, S. Buecheler, A. N. Tiwari, and M. Bär. Formation of a K-In-Se Surface Species by NaF/KF Postdeposition Treatment of Cu(In,Ga)Se_2 Thin-Film Solar Cell Absorbers. *ACS Applied Materials & Interfaces*, 9(4):3581–3589, 2017.

[55] I. Khatri, H. Fukai, H. Yamaguchi, M. Sugiyama, and T. Nakada. Effect of potassium fluoride post-deposition treatment on Cu(In,Ga)Se_2 thin films and solar cells fabricated onto sodalime glass substrates. *Solar Energy Materials and Solar Cells*, 155:280–287, 2016.

[56] M. Mezher, L. M. Mansfield, K. Horsley, M. Blum, R. Wieting, L. Weinhardt, K. Ramanathan, and C. Heske. KF post-deposition treatment of industrial Cu(In,Ga)$(S,Se)_2$ thin-film surfaces: Modifying the chemical and electronic structure. *Applied Physics Letters*, 111(7):071601, 2017.

[57] T. Lepetit, S. Harel, L. Arzel, G. Ouvrard, and N. Barreau. KF post deposition treatment in co-evaporated Cu(In,Ga)Se_2 thin film solar cells: Beneficial or detrimental effect induced by the absorber characteristics. *Progress in Photovoltaics: Research and Applications*, 25(12):1068–1076, 2017.

[58] T. Haalboom, T. Gödecke, F. Ernst, M. Rühle, R. Herberholz, H.-W. Schock, C. Beilharz, and K.-W. Benz. Phase relations and microstructure in bulk materials and thin films of the ternary system cu-in-se. In *In Proceedings of the 11th International Conference on Ternary and Multinary Compounds*, volume 152, pages 249–252. CRC Press, 1997.

[59] R. Caballero, C. A. Kaufmann, V. Efimova, T. Rissom, V. Hoffmann, and H.-W. Schock. Investigation of Cu(In,Ga)Se_2 thin-film formation during the multi-stage co-evaporation process: CIGSe thin-film formation multi-stage co-evaporation process. *Progress in Photovoltaics: Research and Applications*, 21(1):30–46, 2013.

[60] M. Malitckaya, H.-P. Komsa, V. Havu, and M. J. Puska. Effect of Alkali Metal Atom Doping on the $CuInSe_2$-Based Solar Cell Absorber. *The Journal of Physical Chemistry C*, 121(29):15516–15528, 2017.

[61] A. Laemmle, R. Wuerz, and M. Powalla. Investigation of the effect of potassium on Cu(In,Ga)Se_2 layers and solar cells. *Thin Solid Films*, 582:27–30, 2015.

[62] N. Taguchi, S. Tanaka, and S. Ishizuka. Direct insights into $RbInSe_2$ formation at $Cu(In,Ga)Se_2$ thin film surface with RbF postdeposition treatment. *Applied Physics Letters*, 113(11):113903, 2018.

[63] N. Maticiuc, T. Kodalle, J. Lauche, R. Wenisch, T. Bertram, C. A. Kaufmann, and I. Lauermann. In vacuo XPS investigation of Cu(In,Ga)Se $_2$ surface after RbF post-deposition treatment. *Thin Solid Films*, 665:143–147, 2018.

[64] P. Reinhard, B. Bissig, F. Pianezzi, E. Avancini, H. Hagendorfer, D. Keller, P. Fuchs, M. Döbeli, C. Vigo, P. Crivelli, S. Nishiwaki, S. Buecheler, and A. N. Tiwari. Features of KF and NaF Postdeposition Treatments of $Cu(In,Ga)Se_2$ Absorbers for High Efficiency Thin Film Solar Cells. *Chemistry of Materials*, 27(16):5755–5764, 2015.

[65] T. Lepetit, S. Harel, L. Arzel, G. Ouvrard, and N. Barreau. Coevaporated $KInSe_2$: A Fast Alternative to KF Postdeposition Treatment in High-Efficiency $Cu(In,Ga)Se_2$ Thin Film Solar Cells. *IEEE Journal of Photovoltaics*, 6(5):1316–1320, 2016.

[66] F. Larsson, O. Donzel-Gargand, J. Keller, M. Edoff, and T. Törndahl. Atomic layer deposition of Zn(O,S) buffer layers for $Cu(In,Ga)Se_2$ solar cells with KF post-deposition treatment. *Solar Energy Materials and Solar Cells*, 183:8–15, 2018.

[67] S. Ishizuka, N. Taguchi, J. Nishinaga, Y. Kamikawa, S. Tanaka, and H. Shibata. Group III Elemental Composition Dependence of RbF Postdeposition Treatment Effects on $Cu(In,Ga)Se_2$ Thin Films and Solar Cells. *The Journal of Physical Chemistry C*, 122(7):3809–3817, 2018.

[68] T. Kodalle, T. Bertram, R. Schlatmann, and C. A. Kaufmann. Effectiveness of an RbF Post Deposition Treatment of CIGS Solar Cells in Dependence on the Cu Content of the Absorber Layer. *IEEE Journal of Photovoltaics*, 9(6):1839–1845, 2019.

[69] N. Nicoara, T. Kunze, P. Jackson, D. Hariskos, R. F. Duarte, R. G. Wilks, W. Witte, M. BÃ¤r, and S. Sadewasser. Evidence for Chemical and Electronic Nonuniformities in the Formation of the Interface of RbF-Treated $Cu(In,Ga)Se_2$ with CdS. *ACS Applied Materials & Interfaces*, 9(50):44173–44180, 2017.

[70] F. Pianezzi, P. Reinhard, A. Chirilă, B. Bissig, S. Nishiwaki, S. Buecheler, and A. N. Tiwari. Unveiling the effects of post-deposition treatment with different alkaline elements on the electronic properties of CIGS thin film solar cells. *Physical Chemistry Chemical Physics*, 16(19):8843, 2014.

[71] T. Lepetit. *Influence of KF post deposition treatment on the polycrystalline Cu(In,Ga)Se_2/CdS heterojunction formation for photovoltaic application.* PhD thesis, University of Nantes, 2015.

[72] T. M. Friedlmeier, P. Jackson, D. Kreikemeyer-Lorenzo, D. Hauschild, O. Kiowski, D. Hariskos, L. Weinhardt, C. Heske, and M. Powalla. A closer look at initial CdS growth on high-efficiency Cu(In,Ga)Se $_2$ absorbers using surface-sensitive methods. In *Proceedings of the 43rd IEEE Photovoltaic Specialists Conference (PVSC)*, pages 0457–0461, Portland, OR, USA, 2016.

[73] M. A. Contreras, M. J. Romero, B. To, F. Hasoon, R. Noufi, S. Ward, and K. Ramanathan. Optimization of CBD CdS process in high-efficiency Cu(In,Ga)Se_2-based solar cells. *Thin Solid Films*, 403-404:204–211, 2002.

[74] R. Wuerz, W. Hempel, and P. Jackson. Diffusion of Rb in polycrystalline Cu(In,Ga)Se_2 layers and effect of Rb on solar cell parameters of Cu(In,Ga)Se_2 thin-film solar cells. *Journal of Applied Physics*, 124(16):165305, 2018.

[75] H. Jenny. Studies on the Mechanism of Ionic Exchange in Colloidal Aluminum Silicates. *The Journal of Physical Chemistry*, 36(8):2217–2258, 1932.

[76] D. Shin, J. Kim, T. Gershon, R. Mankad, M. Hopstaken, S. Guha, B. T. Ahn, and B. Shin. Effects of the incorporation of alkali elements on Cu(In,Ga)Se_2 thin film solar cells. *Solar Energy Materials and Solar Cells*, 157:695–702, 2016.

[77] P. Schöppe, S. Schönherr, P. Jackson, R. Wuerz, W. Wisniewski, M. Ritzer, M. Zapf, A. Johannes, C. S. Schnohr, and C. Ronning. Overall Distribution of Rubidium in Highly Efficient Cu(In,Ga)Se_2 Solar Cells. *ACS Applied Materials & Interfaces*, 10(47):40592–40598, 2018.

[78] T. P. Weiss, S. Nishiwaki, B. Bissig, R. Carron, E. Avancini, J. Löckinger, S. Buecheler, and A. N. Tiwari. Injection Current Barrier Formation for RbF Postdeposition-Treated Cu(In,Ga)Se_2-Based Solar Cells. *Advanced Materials Interfaces*, 5(4):1701007, 2018.

[79] N. Nicoara, T. Lepetit, L. Arzel, S. Harel, N. Barreau, and S. Sadewasser. Effect of the KF post-deposition treatment on grain boundary properties in Cu(In,Ga)Se_2 thin films. *Scientific Reports*, 7(1):41361, 2017.

[80] M. Raghuwanshi, E. Cadel, S. Duguay, L. Arzel, N. Barreau, and P. Pareige. Influence of Na on grain boundary and properties of Cu(In,Ga)Se_2 solar cells: Influence of Na on grain boundary and properties of Cu(In,Ga)Se_2 solar cells. *Progress in Photovoltaics: Research and Applications*, 25(5):367–375, 2017.

[81] O. Cojocaru-Mirédin, P.-P. Choi, D. Abou-Ras, S. S. Schmidt, R. Caballero, and D. Raabe. Characterization of Grain Boundaries in Cu(In,Ga)Se_2 Films Using Atom-Probe Tomography. *IEEE Journal of Photovoltaics*, 1(2):207–212, 2011.

[82] P.-P. Choi, O. Cojocaru-Mirédin, R. Wuerz, and D. Raabe. Comparative atom probe study of Cu(In,Ga)Se_2 thin-film solar cells deposited on soda-lime glass and mild steel substrates. *Journal of Applied Physics*, 110(12):124513, 2011.

[83] A. Laemmle, R. Wuerz, T. Schwarz, O. Cojocaru-Mirédin, P.-P. Choi, and M. Powalla. Investigation of the diffusion behavior of sodium in Cu(In,Ga)Se_2 layers. *Journal of Applied Physics*, 115(15):154501, 2014.

[84] D. Colombara, H. Elanzeery, N. Nicoara, D. Sharma, M. Claro, T. Schwarz, A. Koprek, M. H. Wolter, M. Melchiorre, M. Sood, N. Valle, O. Bondarchuk, F. Babbe, C. Spindler, O. Cojocaru-Miredin, D. Raabe, P. J. Dale, S. Sadewasser, and S. Siebentritt. Chemical instability at chalcogenide surfaces impacts chalcopyrite devices well beyond the surface. *Nature Communications*, 11(1):3634, 2020.

[85] M. Chugh, T. D. Kühne, and H. Mirhosseini. Diffusion of Alkali Metals in Polycrystalline $CuInSe_2$ and Their Role in the Passivation of Grain Boundaries. *ACS Applied Materials & Interfaces*, 11(16):14821–14829, 2019.

[86] R. Kormath Madam Raghupathy, T. D. Kühne, G. Henkelman, and H. Mirhosseini. Alkali Atoms Diffusion Mechanism in $CuInSe_2$ Explained by Kinetic Monte Carlo Simulations. *Advanced Theory and Simulations*, page 1900036, 2019.

[87] S. Zahedi-Azad and R. Scheer. Quenching interface recombination in wide bandgap Cu(In,Ga)Se_2 by potassium treatment. *physica status solidi c*, 14(6):1600203, 2017.

[88] I. Khatri, K. Shudo, J. Matsuura, M. Sugiyama, and T. Nakada. Impact of heat-light soaking on potassium fluoride treated CIGS solar cells with CdS buffer layer. *Progress in Photovoltaics: Research and Applications*, 26(3):171–178, 2018.

[89] C. P. Muzzillo. Review of grain interior, grain boundary, and interface effects of K in CIGS solar cells: Mechanisms for performance enhancement. *Solar Energy Materials and Solar Cells*, 172:18–24, 2017.

[90] T. Kato, J.-L. Wu, Y. Hirai, H. Sugimoto, and V. Bermudez. Record Efficiency for Thin-Film Polycrystalline Solar Cells Up to 22.9% Achieved by Cs-Treated Cu(In,Ga)$(Se,S)_2$. *IEEE Journal of Photovoltaics*, 9(1):325–330, 2019.

[91] S. Karki, S. Marsillac, P. Paul, G. Rajan, B. Belfore, D. Poudel, A. Rockett, E. Danilov, F. Castellano, and A. Arehart. Analysis of Recombination Mechanisms in RbF-Treated CIGS Solar Cells. *IEEE Journal of Photovoltaics*, 9(1):313–318, 2019.

[92] J. M. Raguse, C. P. Muzzillo, J. R. Sites, and L. Mansfield. Effects of Sodium and Potassium on the Photovoltaic Performance of CIGS Solar Cells. *IEEE Journal of Photovoltaics*, 7(1):303–306, 2017.

[93] A. Villanueva-Tovar, T. Kodalle, C. A. Kaufmann, R. Schlatmann, and R. Klenk. Limitation of Current Transport across the Heterojunction in Cu(In,Ga)Se_2 Solar Cells Prepared with Alkali Fluoride Postdeposition Treatment. *Solar RRL*, 4(4):1900560, 2020.

[94] S. Ishizuka, T. Koida, N. Taguchi, S. Tanaka, P. Fons, and H. Shibata. Si-Doping Effects in Cu(In,Ga)Se_2 Thin Films and Applications for Simplified Structure High-Efficiency Solar Cells. *ACS Applied Materials & Interfaces*, 9(36):31119–31128, 2017.

[95] R. Knecht, M. S. Hammer, J. Parisi, and I. Riedel. Impact of varied sulfur incorporation on the device performance of sequentially processed Cu(In,Ga)$(Se,S)_2$ thin film solar cells: Device performance of sequentially processed Cu(In,Ga)$(Se,S)_2$ thin film solar cells. *physica status solidi (a)*, 210(7):1392–1399, 2013.

[96] P. Schöppe, S. Schönherr, R. Wuerz, W. Wisniewski, G. Martínez-Criado, M. Ritzer, K. Ritter, C. Ronning, and C. S. Schnohr. Rubidium segregation at random grain boundaries in Cu(In,Ga)Se_2 absorbers. *Nano Energy*, 42:307–313, 2017.

[97] T. Kodalle. *Unraveling the Structural and Optoelectronic Effects of Rb on Chalcopyrite Solar Cells*. PhD thesis, Martin Luther University of Halle-Wittenberg, 2020.

[98] M. Troviano and K. Taretto. Analysis of internal quantum efficiency in double-graded bandgap solar cells including sub-bandgap absorption. *Solar Energy Materials and Solar Cells*, 95(3):821–828, 2011.

[99] R. Mainz. Private communication.

[100] M. Burgelman, P. Nollet, and S. Degrave. Modelling polycrystalline semiconductor solar cells. *Thin Solid Films*, 361-362:527–532, 2000.

[101] S. Selberherr. *Analysis and simulation of semiconductor devices*. Springer Verlag, 1984.

[102] A. Niemegeers and M. Burgelman. Numerical modelling of AC-characteristics of CdTe and CIS solar cells. In *Conference Record of the 25th IEEE Photovoltaic Specialists Conference*, pages 901–904, Washington, DC, USA, 1996.

[103] K. Decock, S. Khelifi, and M. Burgelman. Modelling multivalent defects in thin film solar cells. *Thin Solid Films*, 519(21):7481–7484, 2011.

[104] M. Burgelman and J. Marlein. Analysis of graded band gap solar cells with SCAPS. In *Proceedings of the 23rd European Photovoltaic Solar Energy Conference*, pages 2151–2155, Valencia, Spain, 2008.

[105] J. Verschraegen and M. Burgelman. Numerical modeling of intra-band tunneling for heterojunction solar cells in scaps. *Thin Solid Films*, 515(15):6276–6279, 2007.

[106] S. Degrave, M. Burgelman, and P. Nollet. Modelling of polycrystalline thin film solar cells: new features in SCAPS version 2.3. In *Proceedings of the 3rd World Conference on Photovoltaic Energy Conversion*, pages 487–490. IEEE, 2003.

[107] M. Gloeckler, A. L. Fahrenbruch, and J. R. Sites. Numerical modeling of CIGS and CdTe solar cells: Setting the baseline. In *Proceedings of the 3rd World Conference on Photovoltaic Energy Conversion, 2003*, pages 491–494. IEEE, 2003.

[108] A. J. Nelson, S. Gebhard, A. Rockett, E. Colavita, M. Engelhardt, and H. Höchst. Synchrotron-radiation photoemission study of CdS/$CuInSe_2$ heterojunction formation. *Physical Review B*, 42(12):7518–7523, 1990.

[109] S. Wei and A. Zunger. Band offsets at the CdS/$CuInSe_2$ heterojunction. *Applied Physics Letters*, 63(18):2549–2551, 1993.

[110] D. Schmid, M. Ruckh, and H.-W. Schock. A comprehensive characterization of the interfaces in Mo/CIS/CdS/ZnO solar cell structures. *Solar Energy Materials and Solar Cells*, 63:281–294, 1996.

[111] A. Niemegeers, M. Burgelman, R. Herberholz, U. Rau, and D. Hariskos. Model for electronic transport in Cu(In,Ga)Se_2 solar cells. *Progress in Photovoltaics: Research and Applications*, 6:407–421, 1998.

[112] R. Klenk. Characterisation and modelling of chalcopyrite solar cells. *Thin Solid Films*, 387(1-2):135–140, 2001.

[113] G. Sozzi, S. Di Napoli, R. Menozzi, F. Werner, S. Siebentritt, P. Jackson, and W. Witte. Influence of Conduction Band Offsets at Window/Buffer and Buffer/Absorber Interfaces on the Roll-Over of J-V Curves of CIGS Solar Cells.

In *Proceedings of the 44th IEEE Photovoltaic Specialist Conference (PVSC)*, pages 2205–2208, Washington, DC, 2017.

[114] F. Werner, M. H. Wolter, S. Siebentritt, G. Sozzi, S. Di Napoli, R. Menozzi, P. Jackson, W. Witte, R. Carron, E. Avancini, T. P. Weiss, and S. Buecheler. Alkali treatments of Cu(In,Ga)Se_2 thin-film absorbers and their impact on transport barriers. *Progress in Photovoltaics: Research and Applications*, 26(11):911–923, 2018.

[115] X. Zhang, Z. Yuan, and S. Chen. Low Electron Carrier Concentration Near the p-n Junction Interface: A Fundamental Factor Limiting Short-Circuit Current of Cu(In,Ga)Se_2 Solar Cells. *Solar RRL*, 3(6):1900057, 2019.

[116] T. Walter, D. Braunger, D. Hariskos, C. Köble, and H.-W. Schock. In *Proceedings of the 13th EU PVSEC*, page 597, Munich, Germany, 1995.

[117] P. Pistor and R. Klenk. On the advantage of a buried pnjunction in chalcopyrite solar cells: An urban legend. In *Proceedings of the International Workshop on Numerical Modelling of Thin Film Solar Cells*, pages 179–182, Gent, Belgium, 2007.

[118] J. Zhang, G. He, L. Zhu, M. Liu, S. Pan, and L. Zhang. Effect of oxygen partial pressure on the structural and optical properties of ZnO film deposited by reactive sputtering. *Applied Surface Science*, 253(24):9414–9421, 2007.

[119] M. Heinemann. *CIGSe Superstrate Solar Cells: Growth and Characterization of CIGSe Thin Films on Transparent Conductive Oxides*. PhD thesis, Technical University Berlin, 2015.

[120] T. Hölscher, T. Schneider, M. Maiberg, and R. Scheer. Impact of air-light exposure on the electrical properties of Cu(In,Ga)Se_2 solar cells. *Progress in Photovoltaics: Research and Applications*, 26(11):934–941, 2018.

[121] T. Ott, T. Walter, and T. Unold. Phototransistor effects in Cu(In,Ga)Se_2 solar cells. *Thin Solid Films*, 535:275–278, 2013.

[122] T. Eisenbarth, R. Caballero, M. Nichterwitz, C. A. Kaufmann, H.-W. Schock, and T. Unold. Characterization of metastabilities in Cu(In,Ga)Se_2 thin-film solar cells by capacitance and current-voltage spectroscopy. *Journal of Applied Physics*, 110(9):094506, 2011.

[123] A. Niemegeers and M. Burgelman. Effects of the Au/CdTe back contact on IV and CV characteristics of Au/CdTe/CdS/TCO solar cells. *Journal of Applied Physics*, 81(6):2881–2886, 1997.

[124] A. Rockett, J. van Duren, A. Pudov, and W. Shafarman. First quadrant phototransistor behavior in Cu(In,Ga)Se_2 photovoltaics. *Solar Energy Materials and Solar Cells*, 118:141–148, 2013.

[125] D. Schmid, M. Ruckh, F. Grunwald, and H.-W. Schock. Chalcopyrite/defect chalcopyrite heterojunctions on the basis of $CuInSe_2$. *Journal of Applied Physics*, 73(6):2902–2909, 1993.

[126] H. Mönig, C.-H. Fischer, R. Caballero, C. Kaufmann, N. Allsop, M. Gorgoi, R. Klenk, H.-W. Schock, S. Lehmann, and M. Lux-Steiner. Surface Cu depletion of Cu(In,Ga)Se_2 films: An investigation by hard X-ray photoelectron spectroscopy. *Acta Materialia*, 57(12):3645–3651, 2009.

[127] T. Ott, F. Schönberger, T. Walter, D. Hariskos, O. Kiowski, O. Salomon, and R. Schäffler. Verification of phototransistor model for Cu(In,Ga)Se_2 solar cells. *Thin Solid Films*, 582:392–396, 2015.

[128] A. Villanueva-Tovar, T. Kodalle, R. Klenk, C. A. Kaufmann, and R. Schlatmann. Influence of RbF on recombination mechanisms in Cu(In,Ga)Se_2 thin film solar cells. E-MRS Spring Meeting Strasbourg, France, 18.06.2018 - 22.06.2018 (2018).

[129] T. Kato, A. Handa, T. Yagioka, T. Matsuura, K. Yamamoto, S. Higashi, J.-L. Wu, K. F. Tai, H. Hiroi, T. Yoshiyama, T. Sakai, and H. Sugimoto. Enhanced Efficiency of Cd-Free Cu(In,Ga)$(Se,S)_2$ Minimodule Via (Zn,Mg)O Second Buffer Layer and Alkali Metal Post-Treatment. *IEEE Journal of Photovoltaics*, 7(6):1773–1780, 2017.

[130] J. Nishinaga, T. Koida, S. Ishizuka, Y. Kamikawa, H. Takahashi, M. Iioka, H. Higuchi, Y. Ueno, H. Shibata, and S. Niki. Effects of long-term heat-light soaking on Cu(In,Ga)Se_2 solar cells with kf postdeposition treatment. *Applied Physics Express*, 10(9):092301, 2017.

[131] O. Dupré, R. Vaillon, and M. A. Green. Temperature coefficients of photovoltaic devices. In *Temperature Coefficients of Photovoltaic Devices. In: Thermal Behavior of Photovoltaic Devices*, pages 29–74. Springer, 2017.

[132] T. Dullweber, G. Hanna, W. Shams-Kolahi, A. Schwartzlander, M. Contreras, R. Noufi, and H. Schock. Study of the effect of gallium grading in Cu(In,Ga)Se_2. *Thin Solid Films*, 361-362:478–481, 2000.

[133] H. A. Yetkin, T. Kodalle, T. Bertram, A. Villanueva-Tovar, M. Rusu, R. Klenk, B. Szyszka, R. Schlatmann, and C. A. Kaufmann. Decay Mechanisms in CdS-Buffered Cu(In,Ga)Se_2 Thin-Film Solar Cells After Exposure to Thermal

Stress:Understanding the Role of Na. *Progress in Photovoltaics: Research and Applications*, pages 1–20, 2021.

[134] P. Reyes-Figueroa, T. Kodalle, T. Bertram, A. Villanueva-Tovar, E. Waack, R. Haberecht, C. A. Kaufmann, R. Schlatmann, and R. Klenk. Alkali post-deposition treatment of Cu(In,Ga)(S,Se)$_2$ solar cell absorbers grown under atmospheric pressure. In *Proceedings of the 37th EU PVSEC*, pages 718–721, 2020.

[135] I. Hengel, A. Neisser, R. Klenk, and M. Lux-Steiner. Current transport in CuInS2:Ga/Cds/ZnO - solar cells. *Thin Solid Films*, 361-362:458–462, 2000.

[136] I. Hengel. *Ladungsträgertransport und Rekombinationsmechanismen in Chalkopyrit-Dünnschichtsolarzellen*. PhD thesis, Free University of Berlin, 2000.

[137] I. Lauermann, A. Steigert, R. Klenk, L. Risch, R. Sáez-Araoz, J. Krammer, C.-H. Fischer, M. C. Lux-Steiner, F. Stober, and F. Hergert. Analysis of the dynamic behavior of sodium on surfaces and interfaces of chalcopyrite thin film solar cell absorbers and its influence on solar cell characteristics. 28th EU PVSEC Paris, France, 30.09.2013 - 04.10.2013 (2013).

[138] C. H. Park, S. B. Zhang, and S.-H. Wei. Origin of *p*-type doping difficulty in ZnO: The impurity perspective. *Physical Review B*, 66(7):073202, 2002.

[139] B. Meyer, J. Stehr, A. Hofstaetter, N. Volbers, A. Zeuner, and J. Sann. On the role of group I elements in ZnO. *Applied Physics A*, 88(1):119–123, 2007.

[140] M. D. Heinemann, D. Greiner, T. Unold, R. Klenk, H.-W. Schock, R. Schlatmann, and C. A. Kaufmann. The Importance of Sodium Control in CIGSe Superstrate Solar Cells. *IEEE Journal of Photovoltaics*, 5(1):378–381, 2015.

[141] R. Klauser, M. Oshima, H. Sugahara, Y. Murata, and H. Kato. RbF as reactive and dipole interlayers between the Ge/GaAs interface. *Physical Review B*, 43(6):4879–4884, 1991.

[142] T. Kodalle, H. A. Yetkin, A. Villanueva-Tovar, T. Bertram, R. Klenk, R. Schlatmann, and C. A. Kaufmann. A Device Model for Rb-Conditioned Chalcopyrite Solar Cells. *IEEE Journal of Photovoltaics*, 11(1):232–240, 2021.

[143] T. Kodalle, H. A. Yetkin, T. Bertram, R. Schlatmann, and C. A. Kaufmann. Setting up a Device Model for Rb-Conditioned Chalcopyrite Solar Cells. In *Proceedings of the 47th IEEE Photovoltaic Specialists Conference (PVSC)*, pages 1156–1162, Calgary, OR, 2020.

[144] S. Sharbati and J. R. Sites. Impact of the Band Offset for n-Zn(O,S)/p-Cu(In,Ga)Se_2 Solar Cells. *IEEE Journal of Photovoltaics*, 4(2):697–702, 2014.

[145] T. H. Kim, J. J. Park, S. H. Nam, H. S. Park, N. R. Cheong, J. K. Song, and S. M. Park. Fabrication of Mg-doped ZnO thin films by laser ablation of Zn:Mg target. *Applied Surface Science*, 255(10):5264–5266, 2009.

[146] T. Bertram, T. Kodalle, P. Reyes-Figueroa, J. Lauche, R. Klenk, R. Schlatmann, and C. A. Kaufmann. How is the back-contact in CIGSe thin film devices affected by heavy alkali treatments?. 37th EU PVSEC, 07.09.2020 - 11.09.2020 (2020).

[147] S. S. Schmidt, C. Wolf, H. Rodriguez-Alvarez, J.-P. Bäcker, C. A. Kaufmann, S. Merdes, F. Ziem, M. Hartig, S. Cinque, I. Dorbandt, C. Köble, D. Abou-Ras, R. Mainz, and R. Schlatmann. Adjusting the Ga grading during fast atmospheric processing of Cu(In,Ga)Se_2 solar cell absorber layers using elemental selenium vapor: Adjusting the Ga grading in fast processing of CIGSe. *Progress in Photovoltaics: Research and Applications*, 25(5):341–357, 2017.

List of publications

First-authorship:

- A. Villanueva-Tovar, T. Kodalle, C. A. Kaufmann, R. Schlatmann, and R. Klenk. Limitation of Current Transport across the Heterojunction in Cu(In,Ga)Se_2 Solar Cells Prepared with Alkali Fluoride Postdeposition Treatment. *Solar RRL*, 4(4):1900560, 2020.

Co-authorship:

- T. Kodalle, H. A. Yetkin, A. Villanueva-Tovar, T. Bertram, R. Klenk, R. Schlatmann, and C. A. Kaufmann. A Device Model for Rb-Conditioned Chalcopyrite Solar Cells. *IEEE Journal of Photovoltaics*, 11(1):232-240, 2021.
- P. Reyes-Figueroa, T. Kodalle, T. Bertram, A. Villanueva-Tovar, E. Waack, R. Haberecht, C. A. Kaufmann, R. Schlatmann, and R. Klenk. Alkali post-deposition treatment of Cu(In,Ga)$(S,Se)_2$ solar cell absorbers grown under atmospheric pressure. In *Proceedings of the 37th EU PVSEC*, pages 718-721, 2020.
- H. A. Yetkin, T. Kodalle, T. Bertram, A. Villanueva-Tovar, R. Klenk, B. Szyszka, R. Schlatmann, and C. A. Kaufmann. Comparison of the Thermal Stability of Differently Buffered CIGSe Solar Cells. In *Proceedings of the 47th IEEE Photovoltaic Specialists Conference (PVSC)*, pages 1192-1197, 2020.
- H. A. Yetkin, T. Kodalle, T. Bertram, A. Villanueva-Tovar, R. Klenk, M. Rusu, J. Ibaceta-Jaña, F. Ruske, I. Simsek, R. Muydinov, B. Szyszka, R. Schlatmann, and C. A. Kaufmann. Elucidating the Effect of the Different Buffer Layers on the Thermal Stability of CIGSe Solar Cells. *IEEE Journal of Photovoltaics*, 11(3):648-657, 2021.
- H. A. Yetkin, T. Kodalle, T. Bertram, A. Villanueva-Tovar, M. Rusu, R. Klenk, B. Szyzska, R. Schlatmann, and C. A. Kaufmann. Decay Mechanisms in CdS-Buffered Cu(In,Ga)Se_2 Thin-Film Solar Cells After Exposure to Thermal Stress: Understanding the Role of Na. *Progress in Photovoltaics: Research and Applications*, pages 1-20, 2021.

Acknowledgments

First of all I would like to thank Reiner Klenk who shared his valuable knowledge with me, for supervising my work, for his patience and time throughout these years. Furthermore, I want to thank Rutger Schlatmann and Bernd Rech for their support, for reviewing my thesis and making my stay and work at HZB/PVcomB possible.
Special thanks to Marin Rusu, who was my first contact at HZB and helped me with everything I needed to apply to my doctoral studies, and also together with Sven Wiesner, thanks for instructing me to operate the JVT and some other setups while working in Wannsee.
I want to acknowledge Christian Kaufmann, Tim Kodalle, Hasan A. Yetkin and Tobias Bertram for their fruitful discussions and for providing me the samples for my research.
Many thanks to the amazing RTP group, Erik Waack, Pablo Reyes, Guillermo Farias, Ralf Haberecht, Michael Kirsch and Stefanie Stutzke, for the good time spent at PVcomB and during our meetings.
Also, thanks to my PhD colleagues Alex Cruz, Fuxi Bao and Stefan Körner for their company and for the de-stressing moments lived in the PhD office.

I would especially like to acknowledge the Mexican National Council for Science and Technology (CONACYT), the German Academic Exchange Service (DAAD) and EDUCAFIN for their trust in me and my work and for financing my studies in Berlin.

I am also very grateful to all my dear friends that I met in Berlin, Elisa, Ana Lucía, Alejandro, Silvina, Flor, John, Richy, Tim S. and Isheta, thank you all for always being there with me during the hardest and most stressful times but also during the most amazing and unforgettable moments. Thanks for being my family in Berlin.

Finally, I want to thank my beloved family, my parents, Lourdes and José Isaac, my sister and brother-in-law, Mariana and Miguel, and my lovely nieces, Miranda, Marianita and Sofía, for being an important part for the completion of my studies, for their great support even at a distance and their unconditional love.